CWP-1029

MODELING AND IMAGING MARINE VIBRATOR DATA

by

Khalid Almuteri

© **Copyright by Khalid Almuteri, 2023**

All Rights Reserved

A thesis submitted to the Faculty and the Board of Trustees of the Colorado School of Mines in partial fulfillment of the requirements for the degree of Doctor of Philosophy (Geophysics).

Golden, Colorado

Date _____

Signed: _____

Khalid Almuteri

Signed: _____

Dr. Paul Sava
Thesis Advisor

Golden, Colorado

Date _____

Signed: _____

Dr. Paul Sava
Professor and Department Head
Department of Geophysics

ABSTRACT

Marine vibrators are an emerging alternative technology to conventional air guns in ocean-bottom seismic acquisition. They promise to deliver greater low-frequency information about the subsurface while minimizing the adverse impact on marine wildlife. However, using marine vibrators introduces challenges not found in conventional air-gun-based acquisition. Even though marine vibrators move at a much slower velocity than the acoustic wave subsurface speed, source motion introduces a noticeable offset and time-dependent frequency shift to the data. Phase distortions also occur in seismic signals and are proportional to the source velocity and moveout of seismic events. The time-varying nature of the sea surface and the long duration of the seismic sweep present an additional set of modeling, processing, and imaging challenges. A dynamic sea surface significantly affects the phase and amplitude of seismic data, posing challenges for time-lapse studies, seismic deghosting, and surface-related multiple elimination. Conventional seismic data processing assumes a horizontal sea surface for simplification. However, characterizing the sea surface state and accurately modeling seismic data under such conditions is important for investigating the implications of realistic acquisition and for proper processing and imaging workflow design.

In this thesis, I develop a numerical approach to model long-emitting non-impulsive sources in the presence of a time-varying sea surface using the tensorial acoustic wave equation. I also derive analytical expressions to predict the frequency shifts in the seismic signal due to source motion (Doppler effect) and predict the seismic wavefield in homogeneous media triggered by a moving source (Green's function), which I use to validate the developed modeling approach. Furthermore, I use the developed tools to account for the source motion effects in reverse-time migration, mitigating the need for pre-processing steps to remove such effects from the seismic data. I present numerical examples that demonstrate the accuracy, stability, and robustness of the tensorial formulation of the acoustic wave equation in modeling and

imaging marine vibrator data, even for typically unincorporated high source velocities in field data acquisition.

TABLE OF CONTENTS

ABSTRACT iii

LIST OF FIGURES ix

LIST OF TABLES xvi

LIST OF ABBREVIATIONS xvii

ACKNOWLEDGMENTS xix

DEDICATION xxi

CHAPTER 1 INTRODUCTION 1

1.1 Seismic air-gun data 1

1.2 Marine vibrator data 2

1.3 Thesis outline 4

CHAPTER 2 SEISMIC DEGHOSTING USING CONVOLUTIONAL NEURAL NETWORKS 7

2.1 Introduction 8

2.1.1 Acquisition deghosting 8

2.1.2 Processing deghosting 10

2.2 CNN-based deghosting 12

2.2.1 Background 12

2.2.2 Neural network architecture 16

2.3 Numerical example 19

2.3.1 Neural network training dataset 19

2.3.2 Seismic deghosting: Synthetic data example 21

2.3.3 Seismic deghosting: Field data example 29

2.4 Discussion 33

2.5 Conclusion 37

2.6 Acknowledgments 38

2.7 Data and materials availability 38

CHAPTER 3 MODELING THE SEISMIC WAVEFIELD OF MOVING MARINE VIBRATOR SOURCE 39

3.1 Introduction 40

3.2 Theory 43

3.2.1 Tensorial acoustic wave equation 44

3.2.2 Numerical implementation 47

3.2.3 Doppler effect 48

3.3 Numerical Examples 50

3.3.1 Modeling in homogeneous media 51

3.3.2 Modeling in a single-reflector model 53

3.3.3 Modeling in a velocity gradient medium 56

3.3.4 Modeling in heterogeneous media 59

3.4 Discussion 69

3.5 Conclusions 70

3.6 Acknowledgments 70

3.7 Data and materials availability 71

3.8 APPENDIX: Analytical solution to the acoustic wave equation for a moving source 71

CHAPTER 4 MODELING ACOUSTIC WAVEFIELDS FROM MOVING SOURCES IN THE PRESENCE OF A TIME-VARYING FREE-SURFACE 74

4.1 Introduction 75

4.2 Theory 78

4.2.1 Tensorial AWE 79

4.2.2 Coupled first-order acoustic PDE system 81

4.2.3 3D moving source with time-varying sea surface 82

4.2.4 Coordinate transformation 83

4.2.5 Time-varying sea surface 84

4.3 Numerical approach 84

4.3.1 Fully staggered grid 84

4.3.2 Mimetic finite-difference operators 86

4.3.3 Prediction step staggered-in-time 87

4.4 Numerical Examples 90

4.4.1 Exaggerated sea state 91

4.4.2 Realistic sea state 93

4.5 Discussion 96

4.6 Conclusions 98

4.7 Acknowledgments 99

4.8 Data and materials availability 99

4.9 APPENDIX: Taylor-based coefficients to approximate advection terms . . . 100

CHAPTER 5 REVERSE-TIME MIGRATION OF MARINE VIBRATOR DATA . . 101

5.1 Introduction 102

5.2 Theory . . . 103
5.2.1 Tensorial AWE . . . 103
5.2.2 Reverse-time migration . . . 105
5.3 Numerical Example . . . 106
5.4 Marmousi model . . . 106
5.5 Dipping reflectors model . . . 111
5.6 Discussion . . . 117
5.7 Conclusions . . . 120
5.8 Acknowledgments . . . 121
5.9 Data and materials availability . . . 121
5.9.1 APPENDIX: Adjoint modeling operator . . . 121
5.9.2 APPENDIX: Born modeling (single scattering) . . . 124
CHAPTER 6 CONCLUSIONS . . . 126
REFERENCES . . . 129
APPENDIX A ABSORBING BOUNDARY CONDITIONS . . . 144
A.1 Clayton-Enquist boundary condition . . . 144
A.2 Perfectly matched layer boundary condition . . . 145
APPENDIX B COPYRIGHT PERMISSION . . . 147

LIST OF FIGURES

Figure 2.1 (a) An example of a fully-connected NN with two input units, two hidden layers with four units in each layer, and one output unit. (b) A simple model of a neuron connected to four other neurons from a preceding layer. The neuron's output is $a_j^l = g\left(\sum_{i=0}^{n} w_{ij}^l a_i^{l-1}\right)$, where a_j^l is the value at the jth neuron at the lth layer, w_{ij}^l is the weight that connects the ith neuron at the $(l-1)$th layer with the jth neuron at the lth layer, n is the number of neurons in the $(l-1)$th layer, and g is a nonlinear activation function. 13

Figure 2.2 An illustration of the architecture of the network we use for seismic deghosting on 2D data. Each gray cuboid labeled with Conv represents a multichannel feature map generated using N convolutional filters ($N = 16$). The height of each cuboid corresponds to the number of time samples ($n_t = 3526$) and the width corresponds to the number of traces in the gather ($n_r = 564$). Each yellow cuboid represents a temporal masking layer in the network. 17

Figure 2.3 submodels from the Marmousi model, with 710 m added water layer on top, used for training. The black line corresponds to the air-water interface. 20

Figure 2.4 submodel from the Amoco statics test model to test the CNN. The velocity values of this model are not within the range of the velocity values of the training models. We add a water layer with 710 m depth to the top. The black line corresponds to the air-water interface. 21

Figure 2.5 Comparison among (a) true ghost-free, (b) ghost-contaminated, and (c) ghost-free prediction shot gathers. (d-f) After applying 20 Hz high-cut filtering in Figure 2.5(a-c), respectively. 23

Figure 2.6 Comparison among the average amplitude spectra of the ghost-free data (black line), the ghost-contaminated data (red line), and the ghost-free prediction data (blue line). (a) Comparison between the full bandwidth data shown in Figure 2.5(a-c). (b) Comparison between the band-limited data shown in Figure 2.5(d-f). 24

Figure 2.7 Relative ℓ^2 residual between the true ghost-free gather (Figure 2.5(a)) and the ghost-contaminated gather (Figure 2.5(b)) (red) over different frequency bands, with a bandwidth of 3.5 Hz for each band, and between the true ghost-free gather and the ghost-free prediction (Figure 2.5(c)) (blue). 25

Figure 2.8 The frequency-wavenumber spectra of (a) Figure 2.5(a), (b) Figure 2.5(b), (c) Figure 2.5(c), (d) Figure 2.5(d), (e) Figure 2.5(e), (f) Figure 2.5(f). 26

Figure 2.9 Comparison between traces recorded at a receiver that is 3930 m away from the source. (a) Comparison between ghost-free (black line) and ghost-contaminated (red line) traces. (b) Comparison between ghost-free and ghost-free prediction (blue line) traces. (c) and (d) Comparison between the amplitude spectra of the traces shown in Figure 2.9(a) and Figure 2.9(b), respectively. 27

Figure 2.10 Comparison between traces recorded at a receiver that is 3930 m away from the source after applying a 20 Hz low-pass filter. (a) Comparison between ghost-free (black line) and ghost-contaminated (red line) traces. (b) Comparison between ghost-free and ghost-free prediction (blue line) traces. (c) and (d) Comparison between the amplitude spectra of the traces shown in Figure 2.10(a) and Figure 2.10(b), respectively. 28

Figure 2.11 (a) The correlation coefficient between the true ghost-free data and ghost-contaminated data (red) and true ghost-free data and ghost-free prediction (blue) for the full bandwidth individual traces. (b) The correlation coefficient between the true-ghost free data and ghost-contaminated data (red) and true ghost-free data and ghost-free prediction (blue) for the band-limited individual traces 30

Figure 2.12 Comparison between (a) ghost-contaminated and (b) ghost-free prediction shot gathers. Figure 2.12(c) and Figure 2.12(d) After applying 20 Hz high-cut filtering in Figure 2.12(a) and Figure 2.12(b), respectively. The dashed red lines are for cross referencing. 31

Figure 2.13 Comparison between the average amplitude spectra of the ghost-contaminated data (red line) and the ghost-free prediction data (blue line). (a) Comparison between the full bandwidth data shown in Figure 2.12(a) and Figure 2.12(b). (b) Comparison between the band limited data shown in Figure 2.12(c) and Figure 2.12(d). 32

Figure 2.14 Comparison between (a) ghost-contaminated and (b) ghost-free prediction stacked sections. (c) and (d) Comparison between the sections shown in Figure 2.14(a) and Figure 2.14(b), respectively, after applying a 20 Hz low-pass filter. 34

Figure 2.15 Comparison between the average amplitude spectra of the ghost-contaminated (red line) and ghost-free prediction stacked sections. (a) Comparison between the full bandwidth sections shown in Figure 2.14(a) and Figure 2.14(b). (b) Comparison between the band-limited sections shown in Figure 2.14(c) and Figure 2.14(d). 35

Figure 3.1 Graphical representation of (a) physical and (b) computational domains. The red dot indicates the source location. The blue mesh represents a homogeneous region, whereas the black mesh represents a variable velocity region. 46

Figure 3.2 Schematic plot of (a) source motion direction ($\mathbf{S}$) relative to a stationary receiver or a scatterer point location ($\mathbf{R}$) in a constant velocity medium, and (b) a source moving from S_1 to S_2 with ray paths from source locations S_1 and S_2 to a point R in the subsurface given by P_1 and P_2, respectively, in a variable velocity medium. 49

Figure 3.3 Wavefield snapshot in a homogeneous medium using (a) stationary and (b) mobile source. 52

Figure 3.4 Shot gathers acquired in a homogeneous medium using (a) stationary and (b) mobile sources. 53

Figure 3.5 Pressure amplitude of (a) 30 Hz monochromatic wave (source function), and seismic data measured by receivers located (b) behind ($x^1 = 1.75$ km) and (c) ahead ($x^1 = 2.75$ km) of the source. The dashed line is the analytical solution, which overlay the numerical solution shown in solid line. 54

Figure 3.6 (a-c) Amplitude spectra of traces shown in Figure 3.5(a-c), respectively. The dashed line is the analytical solution, which overlay the numerical solution shown in solid line. 55

Figure 3.7 Single-reflector velocity model (quantity c in equation 3.8) with the source position at time $t = 0$ s (red) and stationary receivers locations (white). 56

Figure 3.8 Shot gathers acquired in a single-reflector model using (a) stationary and (b) mobile sources with ghost reflections. 57

Figure 3.9 Frequency-wavenumber spectra of shot gathers shown in (a) Figure 3.8(a) and (b) Figure 3.8(b). The red and white arrows indicate constructive and destructive interference, respectively. 58

Figure 3.10 (a) Homogeneous and (b) constant vertical velocity gradient models (quantity c in equation 3.8) with the source position at time $t = 0$ s (red) and stationary receivers locations (white). 60

Figure 3.11 Mobile source in a homogeneous medium. Top: seismic data measured by receivers located at $x^3 = 1.25$ km (blue) and $x^3 = 2.75$ km (red). Middle: corresponding amplitude spectra of traces shown in the top panel. Bottom: theoretical observed frequencies as a function of depth. . 61

Figure 3.12 Mobile source in a velocity gradient medium. Top: seismic data measured by receivers located at $x^3 = 1.25$ km (blue) and $x^3 = 2.75$ km (red). Middle: corresponding amplitude spectra of traces shown in the top panel. Bottom: theoretical observed frequencies as a function of depth. 62

Figure 3.13 Marmousi II velocity model (quantity c in equation 3.8) with the source position (red) and receiver locations (white) at time $t = 0$ s for (a) moving source and stationary receivers (ocean bottom) acquisition and (b) stationary source and moving receivers (streamer) acquisition. Figure is not displayed with the true aspect ratio. 64

Figure 3.14 Shot gathers acquired using the Marmousi II model for (a) a stationary source and (b) mobile source. (c) difference between Figure 3.14(a) and Figure 3.14(b). 65

Figure 3.15 Seismic data measured by a receiver located at $x^1 = 4.5$ km for a stationary source (black) and mobile source (red). 66

Figure 3.16 RTM image for (a) stationary acquisition and imaging and (b) mobile acquisition and stationary imaging. (c) Difference between Figure 3.16(a) and Figure 3.16(b). 67

Figure 3.17 Shot gathers acquired using the Marmousi II model for (a) stationary and (b) mobile receivers. (c) Difference between Figure 3.17(a) and Figure 3.17(b). 68

Figure 3.18 Seismic data measured by a receiver located at $x^1 = 9$ km at time $t = 0$ s (trace number 2000) for a stationary receiver (black) and mobile receiver (red). 69

Figure 4.1 2D graphical representation of (a) physical and (b) computational domains. 85

Figure 4.2 2D graphical representation of (a) SSG, (b) FSG, and (c) MFD staggered grid computational domains. 88

Figure 4.3 2D graphical representation of pressure field defined at (a) $[\xi^1, \xi^3] = [\mathbf{f}, \mathbf{f}]$ and (b) $[\xi^1, \xi^3] = [\mathbf{h}, \mathbf{h}]$ grid points, and particle velocity field defined at (c) $[\xi^1, \xi^3] = [\mathbf{f}, \mathbf{h}]$ and (d) $[\xi^1, \xi^3] = [\mathbf{h}, \mathbf{f}]$ grid points ($\xi^2 = \mathbf{f}$ in all 2D graphical representations). 89

Figure 4.4 Wavefield snapshots simulated using (a) flat and (b) rough sea surface with $\pm$14 m SWH, showing distortions in ghost reflections because of the rough sea surface. 93

Figure 4.5 Shot gathers for (a) flat and (b) rough sea surface with $\pm$14 m SWH, showing distortions in ghost reflections because of the rough sea surface. . 94

Figure 4.6 Frequency-wavenumber spectra of shot gathers shown in (a) Figure 4.5(a) and (b) Figure 4.5(b). The ghost notches in the flat sea surface case are symmetric and clearly visible, whereas they are dispersed and blurred in the rough sea surface case. 95

Figure 4.7 Time window of correlated shot gathers simulated using a stationary source with (a) flat and (b) rough sea surface with $\pm$14 m SWH. Events are easily trackable in the flat sea surface case, unlike in the rough sea surface case. 95

Figure 4.8 Shot gathers for (a) flat and (b) rough sea surface with $\pm$5 m SWH, and receiver gathers for (c) flat and (d) rough sea surface with $\pm$5 m SWH. The effects of a realistic rough sea surface is more noticeable in the common-gather domain than the common-shot domain. 97

Figure 4.9 Time window of common-receiver gathers simulated using a moving source with (a) flat and (b) rough sea surface with $\pm$5 m SWH. A rough sea surface introduces trace-to-trace jitter in the common-receiver domain because of the variable source depth from one source point to the next. 98

Figure 5.1 Marmousi II velocity submodel (quantity c in equation 5.7) used to validate the developed RTM imaging framework. 107

Figure 5.2 Reference RTM image for stationary acquisition and imaging. 109

Figure 5.3 (a) RTM image for mobile acquisition and stationary imaging. (b) Difference image between Figure 5.2 and Figure 5.3(a). The difference image shows phase change and mispositioning of imaged structures ignoring source-motion effects in imaging. 110

Figure 5.4 Vertical profiles at $x^1 = 1.25$ km (solid curve) from stationary acquisition and imaging (Figure 5.2), and (dashed curve) from mobile acquisition and stationary imaging (Figure 5.3(a)). The vertical profiles clearly illustrate the changes in phase and amplitude as a result of ignoring source-motion effects in imaging. 111

Figure 5.5 (a) RTM image for mobile acquisition and imaging. (b) Difference image between Figure 5.2 and Figure 5.5(a). The difference image shows that the developed approach can correctly account for source-motion effects and imaged structures are correctly positioned. 112

Figure 5.6 Magnitude spectra extracted from the source wavefield at $(x^1, x^3) = (1.25, 1.3)$ km (solid) from stationary acquisition and (dashed) from mobile acquisition. The frequency bandwidth change between the two acquisitions, although observable, is negligible. 113

Figure 5.7 Vertical profiles at $x^1 = 1.25$ km (solid curve) from stationary acquisition and imaging (Figure 5.2), and (dashed curve) from mobile acquisition and imaging (Figure 5.5(a)). The vertical profiles from the two acquisition and imaging scenarios closely match, demonstrating the robustness of the developed approach to account for source motion effects in imaging. 113

Figure 5.8 (a) Kinematic correction vector field overlaying the RTM image for mobile acquisition and stationary imaging for a right-going source. (b) Kinematic correction vector field overlaying the magnitude of the vector field. The kinematic correction vector field points toward the source motion direction. 114

Figure 5.9 (a) Kinematic correction vector field overlaying the RTM image for mobile acquisition and stationary imaging for a left-going source. (b) Kinematic correction vector field overlaying the magnitude of the vector field. The kinematic correction vector field points toward the source motion direction. 115

Figure 5.10 Dipping reflectors model used to investigate the effects of sweep duration and dipping angle on imaging marine vibrator data. 117

Figure 5.11 (a) Kinematic correction vector field overlaying the RTM image for mobile acquisition and stationary imaging for a short-duration sweep acquisition. (b) Kinematic correction vector field overlaying the magnitude of the vector field. 118

Figure 5.12 (a) Kinematic correction vector field overlaying the RTM image for mobile acquisition and stationary imaging for a long-duration sweep acquisition. (b) Kinematic correction vector field overlaying the magnitude of the vector field. 119

Figure B.1 Permission from *Geophysics*. 148

LIST OF TABLES

Table 4.1 Pressure and particle velocity grid locations in 3D. Within an MFD scheme, the pressure and particle velocity wavefields are computed at four complementary staggered grids. 90

Table 4.2 Differential operators as applied to particle velocity fields to updated pressure field within an MFD scheme. 91

Table 4.3 Differential operators as applied to pressure field to update u_ξ^i within an MFD scheme, where $i = 1, 2, 3$. 92

Table 5.1 Moving source acquisition parameters for the Marmousi example. 108

Table 5.2 Moving source acquisition parameters for the dipping reflectors example. . 116

Table 5.3 Forward and adjoint operators within the AWE for a moving source. . . . 124

LIST OF ABBREVIATIONS

Acoustic wave equation . . . . . AWE

Artificial intelligence . . . . . AI

Artificial neural network . . . . . ANN

Center for Wave Phenomena . . . . . CWP

Colorado School of Mines . . . . . CSM

Convolutional neural network . . . . . CNN

Finite difference . . . . . FD

Free surface . . . . . FS

Full-waveform inversion . . . . . FWI

Fully staggered grid . . . . . FSG

Machine learning . . . . . ML

Mimetic finite difference . . . . . MFD

Neural network . . . . . NN

Perfectly matched layer . . . . . PML

Prediction Step Staggered-In-Time . . . . . PSIT

Reverse-time migration . . . . . RTM

Significant wave height . . . . . SWH

Society of Exploration Geophysicists . . . . . SEG

Standard staggered grid . . . . . SSG

linearized Euler equation . . . . . LEE

linearized continuity equation . . . . . LCE

ACKNOWLEDGMENTS

This work wouldn't have been possible without the help and support of many people. First and foremost, I would like to express my deepest gratitude to my advisor, Dr. Paul Sava, for his invaluable guidance, support, and contribution to this work. His expertise and mentorship have been instrumental in shaping my research approach and enhancing my critical thinking skills. I am truly grateful for the time and energy he dedicated to discussing my work, reviewing my manuscripts, and providing me with constructive feedback to improve the quality of my research. Furthermore, I am grateful for his unwavering support during challenging personal times, which played a crucial role in enabling me to successfully complete my studies.

I would also like to thank Dr. Jeffery Shragge for his help and support in making my research work possible. He suggested and provided insights about modeling marine vibrator data, and helped me better understand the problem and how to approach it. I appreciate the time he put into reading my manuscripts and providing useful suggestions.

I would like to thank my committee members Dr. Mahadevan Ganesh, Dr. Ge Jin, and Dr. Hua Wang for taking the time to be part of my committee, reading my manuscripts, and providing useful feedback about my research. I am grateful for the opportunity to take some classes with Dr. Ganesh, from whom I learned a lot about parallel computing and finite-element methods. I appreciate the help and support of Michelle Szobody, Lynn Lundebrek, and Noelle Vance, who have been patient with my never-ending questions. I am also thankful to Diane Witters for helping me improve my writing and soft skills. I would like to thank Antoine Guitton for many useful discussions about marine vibrator technology, and Aaron Girard for many useful and engaging conversations on various topics.

During my time at Colorado School of Mines (CSM), I had the pleasure of meeting and interacting with many great individuals who made my journey enjoyable. I am grateful

to have had the opportunity to call Iga Pawelec a true friend. She was always there to encourage me when I lost hope and shared many good cups of coffee with me. I would also like to express my gratitude to Tugrul Konuk for engaging in numerous useful discussions about his work and mine, which greatly contributed to the successful completion of my research. Additionally, I am thankful for the support and camaraderie of Taqi Alyousuf, Aun Al Ghaithi, Maitham Alabbad, Hani Alzahrani, Odette Aragao, Mert Kiraz, Werter Silva, Nicholas Dorogy, Yanhua Liu, Manuel Caballero, Jihyun Yang, Ahmed Ahmed, and many others.

I would like to express my gratitude to Saudi Aramco for sponsoring my studies. Also, I would like to thank Mohammed Al-Otaibi, Abdulaziz Saad, Khaled Al Dulaijan, and Aiman Bakhorji for their help and support during my studies.

Finally, I would like to thank my family for their continuous and never-ending support. My wife, Meha, made great efforts to help me reach the finish line of my PhD, for which I will always be grateful. My little princess, Samara, whose smile brings joy and warmth to my heart. To my newly born baby boy Abdullah, whose presence showers me with love. My parents, Abdullah and Ehsan, have always supported me, been there for me, and love me unconditionally. My siblings have always helped me achieve my goals.

For my family.

CHAPTER 1
INTRODUCTION

Seismic data play an essential role in a wide range of applications that are not limited to oil and gas exploration. There is an ever-growing need for robust and reliable seismic imaging techniques for various applications, from locating and mapping aquifers to characterizing the subsurface for geohazards (e.g., active faults). Seismic data are being used for environmental monitoring (e.g., evaluating carbon storage integrity in reservoirs), making such data critical for addressing climate change challenges. To properly use seismic data in any of the aforementioned applications, one must (1) be able to process such data (e.g., seismic deghosting), (2) extract useful information from them (e.g., subsurface imaging), and (3) understand how such data provide information about the subsurface (i.e., governing physical laws). The work presented here addresses the challenges of modeling, processing, and imaging marine seismic data. The theme of this thesis can be divided into two parts: (1) deghosting seismic air-gun data, and (2) modeling and imaging marine vibrator data. This work spans fields from differential geometry, numerical modeling, machine learning, seismic data processing, and acquisition design.

1.1 Seismic air-gun data

Ghost reflections have been a long-standing issue in towed-streamer seismic acquisition, especially since ghost-free data are a prerequisite for many geophysical applications. Ghost reflections deteriorate the quality of seismic data as they introduce frequency notches into the amplitude spectrum, limiting the usable data bandwidth (Amundsen and Zhou, 2013; Dondurur, 2018), thus lowering the seismic resolution (Knapp, 1990), among other issues. Furthermore, ghost reflections distort the source signature, which leads to erroneous impedance inversion (Jovanovich et al., 1983). Various acquisition and processing solutions have been proposed to remove ghost reflections from seismic data. However, a common issue with

the proposed solutions is their limited ability to remove source-side ghosts because of the sparse source sampling. To circumvent this problem, I employ a machine learning approach to process and remove ghost reflections from streamer data. Exploring machine learning methodologies facilitates developments of a wide range of seismic data processing and imaging techniques based on those methodologies. In addition, machine learning has the potential to reveal information carried by seismic data that are not easily accessible through conventional processing and interpretations techniques.

1.2 Marine vibrator data

Environmental concerns about conventional marine impulsive sources (i.e., air-guns) makes a transition to environmentally-friendly marine vibrators likely in the near future. Non-impulsive marine sources (i.e., marine vibrators) are viable lower-impact alternatives to air-guns. Marine vibrators are not just advantageous for environmental reasons, but also have geophysics-related merits. From a seismic exploration perspective, marine vibrators provide lower-frequency content than air-guns (Guitton et al., 2021), and enable simultaneous acquisition by blending phase-encoded sources (Laws et al., 2019). However, processing and imaging challenges emerge because of the motion and long duration of marine vibrator source signals, including Doppler effects and time-dependent source-receiver offsets in the context of ocean-bottom acquisition. Even though marine vibrators move at a much slower velocity than the subsurface sound speed, source motion causes noticeable offset- and time-dependent frequency shifts to the data (Dragoset, 1988; Hampson and Jakubowicz, 1995; Schultz et al., 1989). Further, phase distortions also occur in seismic signals and are proportional to the source velocity and moveout of seismic events. Additional complexities arise when considering ghost reflections and dynamic sea surfaces.

Current seismic data processing and imaging techniques usually assume stationary and impulsive sources in marine acquisition. Developing appropriate processing and imaging algorithms for data acquired using moving sources requires accurate modeling of the associated effects. Various methods are proposed in the literature to model marine vibrator data.

Dellinger and Díaz (2020) present a segmentation-deconvolution approach to model moving sources. Duquet et al. (2021) apply a finite-difference (FD) method to model source motion by moving and interpolating the source injection locations in space as a function of time. Such solutions are limited to static sea surface conditions. JafarGandomi and Grion (2021) propose an approach to model marine vibrator data, which is capable of incorporating time-varying sea surfaces, by interpolating unaliased impulsive sources data to desired source locations and convolving with the vibrator sweep. However, such an approach requires unaliased data that are not easily available, and involves costly interpolations.

Accurate and stable modeling of marine vibrator acquisition under time-varying sea surface conditions is difficult because of the complications of representing time-dependent curved surfaces in Cartesian coordinates. Curved surfaces can be approximated in Cartesian coordinates using smaller grid spacing at and near such surfaces, but this approach results in unjustifiable and significant increase in numerical computations while alternative solutions exist. A more natural approach is to employ a coordinate transformation that considers the intrinsic nature of time-varying meshes.

A host of methods exist to generate numerical solutions for surfaces characterized by non-Cartesian geometries. These include methods that employ coordinate transformation and FD (Appelö and Petersson, 2009; Carcione, 1994; de la Puente et al., 2014; Hestholm, 1999; Hestholm and Ruud, 2002; Komatitsch et al., 1996), finite-element (Marfurt, 1984), spectral-element (Komatitsch and Vilotte, 1998), and discontinuous Galerkin methods (Käser and Dumbser, 2006). FD methods are characterized by ease of implementation, lower computational complexities, and parallelism. However, FD methods require careful grid construction for numerical accuracy and stability, especially at the boundary region. On the other hand, the latter approaches provide higher accuracy even for complex and highly irregular geometries, at the expense of a higher computational cost with complex meshing and implementation.

In my thesis, I develop the necessary tools to simulate marine vibrator acquisition with and without time-varying sea surfaces. Building a robust seismic modeling framework facilitates numerical solutions for acquisition and processing workflows, and provides the foundation required for seismic imaging and inversion. Based on the advantages of the FD methods discussed in Shragge (2014), Shragge and Tapley (2017), and Konuk and Shragge (2020), I develop a tensorial formulation of the acoustic wave equation to model marine vibrator acquisition with dynamic sea surface conditions. This approach consists of two steps through which I develop analytical expressions for the tensorial AWE in vertically and horizontally deformed coordinate systems. First, I formulate the tensorial AWE for moving sources assuming a flat sea surface, by introducing a depth-dependent horizontal transformation to mitigate the need for velocity model interpolation at every time-step. This formulation leads to a second-order partial differential equation that incorporates source motion which I solve using a FD approach. Second, I formulate the tensorial AWE as a first-order coupled-system for moving sources and dynamic sea surfaces. Modeling a free-surface boundary condition for a dynamic sea surface requires using mimetic FD to ensure numerical accuracy and stability near the free-surface boundary (Konuk and Shragge, 2020).

Continuing this work, I utilize the developed framework to image marine vibrator acquisition, assuming a flat sea surface. The objective of this part of the thesis is to investigate the implications of source motion on seismic processing and imaging. I investigate the consequences of source motion under a static sea surface condition on conventional imaging techniques, and develop an appropriate solution to address imaging distortions.

1.3 Thesis outline

This thesis is structured into four main chapters that are based on published/accepted or submitted articles to peer-reviewed journals. In each chapter, I provide an overview of the problem at hand, the relevant literature review, the theoretical developments of the proposed solution, and numerical results that validate such solutions. The chapters of this thesis are as follows:

- Chapter 2, titled "Seismic deghosting using convolutional neural networks," covers processing seismic air-gun streamer data to remove source- and receiver-side ghost reflections in the shot gather domain using convolutional neural networks. To validate the proposed solution, I test using synthetic and field data. This chapter was presented at the First International Meeting for Applied Geoscience & Energy, and it is published in *Geophysics*:
  - Almuteri, K., and P. Sava, 2021, A convolutional neural network approach for ghost removal: First International Meeting for Applied Geoscience & Energy, SEG, Expanded Abstracts, 2550–2554, doi: 10.1190/segam2021-3584059.1
  - ———, 2023, Seismic deghosting using convolutional neural networks: Geophysics, **88**, no. 3, V113–V125, doi: 10.1190/geo2021-0521.1
- Chapter 3, title "Modeling the seismic wavefield of moving marine vibrator source," covers marine vibrator source simulation (moving sources) assuming a flat and static sea surface using a second-order formulation of the tensorial acoustic wave equation. I also investigate the impact of source motion on seismic data, theoretically and numerically. Further, I formulate the Doppler formula that predicts frequency shift in heterogeneous media and the Green's function for a moving source in a homogeneous media. This chapter was presented at the Second International Meeting for Applied Geoscience & Energy, and it is accepted for publication in *Geophysics*:
  - Almuteri, K., J. Shragge, and P. Sava, 2022b, Finite-difference modeling of marine vibrator sources: Second International Meeting for Applied Geoscience & Energy, SEG, Expanded Abstracts, 2561–2565, doi: 10.1190/image2022-3746278.1
  - ———, 2023, Modeling the seismic wavefield of moving marine vibrator source: Geophysics (accepted).
- Chapter 4, titled "Modeling acoustic wavefields from moving sources in the presence of a time-varying free surface," extends the work of modeling marine vibrator data

by incorporating a time-varying free surface (i.e., sea surface) and using a first-order formulation of the tensorial acoustic wave equation. In this chapter, I develop the first-order tensorial approach for modeling the acoustic wavefield in time-varying meshes for heterogeneous media, and investigate the effects of a time-varying free surface on marine vibrator data. This chapter was presented at the Third International Meeting for Applied Geoscience & Energy, and has been submitted to *Geophysics*:

  - Almuteri, K., J. Shragge, and P. Sava, 2023, Modeling marine vibrator sources in the presence of a time-varying sea surface: Presented at the Third International Meeting for Applied Geoscience & Energy, SEG.
  - ———, 2023, Modeling acoustic wavefields from moving sources in the presence of a time-varying free surface: Geophysics (submitted).

- Chapter 5, titled "Reverse-time migration of mobile marine vibrator data," exploits the developed marine vibrator modeling tool to account for source motion effects in reverse-time migration. In this chapter, I formulate the required forward, adjoint, and Born approximation modeling operators. Further, investigate the consequences of ignoring source motion effects on seismic images and demonstrate the ability of the proposed solution to produce accurate subsurface images that matches those from stationary acquisition and imaging. This chapter was presented at the Second International Meeting for Applied Geoscience & Energy, and will be submitted to *Geophysics*:

  - Almuteri, K., P. Sava, and J. Shragge, 2022a, Reverse-time migration of mobile marine vibrator data: Second International Meeting for Applied Geoscience & Energy, 2694–2698, doi: 10.1190/image2022-3751755.1
  - ———, 2023, Reverse-time migration of mobile marine vibrator data: Geophysics (ready for submission).

CHAPTER 2

SEISMIC DEGHOSTING USING CONVOLUTIONAL NEURAL NETWORKS

A paper published in *Geophysics*[1]

Khalid Almuteri[2,3,4] and Paul Sava[5]

Ghost reflections deteriorate the quality of seismic data in towed-streamer acquisition, and various acquisition and processing solutions have been proposed to remove them from seismic data. A common issue with the proposed solutions is their limited ability to remove source-side ghosts because of the sparse source sampling. Satisfactory receiver-side deghosting solutions are facilitated by complementary measurements (e.g., particle motion data) for wavefield separation and also can be achieved using pressure data acquired at a single recording level only. We develop a solution based on convolutional neural networks (CNNs) to remove source- and receiver-side ghosts in the shot domain. The solution does not require complementary measurements, i.e., it can remove ghost reflections in conventional pressure data measured at a single recording level. Our method requires knowledge of the acquisition geometry to create training data that replicate the field acquisition geometry and require the ocean floor bathymetry to be known. A CNN learns to map ghost-contaminated gathers to corresponding ghost-free gathers through an iterative training process. We find that the CNN-based deghosting operator can remove ghost reflections from previously unseen data and demonstrate that the solution generalizes well when training is done on models unrelated to the actual field geology.

[1]Reprinted with permission of *Geophysics*, 88(3), V113-V125.
[2]Graduate student, Center for Wave Phenomena, Department of Geophysics, Colorado School of Mines
[3]Saudi Aramco
[4]Author for correspondence
[5]Professor, Center for Wave Phenomena, Department of Geophysics, Colorado School of Mines

2.1 Introduction

Ghost reflections have been a long-standing issue in towed-streamer seismic acquisition. They introduce frequency notches into the amplitude spectrum, limiting the usable data bandwidth (Amundsen and Zhou, 2013; Dondurur, 2018), thus lowering the seismic resolution (Knapp, 1990). Furthermore, ghost reflections distort the source signature by altering its phase, leading to erroneous impedance inversion (Jovanovich et al., 1983). Ghost-free data are a prerequisite for many geophysical applications. Absent low frequencies make full-waveform inversion more susceptible to cycle skipping (Bunks et al., 1995; Virieux and Operto, 2009). Low frequencies help constrain and improve impedance inversion (ten Kroode et al., 2013; Wang et al., 2017; Whitcombe and Hodgson, 2007). Moreover, low frequencies are less prone to scattering and attenuation, making them ideal for subsalt imaging (Kapoor et al., 2005; ten Kroode et al., 2013).

Conventionally, streamers are towed at a shallow depth to broaden the bandwidth of the seismic signal (Wang et al., 2017). However, shallow tow attenuates low frequencies and yields data with a low signal-to-noise ratio (He et al., 2013; Kragh et al., 2010; Wang et al., 2017). A deep tow has reciprocal effects; it allows for the acquisition of low-frequency content and increases the signal-to-noise ratio, especially at the lower end of the spectrum, at the expense of a narrowband signal. There are two types of ghost reflections that coexist in marine data: source- and receiver-side ghosts. A source-side ghost starts its propagation from a source as an upgoing wave, whereas a receiver-side ghost ends its propagation at a receiver as a downgoing wave. Deghosting solutions fall into two main categories: receiver- and source-side solutions. The categories can be further classified into acquisition and processing based, as discussed next.

2.1.1 Acquisition deghosting

Acquisition solutions for receiver-side deghosting include slanted streamers (Bearnth and Moore, 1989; Soubaras and Dowle, 2010), over/under streamers (Moldoveanu et al.,

2007; Posthumus, 1993; Sønneland et al., 1986), shallow-over/deep-under streamers (Kragh et al., 2010), and dual-sensor streamers (Carlson et al., 2007; Tenghamn et al., 2007). In a slanted-streamer acquisition, hydrophones vary in depth along the cable, which results in ghost notch diversity (Bearnth and Moore, 1989; Soubaras and Dowle, 2010). This diversity improves the bandwidth of poststack seismic data (Provenzano et al., 2020; Soubaras and Dowle, 2010), making the solution unsuitable for applications that require ghost-free prestack data or applications that require receivers to have the same frequency content. An over/under streamer, at which pressure data are acquired at two different reference surfaces, enables removing receiver-side ghosts through an upgoing/downgoing wavefield separation process (Moldoveanu et al., 2007; Posthumus, 1993; Sønneland et al., 1986). However, it requires twice as many streamers with accurate positioning of vertically aligned cables (Reilly, 2016), which is difficult to implement in the field. Kragh et al. (2010) propose a shallow over with a sparse deep-under acquisition configuration. Shallow streamers contribute the mid- and high-frequency content to the seismic data, whereas deep streamers contribute to the low-frequency content. A shallow-over/deep-under acquisition requires fewer streamers than an over/under acquisition because deep streamers are sparse and contribute only low frequencies. However, a shallow-over/deep-under acquisition requires accurate positioning of the cables and a proper interpolation of the low-frequency data to compensate for the sparse acquisition.

Dual-sensor streamers (Carlson et al., 2007; Tenghamn et al., 2007) exploit the fact that upgoing/downgoing wavefield separation is possible if pressure and particle velocity data are measured simultaneously (Amundsen, 1993; Claerbout, 1976; Day et al., 2013; Ikelle and Amundsen, 2018). However, particle motion sensors are sensitive to mechanical noise below 20 Hz (Carlson et al., 2007; Day et al., 2013; Tenghamn et al., 2007). To overcome this issue, one needs to estimate particle motion data below 20 Hz from pressure data. When sources are below the streamer, estimating such data is done by applying a simple operator to pressure data (Amundsen, 1993; Amundsen et al., 1995). For sources shallower than the streamer, one needs to compute the direct arrival and its ghost to estimate the particle motion

data. Computing the direct arrival and its ghost requires knowledge of the source function. Alternatively, Ozdemir et al. (2012) and Rentsch et al. (2013) propose noise attenuation algorithms to enhance the low-frequency signal-to-noise ratio in the particle motion data. Özdemir et al. (2010), Vassallo et al. (2010), and Özbek et al. (2010) develop optimization-based algorithms to reconstruct and deghost the pressure wavefield using multicomponent marine streamer data. Still, data acquired with different sensor types require calibration with an unknown factor (Grobbe et al., 2016), which can be carried using a deterministic approach (Day et al., 2013) or a statistical approach (Alexandrov et al., 2014; Cambois et al., 2009).

One can extend the acquisition solutions for receiver-side deghosting to address source-side ghosts. Haavik and Landrø (2015) propose varying the source depth during acquisition to diversify frequency notches in the amplitude spectra of different shot gathers. This improves the bandwidth of the seismic signal poststack in a way similar to slanted-streamer acquisition. An over/under source configuration, in which data are acquired twice at the same inline location for sources at different depths (Moldoveanu, 2000), uses reciprocity to remove source-side ghosts in common-receiver gathers (CRGs) (Egan et al., 2007; Moldoveanu et al., 2007). However, source-side deghosting in the CRG domain requires dense shot sampling that towed-streamer acquisition generally lacks.

2.1.2 Processing deghosting

Soubaras (2010) proposes an imaging solution to deghost and improve seismic data poststack. The method works by jointly deconvolving two migration images: a conventional migration image and a mirror migration image. Amundsen and Zhou (2013) derive a low-frequency deghosting filter that can improve the data at least up to half the frequency of the second ghost notch. The solution can be applied in the time-space domain on a trace-by-trace basis (Amundsen and Zhou, 2013; Wang et al., 2017). However, it is only applicable to data acquired with horizontal streamers or streamers with mild variations in depth (Wang et al., 2017). Beasley et al. (2013a,b) propose a physics-based solution to separate 1C measurements, e.g., pressure data acquired at a single reference surface, into upgoing and

downgoing wavefields using the wave equation. The wavefield separation process is iterative and uses causality but is sensitive to noise. Zhang and Weglein (2005), Weglein et al. (2013) and Mayhan and Weglein (2013) propose wavefield separation methods based on Green's theorem that can accommodate streamers of arbitrary shapes (Amundsen et al., 2013).

King and Poole (2015) propose a processing workflow to remove receiver-side ghost reflections from pressure-only data that can handle a dynamic sea surface. The method requires an estimation of the sea-surface profile prior to deghosting. Furthermore, the deghosting method is implemented by solving a linear Radon system of equations. Grion et al. (2016) propose a deghosting method that works for rough sea surfaces and slanted streamers, given that the sea-surface profile is known. The method uses phase-shift redatuming operators to separate the up- and downgoing components of the wavefield. Processing solutions for receiver-side deghosting are applicable to source-side ghosts in the CRG domain. However, source-side deghosting is more challenging than receiver-side deghosting and remains mainly an unsolved problem (Amundsen et al., 2017; Ikelle and Amundsen, 2018) because shots are sparse. Vrolijk and Blacquière (2021) propose an approach that uses a convolutional neural network (CNN) to remove source-side ghost reflections in CRGs for coarsly acquired sources. Because the source deghosting process is carried in the common-receiver domain, this solution is applicable to horizontal and slated streamers alike.

In this paper, we propose seismic deghosting using CNNs, which is a special type of artificial neural networks (ANNs). Our solution does not require any particular acquisition configuration but requires that its geometry and the bathymetry of the ocean floor be known. It can remove source- and receiver-side ghosts simultaneously in the shot gather domain. This feature offers an opportunity to deghost conventional pressure data acquired at a single reference surface. We develop a CNN as a deghosting operator that inputs ghost-contaminated data and outputs a ghost-free prediction. In the following sections, we provide the theoretical foundation of CNNs, explain how they work, and discuss their benefits and pitfalls. We demonstrate how CNNs can remove ghost reflections using examples inspired by realistic

acquisition and using field data.

2.2 CNN-based deghosting

2.2.1 Background

ANNs are machine learning (ML) models inspired by biological neurons found in the brain (Goodfellow et al., 2016; Géron, 2019; Russell and Norvig, 2016). Neural networks (NNs) are capable of tackling complex problems from various fields, such as natural language processing (Sutskever et al., 2014), object recognition (Krizhevsky et al., 2017), and speech recognition (Hinton et al., 2012) with a great degree of success (LeCun et al., 2015). The interest in the geophysics community is not new (Van der Baan and Jutten, 2000), but recent advances in ML have expanded their use in the field. Geophysical applications include velocity model building (Araya-Polo et al., 2018; Wu and McMechan, 2018; Yang and Ma, 2019), normal-moveout velocity picking (Biswas et al., 2018; Ma et al., 2018), petrophysical properties and impedance inversion (Biswas et al., 2019; Das and Mukerji, 2020; Das et al., 2019), and seismic deblending (Sun et al., 2020).

Various types of ANNs exist, the simplest of which is fully connected NNs, which consists of layers of neurons stacked together as shown in Figure 2.1(a). The links that connect different neurons represent learnable parameters known as weights. One can find such weights through an iterative data-fitting procedure called training. The weights map inputs to outputs according to

$$a_j^l = g\left(\sum_{i=0}^{n} w_{ij}^l a_i^{l-1}\right), \tag{2.1}$$

where a_j^l is the value at the jth neuron at the lth layer, w_{ij}^l is the weight that connects the ith neuron at the $(l-1)$th layer with the jth neuron at the lth layer, n is the number of neurons in the $(l-1)$th layer, and g is a nonlinear activation function. Figure 2.1(b) shows a visual representation of equation 2.1. The activation function in the NN is critical; a

linear activation function allows only linear mapping between inputs and outputs, whereas a nonlinear activation function enables the NN to learn nonlinear mappings.

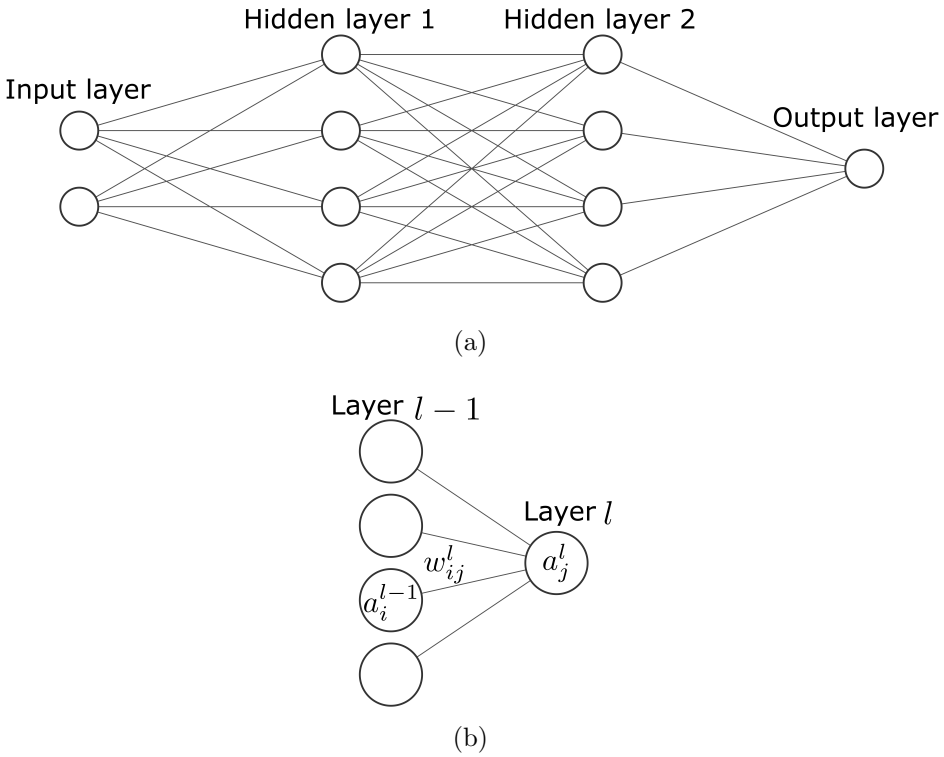

Figure 2.1 (a) An example of a fully-connected NN with two input units, two hidden layers with four units in each layer, and one output unit. (b) A simple model of a neuron connected to four other neurons from a preceding layer. The neuron's output is $a_j^l = g\left(\sum_{i=0}^{n} w_{ij}^l a_i^{l-1}\right)$, where a_j^l is the value at the jth neuron at the lth layer, w_{ij}^l is the weight that connects the ith neuron at the $(l-1)$th layer with the jth neuron at the lth layer, n is the number of neurons in the $(l-1)$th layer, and g is a nonlinear activation function.

A fully connected NN suffers from multiple issues that limit its usefulness in some applications. One such issue is fixed input and output size (Goodfellow et al., 2016; LeCun et al., 2015, 1998). Processing seismic data using NNs requires them to have a structure that can intrinsically handle data with variable recording lengths and variable number of traces. Also, the memory requirement of fully connected NNs with a large input size can be prohibitively expensive (Goodfellow et al., 2016; Géron, 2019; LeCun et al., 1998). In addition, as the input size to an NN increases, the number of learnable parameters increases as well. In such cases, one needs to use more training examples to avoid overfitting (Géron,

2019; LeCun et al., 2015, 1998). Fully connected NNs are not robust to any translation of features (e.g., faults in a stacked section or first break in a shot gather) in the inputs. This implies that if a fully connected NN is trained to detect faults in a stacked section, it will only detect faults in locations where they existed in training examples. LeCun et al. (1998) and Goodfellow et al. (2016) discuss in depth the limitations of fully connected layers and point out the advantages of using CNNs as an alternative. In CNNs, convolutional filters replace the weights characterizing a fully connected layer. CNNs generalize better than fully connected NNs, i.e., they outperform fully connected NNs on previously unseen data (LeCun et al., 2015). In addition, CNNs have fewer parameters than fully connected NNs, making them ideal for complex and large-scale problems.

In the framework of ANNs, a supervised learning approach is the most common form of learning (LeCun et al., 2015). The goal of supervised learning is to find the optimal weights that minimize an objective function given a set of training examples, in which the training examples are in input-output pairs: $(\mathbf{x}_i, \mathbf{y}_i)$, $i = 1, \ldots, N$. The relationship between the input and output is given by an unknown function f such that $\mathbf{y}_i = f(\mathbf{x}_i)$. The goal of training is to find a function $h_{\mathbf{w}}$, which is represented by an ANN and parameterized by the learnable weights $\mathbf{w}$, which approximates the function f. In our work, the input $(\mathbf{x}_i)$ is a ghost-contaminated shot gather, the output $(\mathbf{y}_i)$ is a true ghost-free gather, and $h_{\mathbf{w}}$ is the deghosting operator. We arrive at function $h_{\mathbf{w}}$ by minimizing the objective function

$$E(\mathbf{w}) = \frac{1}{N} \sum_{i=1}^{N} \left\| \mathbf{y}_i - h_{\mathbf{w}}(\mathbf{x}_i) \right\|^2, \tag{2.2}$$

with respect to the weights $(\mathbf{w})$ of the NN. A common minimization method used is gradient descent, which iteratively updates the weights using the gradient of the objective function

$$\mathbf{w}_{k+1} = \mathbf{w}_k - \alpha \frac{\partial E(\mathbf{w}_k)}{\partial \mathbf{w}_k}, \tag{2.3}$$

where α is the learning rate selected experimentally; a small learning rate results in slow convergence, whereas a large learning rate potentially results in divergence (Géron, 2019).

ANNs are useful and powerful ML models. According to the universal approximation theorem (Cybenko, 1989; Hornik, 1991; Hornik et al., 1989), ANNs are universal approximators, i.e., ANNs with a single hidden layer can approximate any continuous function up to an arbitrary order of accuracy. ANNs with two hidden layers, on the other hand, can approximate any function with an arbitrarily small error (Lapedes and Farber, 1987). An exact mapping of input-output pairs is achievable under some constraints (Huang and Huang, 1990; Sartori and Antsaklis, 1991; Tamura and Tateishi, 1997).

The ability to approximate any continuous function arbitrarily well is not unique to ANNs. One can approximate any continuous function up to an arbitrary order of accuracy with polynomials (including trigonometric polynomials) as well (Carothers, 1998; Jeffreys and Jeffreys, 1950; Stein and Shakarchi, 2011). However, the number of coefficients one needs to solve for in polynomial regression makes it prohibitive to approximate high-dimensional functions. The exact number of polynomial coefficients is given by

$$\frac{(n+d)!}{n!d!}, \tag{2.4}$$

where n is the number of dimensions and d is the degree of the polynomial (Géron, 2019). The prohibitive cost of approximating high-dimensional functions, which includes the number of training examples one needs to avoid overfitting, is commonly known as the "curse of dimensionality" (E, 2020; Griebel, 2005; Grohs et al., 2019; Géron, 2019; Hanka and Harte, 1997). The ability of ANNs to approximate any function, including high-dimensional nonlinear functions, makes them useful and gives rise to a wide range of applications that would not be possible otherwise.

The universal approximation theorem (Cybenko, 1989; Hornik, 1991; Hornik et al., 1989) only addresses the ability of ANNs to represent continuous functions and does not consider the learnability aspects of the problem. The existence of an ANN that can approximate an unknown function does not imply one can find it. Furthermore, one cannot characterize which functions can and cannot be approximated by a particular ANN structure (Russell and

Norvig, 2016). An ANN architecture is given by a set of parameters (e.g., number of layers, learning rate, and the type of activation functions) commonly known as hyperparameters. One has to fine tune the hyperparameters, i.e., to experimentally search for the best set of parameters to solve a given problem with adequate accuracy (Goodfellow et al., 2016; Géron, 2019). In the context of seismic deghosting, we make use of the ability of ANNs to exploit any intrinsic relationship between inputs and outputs to construct a deghosting operator. Such an ANN-based operator takes time to train, but after training it can predict ghost-free data in a negligible amount of time. However, to construct the deghosting operator, we must first search for the best set of parameters. The hyperparameters that define the CNN used in our method are as follows: the number of layers, the number of filters, the size of each filter, the learning rate, and the activation function.

2.2.2 Neural network architecture

Our CNN consists of three convolutional layers followed by a masking layer, repeated three times for a total of 12 layers (Figure 2.2). Each convolutional layer has 16 filters. The first two convolutional layers in the sequence use filters with a temporal length of 101 coefficients and a spatial width of three traces in the inline and crossline directions. The third convolutional layer in the sequence has filters with 11 temporal coefficients and identical spatial width as the preceding two layers. We use tanh as activation function throughout our NN because it is centered around zero and bounded between -1 and 1.

In CNNs, it is common to use filters with a small size (e.g., 3×3) because they usually outperform large filters and require fewer computations (Géron, 2019). Given that our objective is to remove ghost reflections in the time domain, we use temporally long filters of 101 samples to reconstruct the low-frequency information of the data. In our numerical example, a filter with 101 samples covers 12 times the dominant period of the data. Smaller filters can achieve the same goal if one uses many more layers. We use temporally short filters for every third convolutional layer of 11 samples to reconstruct the high-frequency information. By choosing temporally long and short filters, we give the CNN freedom to

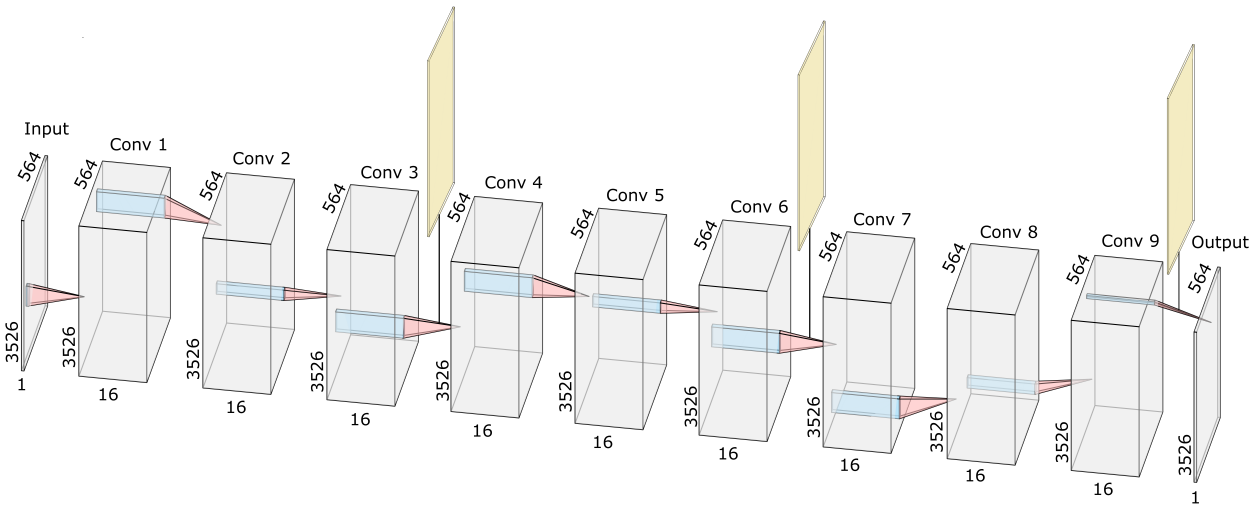

Figure 2.2 An illustration of the architecture of the network we use for seismic deghosting on 2D data. Each gray cuboid labeled with Conv represents a multichannel feature map generated using N convolutional filters ($N = 16$). The height of each cuboid corresponds to the number of time samples ($n_t = 3526$) and the width corresponds to the number of traces in the gather ($n_r = 564$). Each yellow cuboid represents a temporal masking layer in the network.

work at different scales. Our choices of filter sizes are experimental because a theoretically rigorous approach to select such a parameter remains an open problem in ML. As reported in the literature, optimizing such hyperparameters is an experimental process (Goodfellow et al., 2016; Géron, 2019).

Deghosting can be performed on individual traces using 1D filters or can use information from adjacent traces using 3D filters. The 3D filters should outperform 1D filters because ghost reflections have offset dependency, which can be observed using the 3D ghost function in the Fourier domain (Amundsen, 1993) given by

$$G(k_z, z) = 1 + re^{2ik_z z}, \tag{2.5}$$

where $k_z = \sqrt{k^2 - k_x^2 - k_y^2}$ is the vertical wavenumber; $k = \frac{\omega}{c}$; $\omega = 2\pi f$ is the angular frequency; c is the water velocity; k_x and k_y are the horizontal wavenumbers in the inline and crossline directions, respectively; z is the source or receiver depth, and r is the reflection coefficient at the sea surface.

We update the weights ($\mathbf{w}$) using the Nesterov's Accelerated Gradient (NAG) method (Géron, 2019; Sutskever et al., 2013), which is a modified version of the gradient descent (equation 2.3)

$$\mathbf{w}_{k+1} = \mathbf{w}_k + \mathbf{m}_{k+1}, \tag{2.6}$$

where

$$\mathbf{m}_{k+1} = \beta \mathbf{m}_k - \alpha \frac{\partial E(\mathbf{w}_k + \beta \mathbf{m}_k)}{\partial \mathbf{w}_k} \tag{2.7}$$

is the momentum ($\mathbf{m}_0 = 0$), $\beta \in [0, 1]$ is the momentum coefficient, and α is the learning rate. The momentum coefficient (β) defines how much previous gradients contribute toward new updates, and if the momentum coefficient is zero, the method reduces to gradient descent. During the training we use $\beta = 0.9$, i.e., we put much weight on previous directions to speed up the convergence rate. To further speed up convergence, the NAG method computes the gradient of the objective function not at the current location of weights ($\mathbf{w}$) but at the location of weights with a slide in the momentum direction ($\mathbf{w} + \beta \mathbf{m}$). We experimentally determine that the optimum learning rate to train the NN is $\alpha = 0.1$. We use a minibatch of size 32, and run the training for 150 epochs.

The masking layers in our CNN are essential for two reasons: (1) to eliminate noise the NN produces before first arrivals and (2) to help the NN converge to a solution during training. Without masking layers, training fails because the NN tries to fit the data by removing noise the CNN generates and by removing ghost reflections. To create a masking layer, we use the modified Coppens's method (Sabbione and Velis, 2010) to pick the first seismic signal of any kind (whether it is a water-bottom reflection or refraction from a subsequent layer) along the time axis. The masking array defines the regions where a seismic signal could exist, and it accordingly mutes irrelevant signal, i.e., not generated by the source before the first arrival. Knowing the ocean floor bathymetry allows us to perform quality control check of the automatic picks from the modified Coppens's method needed to build the masking layer.

2.3 Numerical example

In this section, we demonstrate CNN ghost removal in the shot domain on 2D data. First, we describe the process of generating the training and testing data. Then, we illustrate the performance of CNN-based deghosting using a synthetic example and field data.

2.3.1 Neural network training dataset

To train our CNN, we use 256 input-output pairs of ghost-free and ghost-contaminated shot gathers simulated using Marmousi submodels (Martin et al., 2002) (Figure 2.3(a) and Figure 2.3(b)). We add a water layer with 710 m depth to the top of models. We simulate data using a primary source at $z = 5$ m and a mirror source for source-side ghost modeling at $z = -5$ m. In addition, we use a source at $z = -390$ m and a mirror source at $z = -400$ m to model the first-order surface-related multiples and their ghost reflections in data. Modeling first-order surface-related multiples and their ghost reflections increases the ghost-free and ghost-contaminated footprint in the training data, i.e., allows us to use fewer training pairs. We use 564 primary receivers at $z = 7$ m and 564 mirror receivers for receiver-side ghost modeling placed at $z = -7$ m, with a receiver spacing of 12.5 m. For all simulations, we use the same source wavelet with a flat spectrum between $2.5 - 110$ Hz. We model data using finite differences for 7 s with a sampling interval of 0.2 ms, later resampled to 2 ms. We model 260 shots from the first training model (Figure 2.3(a)) with a shot spacing of 12.5 m, and 160 shots from the second training model (Figure 2.3(b)) with a shot spacing of 18.5 m. Then, we randomly extract 256 shots from the two modeled data sets for training. Before training the CNN, we normalize the data to the range of the chosen activation function. Our proposed CNN-based deghosting approach reconstructs the relative amplitude of the seismic data because our procedure normalizes the data (input and output) to the range of the chosen activation function.

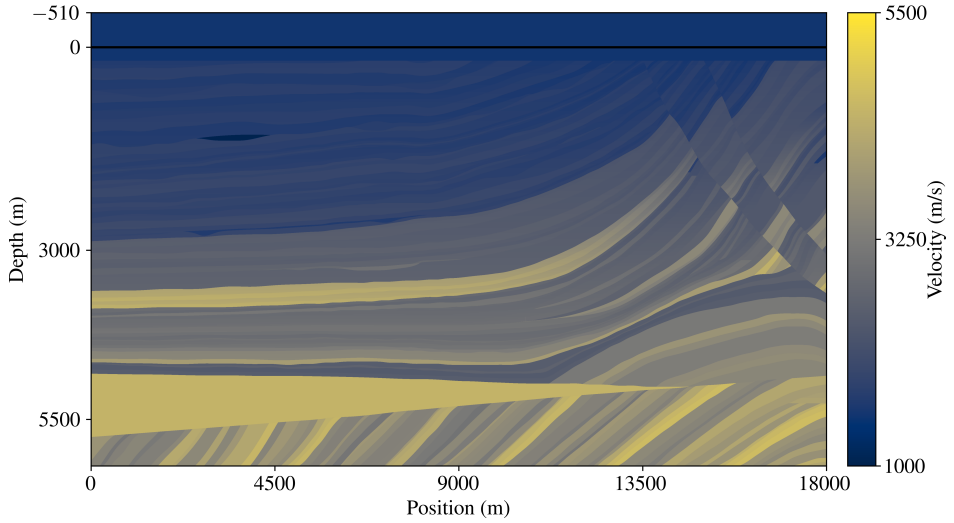

(a)

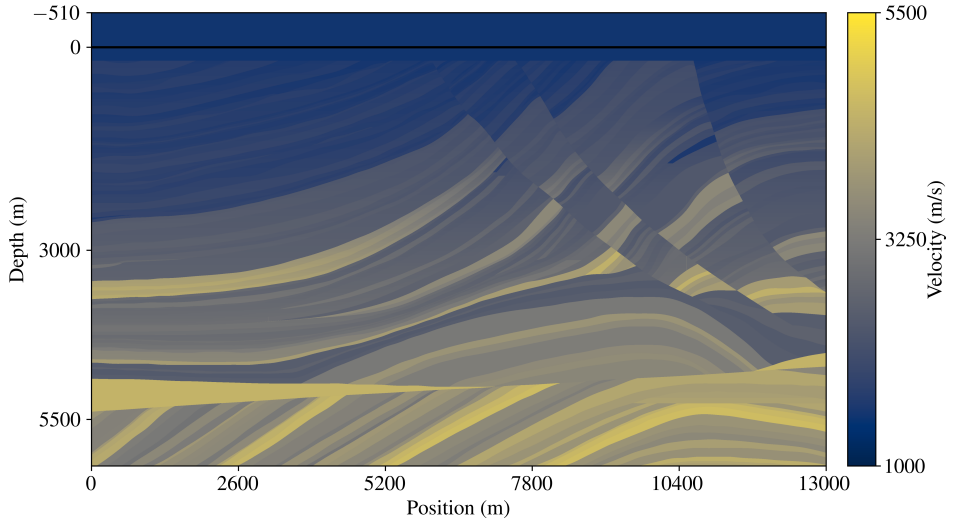

(b)

Figure 2.3 submodels from the Marmousi model, with 710 m added water layer on top, used for training. The black line corresponds to the air-water interface.

2.3.2 Seismic deghosting: Synthetic data example

To test our method, we extract a submodel (Figure 2.4) from the Amoco statics test model (O'Brien, 1994). The velocity values of the testing submodel are not within the range of the training submodels. We choose this testing model to show that with simpler training models, one can remove ghost reflections from more complex models and lower the computational burden of generating training data simultaneously. By complex models, we mean models with stronger velocity contrasts and velocity values outside the range of that of the training models. We generate two gathers, with and without ghosts, for a source at $x = 2303$ m using the same source wavelet that we use to generate the training data. The source depth, receiver depth, receiver spacing, and modeling parameters of the testing data are similar to the training data.

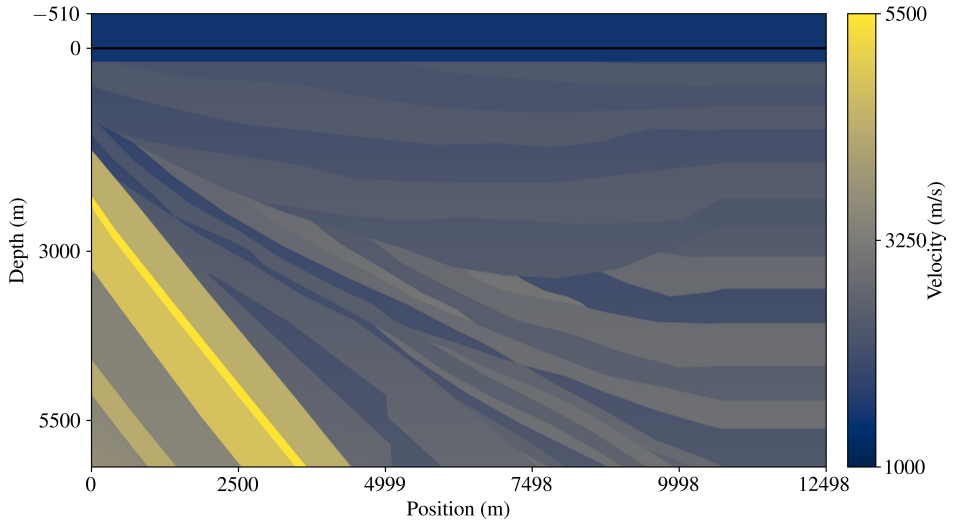

Figure 2.4 submodel from the Amoco statics test model to test the CNN. The velocity values of this model are not within the range of the velocity values of the training models. We add a water layer with 710 m depth to the top. The black line corresponds to the air-water interface.

Figure 2.5(a) and Figure 2.5(b) shows the true ghost-free and ghost-contaminated data generated using the model shown in Figure 2.4, respectively. The ghost-free and ghost-contaminated gathers have different phases, and the low frequencies in the ghost-contaminated

gather are attenuated by ghost reflections. The average amplitude spectra of the two gathers indicate that ghost reflections destructively interfere with the primary signal at 0 Hz and constructively interfere at 60 Hz (Figure 2.6(a)). The destructive interference is more significant at low frequencies than at high frequencies. The amount of energy loss at 5 Hz is 28 dB, whereas the amount of energy loss at 20 Hz is 5 dB.

Using the ghost-contaminated gather (Figure 2.5(b)) as an input to the CNN-based deghosting operator gives the ghost-free prediction shown in Figure 2.5(c). The true and predicted ghost-free gathers closely match in character. The average amplitude spectra (Figure 2.6(a)) indicate that the CNN recovers the spectrum correctly within the constructive interference frequency bands but less accurately within the destructive interference bands. The relative ℓ^2 residual for the predicted ghost-free gather is 0.65, whereas it is 2.04 for the ghost-contaminated gather. Figure 2.7 shows the relative ℓ^2 residual for the predicted ghost-free data and ghost-contaminated data as a function of frequency band. The bandwidth of each band is 3.5 Hz, and the center of each band is changing by 3.5 Hz, starting from 4.5 Hz. Figure 2.7 shows the improvement across different frequency bands as a result of ghost removal. However, the frequency bands centered at approximately 4.5 Hz and 18.25 Hz show higher relative error compared with other bands. The relatively high ℓ^2 for the ghost-free prediction data is because the minimization problem is formulated to reconstruct the relative amplitude instead of the absolute amplitude.

Figure 2.5(d-f) shows the true ghost-free, the ghost-contaminated, and the ghost-free prediction gathers after applying a 20 Hz low-pass filter to the gathers shown in Figure 2.5(a-c), respectively. The ghost-contaminated gather is characterized by weaker amplitudes, indicating that ghost reflections severely reduce the signal-to-noise ratio at low frequencies (Figure 2.6(b)). Our method can recover the low-frequency content in the data. Figure 2.8 shows the frequency-wavenumber spectra of the gathers shown in Figure 2.5. The low frequencies (below 30 Hz) are boosted, and the frequencies within the constructive interference band are reduced. However, frequencies below 5.5 Hz are not recovered well, and the frequencies between 5.5 and 30 are

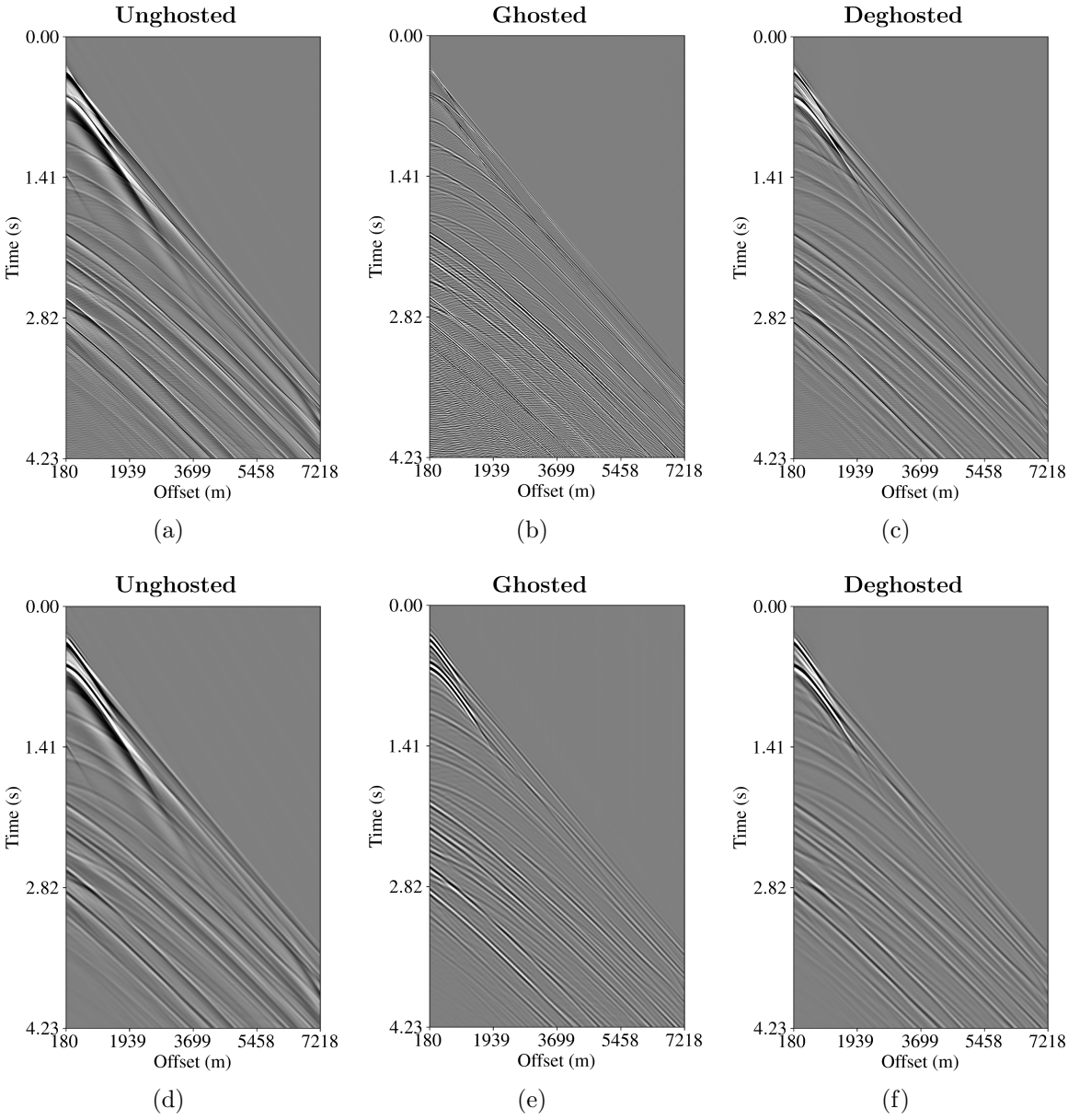

Figure 2.5 Comparison among (a) true ghost-free, (b) ghost-contaminated, and (c) ghost-free prediction shot gathers. (d-f) After applying 20 Hz high-cut filtering in Figure 2.5(a-c), respectively.

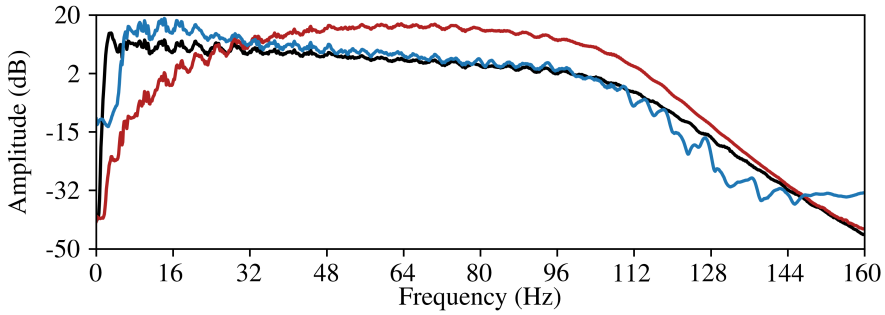

(a)

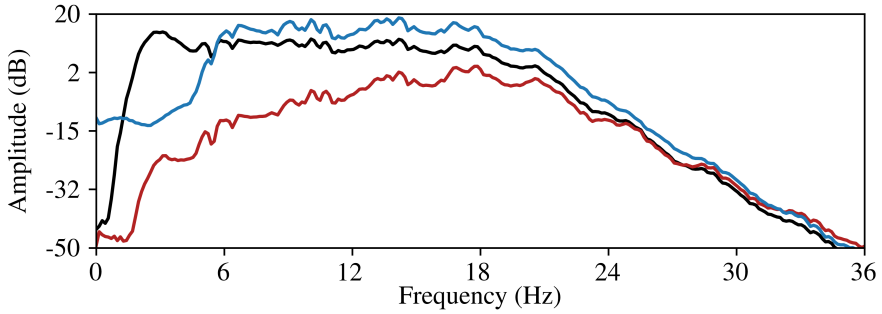

(b)

Figure 2.6 Comparison among the average amplitude spectra of the ghost-free data (black line), the ghost-contaminated data (red line), and the ghost-free prediction data (blue line). (a) Comparison between the full bandwidth data shown in Figure 2.5(a-c). (b) Comparison between the band-limited data shown in Figure 2.5(d-f).

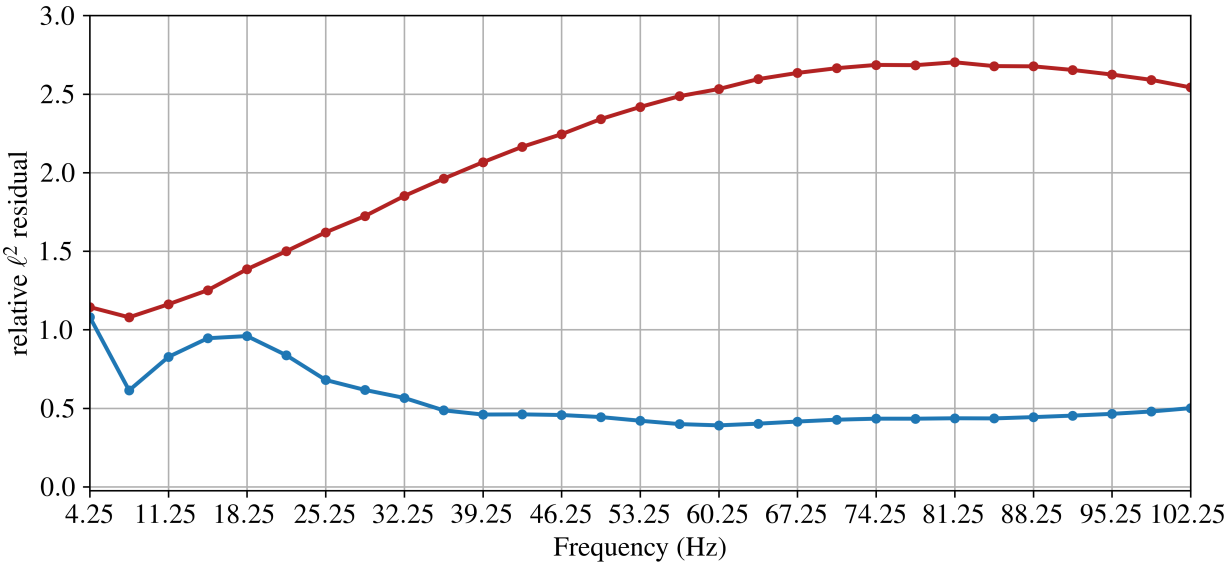

Figure 2.7 Relative ℓ^2 residual between the true ghost-free gather (Figure 2.5(a)) and the ghost-contaminated gather (Figure 2.5(b)) (red) over different frequency bands, with a bandwidth of 3.5 Hz for each band, and between the true ghost-free gather and the ghost-free prediction (Figure 2.5(c)) (blue).

overcompensated.

Individual traces for a receiver 3930 m away from the source (Figure 2.9(a) and Figure 2.9(b)) confirm the ability of the CNN to remove ghost reflections. The correlation coefficient between the true ghost-free and ghost-contaminated traces is 0.31, indicating that ghost reflections severely alter the waveform of the source signature, in terms of amplitude (Figure 2.9(c)) and phase. However, the correlation coefficient between the true and predicted traces is 0.91, indicating that the CNN-based deghosting operator can recover with a great degree of accuracy both the amplitude (Figure 2.9(d)) and phase of the true ghost-free data above 5.5 Hz. The ghost-free prediction improves when seismic events have comparable amplitude range. Therefore, removing direct arrival and ocean-bottom reflections improves the ghost-free prediction of reflections from subsequent layers and also improves the ghost-free prediction of refraction data.

Low-frequency traces from the true ghost-free, the ghost-contaminated, and the ghost-free prediction gathers for a receiver 3930 m away from the source are shown in Figure 2.10(a) and

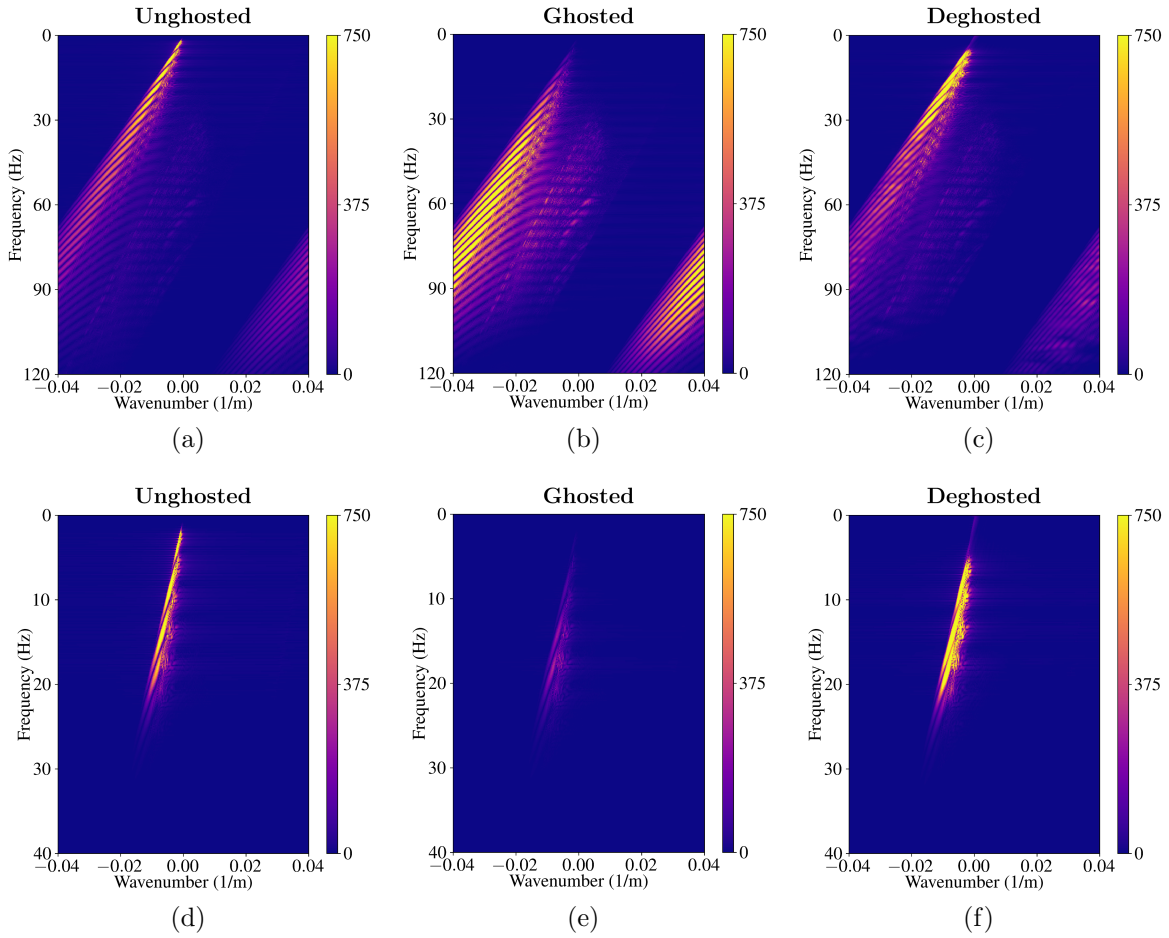

Figure 2.8 The frequency-wavenumber spectra of (a) Figure 2.5(a), (b) Figure 2.5(b), (c) Figure 2.5(c), (d) Figure 2.5(d), (e) Figure 2.5(e), (f) Figure 2.5(f).

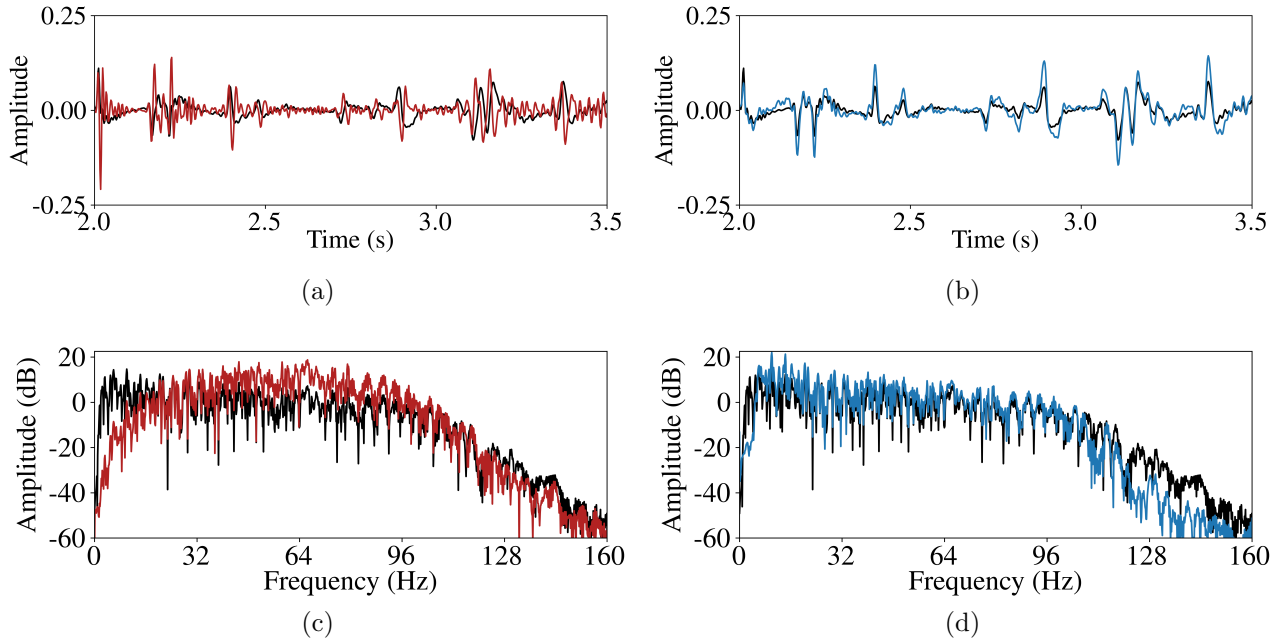

Figure 2.9 Comparison between traces recorded at a receiver that is 3930 m away from the source. (a) Comparison between ghost-free (black line) and ghost-contaminated (red line) traces. (b) Comparison between ghost-free and ghost-free prediction (blue line) traces. (c) and (d) Comparison between the amplitude spectra of the traces shown in Figure 2.9(a) and Figure 2.9(b), respectively.

Figure 2.10(b). Figure 2.10(c) and Figure 2.10(d) shows the corresponding amplitude spectra for the ghost-contaminated and ghost-free prediction traces, respectively. The reconstructed trace matches well the true ghost-free trace in amplitude and phase. The low-frequency ghost-free prediction is nearly noise free, indicating that noise present in the ghost-free prediction is mainly at high frequencies. However, such noise is not introduced by the CNN but appears to be high-frequency residuals from the ghost-contaminated input (Figure 2.9(a) and Figure 2.9(b)).

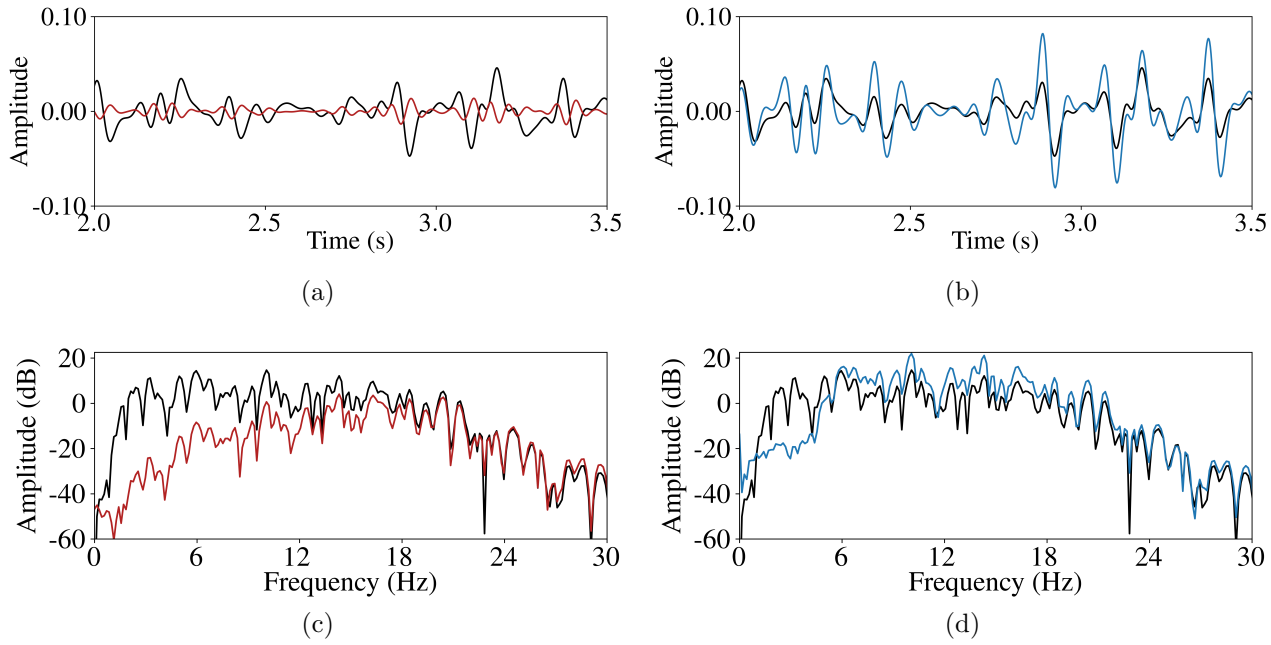

Figure 2.10 Comparison between traces recorded at a receiver that is 3930 m away from the source after applying a 20 Hz low-pass filter. (a) Comparison between ghost-free (black line) and ghost-contaminated (red line) traces. (b) Comparison between ghost-free and ghost-free prediction (blue line) traces. (c) and (d) Comparison between the amplitude spectra of the traces shown in Figure 2.10(a) and Figure 2.10(b), respectively.

The correlation coefficients between individual traces as a function of offset for the full bandwidth and band-limited data are shown in Figure 2.11(a) and Figure 2.11(b), respectively. The correlation coefficients indicate that ghost reflections introduce distortion that is a function of offset and frequency. The overall correlation coefficient for the full bandwidth traces between true and predicted ghost-free data is approximately 0.9. However,

for traces recorded by receivers centered approximately 1939 m away from the source, there is a drop of approximately 20 % in the correlation coefficients, which is likely caused by events crossing (i.e., events with different moveouts). The correlation coefficients between the band-limited traces indicate that low-frequency reconstruction is poor at offset shorter than 1939 m.

2.3.3 Seismic deghosting: Field data example

We test our CNN deghosting method on conventional streamer data acquired offshore of Australia. The data are acquired with a source spacing of 18.5 m and receiver spacing of 12.5 m. The source depth is 5 m, and the cable depth is 7 m. For this test, we use 608 shots to demonstrate the deghosting result pre- and poststack. We preprocess the field data by applying a $2.5 - 110$ Hz band-pass filter. Because the field data acquisition parameters match that of the training data, we use the same trained NN from the synthetic example to predict ghost-free data in this example.

Figure 2.12(a) and Figure 2.12(b) shows a ghost-contaminated input gather to the CNN and the ghost-free prediction, respectively. The two gathers differ by the enhanced low-frequency content after the CNN deghosting (Figure 2.13(a)). The phase change in the data is not clearly visible in the full bandwidth gathers (Figure 2.12(a) and Figure 2.12(b)), but after applying a 20 Hz low-pass filter (Figure 2.12(c) and Figure 2.12(d)) the phase change becomes clear (e.g., at 1.4 s). The average amplitude spectra of the two band-limited gathers (Figure 2.13(b)) illustrate the change in frequency content for low frequencies. The amplitude spectra show that there is a 16 dB increase in amplitude in the range $2.5 - 20$ Hz on average, compensating for the attenuated low frequencies due to ghost reflections.

Figure 2.14(a) and Figure 2.14(b) show the stacked data without and with CNN-based deghosting, respectively. The arrows point to improvements due to deghosting. Horizons are more coherent and appear continuous due to the ghost removal. The waveform in the ghost-contaminated section has a reverberatory character that lowers the resolution of the data, which is not observed in the ghost-free prediction section. Horizons in the deghosted

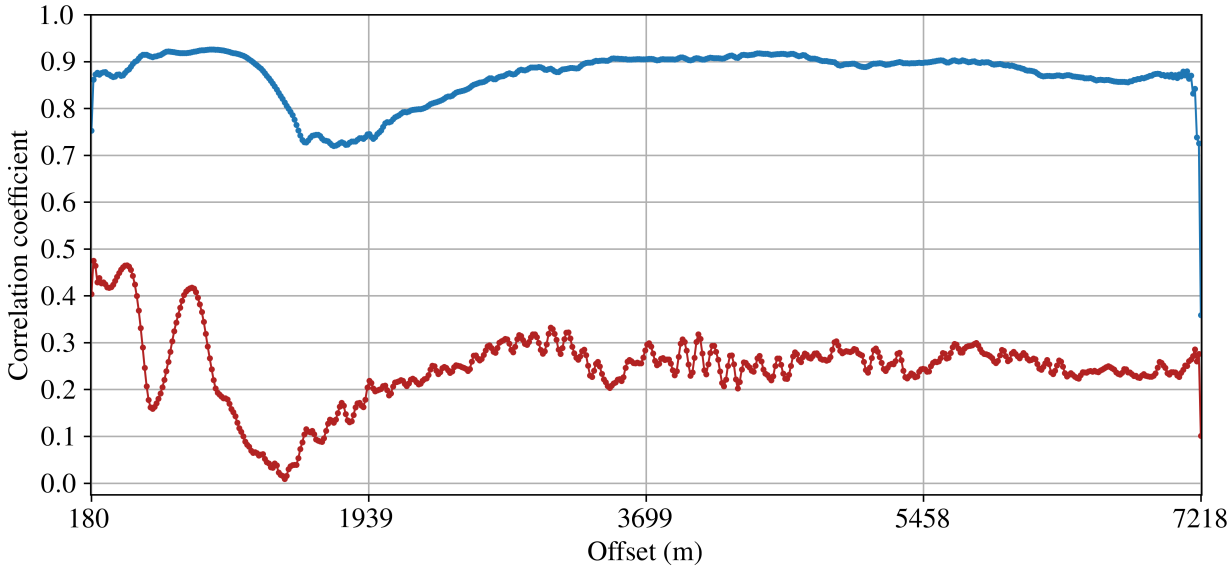

(a)

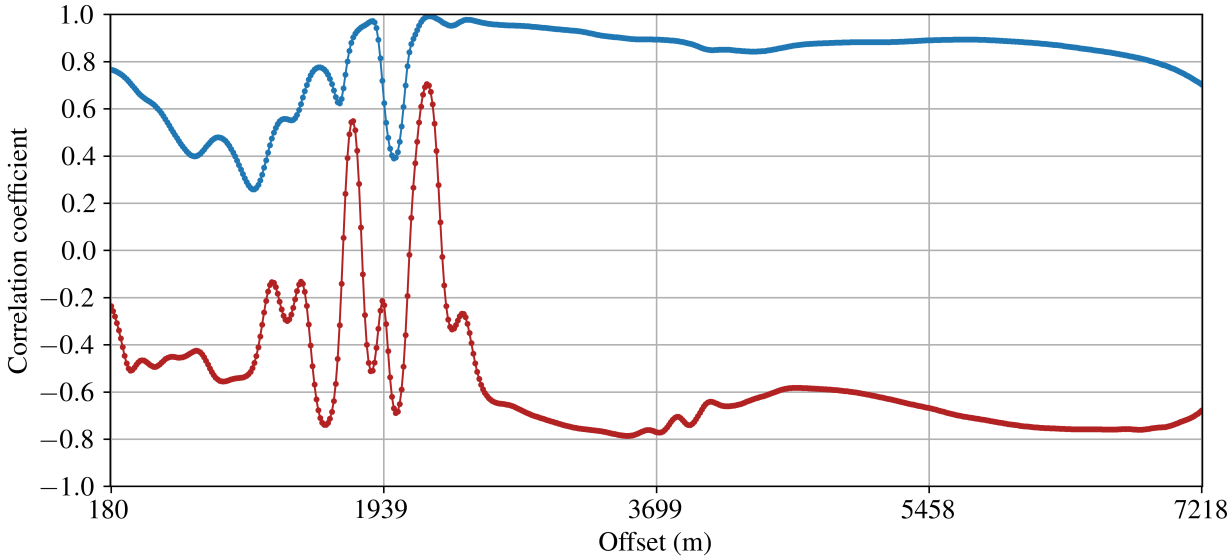

(b)

Figure 2.11 (a) The correlation coefficient between the true ghost-free data and ghost-contaminated data (red) and true ghost-free data and ghost-free prediction (blue) for the full bandwidth individual traces. (b) The correlation coefficient between the true-ghost free data and ghost-contaminated data (red) and true ghost-free data and ghost-free prediction (blue) for the band-limited individual traces

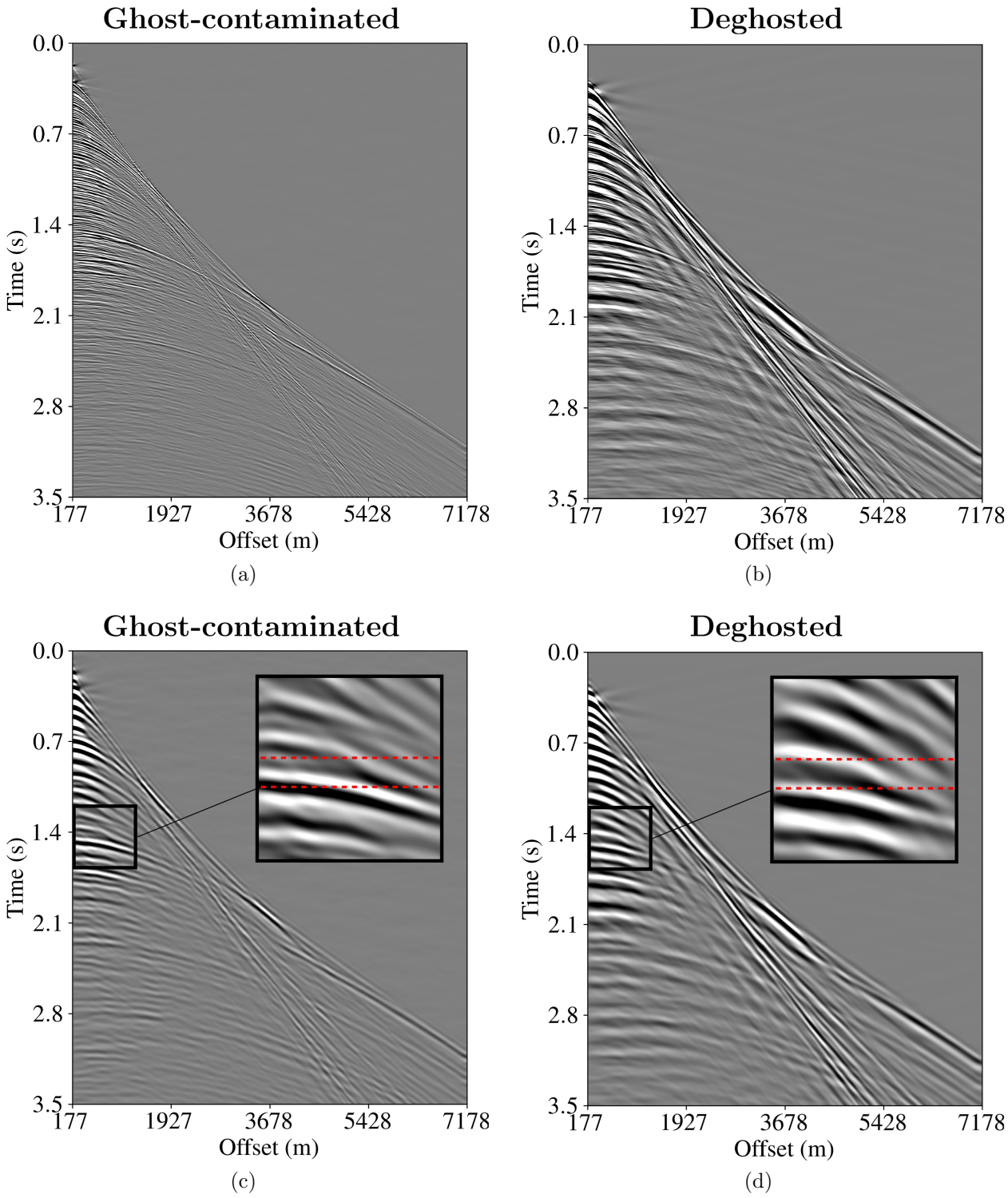

Figure 2.12 Comparison between (a) ghost-contaminated and (b) ghost-free prediction shot gathers. Figure 2.12(c) and Figure 2.12(d) After applying 20 Hz high-cut filtering in Figure 2.12(a) and Figure 2.12(b), respectively. The dashed red lines are for cross referencing.

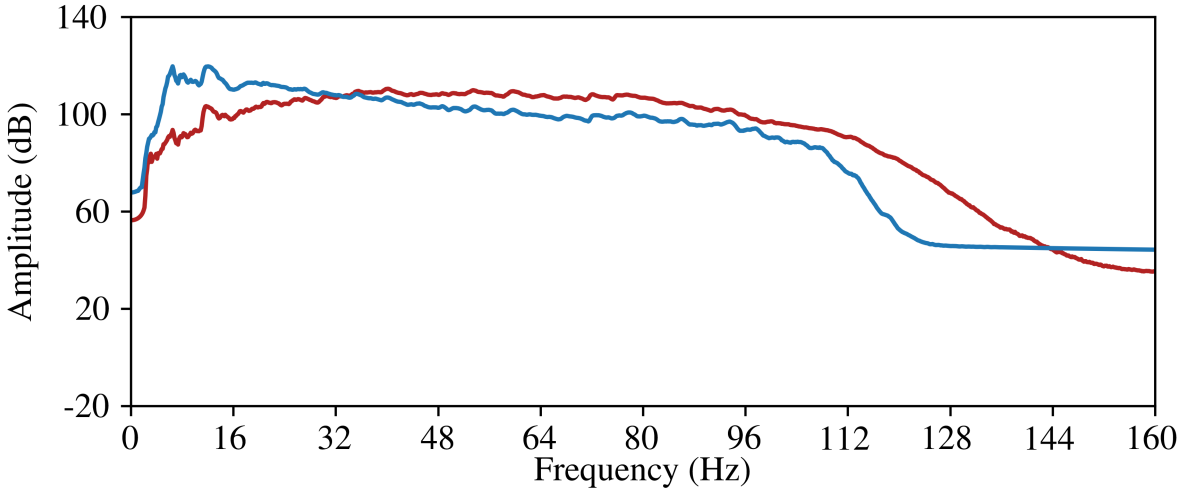

(a)

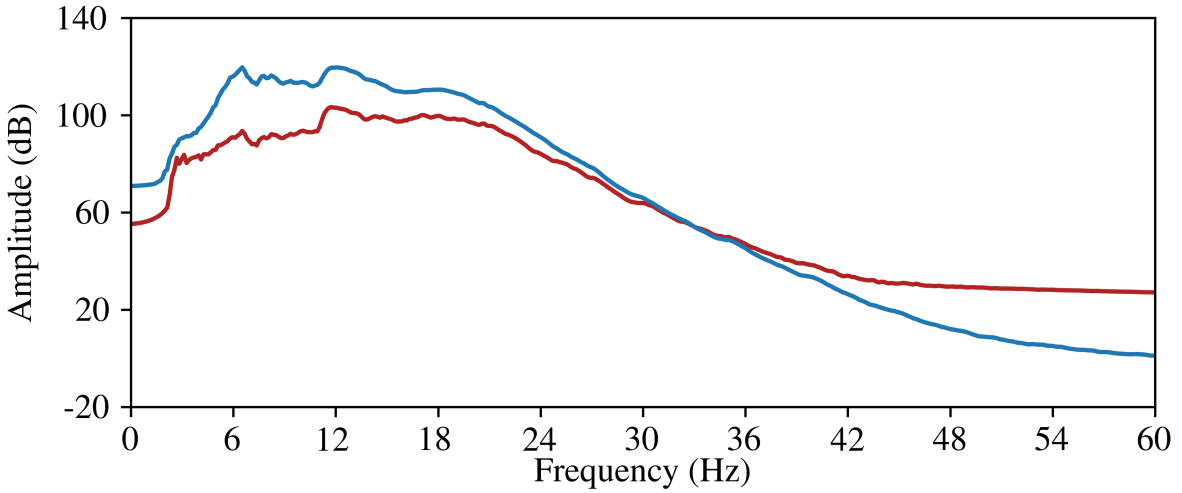

(b)

Figure 2.13 Comparison between the average amplitude spectra of the ghost-contaminated data (red line) and the ghost-free prediction data (blue line). (a) Comparison between the full bandwidth data shown in Figure 2.12(a) and Figure 2.12(b). (b) Comparison between the band limited data shown in Figure 2.12(c) and Figure 2.12(d).

sections are more compact and clearer, making the interpretation easier. Figure 2.15(a) shows the average amplitude spectra of the two stacked sections. Although the amplitude spectra are almost identical, the stacked sections are different in terms of horizons continuity and compactness. Part of the processing sequence we use to generate the stacked sections, is predictive deconvolution. As a consequence, the average amplitude spectra of the ghost-contaminated and ghost-free prediction are very similar. Nonetheless, the stacked sections are very different, with a clear improvement to the continuity of horizons after deghosting. Using the recorded source signature to deconvolve the deghosted data is not an option, because the source signature has the source ghost. Using the recorded source signature to deconvolve the deghosted data requires that we train the CNN to remove receiver-side ghost reflections only.

Given the importance of low-frequency information in seismic data, we apply a 20 Hz low-pass filter to the stacked sections shown in Figure 2.14(a) and Figure 2.14(b) (Figure 2.14(c) and Figure 2.14(d)). For such low frequencies, the continuity and coherency of seismic events after CNN-based ghost removal become more evident. Figure 2.15(b) compares the average amplitude spectra of the stacked sections after a 20 Hz low-pass filter. The average amplitude spectra of the ghost-contaminated and ghost-free prediction are very similar, demonstrating the importance of phase correction in the ghost removal process. Further, the band limited sections show that ghost reflections alter the source signature more significantly at the lower end of the spectrum than at the higher end. This alteration is more significant at low frequencies because the phase of the source-side and receiver-side ghosts coincide at 0 Hz. Since our training data are noise-free, the field example shows that CNN deghosting is robust to random noise because the presence of such noise in field data is inevitable.

2.4 Discussion

The numerical example demonstrates the ability of CNNs to remove source- and receiver-side ghosts from conventional pressure data acquired at a single reference surface in the shot gather domain. The advantage of using our approach is that source and receiver deghosting can be performed as a preprocessing step in the field by constructing the CNN-based deghosting

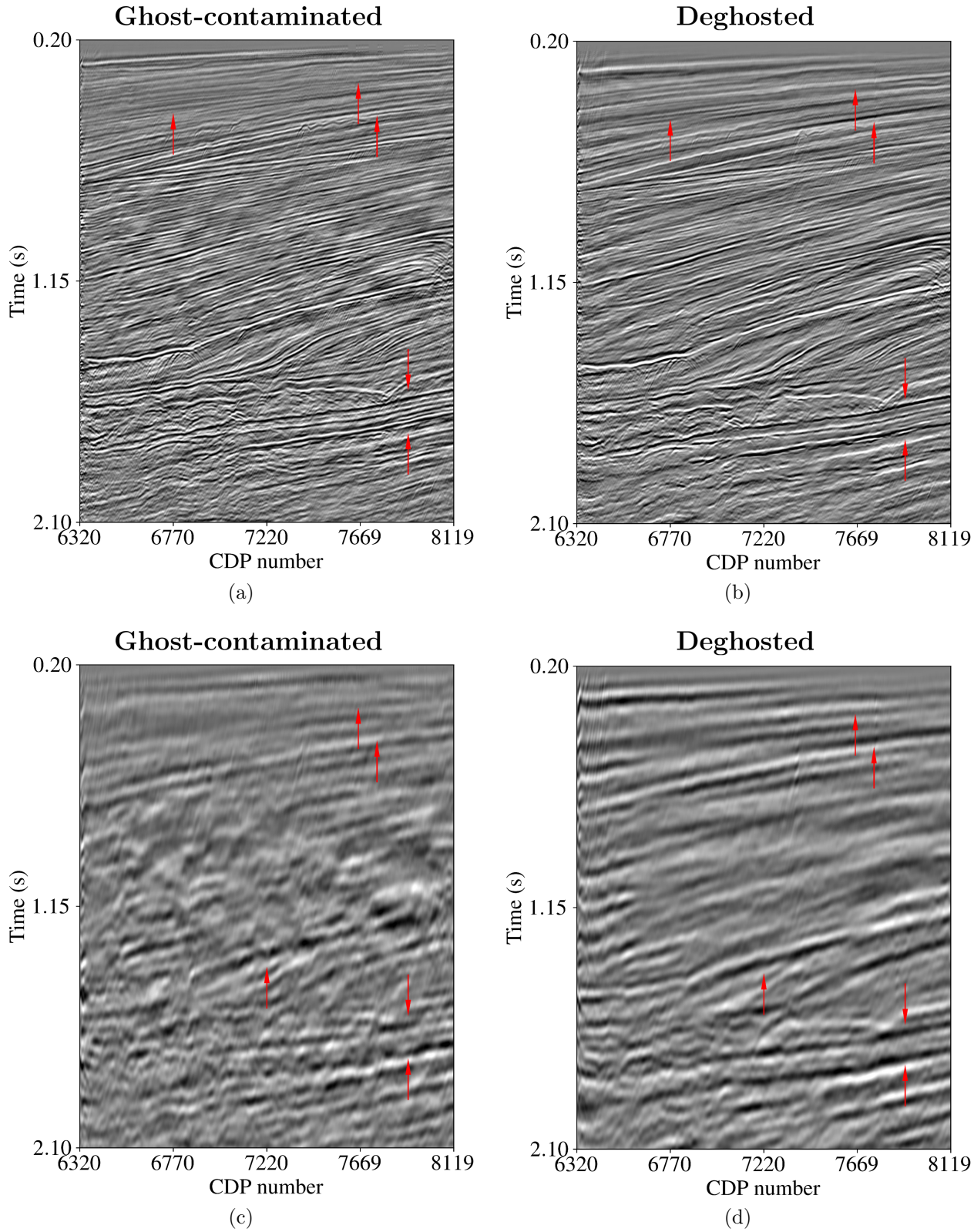

Figure 2.14 Comparison between (a) ghost-contaminated and (b) ghost-free prediction stacked sections. (c) and (d) Comparison between the sections shown in Figure 2.14(a) and Figure 2.14(b), respectively, after applying a 20 Hz low-pass filter.

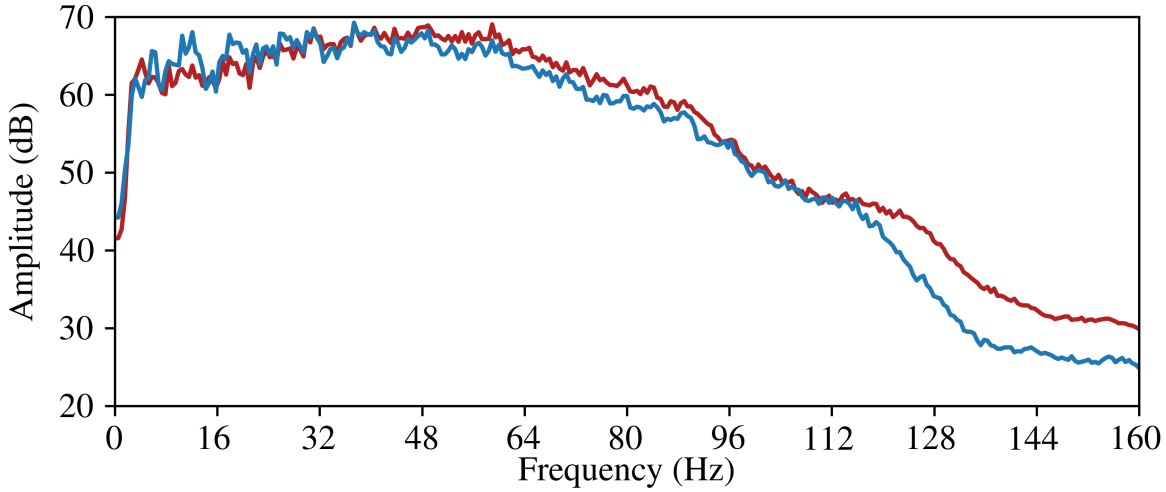

(a)

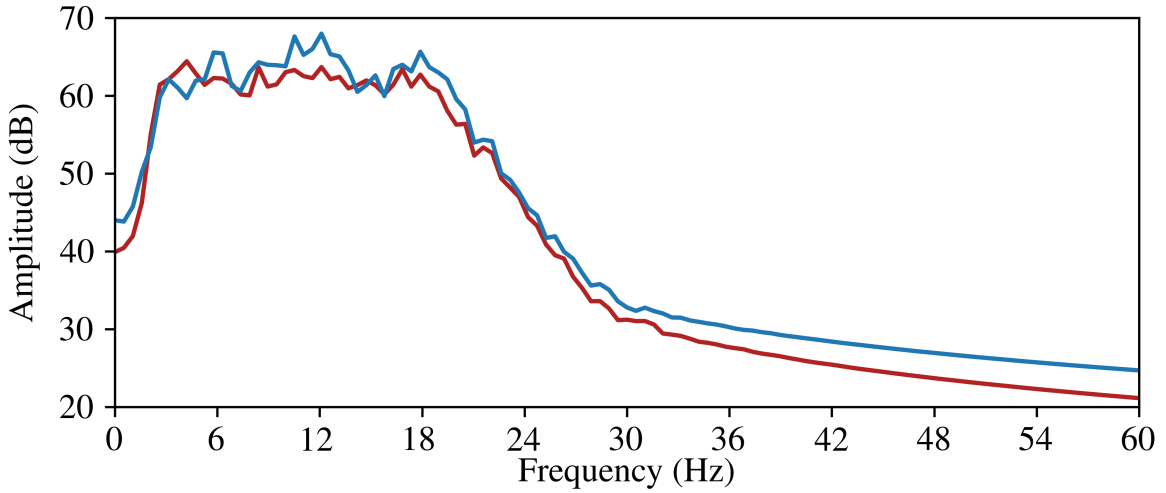

(b)

Figure 2.15 Comparison between the average amplitude spectra of the ghost-contaminated (red line) and ghost-free prediction stacked sections. (a) Comparison between the full bandwidth sections shown in Figure 2.14(a) and Figure 2.14(b). (b) Comparison between the band-limited sections shown in Figure 2.14(c) and Figure 2.14(d).

operator prior to acquisition. This solution does not make assumptions about the acquisition geometry but requires it to be known to create training data that match the actual field acquisition geometry. We assume that data are acquired under a flat sea surface, which is not always a feature of marine acquisitions. Cecconello et al. (2018), Blacquière and Sertlek (2019), and Konuk and Shragge (2020) show that a dynamic sea surface affects the phase and amplitude of seismic data. However, the field example indicates that a flat sea surface assumption is still valid for ghost removal using a deep learning approach. More research is needed to assess the sea state conditions under which our proposed method is applicable. Our field example uses receivers at depth between 6.2 m and 7.7 m, with a nominal streamer depth of 7 m, showing that our method can tolerate depth variations. Changing the acquisition geometry does not require rebuilding the CNN-based deghosting operator, and one can use transfer learning to retrain the NN for use in other field acquisition setups. In our work, we assume a horizontal streamer acquisition with no variation in geometry in the crossline direction. Thus, investigating 3D effects (e.g., feathering) under a 2D acquisition assumption would be needed and remains a subject for future work.

Although the ghost reflections are independent of the source function, they are dependent on the bandwidth of the seismic signal, as shown in equation 2.5. However, given that our solution is based on a data-fitting procedure, its applicability to field data depends on its ability to tolerate source wavelet uncertainties (i.e., depends on the ability of the CNN to learn to remove ghost reflections for arbitrary source functions). Our field data example shows that the proposed approach improves the data quality even though the source wavelet that we use to create the training data is different from the source wavelet of the field data. Moreover, our field data results use a purely statistical source signature deconvolution approach instead of a deterministic approach, thus demonstrating the improvement in the waveform character even when using a statistical deconvolution technique due to ghost removal.

The synthetic example shows that the NN is less capable of reconstructing frequencies below 5.5 Hz, indicating a need to increase the size of the convolutional filters, i.e., increase

the number of trainable parameters in the NN. Prior publications by Sun and Demanet (2020), for low-frequency extrapolation, and by Almuteri and Sava (2021), for seismic deghosting, show that the ability to reconstruct data with a certain bandwidth is proportional to the capacity of the NN (i.e., the number of trainable parameters). Incorporating additional information (e.g., particle motion data) into our method could improve deghosting. Our formulation of the CNN reconstructs the relative amplitude of the seismic data rather than the absolute amplitude because of our choice of a bounded activation function, to whose range we normalize the input and output training data. We leave extending our approach to recover the absolute amplitude for future work. Using the method described in this paper, we can remove source-side ghost reflections in the shot domain without a need to transform the data to the common-receiver domain and without a need for shot interpolation because (1) the imprints of the source-side ghosts are present in shot gathers; otherwise, a mere domain transformation (to a common-receiver gather) would not unveil the source-side ghost, and (2) input-output pairs of ghost-contaminated and ghost-free data are the only way for the NN to learn through supervised learning how to map between the two, thus reducing the problem to amplitude and phase correction. Self-supervised learning is an alternative approach to supervised learning that removes the burden of generating input-output pairs of training data. It is applied in geophysics for noise suppression (Birnie et al., 2021; Liu et al., 2022a,b) and low-frequency extrapolation (Hu et al., 2020; Wang et al., 2020), and it is showing promising results. Self-supervised learning is applicable to seismic deghosting within a physics-guided NN framework.

2.5 Conclusion

We propose a method to remove source- and receiver-side ghosts in the shot domain. The solution works for pressure data acquired at a single recording level and uses a CNN with a supervised learning approach to map ghost-contaminated data to ghost-free data. Our solution alleviates acquisition and processing complexities associated with acquisition systems that use complementary measurements. Because our solution is based on learning

through data fitting, the acquisition geometry and the bathymetry of the ocean floor must be known to create training data that closely mimic field data acquisition conditions. We demonstrate with a synthetic example and field data that CNNs can predict ghost-free data with a reasonable accuracy. Recovering the low frequencies remains a challenge because of the limited capacity of the CNN, i.e., its effectiveness increases proportionally with the number of trainable parameters. Still, we show that the solution is robust to data generated using a model with strong velocity contrasts and velocity values beyond that of the models used to generate the training data. We also show that the method is robust to inputs with random noise, i.e., field data, even though the training data are noise free. Finally, we show that a simple amplitude correction is not sufficient to recover the ghost-free data and highlight the importance of phase correction in the ghost removal process.

2.6 Acknowledgments

The first author would like to thank Saudi Aramco for graduate study sponsorship. We thank the sponsors of the Center for Wave Phenomena at Colorado School of Mines for the support of this research. We also thank CGG for providing the field data, and Tugrul Konuk (CWP) for many useful discussions and for providing the forward-modeling code that made this research possible.

2.7 Data and materials availability

Data associated with this research are confidential and cannot be released.

CHAPTER 3

MODELING THE SEISMIC WAVEFIELD OF MOVING MARINE VIBRATOR SOURCE

A paper accepted in *Geophysics*[1].

Khalid Almuteri[2,3,4], Jeffrey Shragge[5], and Paul Sava[5]

Marine vibrators are an emerging alternative to conventional air guns in ocean-bottom acquisition due to their ability to generate low-frequency waves and limited adverse impact on marine wildlife. However, using marine vibrators introduces challenges not found in conventional air-gun-based acquisition where receivers are placed on the ocean bottom, including handling the phenomena associated with the Doppler effect and time-dependent source-receiver offsets due to the source motion. Standard seismic data processing solutions assume stationary sources and receivers for the duration of any seismic experiment (e.g., a shot); however, accurately accounting for source motion effects in processing is critical for optimal subsurface imaging. To address these challenges, we develop a finite-difference approach for modeling the full acoustic wavefield in a generalized coordinate system that tracks a moving source. Synthetic examples demonstrate that this technique both accurately and stably models high-velocity moving sources and accurately accounts for the wavefield distortion predicted by the Doppler effect. This approach is not limited to modeling wavefield propagation for a moving source and can be used to develop advanced imaging and inversion techniques (e.g., reverse-time migration and full waveform inversion) for data acquired using marine vibrators. Additionally, the developed approach is not limited to modeling mobile sources, but can also model conventional towed-streamer data.

---

[1]Reprinted with permission of *Geophysics*.

[2]Graduate student, Center for Wave Phenomena, Department of Geophysics, Colorado School of Mines
[3]Saudi Aramco
[4]Author for correspondence
[5]Professor, Center for Wave Phenomena, Department of Geophysics, Colorado School of Mines.

3.1 Introduction

Concerns over conventional seismic air guns make a transition to less environmentally adverse marine vibrators desirable. Although marine vibrators have been around since the 1960s (Smith and Jenkerson, 1998), the lack of low frequencies and the perceived unreliability of marine vibrators have historically prevented further development and interest by the exploration industry in the technology (Teyssandier and Sallas, 2019). However, recent technological advancements renewed the interest in marine vibrators not only for environmental reasons but also for their geophysics-related merits. From a seismic exploration perspective, marine vibrators can provide richer low-frequency content than air guns (Dellinger et al., 2016; Guitton et al., 2021), and enable versatile control over the source signature (Laws et al., 2019). Unlike air guns, where phase can only be modified through time delays, the phase in marine vibrators can be independently specified for each frequency. The precise control over phase in marine vibrators allows for the use of advanced acquisition techniques such as phase sequencing, creating source-side wavefield gradients, and simultaneous acquisition, as discussed below:

- Phase sequencing in cascaded sweep acquisition helps attenuate residual source noise, allowing for denser shot acquisition in the inline direction (Laws et al., 2019). In air-gun-based acquisition, a sufficient time period must pass between acquiring two consecutive shots for the shot-generated noise from a shot to be at an acceptable level when acquiring the subsequent shot (Landrø, 2008). This trade-off between source-time interval and the level of residual source noise results in sub-optimal and sparser shot acquisition than desirable. Varying the source phase from one source point to the next can resolve the sparsity of source points in marine data inline. In practice, such changes are hard to execute using seismic air guns, but easily attainable using marine vibrator sources.

- Crossline sampling in marine acquisition is often sparse, resulting in aliased wavefields. One method for reconstructing the non-aliased seismic wavefield uses the multichannel sampling theorem, which extends Shannon's sampling theorem by incorporating the spatial derivative of the seismic wavefield in the reconstruction process (Pawelec et al., 2022; Robertsson et al., 2008; Vassallo et al., 2010). This method reduces the necessary spatial sampling and enables the recovery of non-aliased data from aliased input, allowing for data to be acquired twice as coarsely as when not using the spatial derivative data along the crossline direction (Laws et al., 2019). Thus, acquiring the source-side spatial gradient of the pressure wavefield facilitated by marine vibrator sources can effectively address the issue of spatial aliasing in the crossline direction. Such data can be acquired using two marine vibrators, placed with some offset along the crossline direction, sweeping with opposite polarities. The corresponding airgun acquisition would require sailing each inline twice or acquiring secondary data in the vicinity of primary source points, employing an approach similar to over/under sources (e.g., Egan et al., 2007) to estimate the source-side wavefield gradient in the crossline direction.

- Another advantage of using marine vibrators is acquiring seismic data in a shorter time compared to air-gun-based acquisition when using multiple phase-encoded sources simultaneously. Although simultaneous acquisition is achievable using seismic air guns (e.g., Amundsen et al., 2018; Mueller et al., 2015; Robertsson et al., 2016), the limited phase control in seismic air guns limits the full potential of simultaneous acquisition (Halliday and Moore, 2018; Laws et al., 2019). Laws et al. (2019) numerically demonstrate that employing the aforementioned techniques can reduce acquisition time by one-third compared to conventional air-gun acquisition without compromising the quality of the seismic images.

Processing and imaging challenges emerge due to the source motion and long duration of the marine vibrator sweep, including the Doppler effect and time-dependent source-receiver

offsets in ocean-bottom acquisition. Even though marine vibrators move at a much slower velocity than the wave propagation speed, source motion introduces a noticeable offset- and time-dependent frequency shift to the data (Dragoset, 1988; Hampson and Jakubowicz, 1995; Schultz et al., 1989). Further, phase distortion also occurs in the seismic signal, which is proportional to the source velocity and time slope of seismic events, because of the source motion.

Current seismic data processing and imaging in marine acquisition assume stationary geometry for the duration of a seismic experiment. Appropriate processing and imaging of data acquired using moving sources requires accurate modeling of the associated effects. Numerical wave-equation solutions are necessary for understanding wave propagation under realistic acquisition conditions (e.g., dynamic sea surfaces and/or moving sources), and form the basis of many geophysical applications such as imaging and inversion. Accurate modeling of seismic wavefields is key in advanced seismic imaging and inversion techniques, such as reverse-time migration (RTM) (e.g., Almuteri et al., 2022a) and full-waveform inversion (FWI) (e.g., Kurzmann et al., 2013; Zhang et al., 2023; Zhou et al., 2018). Various methods are proposed in the literature to model marine vibrator data. Dellinger and Díaz (2020) present a sweep segmentation approach to model mobile sources that splits the source function into different segments that can be injected at fixed source positions along the source path. The advantage of this approach is its simplicity and ease of implementation. However, it may require applying a correction filter to the modeled data (Duquet et al., 2021) because it assumes the source jumps to discrete locations along the source path instead of being continuously in motion. JafarGandomi and Grion (2021) propose a method of modeling marine vibrator data by interpolating unaliased impulsive sources data to desired source locations and convolving with segments of the vibrator sweep. This method is similar to the former approach as it employs a source-segmentation technique. However, this method requires densely sampled sources and data interpolation, which can be computationally expensive for irregularly sampled sources. Cartesian-based modeling methods are susceptible to numerical

instabilities and modeling inaccuracies when introducing irregular or dynamic computational geometries such as time-varying sea surfaces (Konuk and Shragge, 2020). Further challenges arise when implementing free-surface boundary conditions for such irregular geometries in a Cartesian coordinate system.

This paper presents a finite-difference approach to model the full acoustic wavefield triggered by a mobile source in a generalized coordinate system that effectively embeds source motion into the coefficients of the governing tensorial acoustic wave equation. Shragge (2014) and Shragge and Tapley (2017) present a time-invariant tensorial representation of the acoustic wave equation (AWE) in a generalized coordinate system. This approach facilitates coordinate transformation to map the irregular physical domain to a regular computational domain, enabling FD modeling. Konuk and Shragge (2020) extend this technique to address the challenge of dynamic sea surfaces by specifying a time-variant 4D coordinate transformation. This extension leads to a time-varying mesh grid in physical Cartesian coordinates, but a stationary mesh grid in a generalized computational coordinate system.

Here, we present a solution to the AWE for a time-varying mesh without the need for repeated velocity model interpolation, eliminating the added computational complexity and accuracy issues associated with this operation. In this framework, the time-varying physical Cartesian domain horizontally shears conformally with the source motion. However, the computational domain is fixed in time, with time- and space-dependent partial differential operator coefficients. The developed approach is not limited to modeling moving sources with ocean-bottom receivers and is also applicable to conventional towed-streamer scenarios. Additionally, we investigate source motion effects on seismic data, including ghost reflections, acquired under a quiescent sea surface condition.

3.2 Theory

3.2.1 Tensorial acoustic wave equation

The 4D tensorial AWE in a generalized coordinate system defined by the variables $\boldsymbol{\xi} = [\xi^0, \xi^1, \xi^2, \xi^3]$ is (Konuk and Shragge, 2020)

$$\Box_\xi P_\xi = F_\xi, \tag{3.1}$$

where $\Box_\xi$ is the generalized d'Alembert operator, P_ξ is the pressure field, and F_ξ is the source function. The ξ^0 coordinate is time-like (time axis scaled by the acoustic velocity) and ξ^1, ξ^2, ξ^3 are space-like components. The generalized d'Alembert operator is

$$\Box_\xi = \frac{-1}{\sqrt{|\boldsymbol{g}|}} \frac{\partial}{\partial \xi^\mu} \left(\sqrt{|\boldsymbol{g}|} g^{\mu\nu} \frac{\partial}{\partial \xi^\nu} \right), \; \mu, \nu = 0, \cdots, 3, \tag{3.2}$$

where $[g^{\mu\nu}]$ is a symmetric rank-two contravariant metric tensor, $|\boldsymbol{g}|$ is the determinant of the covariant metric tensor $[g_{\mu\nu}]$, and $[g^{\mu\nu}] = [g_{\mu\nu}]^{-1}$. Here, we use superscript indices for components with a contravariant representation and subscript indices for components with a covariant representation. The covariant metric tensor relates the generalized coordinate geometry to an equivalent Cartesian coordinate system representation with elements given by

$$g_{\mu\nu} = \frac{\partial x^i}{\partial \xi^\mu} \frac{\partial x^i}{\partial \xi^\nu} \quad \text{for} \quad i, \mu, \nu = 0, \cdots, 3, \tag{3.3}$$

where repeated indices imply summation. The columns of the contravariant and covariant metric tensors form dual bases (i.e., the dot product $\langle \boldsymbol{g}_i \; , \; \boldsymbol{g}^j \rangle = \delta_{ij}$). In Cartesian coordinates with variables $\boldsymbol{x} = [x^0, x^1, x^2, x^3] = [ct, x, y, z]$, the d'Alembert operator (equation 3.2) reduces to

$$\Box = \frac{-1}{c^2} \frac{\partial^2}{\partial t^2} + \nabla^2, \tag{3.4}$$

where $c = c(\boldsymbol{x})$ is the Cartesian medium velocity, and ∇^2 is the 3D Cartesian Laplacian operator.

To simulate wavefields triggered by a moving source, we set the generalized AWE in arbitrary coordinates and then choose a coordinate transformation that maps a horizontally deformed physical domain to a regular computational domain. To simplify the 4D coordinate

transformation, we make a set of plausible assumptions: (1) no stretching of the time coordinate occurs, i.e., $x^0 = \xi^0$ (or $t = \tau$); (2) the horizontal source movement is along the ξ^1-axis only, leaving the ξ^2-axis unchanged (i.e., $x^2 = \xi^2$); (3) the source moves at a fixed depth level (i.e., there is no vertical motion and thus $x^3 = \xi^3$); (4) the source moves at a constant velocity (i.e., $\frac{\partial v}{\partial \xi^0} = 0$); and (5) the source moves in a homogeneous fluid medium. The first four assumptions allow us to express the horizontal mesh deformation $x^1 = T\left(\xi^0, \xi^1, \xi^2, \xi^3\right)$, where T is any arbitrary horizontal deformation function that depends on all variables $(\xi^0, \xi^1, \xi^2, \xi^3)$. Recognizing that $\xi^0 \equiv c\tau$ and $\frac{\partial}{\partial \xi^0} = \frac{1}{c}\frac{\partial}{\partial \tau}$, the generalized d'Alembert operator (equation 3.2) for an arbitrarily deformed mesh along the ξ^1-axis reduces to the second-order AWE

$$\underbrace{\frac{1}{T_1}\frac{\partial}{\partial \tau}\left(\frac{T_1}{c^2}\frac{\partial P_\xi}{\partial \tau}\right)}_{\text{Newtonian acceleration}} = \underbrace{\frac{1}{T_1}\left[\frac{\partial}{\partial \xi^1}\left(\frac{T_0}{c}\frac{\partial P_\xi}{\partial \tau}\right) + \frac{\partial}{\partial \tau}\left(\frac{T_0}{c}\frac{\partial P_\xi}{\partial \xi^1}\right)\right]}_{\text{Fluid advection}} + \underbrace{\frac{1}{T_1}\frac{\partial}{\partial \xi^i}\left(T_1 g^{ij}\frac{\partial P_\xi}{\partial \xi^j}\right)}_{\text{Restoring force}} + F_\xi, \quad (3.5)$$

where $T_k = \frac{\partial T}{\partial \xi^k}$, and $i, j = 1, 2, 3$ are spatial indices. The assumptions stated above allow us to express the relationship between the $\boldsymbol{\xi}$- and $\boldsymbol{x}$-coordinate systems as

$$\begin{bmatrix} x^0 \\ x^1 \\ x^2 \\ x^3 \end{bmatrix} = \begin{bmatrix} \xi^0 \\ T\left(\xi^0, \xi^1, \xi^2, \xi^3\right) \\ \xi^2 \\ \xi^3 \end{bmatrix} = \begin{bmatrix} \xi^0 \\ \xi^1 + v\tau e^{\gamma(s_z - \xi^3)} \\ \xi^2 \\ \xi^3 \end{bmatrix}, \quad (3.6)$$

where v is the constant source velocity, γ is a user-defined decay factor that controls the amount of horizontal deformation as a function of depth, and s_z is the source depth. We confine the time-varying mesh deformation to the homogeneous water layer by introducing a depth-dependent horizontal deformation. This coordinate transformation enables the modeling of a moving source without the need for velocity model interpolation at each time step. Further, it allows one to compute the wavefield at and below the receivers level in ocean-bottom acquisition without the need to interpolate the wavefield to Cartesian coordinates. Figure 3.1 show a deformed physical domain in Cartesian coordinates and the fixed computational domain in a generalized coordinate system, respectively. At the initial

time, the computational and physical domains are identical (i.e., $x^1 = \xi^1$). Extending this approach to include a moving source with a time-dependent velocity, i.e., $v \rightarrow v(\xi^0)$, is straightforward.

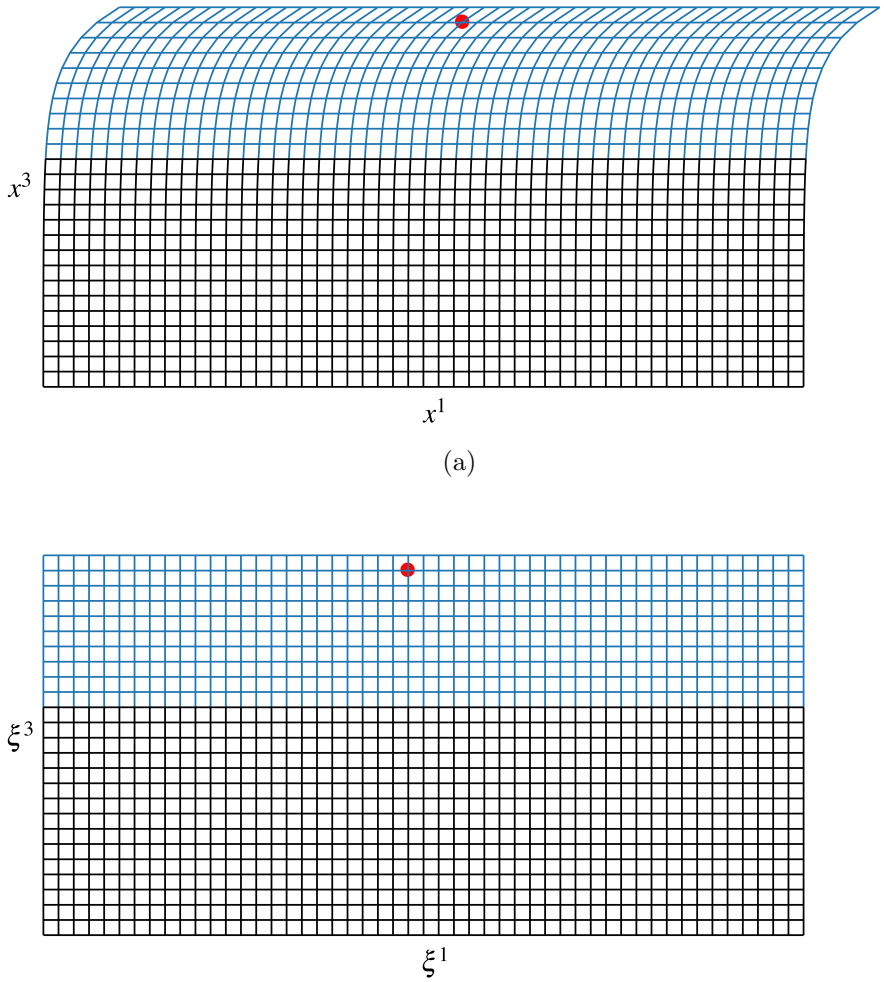

Figure 3.1 Graphical representation of (a) physical and (b) computational domains. The red dot indicates the source location. The blue mesh represents a homogeneous region, whereas the black mesh represents a variable velocity region.

The contravariant metric tensor associated with the depth-dependent horizontally shearing coordinate transformation (equation 3.6) is

$$[g^{\mu\nu}] = \frac{1}{c^2}\begin{bmatrix} -1 & v\alpha & 0 & 0 \\ v\alpha & v^2\alpha^2\left[\beta^2-1\right]+c^2 & 0 & c\beta v\alpha \\ 0 & 0 & c^2 & 0 \\ 0 & c\beta v\alpha & 0 & c^2 \end{bmatrix}, \tag{3.7}$$

where $\alpha = e^{\gamma(s_z-\xi^3)}$ and $\beta = c\gamma\tau$. Thus, equation 3.5 reduces to

$$\begin{aligned} \frac{1}{c^2}\frac{\partial}{\partial\tau}\left(\frac{\partial P_\xi}{\partial\tau}\right) = \frac{2v\alpha}{c^2}\frac{\partial}{\partial\xi^1}\left(\frac{\partial P_\xi}{\partial\tau}\right) + \left[\gamma^2\tau^2v^2\alpha^2 - \frac{v^2\alpha^2}{c^2}\right]\frac{\partial}{\partial\xi^1}\left(\frac{\partial P_\xi}{\partial\xi^1}\right) \\ - \gamma^2\tau v\alpha\frac{\partial P_\xi}{\partial\xi^1} + 2\gamma\tau v\alpha\frac{\partial}{\partial\xi^1}\left(\frac{\partial P_\xi}{\partial\xi^3}\right) + \nabla_\xi^2 P_\xi + F_\xi, \end{aligned} \tag{3.8}$$

where $\nabla_\xi^2 = \frac{\partial}{\partial\xi^1}\left(\frac{\partial}{\partial\xi^1}\right) + \frac{\partial}{\partial\xi^2}\left(\frac{\partial}{\partial\xi^2}\right) + \frac{\partial}{\partial\xi^3}\left(\frac{\partial}{\partial\xi^3}\right)$ and where we assume the medium velocity is slowly varying (i.e., $\frac{\partial c}{\partial\xi^i} \approx 0$ for $i = 1, 2, 3$).

3.2.2 Numerical implementation

We use a finite-difference approach to solve the second-order AWE (equation 3.8) by approximating the partial differential operators with Taylor-expansion coefficients. The numerical scheme uses approximations of order $O(\Delta\xi^4)$ for spatial derivatives and $O(\Delta\tau^2)$ for temporal derivatives. The fluid advection term in equation 3.8 is a first-order mixed derivative that presents a challenge in numerical implementation, as it requires the spatial derivative of the pressure field at a future time step that is unavailable, when using a second-order approximation centered in time. To overcome this problem, we can use either a first-order approximation backward in time or predict the future time step assuming no source motion (e.g., Konuk and Shragge, 2020; Van Renterghem and Botteldooren, 2007). Although the first approach can still use a fourth-order approximation for the first-order spatial partial differential operator, it reduces the accuracy of the numerical scheme by using a first-order approximation for the first-order temporal partial differential operator backward in time. The second approach allows for maintaining a second-order approximation for all temporal differential operators in the AWE by predicting a future pressure wavefield, assuming a

stationary source. Such an assumption is valid because the horizontal mesh deformation is represented by a smooth continuous function with a small contribution to the pressure wavefield (i.e., $v \ll c$) (Konuk and Shragge, 2020). Implementing the second-order AWE permits modeling moving sources using a standard Cartesian-based modeling method with relatively minor modifications. In our numerical implementation, we use Clayton-Enquist absorbing boundary condition[6] (Clayton and Engquist, 1977) for its simplicity and ease of implementation when solving the second-order AWE. Synthetic examples show that the numerical scheme is stable and sufficiently accurate.

3.2.3 Doppler effect

In a constant velocity medium, the source motion causes time-dependent frequency shifts in the data given by

$$f(t) = \frac{c}{c - \mathbf{S} \cdot \mathbf{P}(t)} f_{\circ}(t), \tag{3.9}$$

where $f(t)$ is the time-dependent observed frequency, c is the medium wave propagation speed, $\mathbf{S}$ is the source velocity vector, $\mathbf{P}(t)$ is the time-dependant unit vector that points to the receiver or a scatterer point from the source location (Figure 3.2(a)), and $f_{\circ}(t)$ is the time-dependent input frequency.

For heterogeneous media, the ray paths from a source to a scattering point play a role in the amount of frequency shift. To derive an expression for the frequency change due to source motion in heterogeneous media, we follow the formulation of Kolano (1978). We consider a moving source with velocity v and a stationary point in the subsurface (Figure 3.2(b)). We assume that the source at time $t = 0$ s is at S_1 and after a time interval Δt it is at S_2. If the source emits two pulses, one at each location, the time delay between emitting these pulses will be Δt. The ray paths the two pulses take to arrive at the same location R are P_1 and P_2, with the associated traveltimes T_1 and T_2, respectively. The time delay between the two

[6]In Appendix A, we discuss the details of the boundary condition we use in the numerical implementation of this chapter.

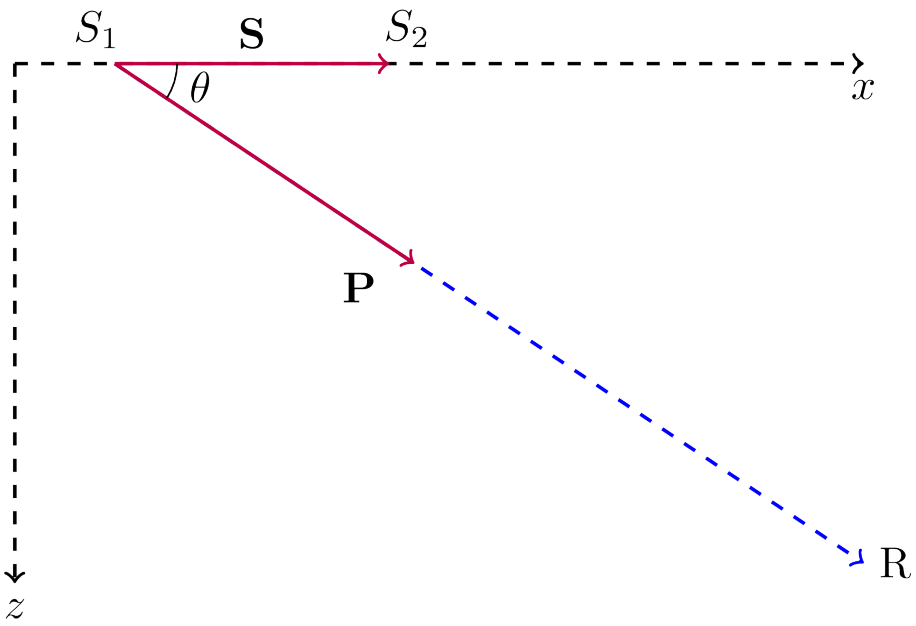

(a)

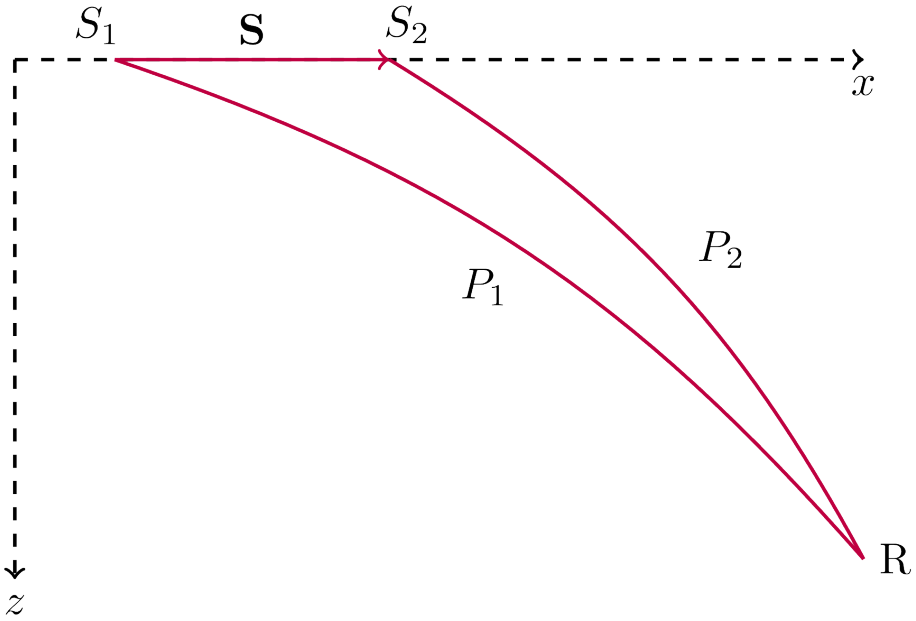

(b)

Figure 3.2 Schematic plot of (a) source motion direction (**S**) relative to a stationary receiver or a scatterer point location (**R**) in a constant velocity medium, and (b) a source moving from S_1 to S_2 with ray paths from source locations S_1 and S_2 to a point R in the subsurface given by P_1 and P_2, respectively, in a variable velocity medium.

pulses at R is

$$\Delta\tau = \Delta t + T_2 - T_1 = \Delta t - \Delta T. \tag{3.10}$$

Considering a source emitting continuously when moving from S_1 to S_2, and because the total number of emitted cycles matches the total number of observed cycles, we have

$$f_\circ \Delta t = f \Delta\tau, \tag{3.11}$$

where $f_\circ$ and f are the emitted and observed frequencies, respectively. Thus, the frequency shift is

$$\Delta f = \frac{\Delta T}{\Delta\tau} f_\circ = \frac{\Delta T}{\Delta t - \Delta T} f_\circ, \tag{3.12}$$

which reduces to

$$\Delta f \approx \frac{\Delta T}{\Delta t} f_\circ \tag{3.13}$$

for $\frac{\Delta T}{\Delta t} \ll 1$ (i.e., the source velocity is much slower than the wave propagation speed). As Δt approaches zero,

$$\Delta f = \lim_{\Delta t \to 0} \frac{T_2 - T_1}{\Delta t} f_\circ = \lim_{\Delta t \to 0} \frac{-\Delta T}{\Delta t} f_\circ = -\frac{dT}{dt} f_\circ. \tag{3.14}$$

Equation 3.14 shows that the Doppler effect in heterogeneous media is related to the material property along the ray path from the source to any point of interest in the subsurface. A more detailed treatment of the Doppler effect in complex media (e.g., anisotropic media) is commonly found in the physics literature concerning radio waves propagating through the ionosphere (e.g., Bennett, 1968; Davies, 1965; Weekes, 1958).

3.3 Numerical Examples

In this section, we present numerical examples to demonstrate the effect of source motion on seismic data in homogeneous media, and on ghost reflections using a single-reflector model. We also investigate the impact of medium heterogeneity on the Doppler effect, and numerically validate our modeling approach by comparing the observed frequencies from our simulations to those predicted by the Doppler theory. Lastly, we examine the effects of source

and receiver motion in complex media.

3.3.1 Modeling in homogeneous media

In horizontally invariant media, one can set $\gamma = 0$ in equation 3.6, reducing the mesh deformation to a pure horizontal translation along the source motion direction. A positive (negative) velocity translates the mesh along the positive (negative) ξ^1 axis. To demonstrate the robustness of the developed approach and highlight the consequences of source motion on seismic data, we use an unrealistically fast source velocity of 0.3 km/s in a homogeneous medium. We simulate a 2D acoustic wavefield in a constant velocity medium of 1.5 km/s using a 30 Hz monochromatic wave. The source is located at $x^1 = 2.0$ km (i.e., $\xi^1 = 2.0$ km) at time $t = 0$ s. In the mobile source case, we compute the acoustic wavefield using our approach and interpolate it to the Cartesian coordinate system at every time step. Figure 3.3 show snapshots at $t = 0.68$ s modeled using stationary and mobile sources, respectively. In the stationary source scenario, the wavefield is symmetric and the amplitudes along a wavefront are uniform. In the mobile source scenario, the right-going waves (along the source movement direction) are compressed, whereas the waves traveling in the opposite direction are dilated, according to the Doppler effect. The amount of compression or dilation is a function of the source velocity, the acoustic wave propagation speed in the medium, the source motion direction, the propagation direction, and the input frequency.

Figure 3.4 show shot gathers acquired using a stationary and mobile source, respectively, recorded using stationary receivers placed 25 m below the source. For the stationary source case (Figure 3.4(a)), the direct arrivals are symmetric around the source location. For the mobile source case (Figure 3.4(b)), the apices of the direct arrivals are shifted because of the source motion, and the lateral shift increases with time. Traces recorded to the left of the source are shifted to a lower frequency, while the traces recorded to the right of the source are shifted to a higher frequency. Figure 3.5 show two traces for stationary receivers at $x^1 = 1.75$ km and $x^1 = 2.75$ km, respectively, placed at the same depth level as the source, computed numerically and analytically (we derive the analytical solution in Appendix 3.8).

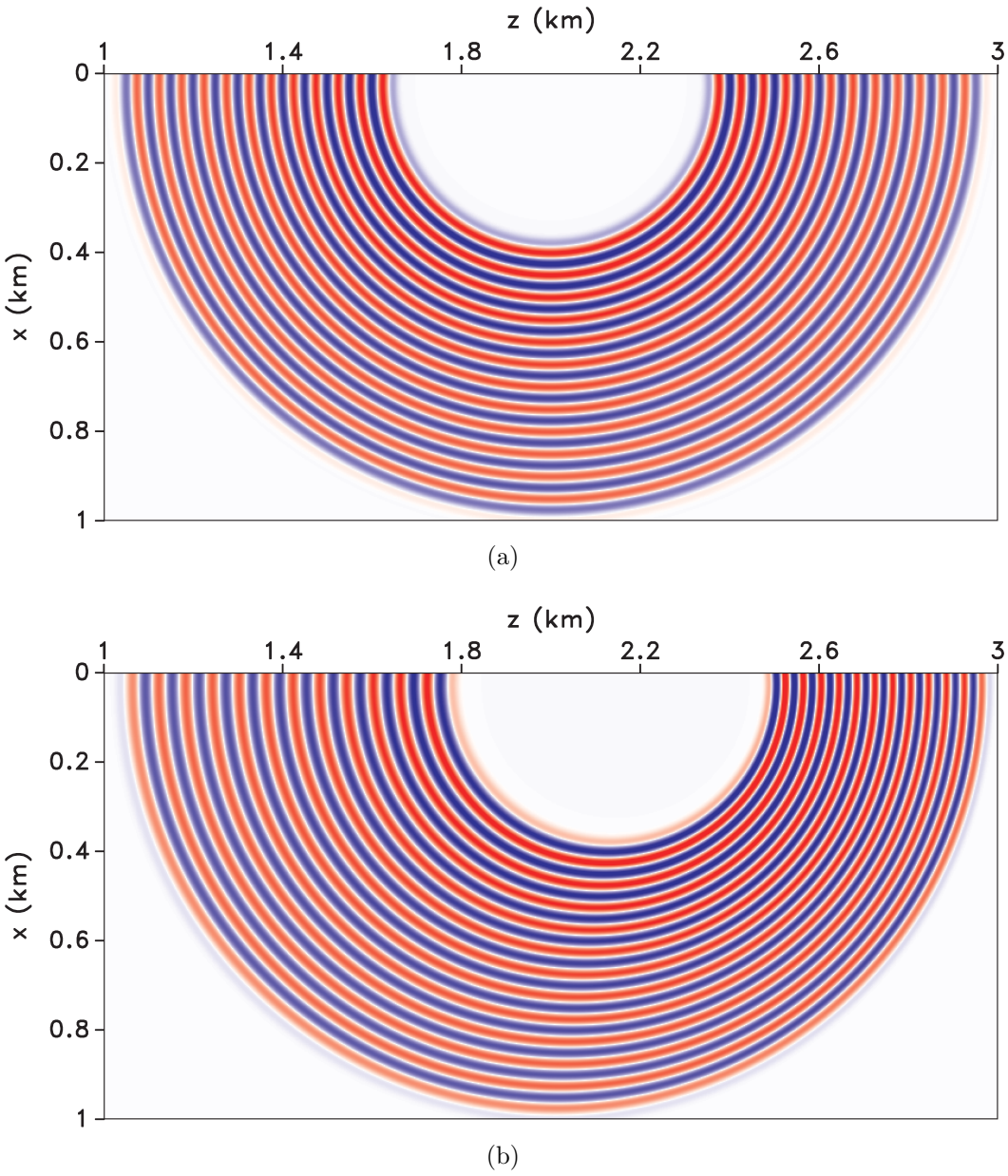

Figure 3.3 Wavefield snapshot in a homogeneous medium using (a) stationary and (b) mobile source.

Although the input source (Figure 3.4(a)) is a 30 Hz monochromatic wave (Figure 3.6(a)), the trace to the left of the source is dilated compared to that to the right of the source. The corresponding amplitude spectra (Figure 3.6(b) and Figure 3.6(c)) indicate that the observed frequency at the left receiver is 25 Hz, whereas the observed frequency at the right receiver is 37.5 Hz. Our numerical results match the theoretical observed frequencies using the Doppler (1842) formula and closely match the analytical results, thereby demonstrating the accuracy and stability of the developed modeling approach outlined above.

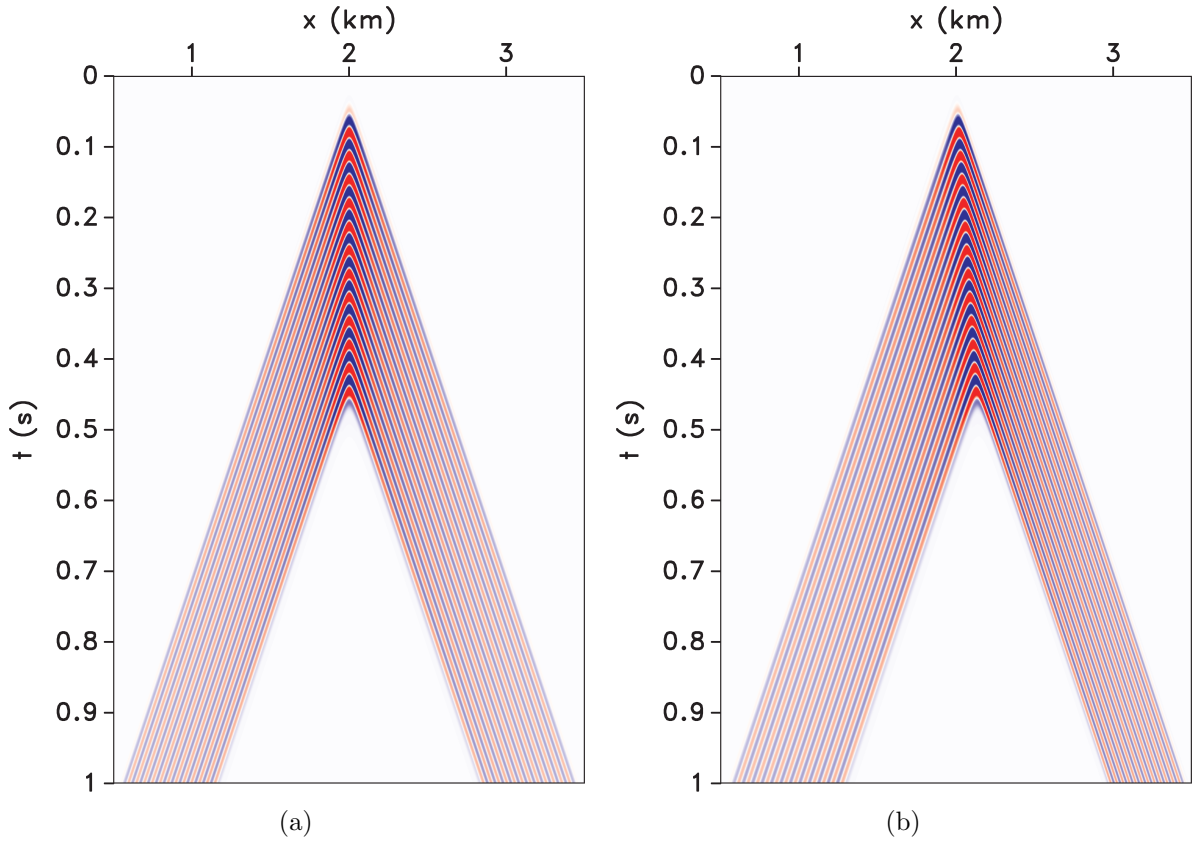

Figure 3.4 Shot gathers acquired in a homogeneous medium using (a) stationary and (b) mobile sources.

3.3.2 Modeling in a single-reflector model

To demonstrate the effects of source motion on ghost reflections, we simulate stationary and mobile source data with ghost reflections in a single-reflector model (Figure 3.7) using a

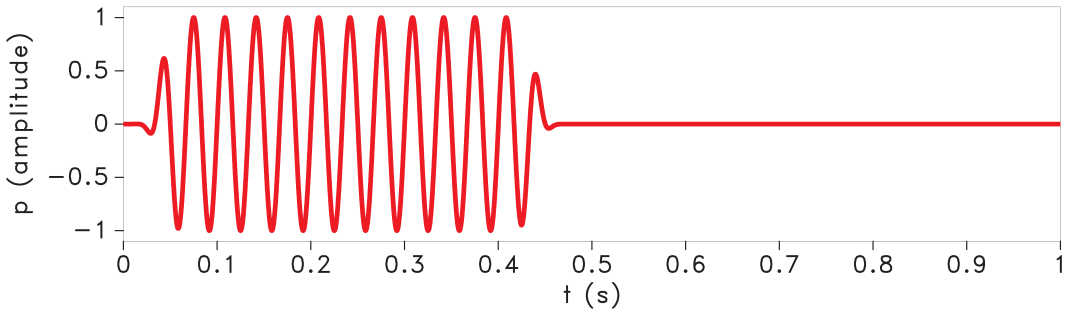

(a)

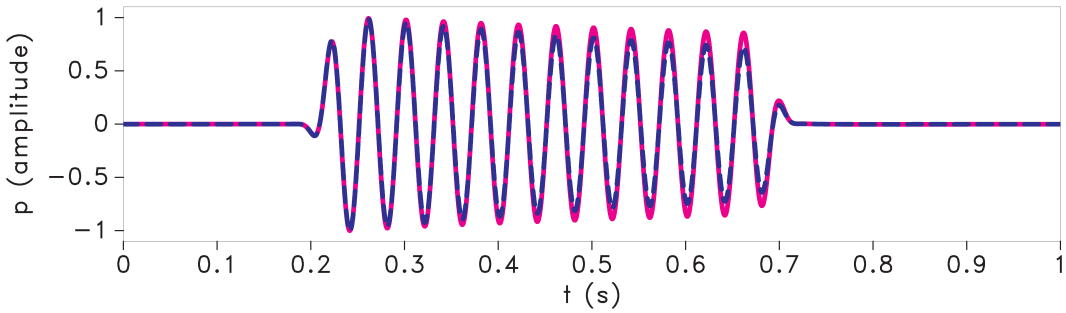

(b)

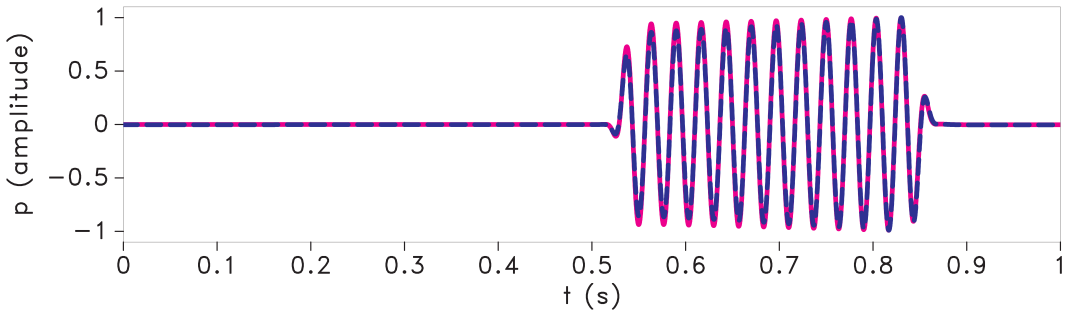

(c)

Figure 3.5 Pressure amplitude of (a) 30 Hz monochromatic wave (source function), and seismic data measured by receivers located (b) behind ($x^1 = 1.75$ km) and (c) ahead ($x^1 = 2.75$ km) of the source. The dashed line is the analytical solution, which overlay the numerical solution shown in solid line.

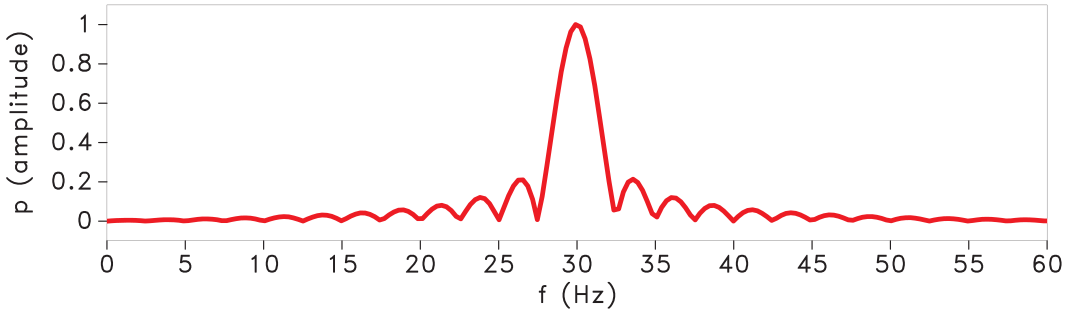

(a)

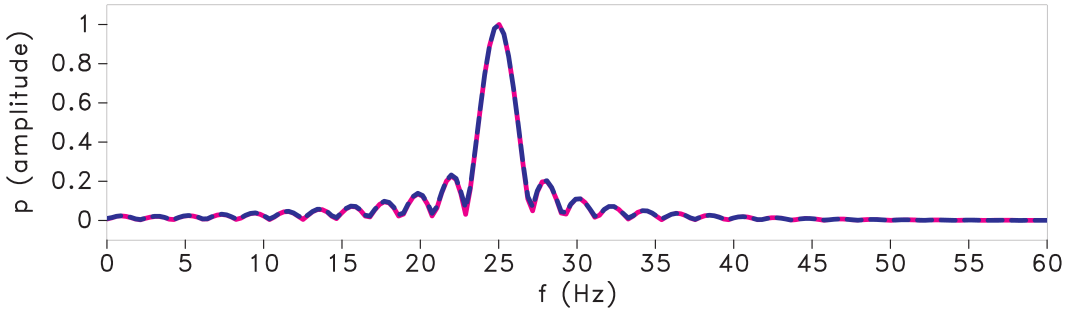

(b)

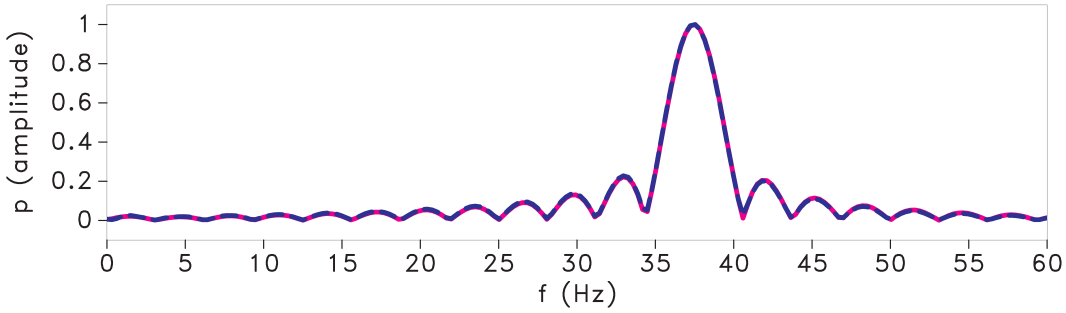

(c)

Figure 3.6 (a-c) Amplitude spectra of traces shown in Figure 3.5(a-c), respectively. The dashed line is the analytical solution, which overlay the numerical solution shown in solid line.

source function with a linear sweep between 25 Hz and 45 Hz placed at $x^3 = 0.05$ km (i.e., $\xi^1 = 0.05$ km) at time $t = 0$ s and stationary receivers placed 25 m below the source. To model mobile source data, we use a fast source velocity of 0.3 km/s. The ghost reflections in the stationary source data (Figure 3.8(a)) are symmetric around the source location, whereas they are slanted in time in the mobile source data (Figure 3.8(b)). However, the frequency-wavenumber spectra of the stationary source data (Figure 3.9(a)) and the mobile source data (Figure 3.9(b)) show that the constructive and destructive interference caused by ghost reflections are unaffected by the source motion because such interference in the Fourier domain are determined solely by the time delay between the primary signal and its ghost, which remains unchanged between stationary and mobile source modeling.

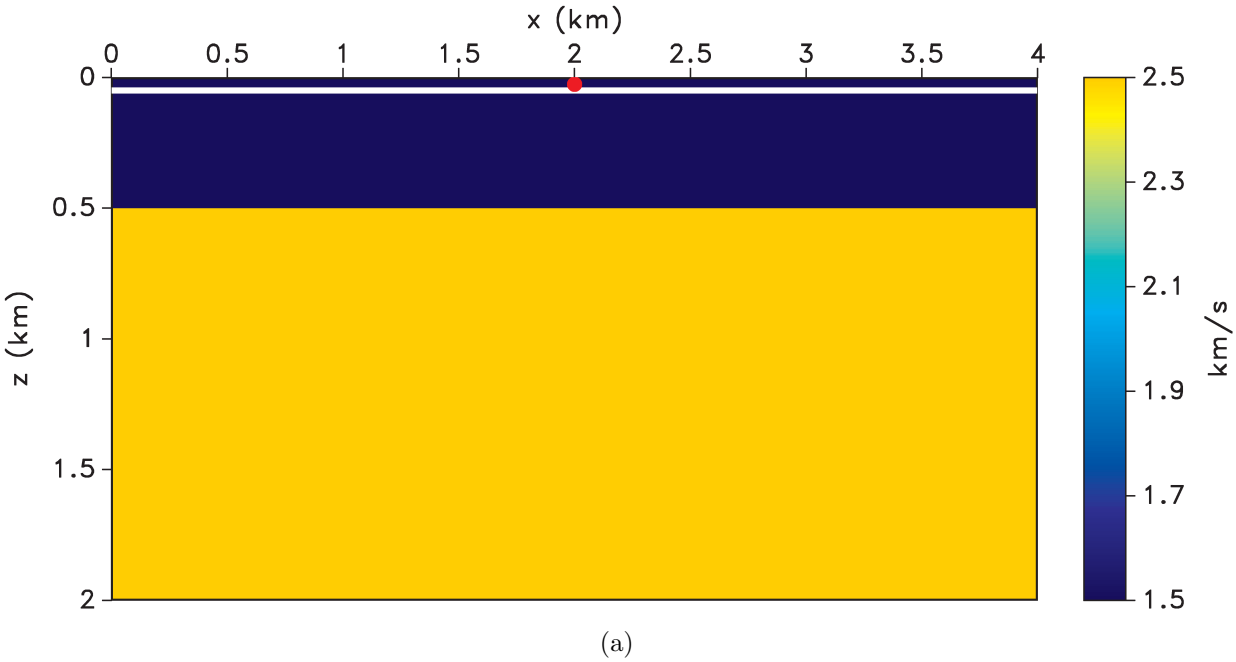

(a)

Figure 3.7 Single-reflector velocity model (quantity c in equation 3.8) with the source position at time $t = 0$ s (red) and stationary receivers locations (white).

3.3.3 Modeling in a velocity gradient medium

To understand the consequences of velocity variation on the Doppler effect, we simulate mobile source data in homogeneous (Figure 3.10(a)) and constant vertical velocity gradient

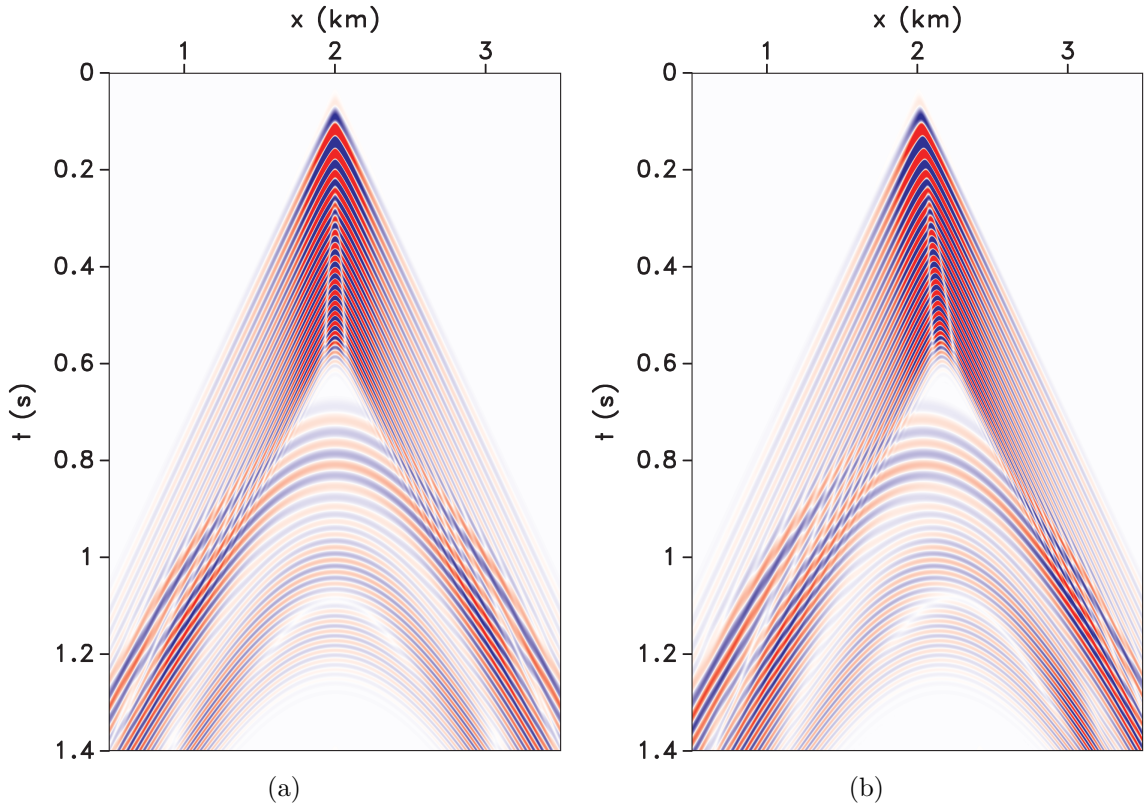

Figure 3.8 Shot gathers acquired in a single-reflector model using (a) stationary and (b) mobile sources with ghost reflections.

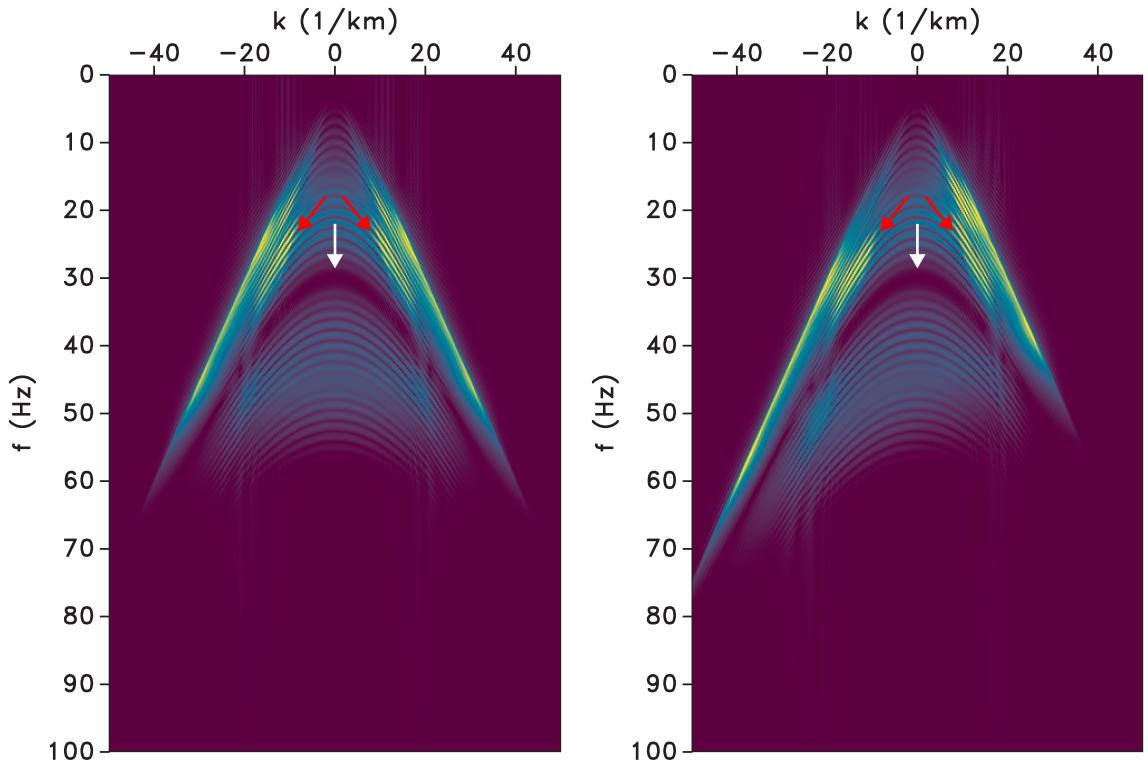

Figure 3.9 Frequency-wavenumber spectra of shot gathers shown in (a) Figure 3.8(a) and (b) Figure 3.8(b). The red and white arrows indicate constructive and destructive interference, respectively.

(Figure 3.10(b)) models using an unrealistically fast source velocity of 0.3 km/s. For the homogeneous model, the medium velocity is 2.0 km/s. For the constant vertical velocity gradient model, the medium velocity is given by the function $c(\xi^3) = 1.0 + 0.5\,\xi^3$ m/s, with a maximum depth of 4.0 km. We simulate both data types using a 40 Hz monochromatic wave placed at $[x^1, x^3] = [2.0, 2.0]$ km (i.e., $[\xi^1, \xi^3] = [2.0, 2.0]$ km) at time $t = 0$ s and stationary vertical receivers placed at $x^1 = 3.0$ km. Figure 3.11 shows traces recorded by receivers placed at $x^3 = 1.25$ km and $x^3 = 2.75$ km, their amplitude spectra, and the theoretical observed frequencies as a function of depth for the homogeneous velocity model. Because the velocity model is constant, and because the two receivers are symmetric around the source depth location, the two traces have the same observed frequency. Further, the theoretical observed frequencies as a function of depth, computed using equation 3.12, show that the observed frequency profile is also symmetric around the source locations, i.e., the Doppler effect depends on the angle between the source and receiver. Figure 3.12 shows traces recorded by receivers placed at $x^3 = 1.25$ km and $x^3 = 2.75$ km, their amplitude spectra, and the theoretical observed frequencies as a function of depth for the constant vertical velocity gradient model. In this case, the source is moving in a constant layer, but the two traces have different observed frequencies even though the two receivers are symmetric around the source depth position. The theoretical observed frequency profile is asymmetric, highlighting the significance of traveltime changes due to velocity variations in the Doppler effect.

3.3.4 Modeling in heterogeneous media

To investigate the impact of source motion on seismic data acquisition in heterogeneous media, we simulate the acoustic wavefield using the Marmousi II model (Martin et al., 2002). We use a source placed at $[\xi^1, \xi^3] = [8.5, 0.0125]$ km and 3601 receivers positioned at $\xi^3 = x^3 = 0.45$ km, with a 2.5 m uniform spacing. We use a source velocity of 5 m/s, which exceeds the typical acquisition source speed of $2 - 3$ m/s, to emphasize the discrepancies between stationary and mobile source acquisition. Figure 3.13(a) shows the velocity model with the source position at time $t = 0$ s and stationary receivers locations. The source

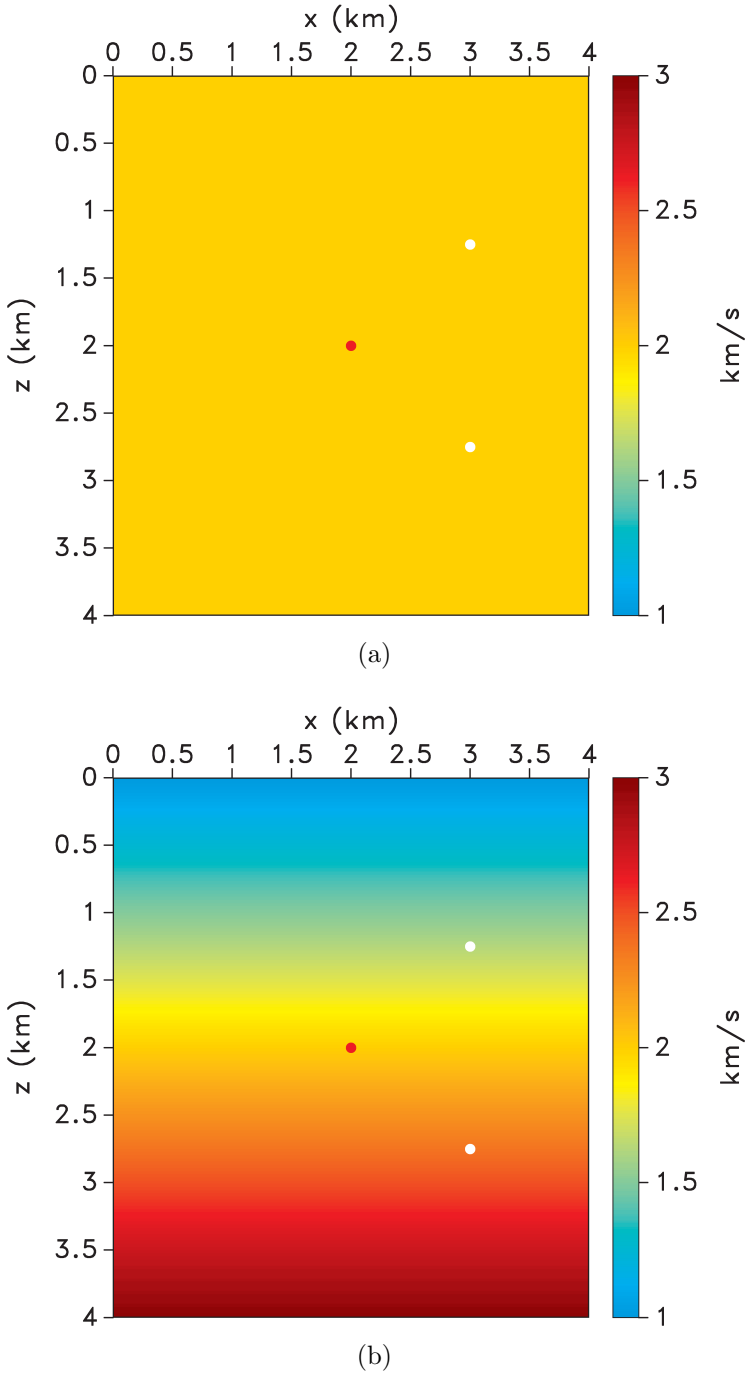

Figure 3.10 (a) Homogeneous and (b) constant vertical velocity gradient models (quantity c in equation 3.8) with the source position at time $t = 0$ s (red) and stationary receivers locations (white).

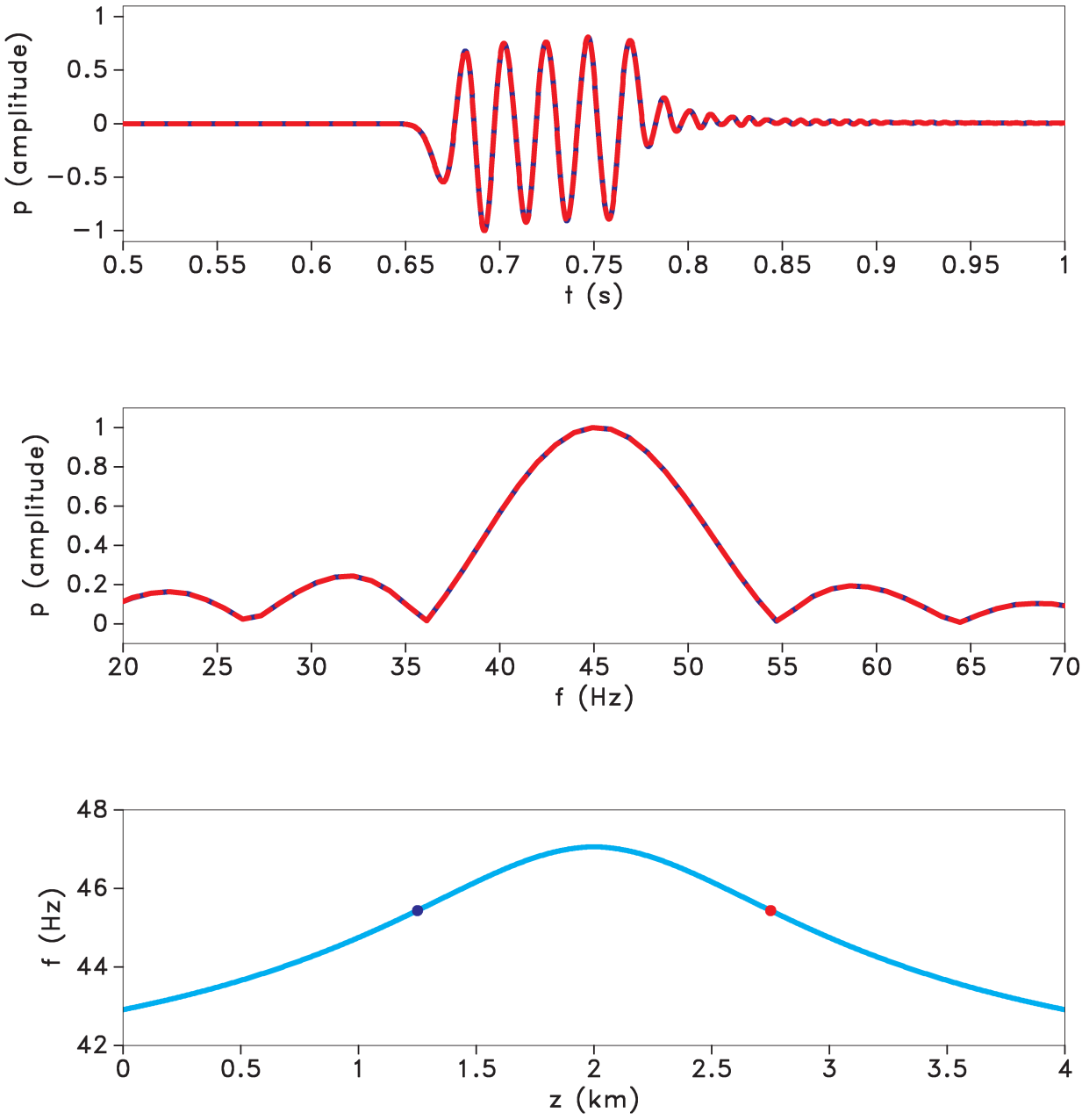

(a)

Figure 3.11 Mobile source in a homogeneous medium. Top: seismic data measured by receivers located at $x^3 = 1.25$ km (blue) and $x^3 = 2.75$ km (red). Middle: corresponding amplitude spectra of traces shown in the top panel. Bottom: theoretical observed frequencies as a function of depth.

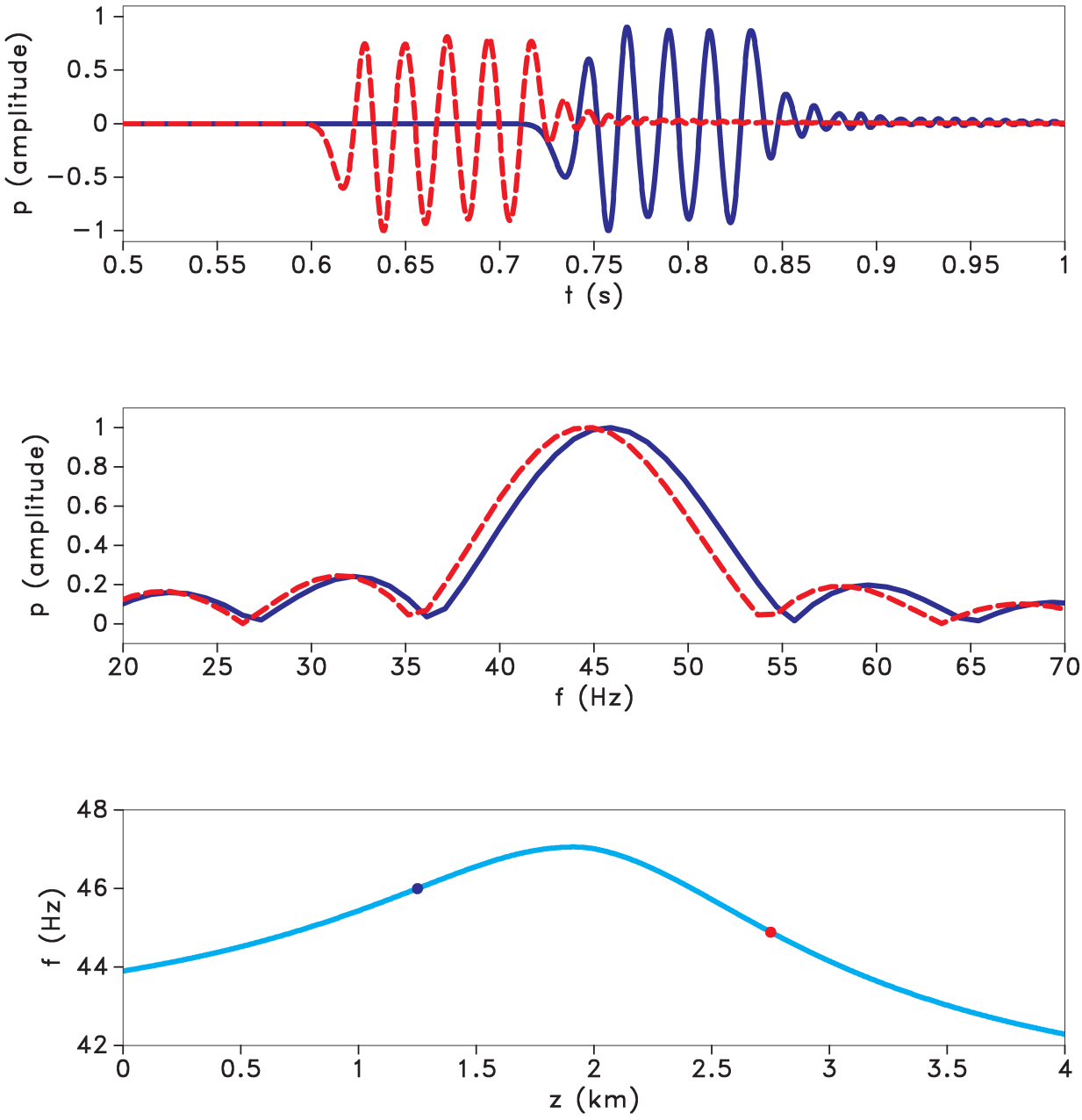

(a)

Figure 3.12 Mobile source in a velocity gradient medium. Top: seismic data measured by receivers located at $x^3 = 1.25$ km (blue) and $x^3 = 2.75$ km (red). Middle: corresponding amplitude spectra of traces shown in the top panel. Bottom: theoretical observed frequencies as a function of depth.

function is a linear sweep from 15 Hz to 43 Hz. Figure 3.14(a) and Figure 3.14(b) show the shot gathers acquired using a stationary and mobile source, respectively. While the shot gathers may appear similar at first glance, the difference between the two demonstrates that source motion has a discernible effect on the seismic data in both amplitude and phase (Figure 3.14(c)). Figure 3.15 shows traces recorded by a receiver located at $x^1 = 4.5$ km for the stationary (black) and mobile (red) source acquisition, demonstrating the amplitude and phase discrepancies between the two acquisitions. It is important to note that, while the discrepancies may be insignificant for low frequencies and slow source velocities, the motion of the source can introduce artifacts if not properly addressed in the processing workflow at high frequencies or when source velocities are high (Guitton et al., 2021).

Guitton et al. (2021) and Almuteri et al. (2022a) show that ignoring source motion effects in RTM introduces phase shift and mispositioning of imaged structures. Because of the long sweep duration and continuous source motion, the wavefield is altered due to the source changing its position while emitting energy (Hampson and Jakubowicz, 1995), i.e., the earth is illuminated differently when using a moving source than when using a stationary source. To show the effects of source motion on RTM results, we use a Marmousi II submodel to simulate two datasets with and without moving sources. We use 93 sources placed at $\xi^3 = 0.0125$ km with a 25 m source-initiation interval spacing, and we use 199 receivers at $\xi^3 = 0.375$ km with a 12.5 m receiver spacing. We model data for a 2.5 s record length at a 0.5 ms temporal sampling interval. For the moving source acquisition, we use a high source velocity of 10 m/s to highlight the significance of source motion on seismic imaging. The source function is a linear sweep from 20 Hz to 40 Hz. The RTM image of the stationary acquisition and imaging (Figure 3.16(a)) and the mobile acquisition and stationary imaging (Figure 3.16b) look similar; however, the difference between the two (Figure 3.16(c)) shows a phase change and mispositioning of imaged structures, demonstrating the importance of accounting for source motion effects in processing or imaging.

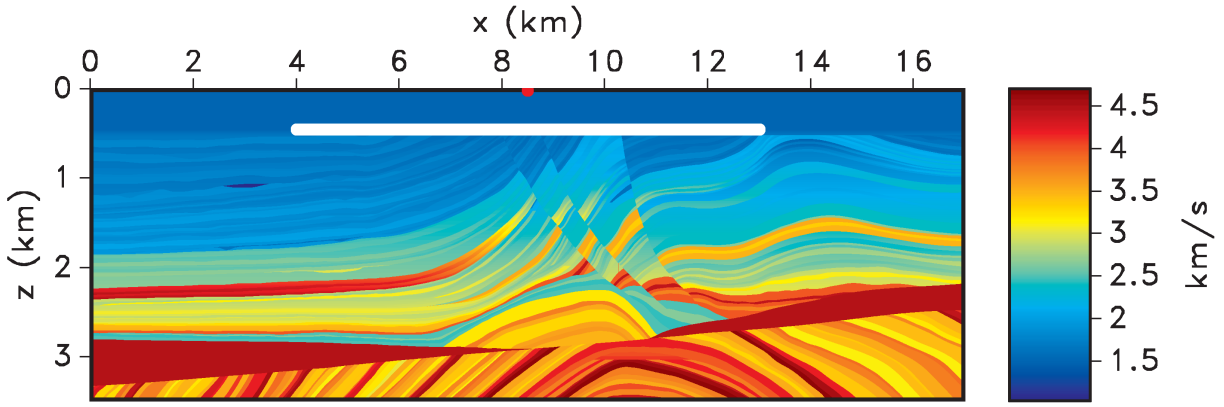

(a)

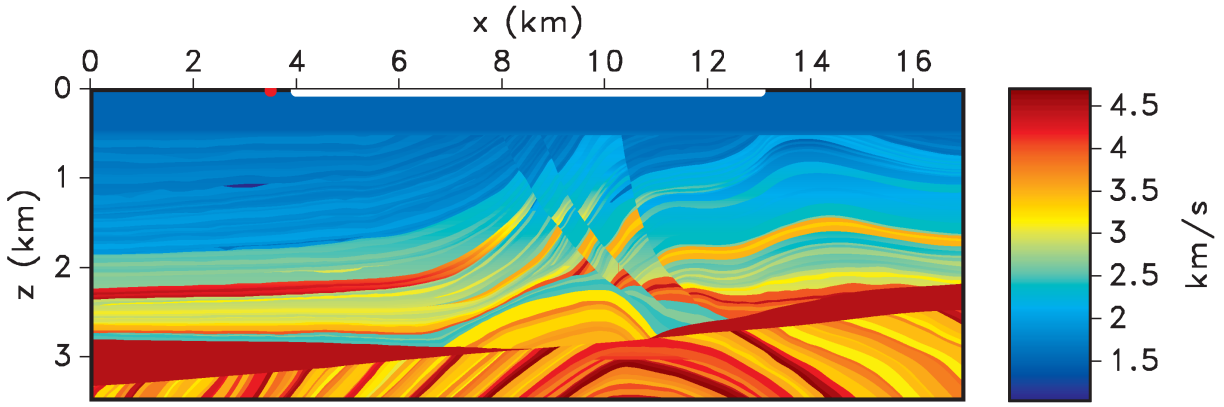

(b)

Figure 3.13 Marmousi II velocity model (quantity c in equation 3.8) with the source position (red) and receiver locations (white) at time $t = 0$ s for (a) moving source and stationary receivers (ocean bottom) acquisition and (b) stationary source and moving receivers (streamer) acquisition. Figure is not displayed with the true aspect ratio.

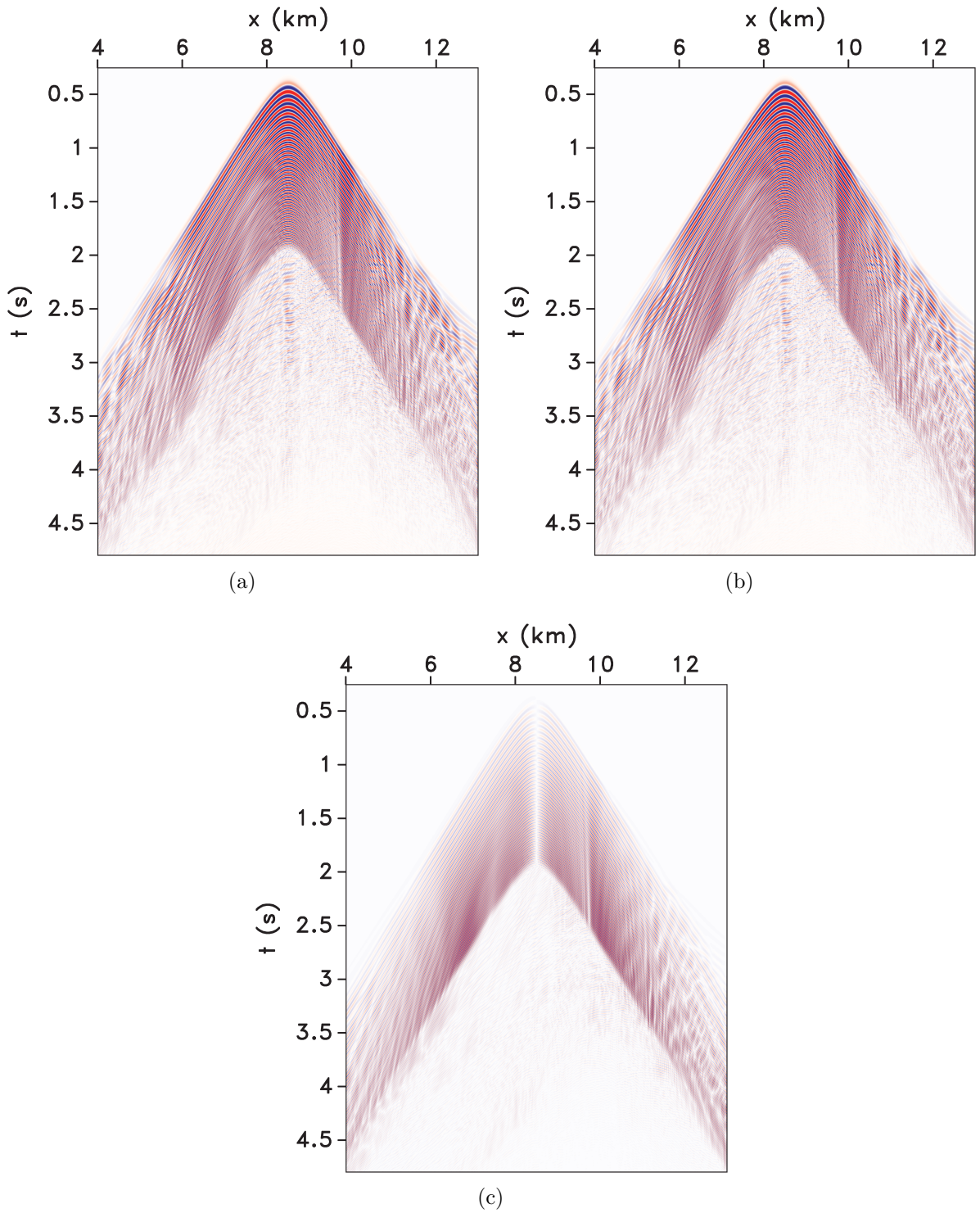

Figure 3.14 Shot gathers acquired using the Marmousi II model for (a) a stationary source and (b) mobile source. (c) difference between Figure 3.14(a) and Figure 3.14(b).

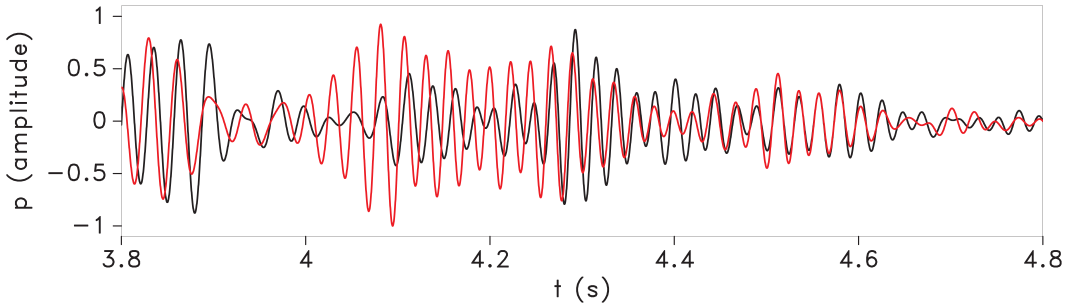

(a)

Figure 3.15 Seismic data measured by a receiver located at $x^1 = 4.5$ km for a stationary source (black) and mobile source (red).

To investigate the impact of receiver motion on seismic data, we simulate the acoustic wavefield using a Ricker wavelet with a 40 Hz dominant frequency to mimic a marine impulsive source. We use a source placed at $[\xi^1, \xi^3] = [3.5, 0.0125]$ km and receivers positioned at the same depth as the source. We use 3601 receivers with a 2.5 m uniform spacing with the first and last receivers at the initial time placed at $\xi^1 = 4.0$ km and $\xi^1 = 13.0$ km, respectively, being towed at a 5 m/s velocity. Figure 3.13(b) shows the velocity model with the stationary source position and receivers locations at time $t = 0$ s. Figure 3.17(a) and Figure 3.17(b) show the shot gathers acquired using stationary and mobile receivers, respectively. Similar to the mobile source example, the receiver motion changes both amplitude and phase compared to the stationary receiver acquisition (Figure 3.17(c)). Figure 3.18 shows traces recorded by a receiver located at $x^1 = 9$ km at time $t = 0$ s (trace number 2000) for the stationary (black) and mobile (red) receiver acquisition, which clearly show the discrepancies between the two acquisitions. The receiver motion does not alter the seismic wavefield, as opposed to a mobile source experiment, but rather samples the wavefield along a slanted trajectory in time and space, which can normally be ignored as discussed by Hampson and Jakubowicz (1995). The source motion in marine vibrator acquisition, however, cannot be ignored because of the long duration of the source and its continuous motion.

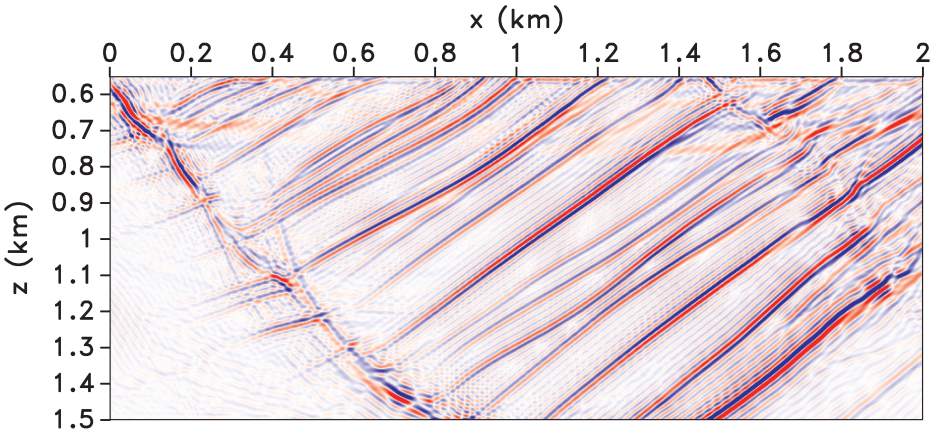

(a)

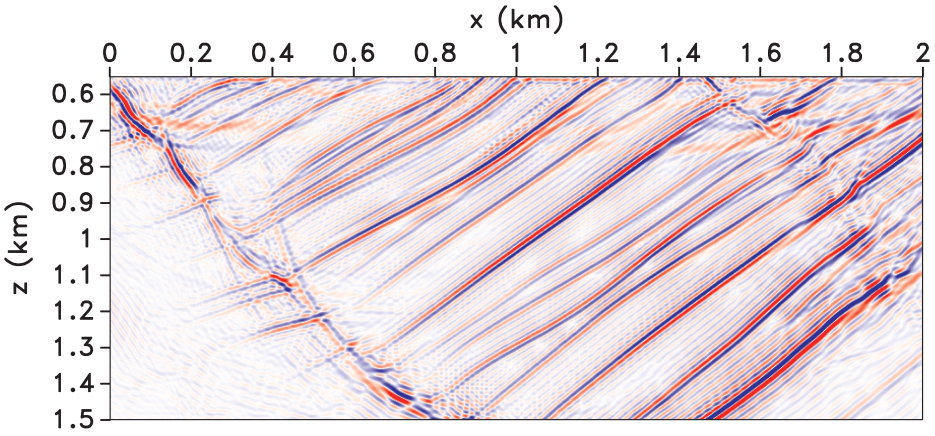

(b)

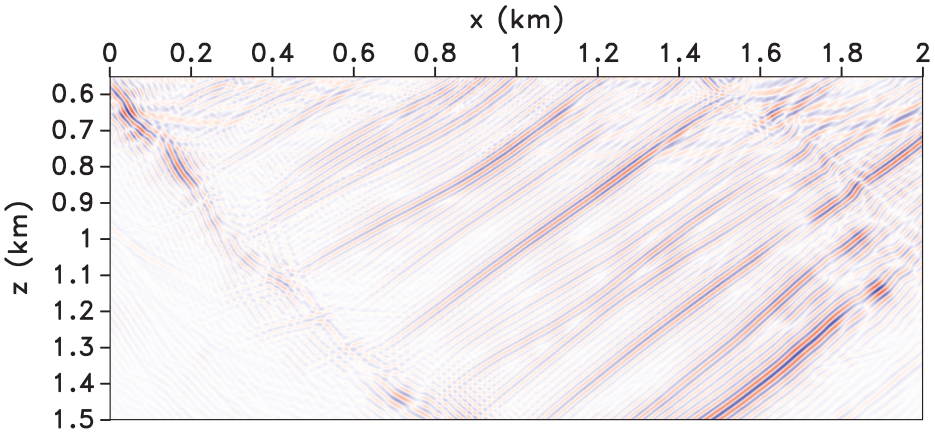

(c)

Figure 3.16 RTM image for (a) stationary acquisition and imaging and (b) mobile acquisition and stationary imaging. (c) Difference between Figure 3.16(a) and Figure 3.16(b).

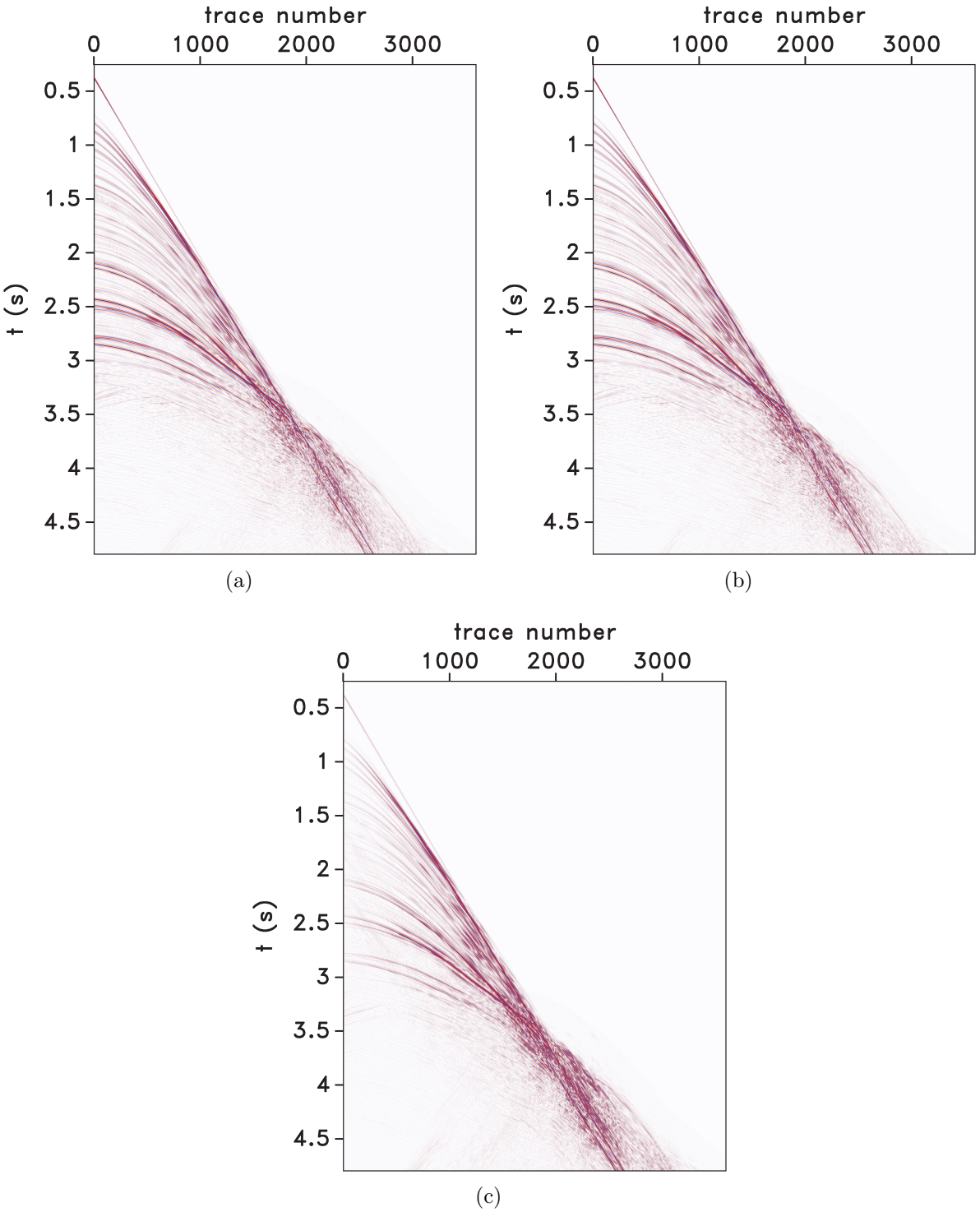

Figure 3.17 Shot gathers acquired using the Marmousi II model for (a) stationary and (b) mobile receivers. (c) Difference between Figure 3.17(a) and Figure 3.17(b).

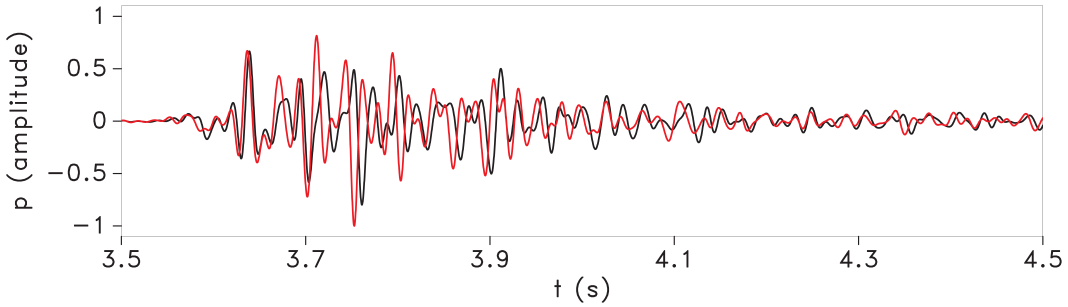

(a)

Figure 3.18 Seismic data measured by a receiver located at $x^1 = 9$ km at time $t = 0$ s (trace number 2000) for a stationary receiver (black) and mobile receiver (red).

3.4 Discussion

Source motion introduces frequency shifts that are proportional to the source velocity, acoustic wave velocity in the medium, propagation direction, and input frequency. The frequency shifts in the modeled seismic data are more pronounced at high frequencies, even with a slow source velocity. More importantly, medium heterogeneity between the source and receiver, or any point in the subsurface, plays a role in the Doppler shift. Neglecting frequency shifts and the time-dependent source-receiver offset in seismic data processing and imaging introduces artifacts in the processed data and ensuing imaging and/or inversion workflows. Although source motion causes noticeable frequency shifts in data, a change in source position when emitting is expected to have a more significant impact on seismic processing and imaging.

Under quiescent sea-surface conditions, ghost reflections interfere with the primary signal in mobile and stationary acquisition in a similar manner. However, in stationary acquisition, source-side ghost reflections are described by an effective static sea surface (Blacquière and Sertlek, 2019), i.e., they occur instantaneously. But for moving and long-emitting sources, source-side ghost reflections are explained using a dynamic sea surface model. Understanding the effects of ghost reflections on marine vibrator data under realistic time-varying sea surface conditions is critical for developing robust seismic deghosting solutions for this type

of acquisition. Therefore, future work involves incorporating a dynamic sea surface to mimic more realistic marine vibrator acquisition scenarios.

Our numerical results show that solving the second-order acoustic wave equation using a finite-difference approach with Taylor-expansion coefficients is accurate and stable. Adopting such an approach enables obtaining reliable subsurface images and reduces interpretation uncertainties. Although time-dependent meshes require repeated and expensive interpolation of the physical properties of the subsurface, the proposed work mitigates the need for such interpolations by using a judicious coordinate transformation to confine the mesh deformation to the homogeneous water layer. Additionally, the proposed methodology helps improve marine acquisition design and processing by providing reliable and robust tools for numerical experimentation. The developed approach can also be used in RTM to image marine vibrator data because of its intrinsic ability to account for source motion effects when computing required source and receiver wavefields, which we leave for future work.

3.5 Conclusions

We present a finite-difference approach for solving the acoustic wave equation to simulate marine vibrator data. The developed method employs a geometric coordinate transformation to compute the full acoustic wavefield on a uniformly spaced and time-invariant mesh grid. Although our implementation assumes constant source motion, incorporating a variable velocity moving source into this framework is straightforward. The proposed numerical approach can accurately and stably model seismic wavefields, even at unrealistically high velocities of the moving source. Furthermore, this work is not limited to modeling marine vibrators, but can also be used to model towed-streamer data using impulsive sources.

3.6 Acknowledgments

The first author would like to thank Saudi Aramco for graduate study sponsorship. We thank the sponsors of the Center for Wave Phenomena at Colorado School of Mines for the support of this research. We also thank A. Guitton (TotalEnergies) and T. Konuk

(Nvidia) for many useful discussions. Reproducible numerical examples were generated using the Madagascar open-source software package freely available from `http://www.ahay.org`. Analytic coordinate system geometry results were verified using the Mathematica software package from `https://www.wolfram.com/mathematica/`.

3.7 Data and materials availability

Data associated with this research are available and can be obtained by contacting the corresponding author.

3.8 APPENDIX: Analytical solution to the acoustic wave equation for a moving source

The Green's function for the acoustic wave equation (AWE) for a moving source is given by (Ahrens and Spors, 2011; Jackson, 1999)

$$G(\mathbf{x}, t; \mathbf{x}_s(t_s), t_s) = \frac{\delta\left(t - t_s - \frac{|\mathbf{x}-\mathbf{x}_s(t_s)|}{c}\right)}{|\mathbf{x} - \mathbf{x}_s(t_s)|}, \tag{3.15}$$

where $\mathbf{x} = [x, y, z]$ is the 3D space variable, t is the time variable, t_s is the source emission time, $\mathbf{x}_s(t_s) = [x_s(t_s), y_s(t_s), z_s(t_s)]$ is the source position as a function of emission time, and c is the constant medium velocity. Thus, the wavefield $P(\mathbf{x}, t)$ for an arbitrary source function $f(t_s)$ is

$$\begin{aligned} P(\mathbf{x}, t) &= \int_{-\infty}^{\infty} f(t_s) G(\mathbf{x}, t; \mathbf{x}_s(t_s), t_s)\, \mathrm{d}t_s \\ &= \int_{-\infty}^{\infty} f(t_s) \frac{\delta\left(t - t_s - \frac{|\mathbf{x}-\mathbf{x}_s(t_s)|}{c}\right)}{|\mathbf{x} - \mathbf{x}_s(t_s)|}\, \mathrm{d}t_s \\ &= \int_{-\infty}^{\infty} f(t_s) \frac{\delta\left(t - t_s - \tau\right)}{c\tau}\, \mathrm{d}t_s, \end{aligned} \tag{3.16}$$

where $\tau(\mathbf{x}, t_s) = \frac{|\mathbf{x}-\mathbf{x}_s(t_s)|}{c}$. To evaluate equation 3.16, we introduce a new variable $u = t_s + \tau(\mathbf{x}, t_s)$, resulting in

$$P(\mathbf{x},t) = \int_{-\infty}^{\infty} f(u-\tau)\frac{\delta\left(t-u\right)}{c\tau}\,\mathrm{d}u$$
$$= \frac{f(t-\tau)}{c\tau}, \tag{3.17}$$

where we use the sifting property of the delta function. Now, considering a source moving along a straight path with a velocity $\mathbf{v} = [v_x, v_y, v_z]$, we can express the source position as a function of emission time as a Galilean transformation

$$\mathbf{x}_s(t_s) = \mathbf{x}_s(0) + \mathbf{v}t_s, \tag{3.18}$$

where $\mathbf{x}_s(0)$ is the source position at time zero. We can rewrite equation 3.18 in terms of an arbitrary recording time t by introducing a new variable R such that $t_s = t - \frac{R}{c}$, where $R = |\mathbf{R}|$ and $\mathbf{R} = \mathbf{x} - \mathbf{x}_s(t_s)$, as

$$\mathbf{x}_s(t) = \mathbf{x}_s(0) + \mathbf{v}\left(t - \frac{R}{c}\right). \tag{3.19}$$

Therefore, we can find the source position for any emitted signal (when emitted) as function of recording time t and receiver position $\mathbf{R}$, needed to evaluate equation 3.17. To derive the analytical solution to the AWE for a moving source, we follow the formulation of Morse and Ingard (1986) to find R. Because $R = |\mathbf{x} - \mathbf{x}_s(t_s)|$, we have

$$\begin{aligned}
R^2 &= (x - x_s(t_s))^2 + (y - y_s(t_s))^2 + (z - z_s(t_s))^2 \\
&= (x - x_s(0) - v_x t_s)^2 + (y - y_s(0) - v_y t_s)^2 + (z - z_s(0) - v_z t_s)^2 \\
&= \left(x - x_s(0) - v_x\left(t - \frac{R}{c}\right)\right)^2 + \left(y - y_s(0) - v_y\left(t - \frac{R}{c}\right)\right)^2 \\
&+ \left(z - z_s(0) - v_z\left(t - \frac{R}{c}\right)\right)^2 \\
&= (x - x_s(0) - v_x t + M_x R)^2 + (y - y_s(0) - v_y t + M_y R)^2 \\
&+ (z - z_s(0) - v_z t + M_z R)^2 \\
&= (\tilde{x} + M_x R)^2 + (\tilde{y} + M_y R)^2 + (\tilde{z} + M_z R)^2,
\end{aligned} \tag{3.20}$$

where $\tilde{x} = x - x_s(0) - v_x t$, $\tilde{y} = y - y_s(0) - v_y t$, $\tilde{z} = z - z_s(0) - v_z t$, and $\mathbf{M} = [M_x, M_y, M_z] = [\frac{v_x}{c}, \frac{v_y}{c}, \frac{v_z}{c}]$. We solve for R in equation 3.20, using the quadratic formula, to obtain

$$R = \frac{\mathbf{M} \cdot \tilde{\mathbf{x}} \pm \sqrt{(1 - \mathbf{M} \cdot \mathbf{M})(\tilde{\mathbf{x}} \cdot \tilde{\mathbf{x}}) + (\mathbf{M} \cdot \tilde{\mathbf{x}})^2}}{1 - \mathbf{M} \cdot \mathbf{M}}, \tag{3.21}$$

where $\tilde{\mathbf{x}} = [\tilde{x}, \tilde{y}, \tilde{z}]$. Assuming $\mathbf{M} \cdot \mathbf{M} < 1$, i.e., the source velocity is slower than the wave propagation speed, R is strictly positive only for (Morse and Ingard, 1986)

$$R = \frac{\mathbf{M} \cdot \tilde{\mathbf{x}} + \sqrt{(1 - \mathbf{M} \cdot \mathbf{M})(\tilde{\mathbf{x}} \cdot \tilde{\mathbf{x}}) + (\mathbf{M} \cdot \tilde{\mathbf{x}})^2}}{1 - \mathbf{M} \cdot \mathbf{M}}. \tag{3.22}$$

As a result, the analytical solution to the AWE for a moving source is

$$P(\mathbf{x}, t) = \frac{f\left(t - \frac{R}{c}\right)}{R}, \tag{3.23}$$

where R is given by equation 3.22. We use equation 3.23 to compute the analytical solution of the AWE for a moving source in a homogeneous medium and validate our numerical approach.

CHAPTER 4

MODELING ACOUSTIC WAVEFIELDS FROM MOVING SOURCES IN THE PRESENCE OF A TIME-VARYING FREE-SURFACE

A paper submitted to *Geophysics*[1].

Khalid Almuteri[2,3,4], Jeffrey Shragge[5], and Paul Sava[5]

Marine vibrators are increasingly being recognized as a viable alternative to seismic airguns for ocean-bottom acquisition due to their ability to generate more low-frequency content and their less adverse impact on marine wildlife. However, their use introduces processing challenges, such as the Doppler effect and time-dependent source-receiver offsets, which are negligible in conventional airgun acquisition. In addition, the time-varying nature of the sea surface during the multi-second acquisition time introduces further challenges for processing and inversion. To accurately account for source motion and time-varying sea surface effects in seismic data processing, we develop a reliable and robust numerical modeling tool. We use a mimetic finite-difference method in a generalized coordinate system to model the full acoustic wavefield triggered by a moving source in the presence of a time-varying sea surface. Our approach uses a time- and space-dependent coordinate transformation, which tracks the source movement and conforms to the irregular time-varying sea surface, to map an irregular physical domain in Cartesian coordinates to a regular computational domain in generalized coordinates. We formulate this coordinate transformation such that both coordinate systems conformally match below the ocean-bottom level. Numerical examples demonstrate that this approach is accurate and stable, even for an unrealistically exaggerated sea state. This

[1]Reprinted with permission of *Geophysics*.

[2]Graduate student, Center for Wave Phenomena, Department of Geophysics, Colorado School of Mines
[3]Saudi Aramco
[4]Author for correspondence
[5]Professor, Center for Wave Phenomena, Department of Geophysics, Colorado School of Mines.

computational tool is not limited to modeling, but could also be used to develop advanced processing techniques for marine vibrator data, such as imaging and inversion.

4.1 Introduction

Conventional ocean-bottom data processing assumes stationary sources with a short excitation duration. Consequently, source-side ghost reflections can be modeled and explained using an effective static rough sea surface, whereas receiver-side ghost reflections require using a time-varying sea surface to account for the long acquisition time. In marine vibrator acquisition, where sources are continuously moving and sweeping for a considerable period (e.g., 5 s), the stationary source-side sea-surface assumption is no longer true as the source motion introduces offset- and time-dependent frequency shifts to the data (Dragoset, 1988; Hampson and Jakubowicz, 1995; Schultz et al., 1989), and source-receiver offsets change as a function of time. The long duration of the source function and the rate at which the sea surface changes during the acquisition sweep require using a time-varying sea-surface model to accurately predict and model source-side ghost reflections. Therefore, simultaneously accounting for moving sources and time-varying sea surfaces in seismic data processing is necessary to avoid introducing artifacts in the marine vibrator processed data.

Marine vibrators are advantageous over conventional seismic airguns for environmental and geophysical reasons. First, marine vibrators have a limited impact on marine wildlife life compared to conventional seismic airguns (Smith and Jenkerson, 1998). In addition, marine vibrators can provide richer low-frequency content (Dellinger et al., 2016; Guitton et al., 2021) and enable a versatile control over the source signature, where the phase can be specified independently for each output frequency (Laws et al., 2019). In contrast, the phase can only be modified through time delays when using airgun arrays. Phase control precision in marine vibrators facilitates the use of advanced acquisition techniques such as phase sequencing, source-side wavefield gradients, and simultaneous acquisition. Laws et al. (2019) discuss in detail the advantages of marine vibrators over conventional seismic airguns and demonstrate numerically that the aforementioned acquisition techniques can reduce acquisition time by

one-third compared to conventional airgun acquisition.

The implications of a rough sea surface on seismic data are extensively studied in the literature. Laws and Kragh (2002) investigate the impact of rough sea surfaces on time-lapse experiments, showing that false structures can appear in time-lapse difference sections. Egorov et al. (2018) study the consequences of rough sea surfaces on seismic deghosting of single-component data, demonstrating that deghosting can introduce noise in the processed data when the sea surface is assumed to be flat and static. Cecconello et al. (2018) show that a time-varying sea surface introduces a Doppler shift into the recorded data. Blacquière and Sertlek (2019) and Konuk and Shragge (2020) show that rough sea surfaces scatter the ghost wavefield, introducing amplitude and phase distortions of the ghost reflections. A common element between these studies is the use of stationary sources to understand the impact of the sea surface on seismic data.

Various methods for modeling the effects of rough sea surfaces on seismic data were proposed in the literature, Kirchhoff-based methods (KMs) being the most common (e.g., Blacquière and Sertlek, 2019; Egorov et al., 2018; Laws and Kragh, 2002; Orji et al., 2012). Alternatively, Cecconello et al. (2018) exploit Rayleigh's reciprocity theorem to include ghost reflections generated from time-varying sea surfaces to ghost-free data. Konuk and Shragge (2020) model the effects of time-varying sea surfaces on the full acoustic wavefield in curvilinear coordinates using the generalized tensorial acoustic wave equation (AWE). Liu (2023) employs the chain rule to model rough sea surfaces and rough bathymetry effects in curvilinear coordinates. Robertsson et al. (2006) compare the ability of finite-differences (FDM), spectral-elements (SEM), and Kirchhoff modeling to simulate the impact of rough sea surface on seismic data. Their work shows that FDM and SEM produce similar results, whereas KM produces results that differ from the former ones, mainly in amplitude. We refer to Konuk and Shragge (2020) for an overview of the different modeling methods to generate numerical solutions for surfaces characterized by non-Cartesian geometries.

To model marine vibrator data, Dellinger and Díaz (2020) propose splitting the sweep into different segments that can be injected at fixed source positions along the source path. JafarGandomi and Grion (2021) propose modeling marine vibrator data by interpolating unaliased impulsive sources data to desired source locations and convolving with the corresponding segments of the marine vibrator sweep. Alternatively, one can move and interpolate the source injection locations in space as a function of time to model marine vibrator sources. However, numerical instabilities and inaccuracies may arise when introducing irregular or dynamic computational geometries in Cartesian-based modeling methods, especially when implementing free-surface boundary conditions for such irregular geometries (de la Puente et al., 2014; Konuk and Shragge, 2020).

Accurate and stable modeling of marine vibrator data under time-varying sea surface conditions is challenging because of the complications of representing time-dependent curved surfaces in Cartesian coordinates. Approximating partial differential operators with Taylor-expansion coefficients in FDMs is a common choice when modeling seismic data because they are straightforward and easy to implement. However, accurately accounting for free surface (FS) effects is difficult using such operators because they require grid points above the FS. Alternatively, one can model FS effects by using low-order accuracy coefficients (de la Puente et al., 2014) or global high-order accuracy finite-element method (FEM) (Komatitsch and Vilotte, 1998). Using FEMs places additional restrictions compared to FDMs because they require: (1) time-varying meshing when considering time-varying sea surfaces; (2) meshing that conforms to all irregular internal boundaries; and (3) honoring the spatio-temporal numerical stability conditions for a time-varying mesh. Using mimetic finite-difference (MFD) operators (Castillo et al., 2001; Castillo and Miranda, 2013; Corbino and Castillo, 2020; de la Puente et al., 2014; Konuk and Shragge, 2020; Shragge and Tapley, 2017) is a viable alternative, promising a global high-order accuracy without a need for a time-dependent meshing. Thus, the MFD approach is suitable for modeling marine vibrator data in the presence of a time-varying sea surface.

In this paper, we use FDM to model the full acoustic wavefield triggered by a moving source in the presence of a time-varying sea surface. We formulate the AWE in a generalized coordinate system that effectively accounts for the source motion and time-varying free surface into the coefficients of the governing tensorial AWE. Our approach is formulated to avoid repeated velocity model interpolations or a need to interpolate the seismic wavefield below the ocean bottom to Cartesian coordinates, eliminating the added computational complexity and accuracy issues associated with this process. To test the stability of our approach, we numerically simulate marine vibrator data for an exaggerated sea state, and then use a realistic sea state to investigate the impact of rough sea surface on marine vibrator data in the common-shot and common-receiver domains.

4.2 Theory

Although curved surfaces can be approximated in Cartesian coordinates using fine grid spacing, this approach results in an unjustifiable and significant increase in numerical computations, while alternative solutions that intrinsically take the non-Cartesian nature of such surfaces exist. These alternatives include methods that employ coordinate transformation within a finite-difference framework (Appelö and Petersson, 2009; Carcione, 1994; de la Puente et al., 2014; Hestholm, 1999; Hestholm and Ruud, 2002; Komatitsch et al., 1996; Konuk and Shragge, 2020; Shragge, 2014; Shragge and Tapley, 2017), finite-element (Marfurt, 1984), spectral-element (Komatitsch and Vilotte, 1998), and discontinuous Galerkin methods (Käser and Dumbser, 2006). FDMs are characterized by ease of implementation with lower computational complexity, compared to other methods, in addition to being easily parallelizable. Thus, a natural approach is to employ a coordinate transformation that considers the intrinsic nature of moving sources and time-varying sea surfaces when modeling seismic data under such conditions.

In this section, we derive a generalized 3D AWE that can model the natural response of a moving source while simultaneously accounting for a time-varying free-surface boundary due to, e.g., a complex sea state. We follow a tensorial approach to encode the geometry of these

two features directly into the generalized coordinate system to model the AWE response to a simulated marine vibrator source. We employ the tensorial method to transform the physical Cartesian coordinate system $\mathbf{x}$ into a static generalized coordinate system $\boldsymbol{\xi}$ that represents a uniform computational mesh. By transforming the problem in this way, we must account for the associated time- and space-varying coefficients of the governing tensorial AWE introduced by the coordinate transformation using the generalized gradient and divergence operators as discussed below.

4.2.1 Tensorial AWE

The tensorial formulation of the 3D AWE on a static computational mesh may be represented by

$$\Box_\xi P_\xi = F_\xi, \tag{4.1}$$

where $\Box_\xi$ is the d'Alembertian operator, subscript $\boldsymbol{\xi}$ indicates a quantity in a generalized coordinate system $\boldsymbol{\xi} = [\xi^0, \xi^1, \xi^2, \xi^3]$, P_ξ is the scalar pressure field, and F_ξ is the source term. Following Konuk and Shragge (2020) we assume that $\boldsymbol{\xi}$ is a four-vector where ξ^0 and $[\xi^1, \xi^2, \xi^3]$ respectively represent time- and space-like coordinate variables. We further assume that ξ^1 and ξ^2 are the inline and crossline acquisition directions and that ξ^3 represents the depth axis.

Accounting for a moving source with a geometry transformation means adopting a Lagrangian description centered on the moving source, which requires a mesh that accounts for its translation. We represent the geometry of the source, assumed to be moving in the ξ^1 direction with an arbitrary function $S(\xi^0, \xi^1, \xi^2, \xi^3)$ (which is independent of the crossline acquisition direction). We also assume that the sea-surface topology and associated vertical coordinate can be modeled by a generalized function $T(\xi^0, \xi^1, \xi^2, \xi^3)$. These specifications allow us to write a generalized transformation connecting the physical generalized observation

coordinates $\mathbf{x}$ with the static computational coordinates $\boldsymbol{\xi}$ according to

$$\begin{bmatrix} x^0 \\ x^1 \\ x^2 \\ x^3 \end{bmatrix} = \begin{bmatrix} i\xi^0 \\ S(\xi^0,\xi^1,\xi^2,\xi^3) \\ \xi^2 \\ T(\xi^0,\xi^1,\xi^2,\xi^3) \end{bmatrix}, \tag{4.2}$$

where the introduction of the imaginary unit i is explained below.

Using the unique mapping between the $\boldsymbol{\xi}$- and $\mathbf{x}$-coordinate systems, we define the corresponding covariant metric tensor $g_{\mu\nu}$, which is a symmetric 4×4 matrix that captures the spatially and temporally varying geometry (i.e., how the mesh compresses, rarefies, and shears as a function of space and time) of this 4D coordinate transformation, such that

$$g_{\mu\nu} = \frac{\partial x^\alpha}{\partial \xi^\mu}\frac{\partial x^\alpha}{\partial \xi^\nu}, \quad \alpha,\mu,\nu = 0,1,2,3. \tag{4.3}$$

The introduction of the imaginary unit i follows the Minkowski space definition, which combines time (imaginary axis) and the 3D Euclidean space (real axes) into a 4D manifold. An immediate consequence of Minkowski space definition is that seismic events are causally connected (e.g., seismic waves reflect when an incident wavefield interacts with reflectors).

The tensorial AWE requires a contravariant representation of the metric tensor $g^{\mu\nu}$ (Shragge, 2014), which may be calculated as a point-wise matrix inverse of the covariant metric tensor $g_{\mu\nu}$. Using the general form of 4D coordinate mapping given in equation 4.2 results in the following analytic metric tensor inverse:

$$g^{\mu\nu} = \begin{bmatrix} -1 & g^{01} & 0 & g^{03} \\ g^{01} & g^{11} & g^{12} & g^{13} \\ 0 & g^{12} & 1 & g^{23} \\ g^{03} & g^{13} & g^{23} & g^{33} \end{bmatrix} \tag{4.4}$$

$$= \begin{bmatrix} -1 & \frac{a_{03}}{a_{13}} & 0 & -\frac{a_{01}}{a_{13}} \\ \frac{a_{03}}{a_{13}} & \frac{{a_{23}}^2-{a_{03}}^2+{S_3}^2+{T_3}^2}{{a_{13}}^2} & -\frac{a_{23}}{a_{13}} & \frac{a_{01}a_{03}-a_{21}a_{23}-S_1S_3-T_1T_3}{{a_{13}}^2} \\ 0 & -\frac{a_{23}}{a_{13}} & 1 & -\frac{a_{12}}{a_{13}} \\ -\frac{a_{01}}{a_{13}} & \frac{a_{01}a_{03}-a_{21}a_{23}-S_1S_3-T_1T_3}{{a_{13}}^2} & -\frac{a_{12}}{a_{13}} & \frac{{a_{21}}^2-{a_{01}}^2+{S_1}^2+{T_1}^2}{{a_{13}}^2} \end{bmatrix}, \tag{4.5}$$

where $S_i \equiv \frac{\partial S}{\partial \xi^i}$, $T_i \equiv \frac{\partial T}{\partial \xi^i}$, and $a_{ij} \equiv S_iT_j - T_iS_j$. In addition, $\sqrt{|g|} = |a_{13}|$, which is required in the tensorial AWE formulation, where g is the determinant of the covariant metric tensor.

4.2.2 Coupled first-order acoustic PDE system

The dynamics of the first-order coupled acoustic PDE system are governed by two operators. The first is the generalized gradient operator $\mathcal{G}^\mu$ that acts on a rank-zero tensor field U

$$\mathcal{G}^\mu[U] = g^{\mu\nu}\frac{\partial U}{\partial \xi^\nu}. \tag{4.6}$$

The second is the generalized divergence operator $\mathcal{D}_\mu$ that acts on a tensor object χ^ν

$$\mathcal{D}_\mu[\chi^\nu] = \frac{1}{\sqrt{|g|}}\frac{\partial}{\partial \xi^\mu}\left(\sqrt{|g|}\chi^\nu\right). \tag{4.7}$$

The acoustic operator in equation 4.1 can be written as

$$\Box_\xi P_\xi = -\mathcal{D}_\mu \mathcal{G}^\mu P_\xi = F_\xi \tag{4.8}$$

or equivalently as (Konuk and Shragge, 2020)

$$-\frac{1}{\sqrt{|g|}}\frac{\partial}{\partial \xi^\mu}\left(\sqrt{|g|}g^{\mu\nu}\frac{\partial}{\partial \xi^\nu}\right)P_\xi = F_\xi. \tag{4.9}$$

In Cartesian coordinates with variables $\boldsymbol{x} = [x^0, x^1, x^2, x^3] = [ct, x, y, z]$, the generalized acoustic wave equation (equation 4.9) reduces to

$$\left(\frac{-1}{c^2}\frac{\partial^2}{\partial t^2} + \nabla^2\right)P = F, \tag{4.10}$$

where $c = c(\boldsymbol{x})$ is the Cartesian medium velocity, ∇^2 is the 3D Cartesian Laplacian operator, P is the scalar pressure field in Cartesian coordinates, and F is the source term. Using these operators, the coupled first-order acoustic PDE system can be written as the generalized linearized continuity equation (LCE):

$$-\mathcal{G}^0\left[P_\xi\right] = \rho_\xi c_\xi \mathcal{D}_i[u^i_\xi] + F_\xi, \tag{4.11}$$

and the vector generalized linearized Euler equation (LEE) (i.e., Newtonian force):

$$\rho_\xi c_\xi \mathcal{D}_0\left[u^i_\xi\right] \;=\; \mathcal{G}^i[P_\xi], \tag{4.12}$$

where $i = 1, 2, 3$ is an index over the spatial variable coordinates and u^i_ξ is the ith component of the particle velocity. Thus, we may rewrite the LCE in equation 4.11 as

$$-g^{0\nu}\frac{\partial P_\xi}{\partial \xi^\nu} = \frac{\rho_\xi c_\xi}{\sqrt{|g|}}\frac{\partial}{\partial \xi^i}\left(\sqrt{|g|}u^i\right) + F_\xi, \tag{4.13}$$

and the vector LEE in equation 4.12 as

$$\frac{\rho_\xi c_\xi}{\sqrt{|g|}}\frac{\partial}{\partial \xi^0}\left(\sqrt{|g|}u^i_\xi\right) = g^{i\nu}\frac{\partial P_\xi}{\partial \xi^\nu}. \tag{4.14}$$

4.2.3 3D moving source with time-varying sea surface

We can write the equations when including the moving source, assumed to be moving laterally in the ξ^1 direction, and a time-varying sea surface. The specific LCE equation for this coordinate transformation is

$$\frac{\partial P_\xi}{\partial \xi^0} - g^{01}\frac{\partial P_\xi}{\partial \xi^1} - g^{03}\frac{\partial P_\xi}{\partial \xi^3} = \frac{\rho_\xi c_\xi}{\sqrt{|g|}}\left[\frac{\partial}{\partial \xi^1}\left(\sqrt{|g|}u^1\right) + \frac{\partial}{\partial \xi^2}\left(\sqrt{|g|}u^2\right) + \frac{\partial}{\partial \xi^3}\left(\sqrt{|g|}u^3\right)\right] + F_\xi, \tag{4.15}$$

which using $\frac{\partial}{\partial \xi^0} \equiv \frac{1}{c_\xi}\frac{\partial}{\partial \tau}$ can be rewritten

$$\frac{1}{c_\xi}\frac{\partial P_\xi}{\partial \tau} - \frac{a_{03}}{a_{13}}\frac{\partial P_\xi}{\partial \xi^1} - \frac{a_{01}}{a_{31}}\frac{\partial P_\xi}{\partial \xi^3} = \frac{\rho_\xi c_\xi}{|a_{13}|}\left[\frac{\partial}{\partial \xi^1}\left(|a_{13}|u^1\right) + \frac{\partial}{\partial \xi^2}\left(|a_{13}|u^2\right) + \frac{\partial}{\partial \xi^3}\left(|a_{13}|u^3\right)\right] + F_\xi, \tag{4.16}$$

where $\tau \equiv t$ is the time axis. Similarly, the vector LEE equation can be rewritten as

$$\frac{\rho_\xi}{|a_{13}|}\frac{\partial}{\partial \tau}\left(|a_{13}|u^1_\xi\right) = \frac{g^{01}}{c_\xi}\frac{\partial P_\xi}{\partial \tau} + g^{11}\frac{\partial P_\xi}{\partial \xi^1} + g^{12}\frac{\partial P_\xi}{\partial \xi^2} + g^{13}\frac{\partial P_\xi}{\partial \xi^3}, \tag{4.17}$$

$$\frac{\rho_\xi}{|a_{13}|}\frac{\partial}{\partial \tau}\left(|a_{13}|u^2_\xi\right) = g^{12}\frac{\partial P_\xi}{\partial \xi^1} + \frac{\partial P_\xi}{\partial \xi^2} + g^{23}\frac{\partial P_\xi}{\partial \xi^3}, \tag{4.18}$$

$$\frac{\rho_\xi}{|a_{13}|}\frac{\partial}{\partial \tau}\left(|a_{13}|u^3_\xi\right) = \frac{g^{03}}{c_\xi}\frac{\partial P_\xi}{\partial \tau} + g^{13}\frac{\partial P_\xi}{\partial \xi^1} + g^{23}\frac{\partial P_\xi}{\partial \xi^2} + g^{33}\frac{\partial P_\xi}{\partial \xi^3}. \tag{4.19}$$

4.2.4 Coordinate transformation

To model a moving source in the presence of a time-varying sea surface, we make a set of plausible assumptions: (1) no stretching of the time axis occurs (e.g., $t \equiv \tau$); (2) the source moves along the ξ^1-axis; (3) the source moves at a fixed depth level below the immediate sea surface above; (4) the source moves at a constant velocity; and (5) the source moves in a homogeneous fluid medium. Assumptions (3) and (5) allow us to define a coordinate transformation that confines the physical mesh deformation to the assumed homogeneous fluid medium. Given the set of assumptions, we can define a depth-dependent coordinate transformation that tracks the source movement such that

$$S(\xi^0 \equiv c\tau, \xi^1, \xi^2 = x^2, \xi^3) = \xi^1 + v\tau e^{\gamma(z_s - \xi^3)}, \tag{4.20}$$

and a depth-dependent coordinate transformation that accounts for the time-varying sea surface such that

$$T(\xi^0 \equiv c\tau, \xi^1, \xi^2, \xi^3) = \xi^3 + W\left(\xi^1, \xi^2, \tau\right)\left(1 - \frac{\xi^3}{\xi^3_m}\right) e^{\lambda \xi^3}, \tag{4.21}$$

where v is the vessel velocity, z_s is the source depth, W is the time-varying sea-surface function, $\xi^3_m = x^3_m$ is the maximum model depth, and γ and λ are user-defined decay factors that control the amount of horizontal and vertical deformations as a function of depth, respectively. A judicious choice of γ and λ confines the mesh deformation to the homogeneous water layer, mitigating the need for a repeated and expensive interpolation of subsurface physical properties (i.e., $c_\xi = c_x$) and seismic wavefield associated with time-varying meshes below the ocean bottom. To compute $\frac{\partial S}{\partial \xi^0}$ and $\frac{\partial T}{\partial \xi^0}$, as required for the metric tensor, we use $\frac{\partial \tau}{\partial \xi^0} = \frac{1}{c_\xi}$ such that

$$\frac{\partial S}{\partial \xi^0} = \frac{v}{c_\xi} e^{\gamma(z_s - \xi^3)} \tag{4.22}$$

and

$$\frac{\partial T}{\partial \xi^0} = \frac{1}{c_\xi}\frac{\partial W}{\partial \tau}\left(1 - \frac{\xi^3}{\xi^3_m}\right) e^{\lambda \xi^3}. \tag{4.23}$$

Figure 4.1(a) and Figure 4.1(b) shows graphical representations of a deformed physical domain in Cartesian coordinates and the fixed computational domain in a generalized coordinate system, respectively.

4.2.5 Time-varying sea surface

We use a modified Pierson and Moskowitz (1964) power spectrum that includes a directivity term to model time-varying sea surfaces (Laws and Kragh, 2002). The modified power spectrum is defined as

$$\tilde{W}(k_x, k_z, \tau) = \frac{\alpha N}{2k^4} \exp\left(\frac{-\beta^2 g^2}{k^2 U^4}\right) \cos^{2s}\left(\frac{\theta}{2}\right) + G\left(k_x, k_z, \tau\right), \tag{4.24}$$

where $\alpha = 0.0081$ and $\beta = 0.74$ are dimensionless constants; N is a normalization factor, such that $\int_\theta N \cos^{2s}\left(\frac{\theta}{2}\right) d\theta = 1$; $k = \sqrt{k_x^2 + k_z^2}$ is the wavenumber in radians per unit length; g is the gravitational acceleration constant; U is the wind speed measured 19 m above the sea surface; θ is azimuthal angle relative to the wind direction; s is an empirical spreading factor; and G is a time-varying random Gaussian number to model a 2D time-varying sea surface.

4.3 Numerical approach

The goal of this section is to provide a practical approach to numerically solve the coupled first-order system. We use a fully-staggered grid (FSG) scheme with MFD operators to ensure numerical stability and accuracy when solving the tensorial AWE in generalized coordinates. We also use a prediction step staggered-in-time (PSIT) scheme to compute the fluid advection terms in the LCE equation.

4.3.1 Fully staggered grid

Modeling wave propagation in Cartesian coordinates using a first-order coupled system allows using a standard staggered grid (SSG) scheme (Figure 4.2(a)), improving the overall accuracy and stability of the numerical solution (e.g., Virieux, 1986). Furthermore, im-

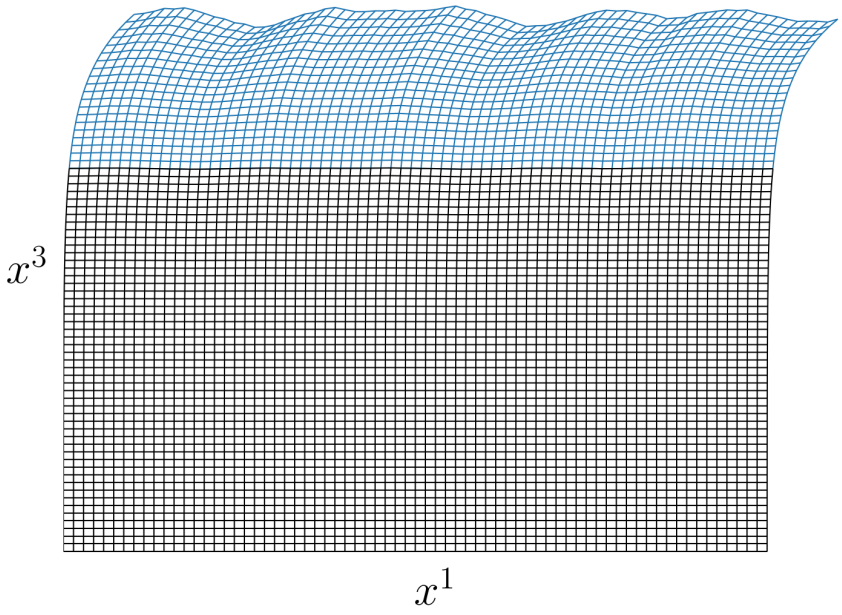

(a)

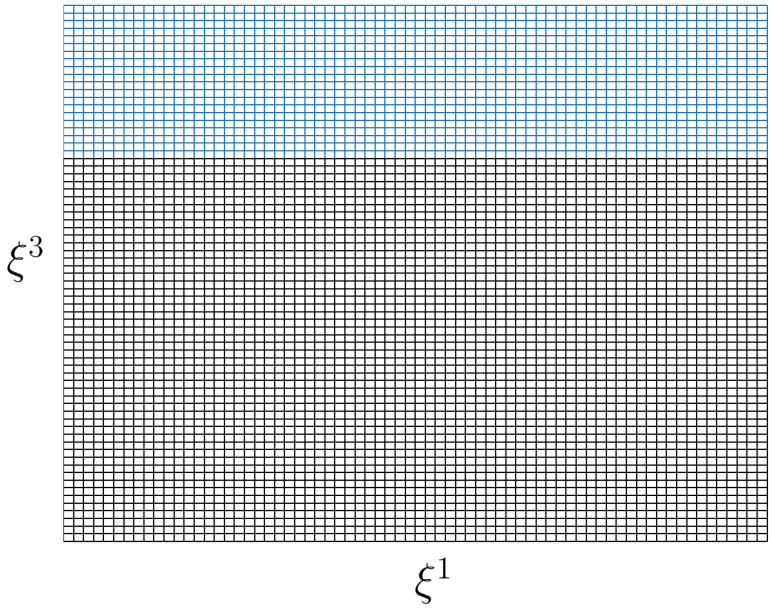

(b)

Figure 4.1 2D graphical representation of (a) physical and (b) computational domains.

plementing robust absorbing boundary conditions[6], e.g., perfectly matched layers, is more straightforward in first-order systems than in second-order formulations of the AWE. However, facilitating Cartesian-to-generalized coordinate transformation to model a moving source with a time-varying sea surface introduces mixed derivatives and advection terms into the governing tensorial AWE; otherwise, these terms would vanish in standard Cartesian-based implementations characterized by flat surfaces and stationary sources. Solving the generalized first-order system requires evaluating mixed partial derivatives at locations where the seismic wavefield is not readily available when using an SSG scheme. One solution is to use a high-order interpolation of the wavefield for all time steps, which is computationally expensive and inefficient. A more natural choice is to use a fully staggered grid (FSG) scheme with complementary grid locations (Lisitsa and Vishnevskiy, 2010) that provides all the required wavefield samples, constructed using four SSG schemes set spatially with a diagonal offset (Figure 4.2(b)).

4.3.2 Mimetic finite-difference operators

Approximating partial differential operators using Taylor-based coefficients is appealing for their simplicity and ease of implementation when solving the AWE. A drawback of such operators is the reduced accuracy at the boundaries of the modeling domain, which can introduce numerical instability when modeling free-surface effects of curved surfaces, and even more so when considering time-varying free surfaces. Alternatively, MFD operators provide a uniform throughout the modeling domain, including the boundary region (Castillo and Miranda, 2013; de la Puente et al., 2014; Konuk and Shragge, 2020; Shragge and Tapley, 2017). These operators are analogs to their continuum gradient and divergence counterparts that mimic the mathematical and physical relations that govern the seismic wavefield and satisfy fundamental properties such as conservation laws, symmetry, and duality of differential operators (Lipnikov et al., 2014).

[6]In Appendix A, we discuss the details of the boundary condition we use in the numerical implementation of this chapter.

To facilitate MFD operators within the boundary region, additional complementary pressure and particle velocity overlapping grid points are required (Figure 4.2(c)). Corbino and Castillo (2020) formulate the numerical operators that act on quantities defined at half-integer ($\mathscr{L}_h$) and full-integer ($\mathscr{L}_f$) grid points, which they name the gradient ($\mathbf{G}$) and divergence ($\mathbf{D}$) operators, respectively. However, it is important to note that the numerical operators are defined based on the grid layout within the numerical scheme [i.e., the numerical gradient ($\mathbf{G} = \mathscr{L}_h$) and divergence ($\mathbf{D} = \mathscr{L}_f$) operators are applied on fields defined on half- and full-integer grids, respectively]. These operators have different coefficients within the boundary region than Taylor-based coefficients, but identical coefficients of the same approximation order away from the boundary region. We differentiate between fields defined on full-integer ($\mathbf{f}$) and half-integer ($\mathbf{h}$) grids.

In an MFD formulation, the pressure and particle velocity fields are defined at four complementary staggering grid locations as given by Table 4.1. Figure 4.3(a) and Figure 4.3(b) shows a 2D graphical representation of pressure field defined at $[\xi^1, \xi^2, \xi^3] = [\mathbf{f}, \mathbf{f}, \mathbf{f}]$ and $[\xi^1, \xi^2, \xi^3] = [\mathbf{h}, \mathbf{f}, \mathbf{h}]$, respectively; and Figure 4.3(c) and Figure 4.3(d) shows a 2D graphical representation of particle velocity field defined at $[\xi^1, \xi^2, \xi^3] = [\mathbf{f}, \mathbf{f}, \mathbf{h}]$ and $[\xi^1, \xi^2, \xi^3] = [\mathbf{h}, \mathbf{f}, \mathbf{f}]$, respectively. To approximate $\mathcal{D}_i[u^i_\xi]$ and $\mathcal{G}^i[P_\xi]$ in equations 4.11 and 4.12, we apply the numerical operators as shown in Table 4.2 and Table 4.3.

4.3.3 Prediction step staggered-in-time

The advection terms in equation 4.16 present two implementation challenges: (1) the partial derivatives are not centered at required pressure grid points, and (2) they are required to be at half-integer time steps when using a leap-frog scheme (the pressure and particle velocity wavefields are advanced alternately for practical memory management). One can use an unstaggered-in-time approach when advancing the pressure and particle velocity wavefields to solve the time-stepping problem. However, this approach requires storing wavefields at different time steps, effectively doubling the memory requirement (Konuk and Shragge, 2020). An alternative approach is to implement a prediction step staggered-in-time (PSIT) scheme

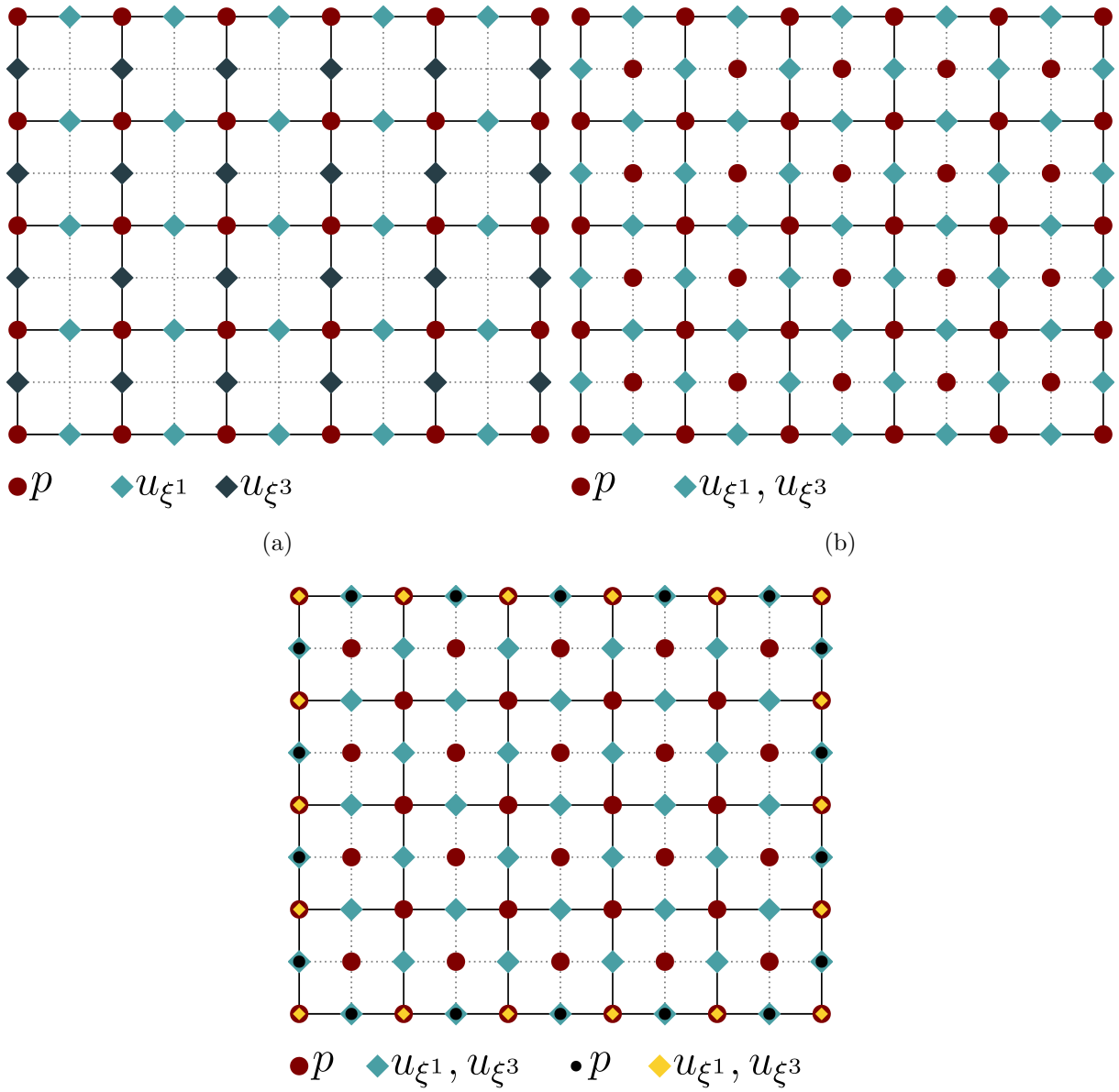

Figure 4.2 2D graphical representation of (a) SSG, (b) FSG, and (c) MFD staggered grid computational domains.

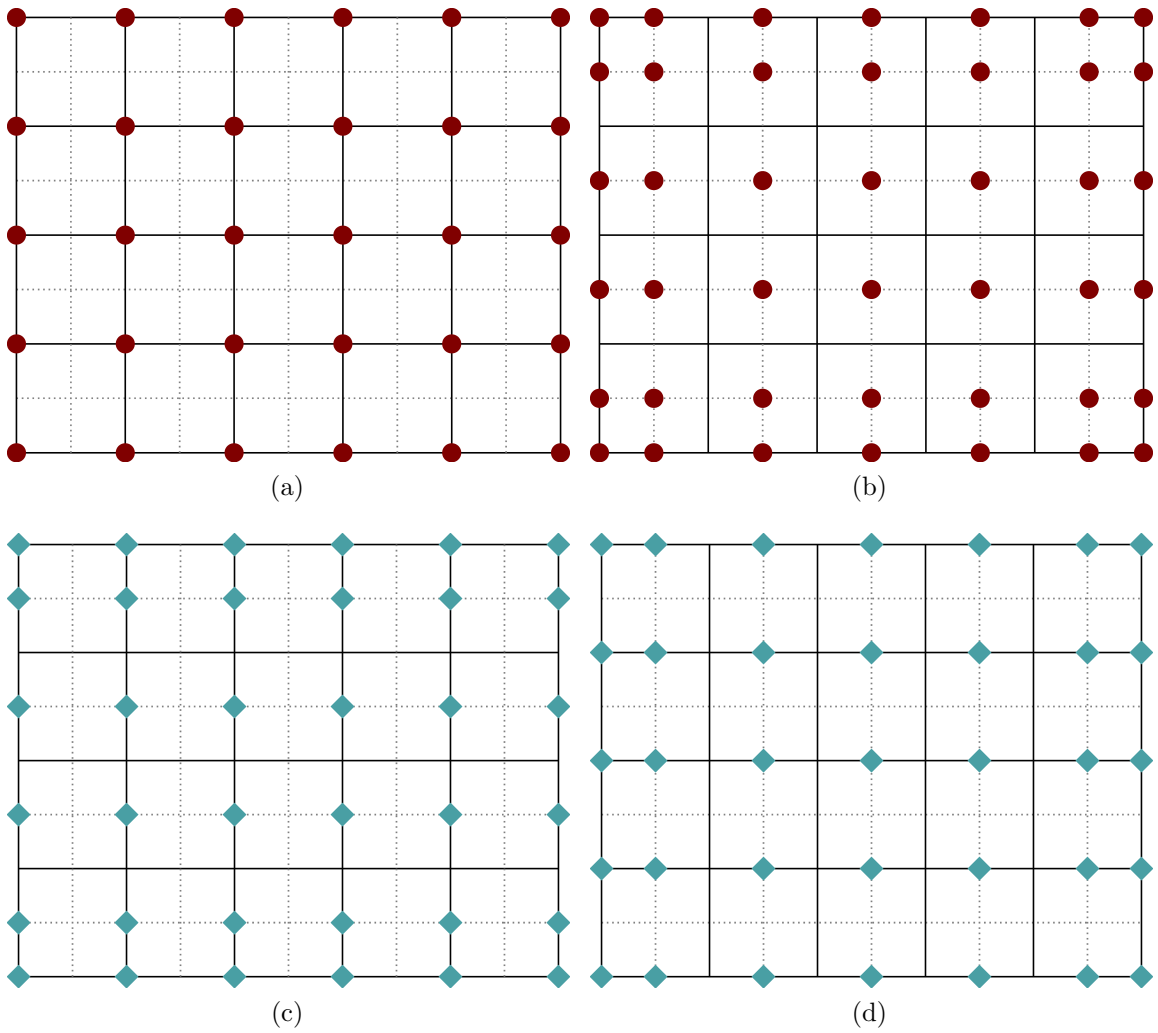

Figure 4.3 2D graphical representation of pressure field defined at (a) $[\xi^1, \xi^3] = [\mathbf{f}, \mathbf{f}]$ and (b) $[\xi^1, \xi^3] = [\mathbf{h}, \mathbf{h}]$ grid points, and particle velocity field defined at (c) $[\xi^1, \xi^3] = [\mathbf{f}, \mathbf{h}]$ and (d) $[\xi^1, \xi^3] = [\mathbf{h}, \mathbf{f}]$ grid points ($\xi^2 = \mathbf{f}$ in all 2D graphical representations).

Table 4.1 Pressure and particle velocity grid locations in 3D. Within an MFD scheme, the pressure and particle velocity wavefields are computed at four complementary staggered grids.

Field type	Grid location	Denoted by
pressure	$[\mathbf{f},\mathbf{f},\mathbf{f}]$	$P_\xi[\mathbf{f},\mathbf{f},\mathbf{f}]$
	$[\mathbf{f},\mathbf{h},\mathbf{h}]$	$P_\xi[\mathbf{f},\mathbf{h},\mathbf{h}]$
	$[\mathbf{h},\mathbf{f},\mathbf{h}]$	$P_\xi[\mathbf{h},\mathbf{f},\mathbf{h}]$
	$[\mathbf{h},\mathbf{h},\mathbf{f}]$	$P_\xi[\mathbf{h},\mathbf{h},\mathbf{f}]$
particle velocity	$[\mathbf{h},\mathbf{f},\mathbf{f}]$	$u^i_\xi[\mathbf{h},\mathbf{f},\mathbf{f}]$
	$[\mathbf{f},\mathbf{h},\mathbf{f}]$	$u^i_\xi[\mathbf{f},\mathbf{h},\mathbf{f}]$
	$[\mathbf{f},\mathbf{f},\mathbf{h}]$	$u^i_\xi[\mathbf{f},\mathbf{f},\mathbf{h}]$
	$[\mathbf{h},\mathbf{h},\mathbf{h}]$	$u^i_\xi[\mathbf{h},\mathbf{h},\mathbf{h}]$

while (reasonably) assuming the mesh moves much slower than the wave propagation speed (Konuk and Shragge, 2020; Van Renterghem and Botteldooren, 2007). In the PSIT scheme, we advance the pressure wavefield for full- and half-time steps, neglecting the advection terms in equation 4.16. Then, we compute and add the spatial derivatives of the pressure wavefield at the half-time step to the pressure wavefield at the full-time step. Because the advection terms must be centered at pressure grid points, we approximate them using Taylor-based coefficients given in Appendix 4.9.

4.4 Numerical Examples

This section demonstrates the effects of time-varying sea surfaces on marine vibrator data in the common-shot and common-receiver domains using 2D numerical examples. In the first example, we use an unrealistically exaggerated sea state with a significant wave height (SWH) of ± 14 m with an apparent lateral velocity of 175 m/s to (1) validate the stability of the numerical scheme and (2) emphasize the effects of a time-varying sea surface on seismic data. In the second example, we use a more realistic SWH of ± 5 m with the same apparent lateral

Table 4.2 Differential operators as applied to particle velocity fields to updated pressure field within an MFD scheme.

Differential operator	Numerical operator	To update
$\mathcal{D}_1\Big[u_\xi^1\big[\mathbf{h},\mathbf{f},\mathbf{f}\big]\Big]$	$\mathscr{L}_h^1 u_\xi^1\big[\mathbf{h},\mathbf{f},\mathbf{f}\big]$	$P_\xi\big[\mathbf{f},\mathbf{f},\mathbf{f}\big]$
$\mathcal{D}_2\Big[u_\xi^2\big[\mathbf{f},\mathbf{h},\mathbf{f}\big]\Big]$	$\mathscr{L}_h^2 u_\xi^2\big[\mathbf{f},\mathbf{h},\mathbf{f}\big]$	$P_\xi\big[\mathbf{f},\mathbf{f},\mathbf{f}\big]$
$\mathcal{D}_3\Big[u_\xi^3\big[\mathbf{f},\mathbf{f},\mathbf{h}\big]\Big]$	$\mathscr{L}_h^3 u_\xi^3\big[\mathbf{f},\mathbf{f},\mathbf{h}\big]$	$P_\xi\big[\mathbf{f},\mathbf{f},\mathbf{f}\big]$
$\mathcal{D}_1\Big[u_\xi^1\big[\mathbf{h},\mathbf{h},\mathbf{h}\big]\Big]$	$\mathscr{L}_h^1 u_\xi^1\big[\mathbf{h},\mathbf{h},\mathbf{h}\big]$	$P_\xi\big[\mathbf{f},\mathbf{h},\mathbf{h}\big]$
$\mathcal{D}_2\Big[u_\xi^2\big[\mathbf{f},\mathbf{f},\mathbf{h}\big]\Big]$	$\mathscr{L}_f^2 u_\xi^2\big[\mathbf{f},\mathbf{f},\mathbf{h}\big]$	$P_\xi\big[\mathbf{f},\mathbf{h},\mathbf{h}\big]$
$\mathcal{D}_3\Big[u_\xi^3\big[\mathbf{f},\mathbf{h},\mathbf{f}\big]\Big]$	$\mathscr{L}_f^3 u_\xi^3\big[\mathbf{f},\mathbf{h},\mathbf{f}\big]$	$P_\xi\big[\mathbf{f},\mathbf{h},\mathbf{h}\big]$
$\mathcal{D}_1\Big[u_\xi^1\big[\mathbf{f},\mathbf{f},\mathbf{h}\big]\Big]$	$\mathscr{L}_f^1 u_\xi^1\big[\mathbf{f},\mathbf{f},\mathbf{h}\big]$	$P_\xi\big[\mathbf{h},\mathbf{f},\mathbf{h}\big]$
$\mathcal{D}_2\Big[u_\xi^2\big[\mathbf{h},\mathbf{h},\mathbf{h}\big]\Big]$	$\mathscr{L}_h^2 u_\xi^2\big[\mathbf{h},\mathbf{h},\mathbf{h}\big]$	$P_\xi\big[\mathbf{h},\mathbf{f},\mathbf{h}\big]$
$\mathcal{D}_3\Big[u_\xi^3\big[\mathbf{h},\mathbf{f},\mathbf{f}\big]\Big]$	$\mathscr{L}_f^3 u_\xi^3\big[\mathbf{h},\mathbf{f},\mathbf{f}\big]$	$P_\xi\big[\mathbf{h},\mathbf{f},\mathbf{h}\big]$
$\mathcal{D}_1\Big[u_\xi^1\big[\mathbf{f},\mathbf{h},\mathbf{f}\big]\Big]$	$\mathscr{L}_f^1 u_\xi^1\big[\mathbf{f},\mathbf{h},\mathbf{f}\big]$	$P_\xi\big[\mathbf{h},\mathbf{h},\mathbf{f}\big]$
$\mathcal{D}_2\Big[u_\xi^2\big[\mathbf{h},\mathbf{f},\mathbf{f}\big]\Big]$	$\mathscr{L}_f^2 u_\xi^2\big[\mathbf{h},\mathbf{f},\mathbf{f}\big]$	$P_\xi\big[\mathbf{h},\mathbf{h},\mathbf{f}\big]$
$\mathcal{D}_3\Big[u_\xi^3\big[\mathbf{h},\mathbf{h},\mathbf{h}\big]\Big]$	$\mathscr{L}_h^3 u_\xi^3\big[\mathbf{h},\mathbf{h},\mathbf{h}\big]$	$P_\xi\big[\mathbf{h},\mathbf{h},\mathbf{f}\big]$

velocity as in the first example to highlight the significance of time-varying sea surfaces on seismic data in the common-receiver domain.

4.4.1 Exaggerated sea state

In this example, we simulate the acoustic wavefield using a Marmousi II sub-model (Martin et al., 2002), resampled at 1.5 m. We use a source placed at $[\xi^1, \xi^3] = [900, 30]$ m that moves at 5 m/s, and 1201 stationary receivers positioned at $\xi^3 = x^3 = 250$ m with a 1.5 m uniform spacing. The source function is a linear sweep from 20 to 60 Hz of 0.5 s duration. Figure 4.4(a) and Figure 4.4(b) shows snapshots of the seismic wavefield triggered by a moving source assuming flat and rough sea surfaces, respectively. The time-varying sea-surface scenario is characterized by amplitude and phase distortions because of the scattering effects on the wavefield introduced by the rough sea surface, whereas the flat sea-surface case exhibits a

Table 4.3 Differential operators as applied to pressure field to update u_ξ^i within an MFD scheme, where $i = 1, 2, 3$.

Differential operator	Numerical operator	To update
$\mathcal{G}_1\big[P_\xi\big[\mathbf{f},\mathbf{f},\mathbf{f}\big]\big]$	$\mathscr{L}_f^1 P_\xi\big[\mathbf{f},\mathbf{f},\mathbf{f}\big]$	$u_\xi^i\big[\mathbf{h},\mathbf{f},\mathbf{f}\big]$
$\mathcal{G}_2\big[P_\xi\big[\mathbf{h},\mathbf{h},\mathbf{f}\big]\big]$	$\mathscr{L}_h^2 P_\xi\big[\mathbf{h},\mathbf{h},\mathbf{f}\big]$	$u_\xi^i\big[\mathbf{h},\mathbf{f},\mathbf{f}\big]$
$\mathcal{G}_3\big[P_\xi\big[\mathbf{h},\mathbf{f},\mathbf{h}\big]\big]$	$\mathscr{L}_h^3 P_\xi\big[\mathbf{h},\mathbf{f},\mathbf{h}\big]$	$u_\xi^i\big[\mathbf{h},\mathbf{f},\mathbf{f}\big]$
$\mathcal{G}_1\big[P_\xi\big[\mathbf{h},\mathbf{h},\mathbf{f}\big]\big]$	$\mathscr{L}_h^1 P_\xi\big[\mathbf{h},\mathbf{h},\mathbf{f}\big]$	$u_\xi^i\big[\mathbf{f},\mathbf{h},\mathbf{f}\big]$
$\mathcal{G}_2\big[P_\xi\big[\mathbf{f},\mathbf{f},\mathbf{f}\big]\big]$	$\mathscr{L}_f^2 P_\xi\big[\mathbf{f},\mathbf{f},\mathbf{f}\big]$	$u_\xi^i\big[\mathbf{f},\mathbf{h},\mathbf{f}\big]$
$\mathcal{G}_3\big[P_\xi\big[\mathbf{f},\mathbf{h},\mathbf{h}\big]\big]$	$\mathscr{L}_h^3 P_\xi\big[\mathbf{f},\mathbf{h},\mathbf{h}\big]$	$u_\xi^i\big[\mathbf{f},\mathbf{h},\mathbf{f}\big]$
$\mathcal{G}_1\big[P_\xi\big[\mathbf{h},\mathbf{f},\mathbf{h}\big]\big]$	$\mathscr{L}_h^1 P_\xi\big[\mathbf{h},\mathbf{f},\mathbf{h}\big]$	$u_\xi^i\big[\mathbf{f},\mathbf{f},\mathbf{h}\big]$
$\mathcal{G}_2\big[P_\xi\big[\mathbf{f},\mathbf{h},\mathbf{h}\big]\big]$	$\mathscr{L}_h^2 P_\xi\big[\mathbf{f},\mathbf{h},\mathbf{h}\big]$	$u_\xi^i\big[\mathbf{f},\mathbf{f},\mathbf{h}\big]$
$\mathcal{G}_3\big[P_\xi\big[\mathbf{f},\mathbf{f},\mathbf{f}\big]\big]$	$\mathscr{L}_f^3 P_\xi\big[\mathbf{f},\mathbf{f},\mathbf{f}\big]$	$u_\xi^i\big[\mathbf{f},\mathbf{f},\mathbf{h}\big]$
$\mathcal{G}_1\big[P_\xi\big[\mathbf{f},\mathbf{h},\mathbf{h}\big]\big]$	$\mathscr{L}_f^1 P_\xi\big[\mathbf{f},\mathbf{h},\mathbf{h}\big]$	$u_\xi^i\big[\mathbf{h},\mathbf{h},\mathbf{h}\big]$
$\mathcal{G}_2\big[P_\xi\big[\mathbf{h},\mathbf{f},\mathbf{h}\big]\big]$	$\mathscr{L}_f^2 P_\xi\big[\mathbf{h},\mathbf{f},\mathbf{h}\big]$	$u_\xi^i\big[\mathbf{h},\mathbf{h},\mathbf{h}\big]$
$\mathcal{G}_3\big[P_\xi\big[\mathbf{h},\mathbf{h},\mathbf{f}\big]\big]$	$\mathscr{L}_f^3 P_\xi\big[\mathbf{h},\mathbf{h},\mathbf{f}\big]$	$u_\xi^i\big[\mathbf{h},\mathbf{h},\mathbf{h}\big]$

simpler radiation pattern for ghost reflections. We note that the source-side ghost reflections are easily visible because of the significant source depth and long duration of the sweep.

Figure 4.5(a) and Figure 4.5(b) shows the corresponding shot gathers of the two simulations in Figure 4.4(a) and Figure 4.4(b), respectively. The ghost reflections in the time-varying sea-surface shot gather exhibit amplitude and phase distortions, making them less predictable compared to the flat sea-surface shot-gather scenario (Figure 4.6). Because the wavefield interacts with a time-varying sea surface, the ghost reflections vary in space and time. Further, the ghost notches are dispersed and blurred. To see the profound effects of a time-varying sea surface on reflection data, we repeat the numerical simulations for a stationary source, keeping all other parameters unchanged. Figure 4.7(a) and Figure 4.7(b) shows a time-windowed shot gathers after correlating with the stationary sweep. We can see that the continuity

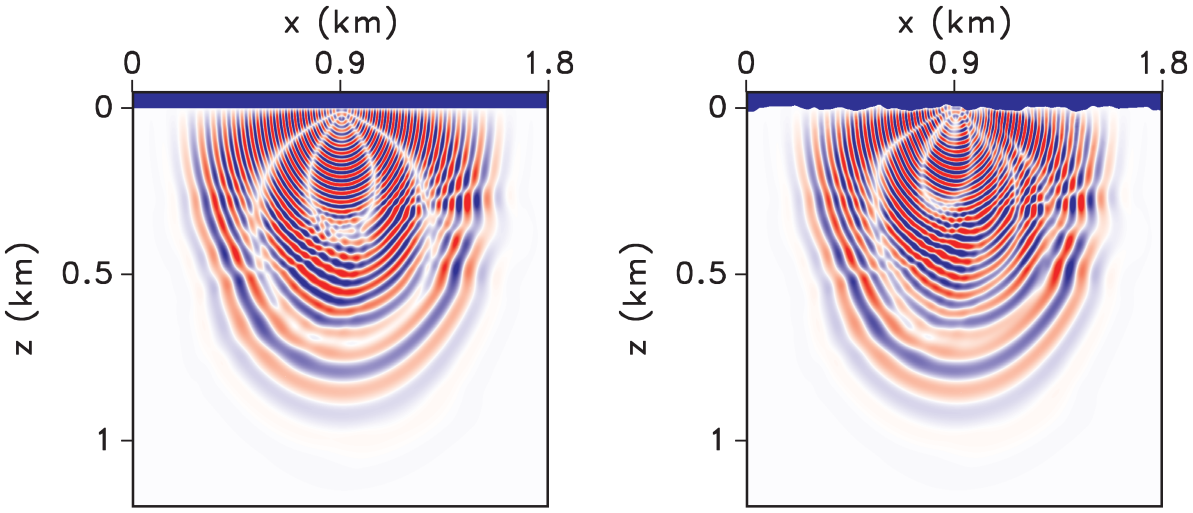

(a) (b)

Figure 4.4 Wavefield snapshots simulated using (a) flat and (b) rough sea surface with ±14 m SWH, showing distortions in ghost reflections because of the rough sea surface.

and amplitude of the seismic events are severely affected when the wavefield interacts with a time-varying sea surface. Such effects make data processing challenging and reduce the repeatability of seismic data.

4.4.2 Realistic sea state

In this example, we investigate the impact of time-varying sea surfaces on seismic data in the common-receiver domain, especially since ocean-bottom data are commonly processed in such a domain due to the sparse receiver sampling. We use the same simulation parameters as in the previous example, but model 301 sources with a 6 m source spacing. Figure 4.8(a) and Figure 4.8(b) shows shot gathers simulated with a flat and time-varying sea surface, respectively. Under a realistic sea-state acquisition condition, the effects of a time-varying sea surface, although present, are hardly visible because of the long duration of the sweep; the ghost wavefield is scattered and dispersed and is thus easily masked by the wavefield generated by later parts of the sweep. In fact, the two gathers are indistinguishable, making an inference about the sea state from shot gathers challenging. Figure 4.8(c) and Figure 4.8(d) shows

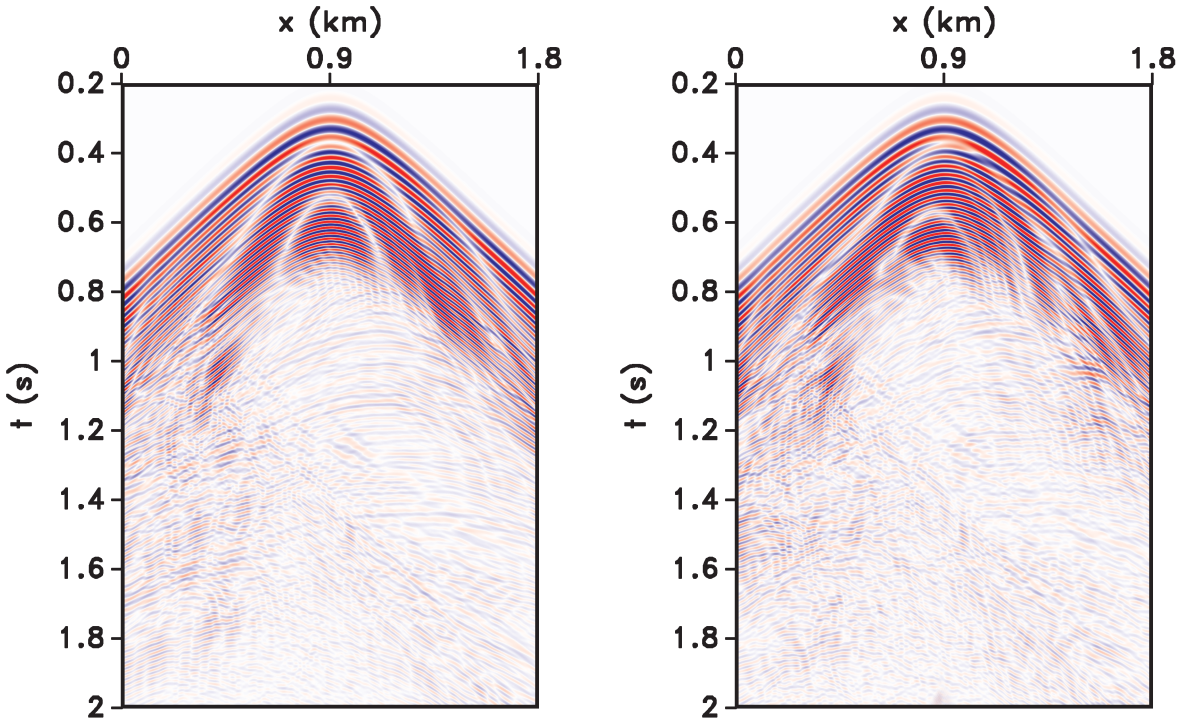

(a) (b)

Figure 4.5 Shot gathers for (a) flat and (b) rough sea surface with ±14 m SWH, showing distortions in ghost reflections because of the rough sea surface.

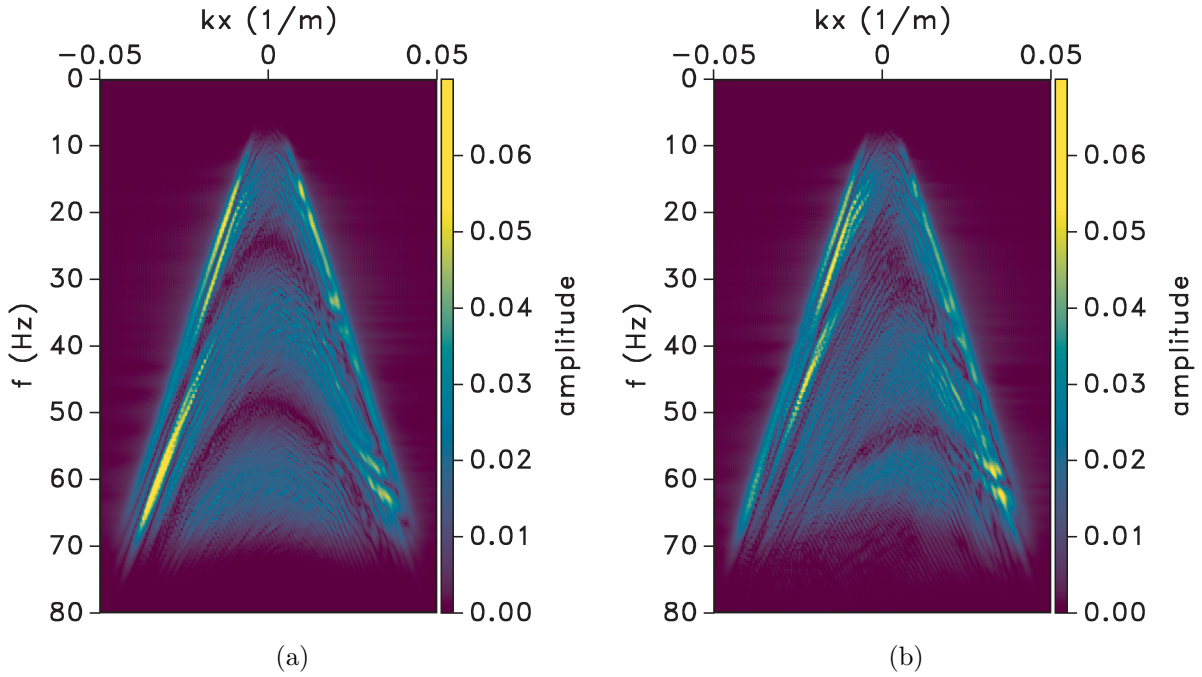

Figure 4.6 Frequency-wavenumber spectra of shot gathers shown in (a) Figure 4.5(a) and (b) Figure 4.5(b). The ghost notches in the flat sea surface case are symmetric and clearly visible, whereas they are dispersed and blurred in the rough sea surface case.

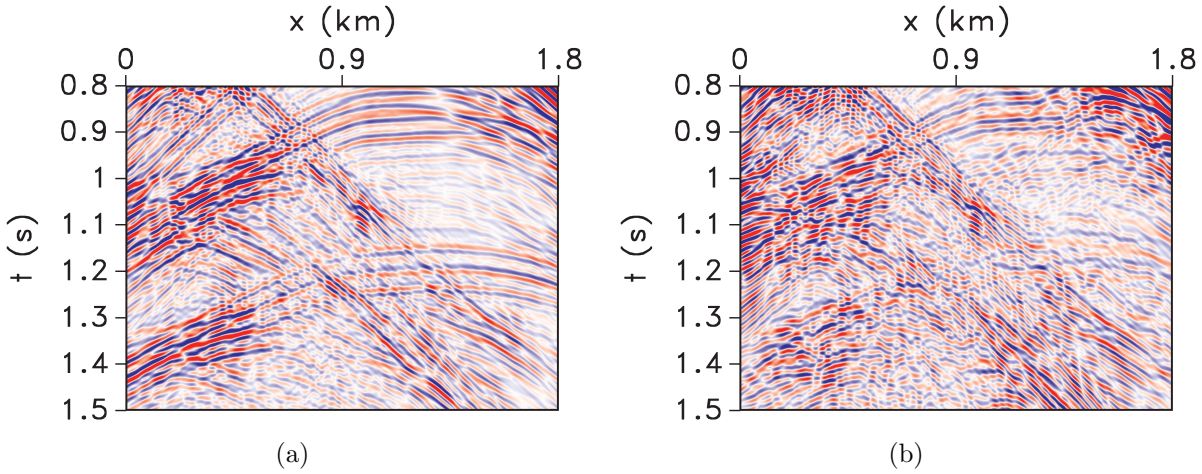

Figure 4.7 Time window of correlated shot gathers simulated using a stationary source with (a) flat and (b) rough sea surface with ±14 m SWH. Events are easily trackable in the flat sea surface case, unlike in the rough sea surface case.

common-receiver gathers simulated with a flat and time-varying sea surface, respectively. In the common-receiver domain, the effects of time-varying sea surfaces are easily noticeable because different traces are simulated with different source positions and time-varying sea surfaces, creating trace-to-trace jitter as also reported by Blacquière and Sertlek (2019). Typical marine sources use a buoy to control their depth during acquisition (Laws and Kragh, 2002); accordingly, the depth of a marine source is measured relative to the sea surface directly above the source. Thus, the incident wavefield that has not interacted with the sea surface is also affected by the time-varying sea surface because of the variable source depth (we inherently account for the variable source depth due to the rough sea surface in our coordinate transformation). Therefore, the variable source depth also creates a trace-to-trace jitter in the common-receiver domain (Figure 4.9. In a shot gather, however, the effect of a variable-depth source manifests as time-dependent frequency shifts (i.e., Doppler effect) for long sweeps.

4.5 Discussion

The time-varying nature of the sea surface poses a processing challenge, especially for time-lapse (4D) studies, because false structures can appear in 4D difference sections even for fairly calm sea states (Laws and Kragh, 2002). Further repeatability challenges arise when considering moving and long-emitting sources, such as source/receiver positioning and the interaction of long sweeps with the time-varying sea surface. Accurately accounting for source motion and time-varying sea surface in modeling is essential for understanding the effects of realistic acquisition conditions on seismic data. More importantly, modeling such effects provides an opportunity to validate 4D seismic data processing workflows.

Modeling marine vibrator data in the presence of a time-varying sea surface requires an MFD approach to ensure accuracy and numerical stability when the seismic wavefield interacts with the time-varying free surface. MFD operators, as opposed to Taylor-based coefficients, provide a uniform high-order accuracy throughout the modeling domain. Inaccurate implementation of the FSBC introduces numerical artifacts, making the numerical

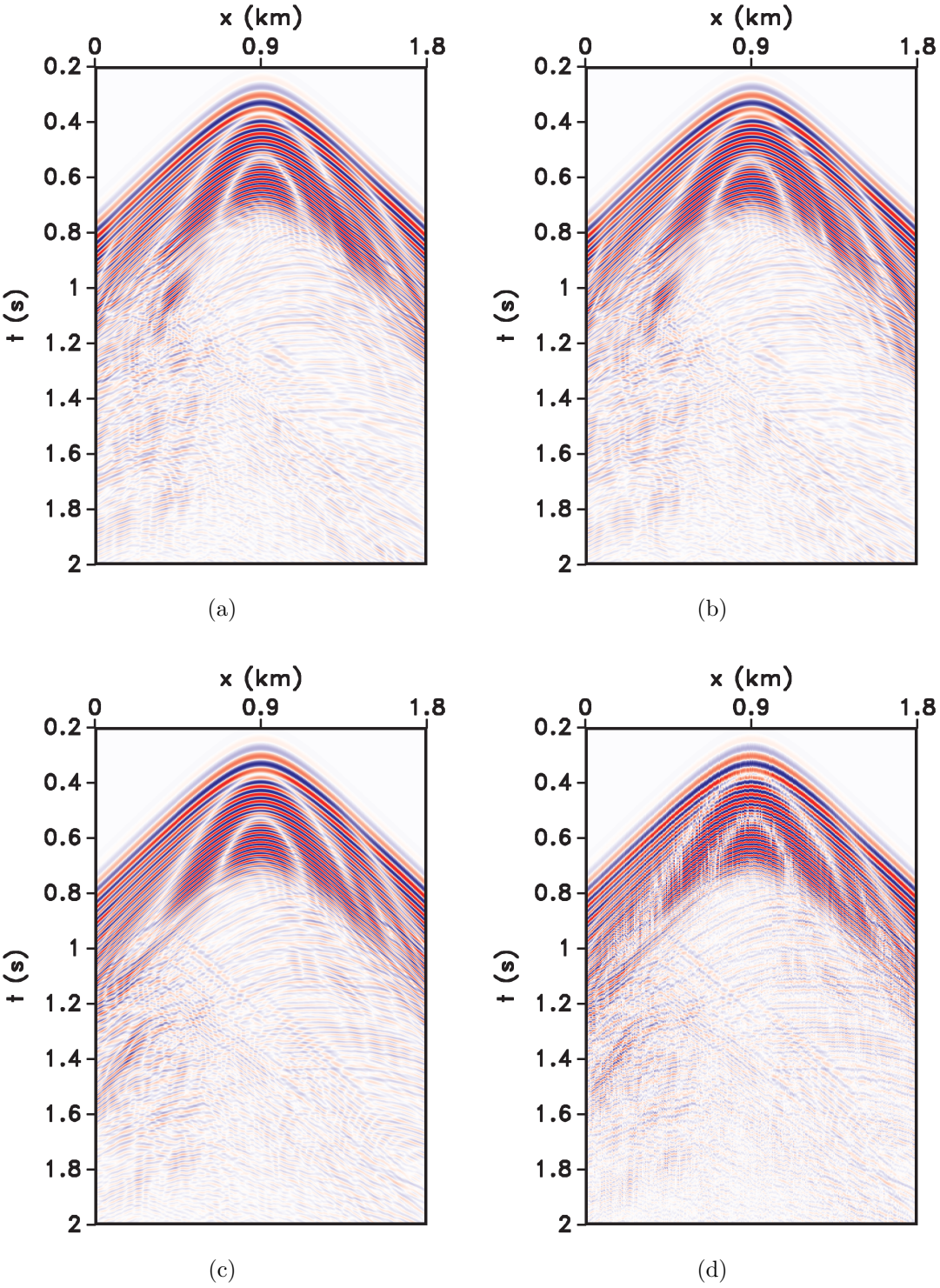

Figure 4.8 Shot gathers for (a) flat and (b) rough sea surface with ±5 m SWH, and receiver gathers for (c) flat and (d) rough sea surface with ±5 m SWH. The effects of a realistic rough sea surface is more noticeable in the common-gather domain than the common-shot domain.

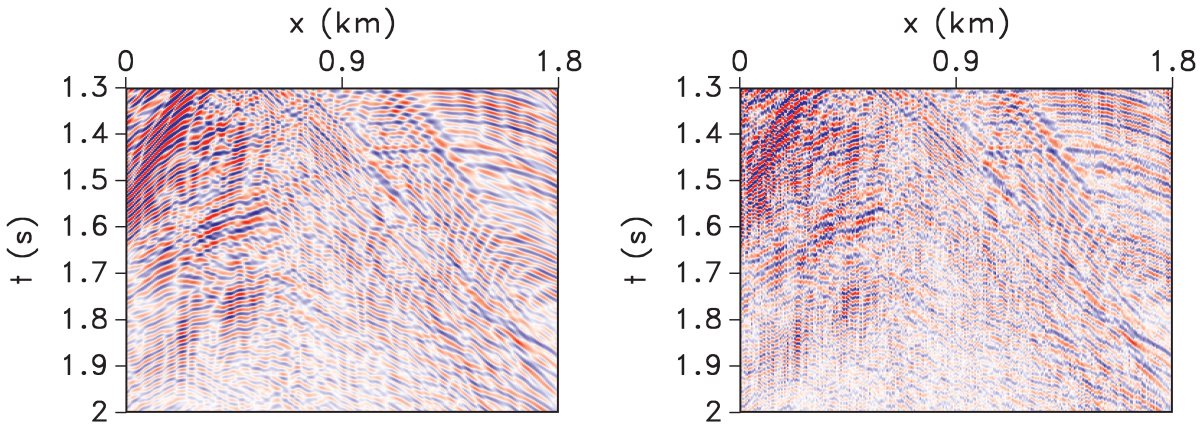

Figure 4.9 Time window of common-receiver gathers simulated using a moving source with (a) flat and (b) rough sea surface with ±5 m SWH. A rough sea surface introduces trace-to-trace jitter in the common-receiver domain because of the variable source depth from one source point to the next.

scheme unstable (Konuk and Shragge, 2020). In addition, using an MFD scheme provides required wavefield samples to compute cross-derivative terms; otherwise, it would require expensive high-order wavefield interpolation when using an SSG scheme.

Modeling the time-dependent tensorial AWE in a generalized coordinate system requires repeated interpolation of the subsurface physical properties (defined in Cartesian coordinates) to conform to the time-varying mesh grid. To preclude that requirement, we introduce depth-dependent decaying factors to confine the mesh deformation to the homogeneous water layer, making the two coordinate systems identical below the ocean-bottom level. An advantage of such an approach is that the wavefield can be sampled at and below the receivers level without a need to interpolate it back to Cartesian coordinates.

4.6 Conclusions

We present a finite-difference approach to model the full acoustic wavefield triggered by a moving source in the presence of a time-varying sea surface. The developed approach employs a time-dependent coordinate transformation to solve the tensorial acoustic wave equation

on a uniformly spaced and time-invariant computational domain. Although we assume the source moves at a constant velocity and depth level, incorporating a variable source velocity and depth is straightforward. This work is not limited to modeling marine vibrator data, but can also model towed-streamer data.

The numerical examples demonstrate that the effects of a time-varying sea surface can be clearly observed in the shot domain for an exaggerated sea state. However, the effects of a realistic time-varying sea surface on seismic data are hardly visible in the shot domain, but clearly visible in the common-receiver domain. The sea-surface effects can have consequences on seismic data processing and imaging, and on subsequent seismic data interpretation and attribute analyses. The developed approach provides a tool to validate marine vibrator data processing and understand the consequences of a moving source and time-varying sea surface on seismic imaging and inversion.

4.7 Acknowledgments

The first author would like to thank Saudi Aramco for graduate study sponsorship. We thank the sponsors of the Center for Wave Phenomena at Colorado School of Mines for the support of this research. We also thank A. Guitton (TotalEnergies) and T. Konuk (Nvidia) for many useful discussions, and Bia Villas Bôas (Colorado School of Mines) for her help with the sea surface modeling. Reproducible numerical examples were generated using the Madagascar open-source software package freely available from `http://www.ahay.org`. Analytic coordinate system geometry results were verified using the Mathematica software package from `https://www.wolfram.com/mathematica/`.

4.8 Data and materials availability

Data associated with this research are available and can be obtained by contacting the corresponding author.

4.9 APPENDIX: Taylor-based coefficients to approximate advection terms

The 1D Taylor-based differential operators we use to approximate the advection terms in equation 4.16 are

$$\frac{1}{840}\begin{bmatrix} -1750 & 3360 & -2520 & 1120 & -210 & 0 & \cdots & \cdots & \cdots \\ -210 & -700 & 1260 & -420 & 70 & 0 & \cdots & \cdots & \cdots \\ 70 & -560 & 0 & 560 & -70 & 0 & \cdots & \cdots & \cdots \\ 0 & 70 & -560 & 0 & 560 & -70 & 0 & \cdots & \cdots \\ \vdots & \ddots & \ddots & \ddots & \ddots & \ddots & \ddots & \ddots & \vdots \\ \cdots & \cdots & 0 & 70 & -560 & 0 & 560 & -70 & 0 \\ \cdots & \cdots & \cdots & 0 & 70 & -560 & 0 & 560 & -70 \\ \cdots & \cdots & \cdots & 0 & -70 & 420 & -1260 & 700 & 210 \\ \cdots & \cdots & \cdots & 0 & 210 & -1120 & 2520 & -3360 & 1750 \end{bmatrix}$$

and

$$\frac{1}{840}\begin{bmatrix} -2816 & 3675 & -1225 & 441 & -75 & 0 & \cdots & \cdots & \cdots \\ -768 & 140 & 840 & -252 & 40 & 0 & \cdots & \cdots & \cdots \\ 256 & -840 & 140 & 504 & -60 & 0 & \cdots & \cdots & \cdots \\ 0 & 70 & -560 & 0 & 560 & -70 & 0 & \cdots & \cdots \\ \vdots & \ddots & \ddots & \ddots & \ddots & \ddots & \ddots & \ddots & \vdots \\ \cdots & \cdots & 0 & 70 & -560 & 0 & 560 & -70 & 0 \\ \cdots & \cdots & \cdots & 0 & 60 & -504 & -140 & 840 & -256 \\ \cdots & \cdots & \cdots & 0 & -40 & 252 & -840 & -140 & 768 \\ \cdots & \cdots & \cdots & 0 & 75 & -441 & 1225 & -3675 & 2816 \end{bmatrix},$$

which we use to update the pressure wavefield at full- and half-integer grids, respectively. The coefficients of the differential operators are computed for a five-point stencil using the method developed by Fornberg (1988).

CHAPTER 5

REVERSE-TIME MIGRATION OF MARINE VIBRATOR DATA

A paper submitted to *Geophysics*[1].

Khalid Almuteri[2,3,4], Paul Sava[5], and Jeffrey Shragge[5]

Marine vibrators are viable alternatives to seismic air guns in ocean-bottom acquisition due to their less adverse impact on the environment, their ability to generate more lower frequency content, and their suitability for simultaneous acquisition. However, mobile marine vibrators introduce a unique set of processing and imaging challenges for ocean-bottom acquisition, the main examples of which are the Doppler effect and the time-dependent source-receiver offsets, which are not features of conventional marine acquisition. Standard seismic data processing and imaging techniques assume stationary sources and are not fully suitable for mobile marine vibrator data without modification. Not accounting for source motion in seismic imaging introduces phase change and mispositioning of imaged structures. Further, ignoring source motion effects in imaging workflow may lead to the estimation of inaccurate migration velocity models or imply the use of incorrect migration velocity, e.g., in seismic-to-well ties. We develop a reverse-time migration (RTM) approach that accounts for the source-motion effects and is capable of producing accurate subsurface images, closely matching stationary acquisition and imaging results. Synthetic examples illustrate the ability of the proposed method to construct accurate subsurface RTM images even for source velocities higher than are commonly used in typical marine acquisition. Our approach is not limited to imaging mobile marine vibrator data in ocean-bottom acquisition, but is also applicable to mobile streamer data using marine vibrators or seismic air-gun sources.

[1]Reprinted with permission of *Geophysics*.

[2]Graduate student, Center for Wave Phenomena, Department of Geophysics, Colorado School of Mines
[3]Saudi Aramco
[4]Author for correspondence
[5]Professor, Center for Wave Phenomena, Department of Geophysics, Colorado School of Mines.

5.1 Introduction

Conventional marine impulsive sources (i.e., air guns) raise concerns over their impact on marine ecosystems, renewing an interest in environmentally less adverse marine vibrators as viable alternatives (Laws et al., 2019). However, marine vibrators are not only attractive for their low environmental impact, but also advantageous from an exploration point of view because they provide data with lower frequencies compared to those acquired using air guns (Guitton et al., 2021). Further, by blending phase-encoded sources, marine vibrators facilitate simultaneous acquisition (Laws et al., 2019), reducing acquisition time, which is more challenging to achieve using conventional air guns (e.g., Wason and Herrmann, 2013). However, because marine vibrators are in continuous motion and have a long sweep duration, they introduce Doppler and time-dependent source-receiver offset effects in ocean-bottom acquisition. Therefore, source motion creates new processing and imaging challenges unique to such acquisition scenarios.

Conventional seismic imaging techniques assume stationary sources or negligible source motion. One such technique is reverse-time migration (RTM) (Baysal et al., 1983; McMechan, 1983; Whitmore, 1983). The concept of RTM follows the Claerbout (1971) imaging principle: a reflector exists at a point (x, y, z) in space where a forward-propagating source wavefield and a backward-propagating receiver wavefield coincide in time. RTM requires the simultaneous availability of source and receiver wavefields to perform wavefield matching through an imaging condition. Neglecting source-motion effects in RTM can introduce artifacts in the final image or inaccuracies in phase and position of imaged structure (Guitton et al., 2021).

In this paper, we present a solution to account for source-motion effects in seismic wavefields. We compute the wavefields required by RTM using the acoustic wave equation (AWE) in a generalized coordinate system that takes into account source motion effects. Our approach uses coordinate transformations to map the physical domain tracking the moving source, to a regular fixed computational domain, enabling modeling wavefields triggered by moving sources. We demonstrate that such an approach produces accurate subsurface images

as if the acquisition were conducted using stationary sources. This computational strategy thus enables the widespread use of marine vibrator sources for high-end techniques like RTM and full-waveform inversion.

5.2 Theory

In this section, we derive the generalized second-order AWE that can model the seismic wavefield triggered by a moving source. We do this by employing a tensorial approach to transform the time-varying physical Cartesian coordinate system $\mathbf{x}$ into a static generalized coordinate system $\boldsymbol{\xi}$ that represents a uniform computational mesh. We also formulate the RTM imaging approach, including the imaging condition. We formulate the associated forward and adjoint operators of the derived AWE in a generalized coordinate system in Appendix 5.9.1 and derive the Born modeling source term in Appendix 5.9.2.

5.2.1 Tensorial AWE

The AWE in a generalized coordinate system defined by the variables $\boldsymbol{\xi} = [\xi^0, \xi^1, \xi^2, \xi^3]$ (Konuk and Shragge, 2020) is

$$\Box_\xi P_\xi = F_\xi, \tag{5.1}$$

where $\Box_\xi$ is the generalized d'Alembert operator, P_ξ is the pressure field, and F_ξ is the source function. The ξ^0 coordinate is a time-like axis (time scaled by medium velocity) and (ξ^1, ξ^2, ξ^3) are space-like components. The generalized coordinate system $\boldsymbol{\xi}$ is related to a Cartesian physical domain defined by $\boldsymbol{x} = [x^0, x^1, x^2, x^3] = [ct, x, y, z]$ through one-to-one mappings $\boldsymbol{x} = \boldsymbol{x}(\boldsymbol{\xi})$ and $\boldsymbol{\xi} = \boldsymbol{\xi}(\boldsymbol{x})$. The generalized d'Alembert operator is

$$\Box_\xi = \frac{-1}{\sqrt{|\boldsymbol{g}|}} \frac{\partial}{\partial \xi^\mu} \left(\sqrt{|\boldsymbol{g}|} g^{\mu\nu} \frac{\partial}{\partial \xi^\nu} \right), \; \mu, \nu = 0, 1, 2, 3, \tag{5.2}$$

where $[g^{\mu\nu}]$ is a contravariant metric tensor defined as the inverse of a covariant metric tensor $[g_{\mu\nu}]$ whose elements are

$$g_{\mu\nu} = \frac{\partial x^i}{\partial \xi^\mu} \frac{\partial x^i}{\partial \xi^\nu} \quad \text{for} \quad i, \mu, \nu = 0, 1, 2, 3, \tag{5.3}$$

and $|\boldsymbol{g}|$ is the determinant of $[g_{\mu\nu}]$. Note that repeated indices in equation 3.3 imply summation. In a Cartesian coordinate system the generalized d'Alembert operator (equation 5.2) reduces to

$$\Box = \frac{-1}{c^2}\frac{\partial^2}{\partial t^2} + \nabla^2, \tag{5.4}$$

where $c(x, y, z)$ is the Cartesian medium velocity and ∇^2 is the Cartesian Laplacian operator.

To model wavefields excited by a moving source, we define a coordinate transformation that maps a horizontally deformed physical domain to a regular computational domain. The deformation in the physical domain is introduced to track the source movement and defined to be depth dependent; thus, the deformation is space and time dependent. To define such a coordinate transformation, we make assumptions (i.e., the source moves along the x^1-axis at a constant depth and velocity in a homogeneous medium), which allow us to express the relationship between the $\boldsymbol{\xi}$- and $\boldsymbol{x}$-coordinate systems as

$$\begin{bmatrix} x^0 \\ x^1 \\ x^2 \\ x^3 \end{bmatrix} = \begin{bmatrix} \xi^0 \\ \xi^1 + \frac{v}{c}\xi^0 e^{\gamma(s_z-\xi^3)} \\ \xi^2 \\ \xi^3 \end{bmatrix} = \begin{bmatrix} c\tau \\ \xi^1 + v\tau e^{\gamma(s_z-\xi^3)} \\ \xi^2 \\ \xi^3 \end{bmatrix}, \tag{5.5}$$

where v is the source velocity, γ is a user-defined decay factor that controls the amount of horizontal deformation as a function of depth (to confine the deformation to the homogeneous water layer), s_z is the source depth, and $\xi^0 = c\tau$ where $\tau = t$. Note that t and τ are the time axis in the Cartesian and generalized coordinate systems, respectively. Therefore, the second-order AWE for a deformed source-tracking mesh is

$$\begin{aligned} \frac{1}{c^2}\frac{\partial}{\partial\tau}\left(\frac{\partial P_\xi}{\partial\tau}\right) = \frac{2v\alpha}{c^2}\frac{\partial}{\partial\xi^1}\left(\frac{\partial P_\xi}{\partial\tau}\right) + \left[\gamma^2\tau^2v^2\alpha^2 - \frac{v^2\alpha^2}{c^2}\right]\frac{\partial}{\partial\xi^1}\left(\frac{\partial P_\xi}{\partial\xi^1}\right) \\ - \gamma^2\tau v\alpha\frac{\partial P_\xi}{\partial\xi^1} + 2\gamma\tau v\alpha\frac{\partial}{\partial\xi^1}\left(\frac{\partial P_\xi}{\partial\xi^3}\right) + \nabla^2_\xi P_\xi + F_\xi, \end{aligned} \tag{5.6}$$

where $\alpha = e^{\gamma(s_z-\xi^3)}$ and $\nabla^2_\xi = \frac{\partial}{\partial\xi^i}\left(\frac{\partial}{\partial\xi^i}\right)$, and where we assume the medium velocity is slowly varying (i.e., $\frac{\partial c}{\partial\xi^i} \approx 0$ for $i = 1, 2, 3$).

To avoid artificial reflections from the boundary region, we add a sponge layer with a damping term (Kosloff and Kosloff, 1986; Sochacki et al., 1987) to equation 5.6 such that

$$\begin{aligned}\frac{1}{c^2}\frac{\partial}{\partial\tau}\left(\frac{\partial P_\xi}{\partial\tau}\right) = \frac{2v\alpha}{c^2}\frac{\partial}{\partial\xi^1}\left(\frac{\partial P_\xi}{\partial\tau}\right) + \left[\gamma^2\tau^2v^2\alpha^2 - \frac{v^2\alpha^2}{c^2}\right]\frac{\partial}{\partial\xi^1}\left(\frac{\partial P_\xi}{\partial\xi^1}\right) \\ - \gamma^2\tau v\alpha\frac{\partial P_\xi}{\partial\xi^1} + 2\gamma\tau v\alpha\frac{\partial}{\partial\xi^1}\left(\frac{\partial P_\xi}{\partial\xi^3}\right) + \nabla^2_\xi P_\xi - \eta\frac{\partial P_\xi}{\partial\tau} + F_\xi,\end{aligned} \tag{5.7}$$

where η is a damping factor that is zero inside the modeling domain and increasing away from it.

5.2.2 Reverse-time migration

We can define seismic data modeled in generalized coordinates due to a moving source $\mathbf{d}_x$ as

$$\mathbf{d}_x = \mathbf{D}\mathbf{S}_x\mathbf{L}_\xi\mathbf{m}, \tag{5.8}$$

where $\mathbf{m}$ is an image (or estimated reflectivity) of the subsurface, $\mathbf{L}_\xi$ is the generalized demigration operator, $\mathbf{S}_x$ is a mapping operator from the generalized to the Cartesian coordinate system, and $\mathbf{D}$ is the data acquisition (or extractor) operator. For ocean-bottom acquisition and a judicious choice of the parameter γ, $\mathbf{D}\mathbf{S}_x \approx \mathbf{D}$ and no interpolation to Cartesian coordinates is required because the second term on the right-hand side of equation 5.5 will be negligible. One can reconstruct a subsurface image using the adjoint operators $\mathbf{L}^\dagger_\xi$ and $\mathbf{D}^\dagger$ such that

$$\mathbf{m} = \mathbf{L}^\dagger_\xi\mathbf{D}^\dagger\mathbf{d}_x, \tag{5.9}$$

where $\mathbf{D}^\dagger$ is an injector operator, and $\mathbf{L}^\dagger_\xi$ is the migration operator. The migration operator $\mathbf{L}^\dagger_\xi$ backpropagates (processed) recorded data $\mathbf{d}_x$, computes the receiver wavefield $\mathbf{U}_r$, and applies an imaging condition that involves the source wavefield $\mathbf{U}_s$ given by

$$\mathbf{U}_s = \mathbf{S}_x\mathbf{L}_\xi\mathbf{m}. \tag{5.10}$$

Assuming ocean-bottom acquisition where receivers are stationary, one can compute the receiver wavefield using a Cartesian finite-difference AWE solver. In the case of ocean-bottom acquisition, and again with a judicious choice of γ, many terms in the generalized AWE will be negligible (i.e., produces no significant wavefield contribution). Ignoring these terms reduces equation 5.6 to the Cartesian-based AWE; thus, one only needs to solve the AWE in a generalized coordinate system to compute the source wavefield in RTM.

To construct a subsurface image, one needs to use an imaging condition to compare the source and receiver wavefields. A common imaging condition is the zero-lag cross-correlation, which is suitable for data acquired using impulsive sources (e.g., air guns). However, for long-duration sources (e.g., marine vibrators), the zero-lag cross-correlation imaging condition produces images with strong artifacts. Alternatively, the deconvolution imaging condition improves seismic resolution (Poole et al., 2010), making it a more suitable imaging condition for long-duration sweeps. A frequency-domain deconvolution imaging condition is

$$\mathbf{m}(x,y,z) = \Re\left[\sum_e \sum_\omega \frac{\overline{\mathbf{U}}_s \mathbf{U}_r}{\overline{\mathbf{U}}_s \mathbf{U}_s + \epsilon}\right], \tag{5.11}$$

where $\overline{\mathbf{U}}_s(x,y,z,\omega)$ is the complex conjugate of $\mathbf{U}_s(x,y,z,\omega)$, ϵ is a stabilization factor to avoid division by zero, and summation is over different frequencies (ω) and experiments (e).

5.3 Numerical Example

In this section, we present numerical examples to demonstrate the effectiveness of our imaging approach and investigate the magnitude of mispositioning of imaged structures when source motion effects are ignored in RTM. In our investigation, we consider the consequences of source motion direction, sweep duration, and the image structure on the magnitude of mispositioning.

5.4 Marmousi model

To illustrate the effectiveness of our imaging approach, we run a test using a subset of the Marmousi II model (Figure 5.1). We simulate stationary and mobile datasets using the

acquisition parameters given in Table Table 5.1. For moving source acquisition, we use a source boat velocity of 15 m/s, which is faster than typical $2-3$ m/s of conventional marine acquisition. This is done to highlight the significance of source motion on seismic imaging as well as the ability of our method to accurately image the subsurface under an unrealistically high source velocity.

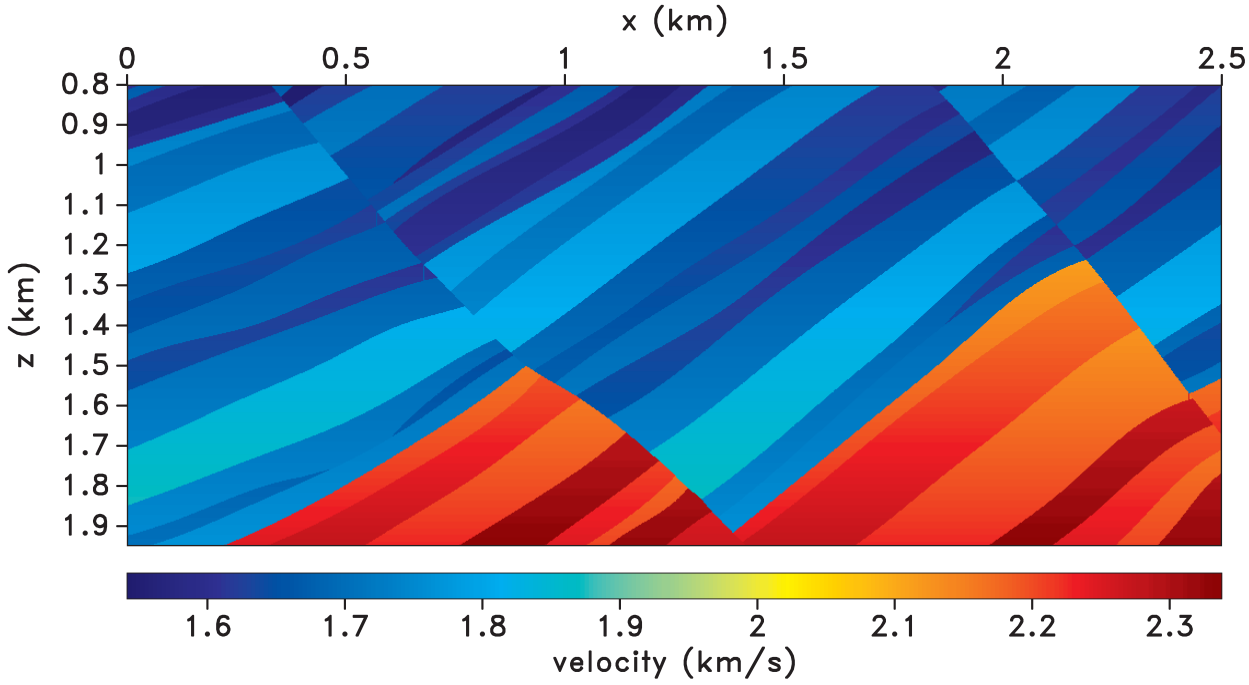

(a)

Figure 5.1 Marmousi II velocity submodel (quantity c in equation 5.7) used to validate the developed RTM imaging framework.

Figure 5.2 shows the RTM image generated using stationary acquisition and imaging, which we consider as the reference case. Figure 5.3(a) shows the RTM image of moving-source acquisition and stationary imaging, ignoring source motion effects. At first glance the RTM results look similar; however, the difference between (1) stationary acquisition and imaging and moving sources acquisition and (2) stationary imaging (Figure 5.3(b)) shows a phase change and mispositioning of imaged structures. These observations are consistent with those reported in Guitton et al. (2021). Taking vertical profiles from the two RTM results at $x^1 = 1.25$ km (Figure 5.4), clearly shows that ignoring source-motion effects in imaging

Table 5.1 Moving source acquisition parameters for the Marmousi example.

parameter	value
sweep duration	1 s
listening time	2 s
total time	3 s
sweep type	linear
minimum frequency	20 Hz
maximum frequency	40 Hz
source depth	12.5 m
source xmin	50 m
source xmax	2450
source interval	25 m
source velocity	15 m/s
receiver depth	600 m
receiver xmin	25 m
receiver xmax	2475 m
receiver spacing	2.5 m

also affects the amplitude of imaged structures. Such issues could falsely imply an erroneous velocity model, inaccurate source and/or receiver coordinate positioning, or a combination of both.

Taking source motion into consideration when computing the source wavefield (i.e., using a moving imaging procedure) produces an image (Figure 5.5(a)) that closely matches that obtained from the stationary acquisition and imaging, with negligible discrepancies between the two results (Figure 5.5(b)). However, the two images are not identical for two potential reasons. First, the source wavefield in the moving source acquisition is influenced by the Doppler effect due to the source motion, whereas the source wavefield in the stationary source acquisition case is free of such effect; thus, the frequency bandwidth changed between the two acquisition scenarios (Figure 5.6), in principle changing the seismic resolution. However, given

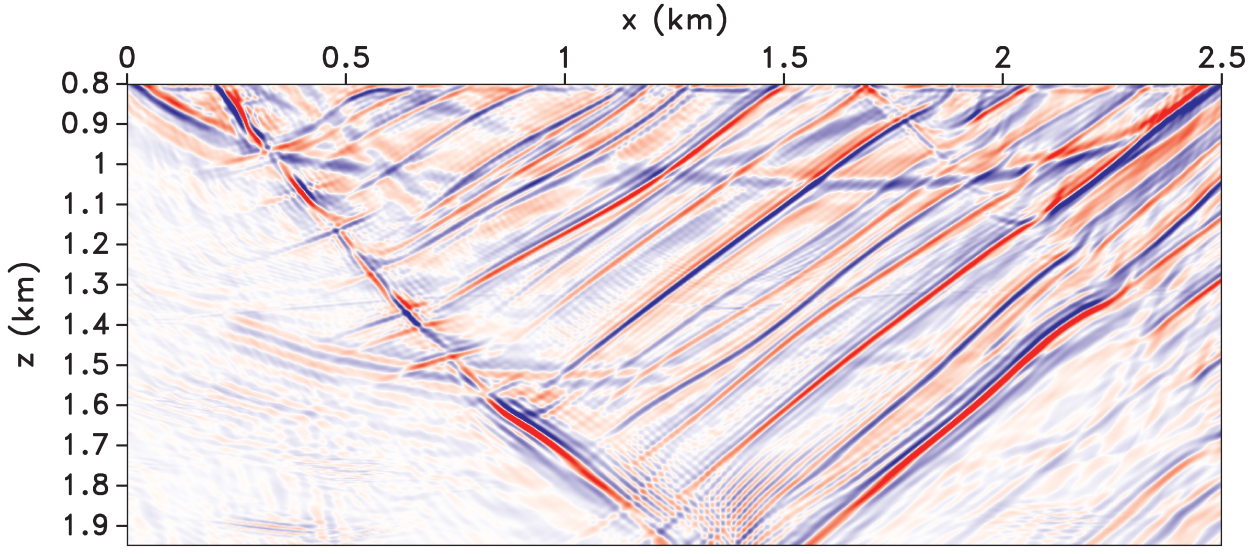

(a)

Figure 5.2 Reference RTM image for stationary acquisition and imaging.

the relatively slow source velocity compared the acoustic medium velocity (two-to-three orders of magnitude for our choice of acquisition parameters), the Doppler effect is an irrelevant reason and should not contribute significantly to the discrepancies between the two RTM images. Second, the subsurface is illuminated differently in the two acquisitions, which makes the recorded data different between the two acquisition geometries (e.g., different amplitude-versus-angle for different frequencies). Therefore, different portions of the wavefield are recorded by the two acquisitions, which we assert is the primary reason for the discrepancies between the two RTM images. Figure 5.7 shows vertical profiles at $x^1 = 1.25$ km from (1) stationary acquisition and imaging and (2) mobile acquisition and imaging. The two profiles closely match in amplitude and phase, demonstrating the robustness of our approach to imaging marine vibrator data, even for data acquired using a high source velocity.

To quantify the magnitude of image mispositioning, we use optical flow estimation (Pérez et al., 2013; Wedel et al., 2009; Zach et al., 2007) to determine the displacement vector field of each point in the subsurface between the RTM image generated using stationary acquisition and imaging (Figure 5.2) and the RTM image of moving-source acquisition and stationary

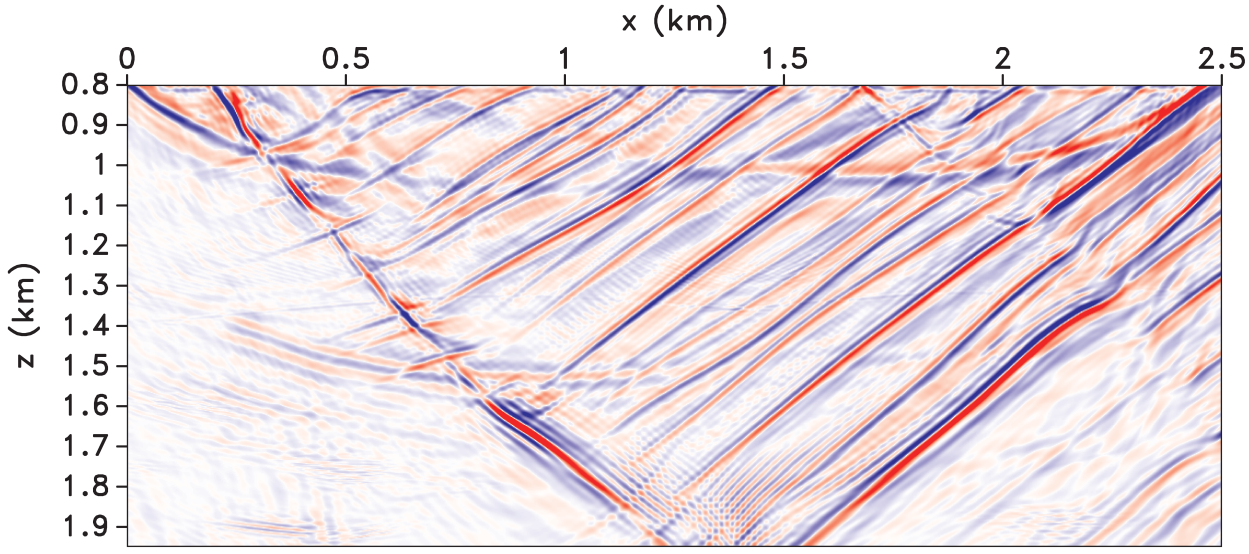

(a)

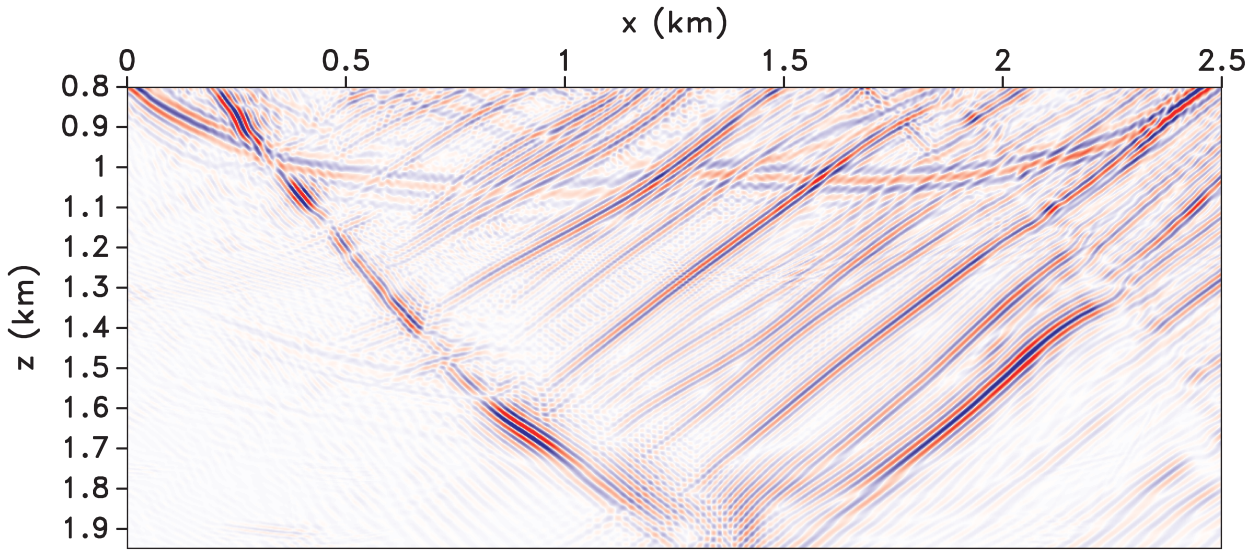

(b)

Figure 5.3 (a) RTM image for mobile acquisition and stationary imaging. (b) Difference image between Figure 5.2 and Figure 5.3(a). The difference image shows phase change and mispositioning of imaged structures ignoring source-motion effects in imaging.

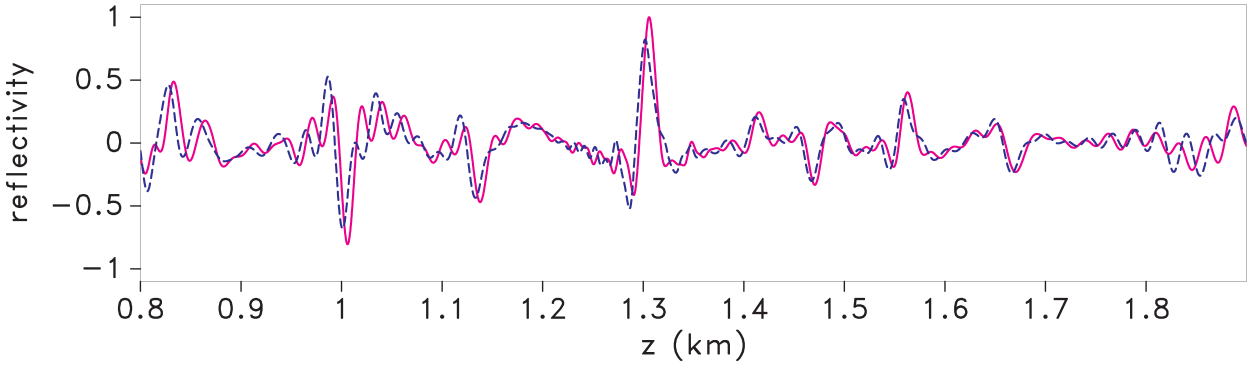

(a)

Figure 5.4 Vertical profiles at $x^1 = 1.25$ km (solid curve) from stationary acquisition and imaging (Figure 5.2), and (dashed curve) from mobile acquisition and stationary imaging (Figure 5.3(a)). The vertical profiles clearly illustrate the changes in phase and amplitude as a result of ignoring source-motion effects in imaging.

imaging (Figure 5.3(a)). This vector field can be used in image warping (e.g., Glasbey and Mardia, 1998) to kinematically correct the RTM image of moving-source acquisition and stationary imaging to structurally match the RTM image generated using stationary acquisition and imaging. Figure 5.8(a) shows the kinematic correction vector field overlaying the RTM image of moving-source acquisition and stationary imaging (Figure 5.3(a). To correct for source motion in the image domain, we would need to shift the imaged structures in the source motion direction. Figure 5.8(b) shows the magnitude of correction for each point in the RTM image. In this example, the shift magnitude is 3.1 m on average. Changing the source motion direction from right-going to left-going (from 15 m/s to -15 m/s) confirms that source motion direction plays a role in the imaged structures mispositioning in RTM. For a left-going source, we would need to shift the imaged structures by approximately 3.4 m to the left to correct for source motion effects in the RTM image (Figure 5.9).

5.5 Dipping reflectors model

To investigate the effects of sweep duration and imaged structure dip on the magnitude of mispositioning, we use a constant velocity of 1.5 km/s with four different-dipping reflectors (Figure 5.10). We simulate stationary and mobile datasets using the acquisition parameters

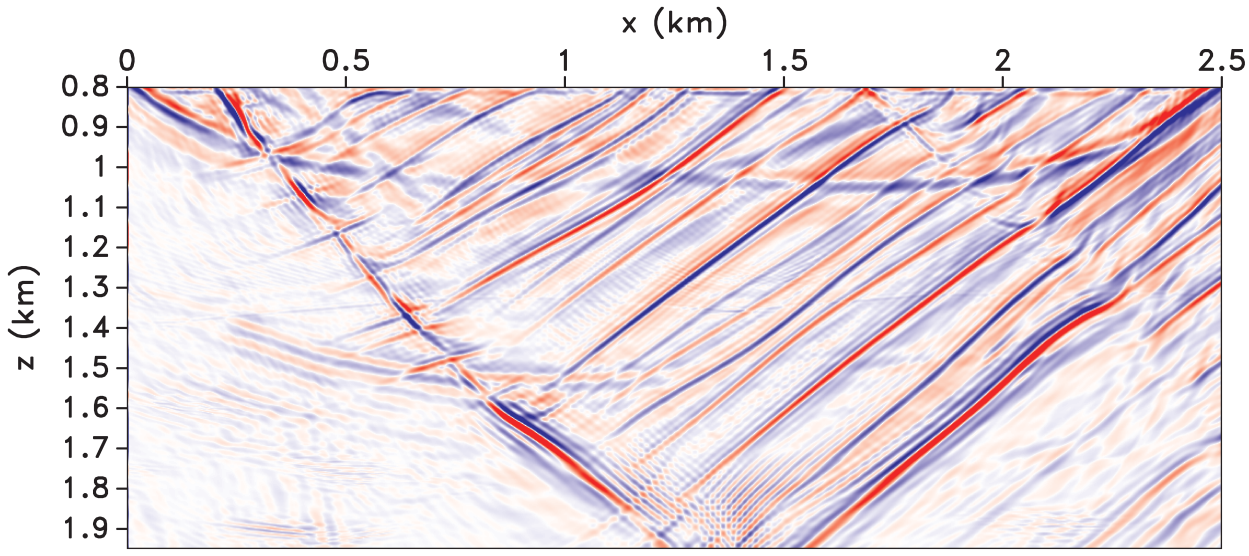

(a)

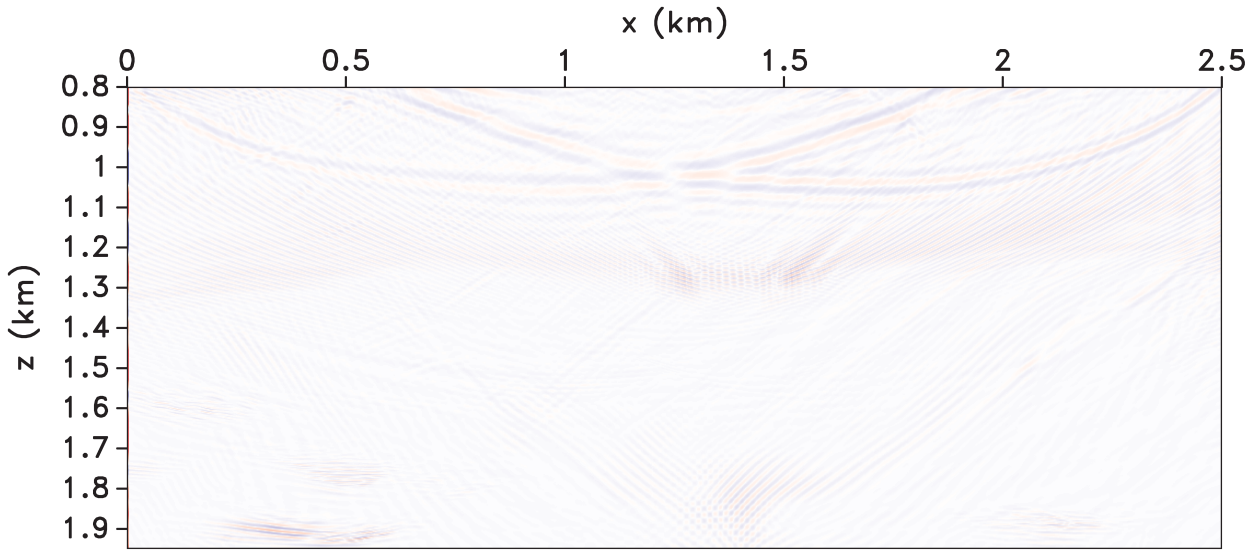

(b)

Figure 5.5 (a) RTM image for mobile acquisition and imaging. (b) Difference image between Figure 5.2 and Figure 5.5(a). The difference image shows that the developed approach can correctly account for source-motion effects and imaged structures are correctly positioned.

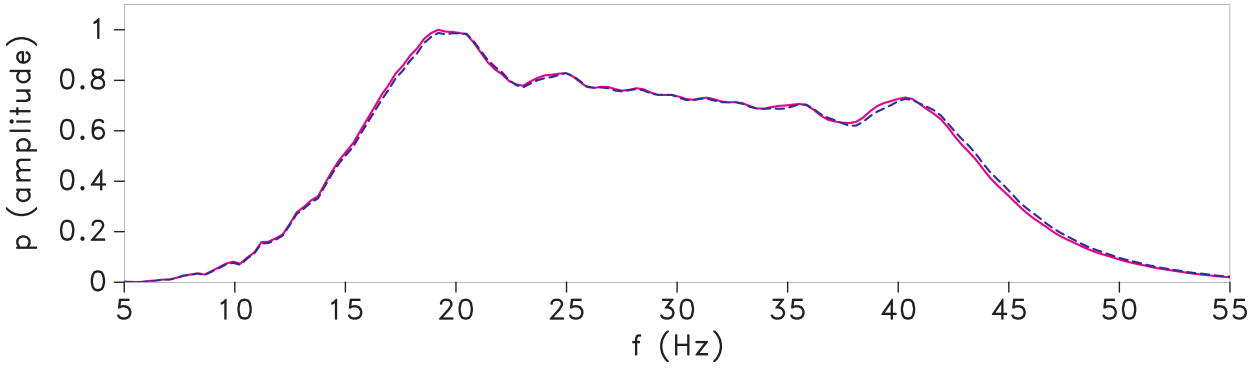

(a)

Figure 5.6 Magnitude spectra extracted from the source wavefield at $(x^1, x^3) = (1.25, 1.3)$ km (solid) from stationary acquisition and (dashed) from mobile acquisition. The frequency bandwidth change between the two acquisitions, although observable, is negligible.

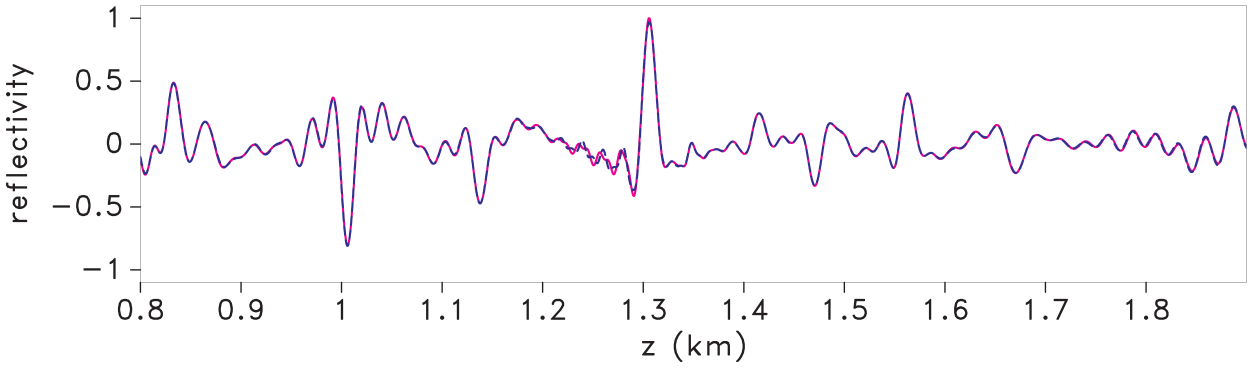

(a)

Figure 5.7 Vertical profiles at $x^1 = 1.25$ km (solid curve) from stationary acquisition and imaging (Figure 5.2), and (dashed curve) from mobile acquisition and imaging (Figure 5.5(a)). The vertical profiles from the two acquisition and imaging scenarios closely match, demonstrating the robustness of the developed approach to account for source motion effects in imaging.

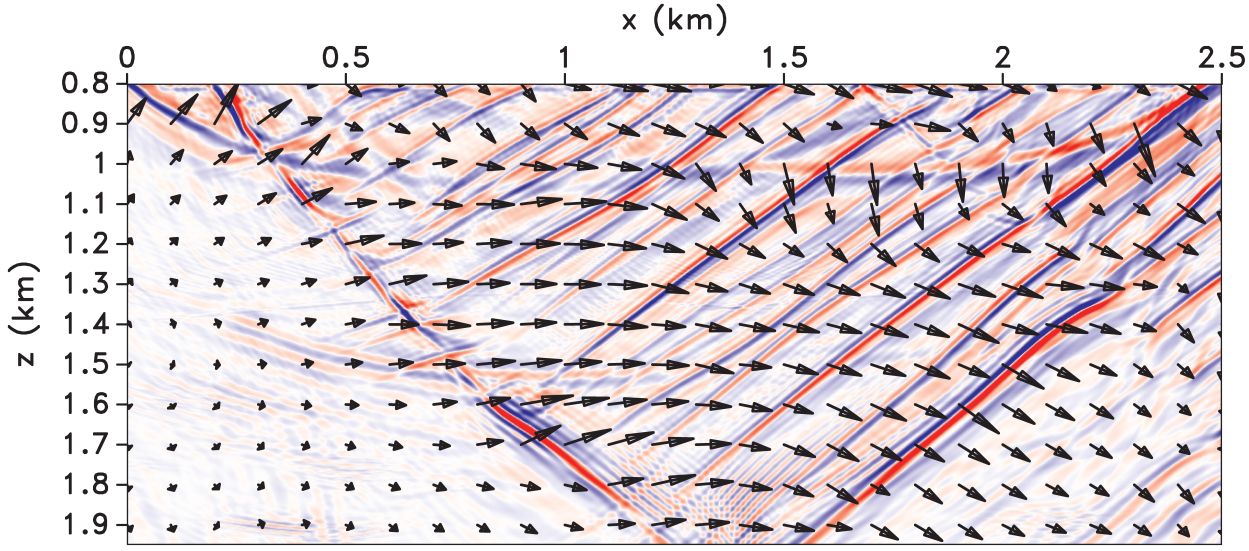

(a)

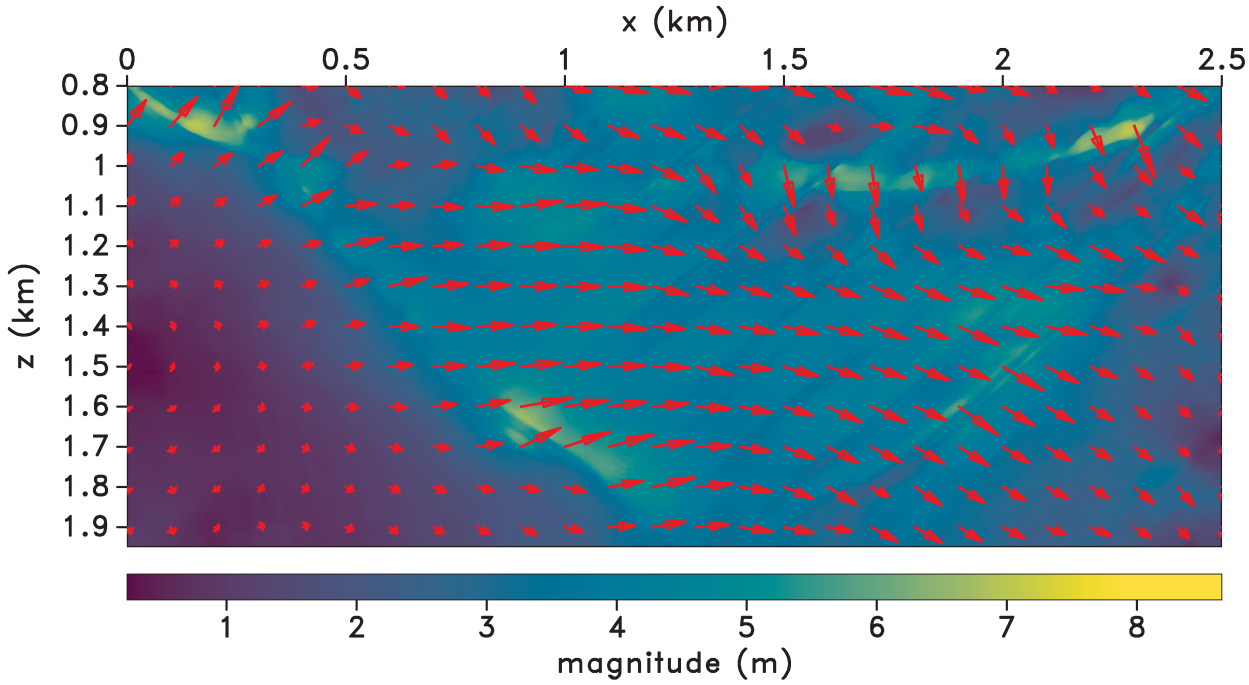

(b)

Figure 5.8 (a) Kinematic correction vector field overlaying the RTM image for mobile acquisition and stationary imaging for a right-going source. (b) Kinematic correction vector field overlaying the magnitude of the vector field. The kinematic correction vector field points toward the source motion direction.

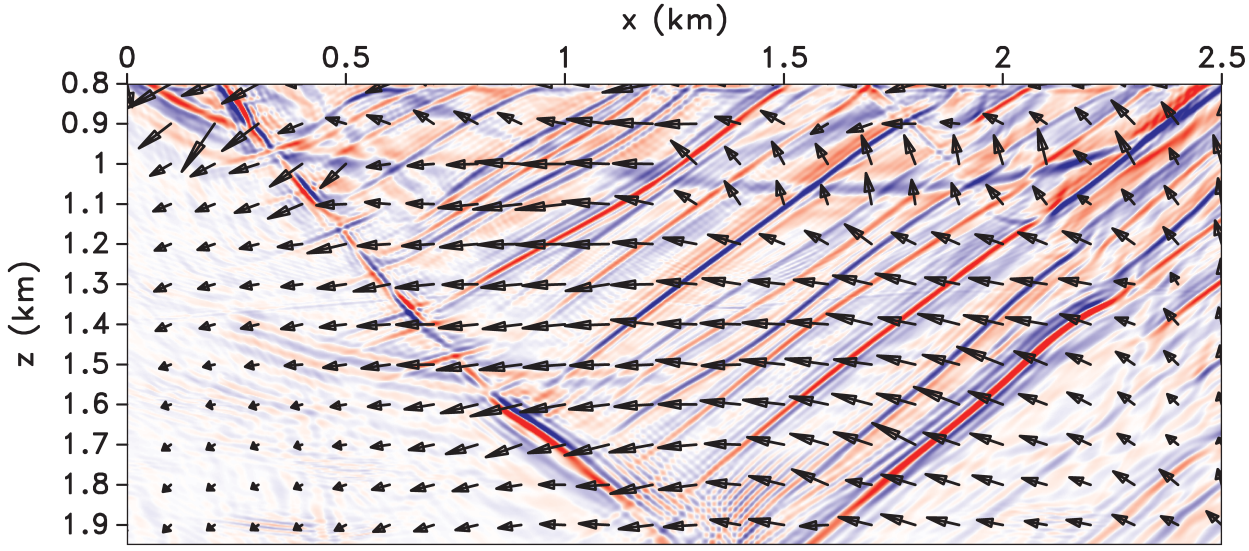

(a)

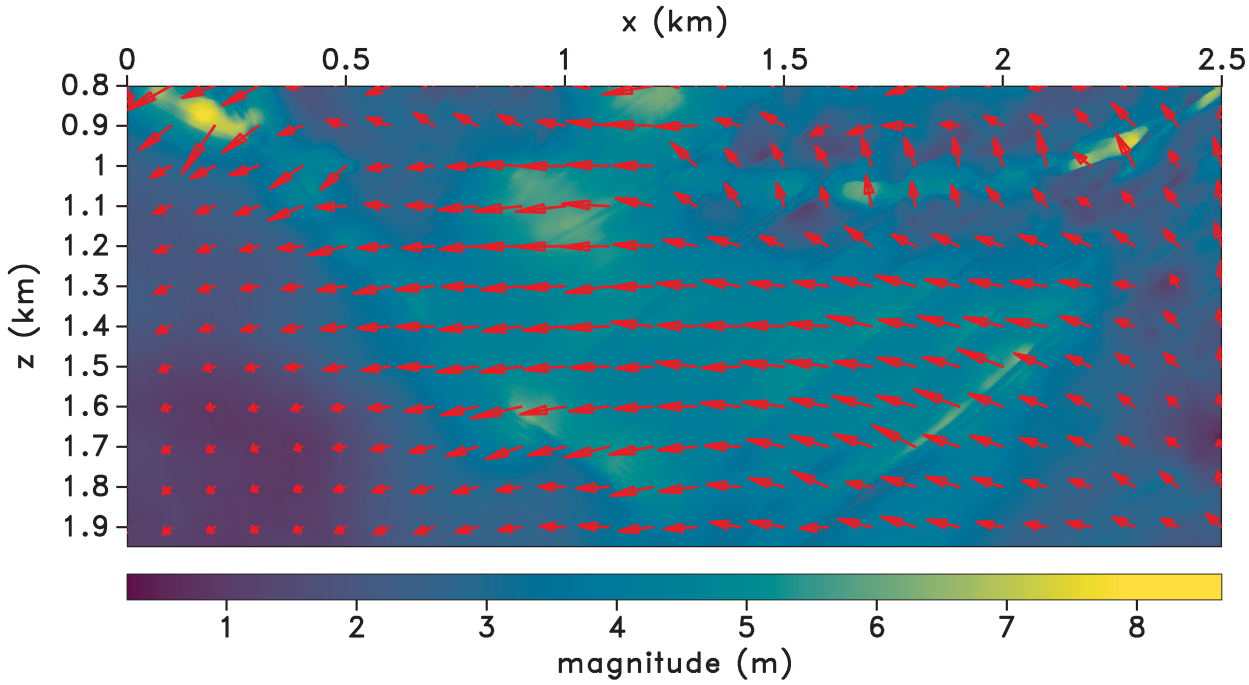

(b)

Figure 5.9 (a) Kinematic correction vector field overlaying the RTM image for mobile acquisition and stationary imaging for a left-going source. (b) Kinematic correction vector field overlaying the magnitude of the vector field. The kinematic correction vector field points toward the source motion direction.

given in Table Table 5.2. In the mobile acquisition scenario, we simulate moving-source data using a short- and long-duration sweep for 1 s and 6 s, respectively, and a 2 s listening time for both simulations. In the short-duration sweep, the source velocity is 15 m/s, i.e., the source moves 15 m while sweeping. However, in the long-duration sweep, the source velocity is 5 m/s, i.e., the source moves 30 m while sweeping.

Table 5.2 Moving source acquisition parameters for the dipping reflectors example.

parameter	value (short sweep)	value (long sweep)
sweep duration	1 s	6 s
listening time	2 s	2 s
total time	3 s	8 s
sweep type	linear	linear
minimum frequency	20 Hz	20 Hz
maximum frequency	40 Hz	40 Hz
source depth	12.5 m	12.5 m
source xmin	50 m	50 m
source xmax	2450	2450
source interval	25 m	25 m
source velocity	15 m/s	5 m/s
receiver depth	600 m	600 m
receiver xmin	25 m	25 m
receiver xmax	2475 m	2475 m
receiver spacing	2.5 m	2.5 m

Figure 5.11(a) shows the kinematic correction vector field when using a short-duration sweep. Similar to the Marmousi example (Figure 5.8 and Figure 5.9), the vector field points toward the source motion direction. In this case, the average amount of shifts required to correct the RTM image is 1.9 m (Figure 5.11(b)). However, for the long-duration sweep (Figure 5.12(a)), the average amount of shifts increases to 2.6 m (Figure 5.12(b)) because the source sweeps over a longer distance. In both cases, the horizontal reflector is the least

affected when ignoring source motion in imaging. The shift magnitude is more significant for shallow targets than deep targets. In addition, whereas the dip angle increases, the shift required to account for source motion in the image domain also increases. However, for the steeply dipping reflector (45°), the shift magnitude decreases, which is a result of poor illumination of the steeply dipping reflector.

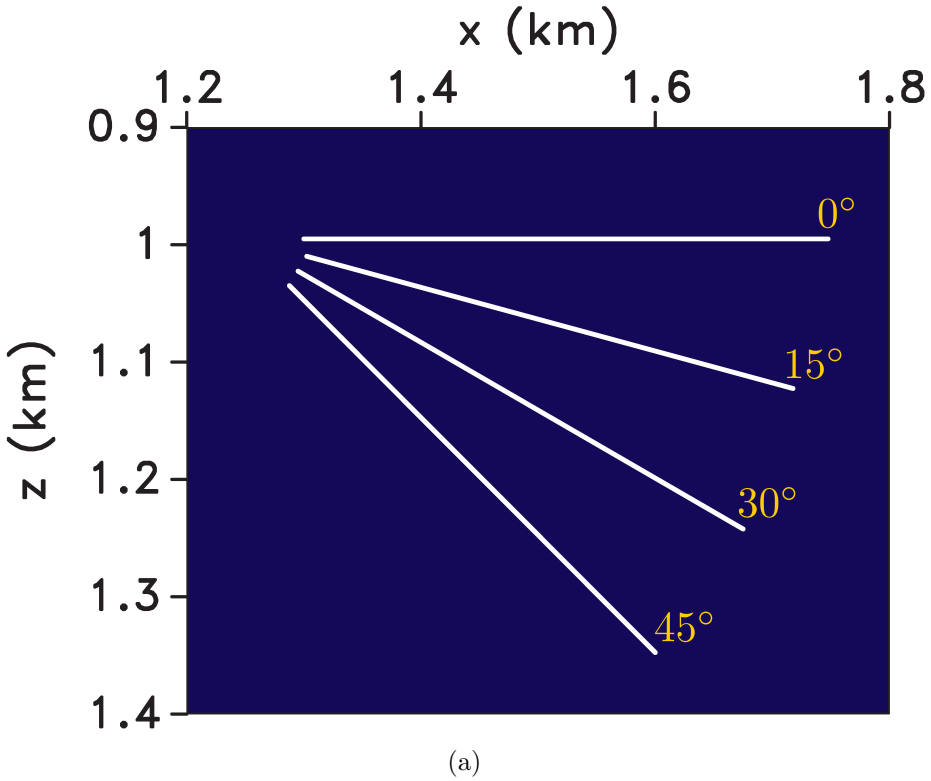

(a)

Figure 5.10 Dipping reflectors model used to investigate the effects of sweep duration and dipping angle on imaging marine vibrator data.

5.6 Discussion

As may be expected, neglecting the time-dependent source-receiver offsets in RTM produces erroneous subsurface images. For low source velocities, the Doppler effect is negligible, as predicted by Doppler (1842) theory, and the time-dependent source-receiver offsets is the primary reason for such erroneous imaging. Further, source motion during a non-impulsive source activation complicates velocity model building because neglecting source

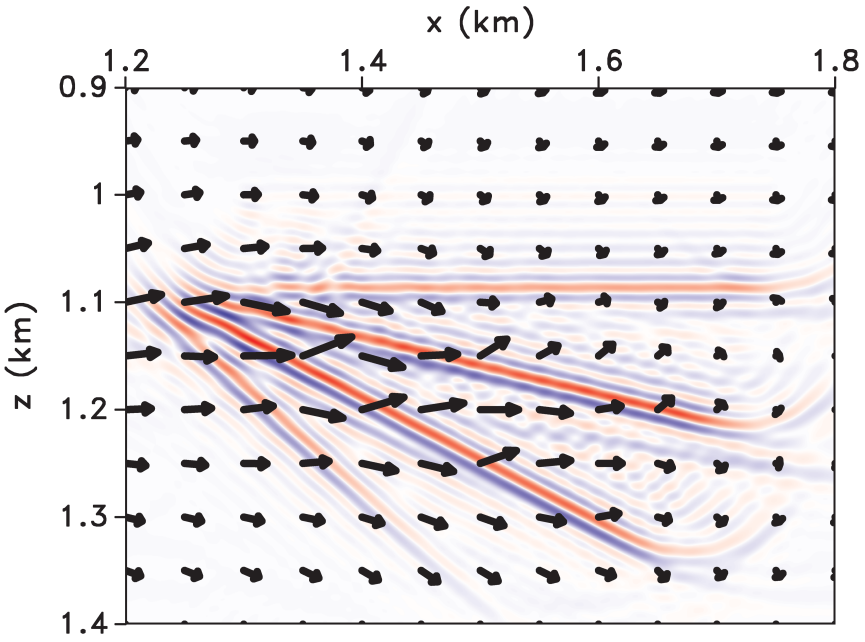

(a)

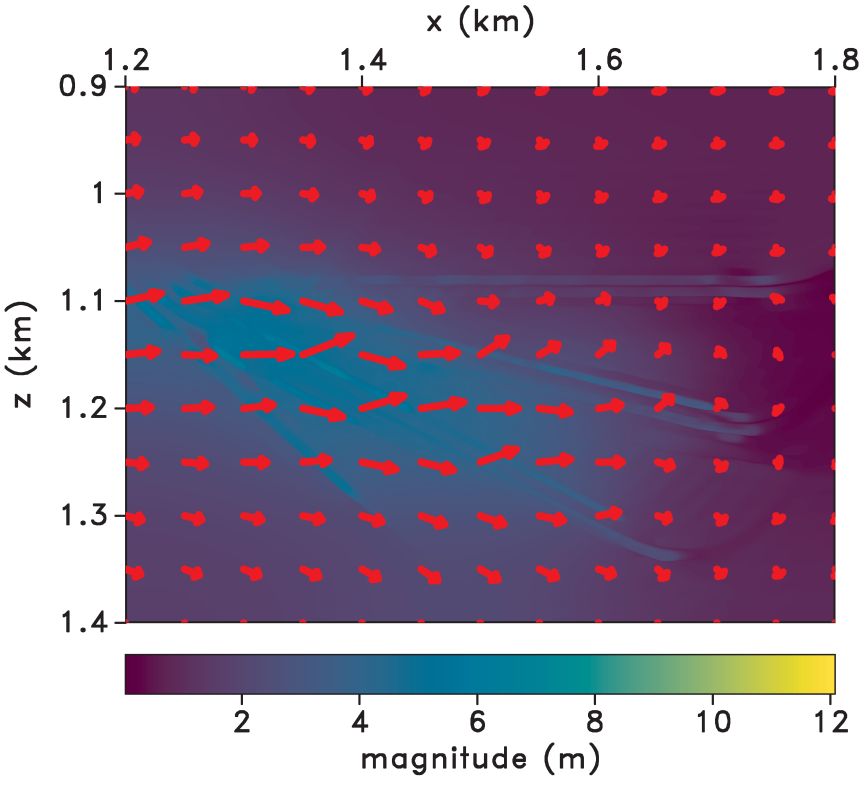

(b)

Figure 5.11 (a) Kinematic correction vector field overlaying the RTM image for mobile acquisition and stationary imaging for a short-duration sweep acquisition. (b) Kinematic correction vector field overlaying the magnitude of the vector field.

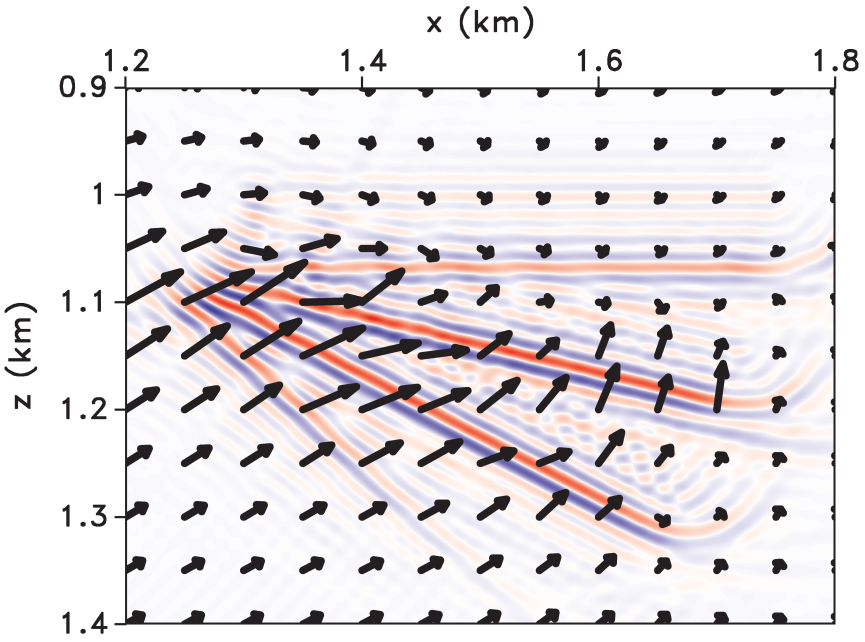

(a)

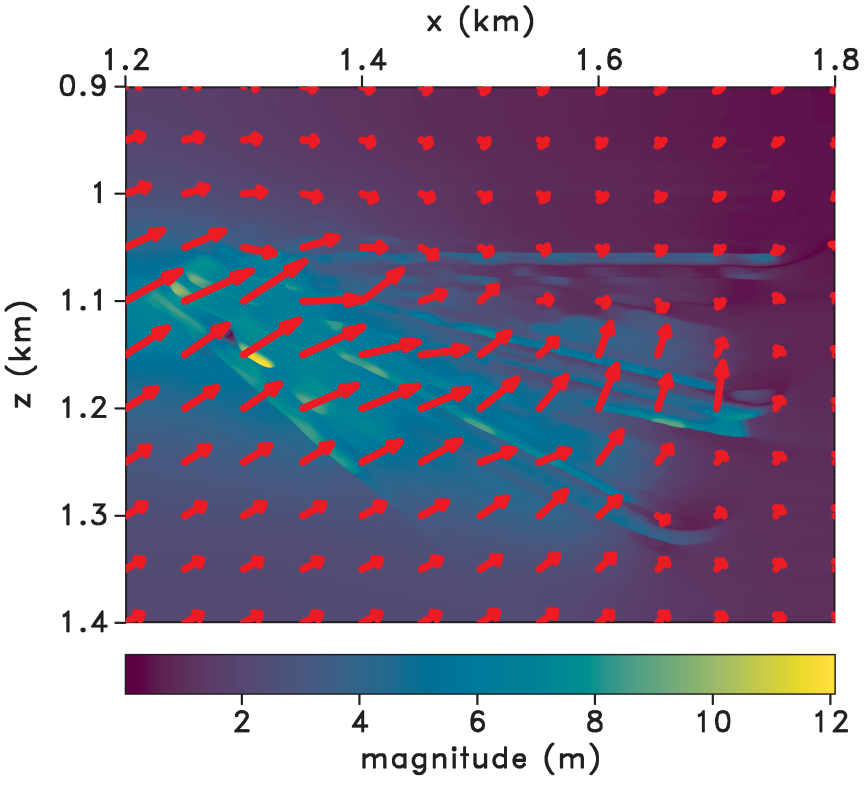

(b)

Figure 5.12 (a) Kinematic correction vector field overlaying the RTM image for mobile acquisition and stationary imaging for a long-duration sweep acquisition. (b) Kinematic correction vector field overlaying the magnitude of the vector field.

motion effects causes the velocity model building process to incorporate errors (e.g., from the incorrect source estimation). In this work, we present an RTM approach for subsurface imaging using marine vibrator data that accounts for the moving source. The developed approach uses a coordinate transformation to compute the required source and receiver wavefields used to evaluate the deconvolution imaging condition. Further, for a judicious choice of grid parameters in ocean-bottom acquisition, one can compute the receiver wavefield using a Cartesian finite-difference AWE solver.

Our examples show that source motion direction, depth of target, and structural dip play a role in the mispositioning direction and magnitude. The magnitude of correction required to kinematically account for source motion effects is proportional to sweep duration. Further investigation is needed to understand the effects of ignoring source motion on RTM results (e.g., emergence angle, sweep bandwidth, and offset-depth ratio). There are other RTM-related issues (e.g., Guitton et al., 2007; Poole et al., 2010; Schleicher et al., 2008) to consider when imaging marine vibrator data, e.g., stability of deconvolution imaging condition and cross-talk, which we leave for future work.

The numerical results demonstrate that our proposed method can accurately image complex subsurface structures even with unrealistically high motion of the mobile marine vibrator source, which typically not incorporated in conventional field data acquisition. In conventional streamer data acquisition, even though air guns are (relatively) instantaneous, streamers are in continuous motion, which introduces the Doppler effect to the data. Therefore, our proposed method is not limited to marine vibrator data, but can also be used to improve imaging techniques in any scenario with mobile streamers. Future work involves incorporating a dynamic sea surface to mimic more realistic marine vibrator acquisition scenarios and using our approach on field data, including conventional streamer data.

5.7 Conclusions

This work presents an RTM imaging solution for mobile marine acquisition that does not require a specialized preprocessing workflow to account for the source motion effects in

data prior to RTM imaging. The approach inherently accounts for source-motion effects by a judicious choice of coordinate transformation that uses the source vessel velocity. There is an added computational cost to account for the source motion effects in the AWE, but it also increases the accuracy and robustness of the results when modeling and imaging marine vibrator data. The numerical results show that ignoring source motion effects incorrectly image structures by changing the phase and amplitude of the recorded waveforms compared to stationary acquisition and imaging. This result demonstrates the robustness of the proposed approach, even for a unreasonably fast source motion that is typically not used in field acquisition.

5.8 Acknowledgments

The first author would like to thank Saudi Aramco for graduate study sponsorship. We thank the sponsors of the Center for Wave Phenomena at Colorado School of Mines for the support of this research. We also thank A. Guitton (TotalEnergies) and T. Konuk (Nvidia) for many useful discussions, and A. Girard (Colorado School of Mines) for proofreading the manuscript and providing useful feedback. Reproducible numerical examples were generated using the Madagascar open-source software package (Fomel et al., 2013) freely available from `http://www.ahay.org`. Analytic coordinate system geometry results were verified using the Mathematica software package (Wolfram Research, Inc., 2021) from `https://www.wolfram.com/mathematica/`.

5.9 Data and materials availability

Data associated with this research are available and can be obtained by contacting the corresponding author.

5.9.1 APPENDIX: Adjoint modeling operator

To formulate the adjoint AWE to equation 5.7, we rewrite it in terms of differential operator such that

$$\frac{\partial^2 P_\xi}{\partial \tau^2} = \mathbf{R}\frac{\partial P_\xi}{\partial \tau} + \mathbf{M}_1 P_\xi - \mathbf{M}_2 P_\xi - \mathbf{H}P_\xi + \mathbf{T}P_\xi + \mathbf{N}P_\xi - \mathbf{Q}\frac{\partial P_\xi}{\partial \tau} + F_\xi, \tag{5.12}$$

$$= \mathbf{R}\frac{\partial P_\xi}{\partial \tau} + \mathbf{A}P_\xi - \mathbf{Q}\frac{\partial P_\xi}{\partial \tau} + F_\xi, \tag{5.13}$$

where $\mathbf{A} = \mathbf{M} - \mathbf{H} + \mathbf{T} + \mathbf{N}$ and $\mathbf{M} = \mathbf{M}_1 - \mathbf{M}_2$, and the differential forward operators are given in Table 5.3. Discretizing equation 5.13 with respect to time using a first- and second-order approximations for the first- and second-order derivatives, respectively, results in

$$\frac{P_\xi^+ - 2P_\xi^0 + P_\xi^-}{\Delta\tau^2} = \frac{1}{\Delta\tau}\mathbf{R}\left(P_\xi^0 - P_\xi^-\right) + \mathbf{A}P_\xi^0 - \frac{1}{2\Delta\tau}\mathbf{Q}\left(P_\xi^+ - P_\xi^-\right) + F_\xi^0, \tag{5.14}$$

where P_ξ^+, P_ξ^0, and P_ξ^- indicate the wavefield at a future, current, and a previous time-step, respectively. Re-ordering equation 5.14 to group wavefields at same time steps gives

$$\begin{aligned}\left(\frac{1}{\Delta\tau^2} + \frac{1}{\Delta\tau}\mathbf{R} - \frac{1}{2\Delta\tau}\mathbf{Q}\right)P_\xi^- - \left(\frac{2}{\Delta\tau^2} + \frac{1}{\Delta\tau}\mathbf{R} + \mathbf{A}\right)P_\xi^0 \\ + \left(\frac{1}{\Delta\tau^2} + \frac{1}{2\Delta\tau}\mathbf{Q}\right)P_\xi^+ = F_\xi^0.\end{aligned} \tag{5.15}$$

In matrix-vector notation, we can write equation 5.14 as

$$\begin{bmatrix} -\left(\frac{2}{\Delta\tau^2} + \frac{1}{\Delta\tau}\mathbf{R} + \mathbf{A}\right) & \left(\frac{1}{\Delta\tau^2} + \frac{1}{2\Delta\tau}\mathbf{Q}\right) & 0 & \dots \\ \left(\frac{1}{\Delta\tau^2} + \frac{1}{\Delta\tau}\mathbf{R} - \frac{1}{2\Delta\tau}\mathbf{Q}\right) & -\left(\frac{2}{\Delta\tau^2} + \frac{1}{\Delta\tau}\mathbf{R} + \mathbf{A}\right) & \left(\frac{1}{\Delta\tau^2} + \frac{1}{2\Delta\tau}\mathbf{Q}\right) & \dots \\ 0 & \left(\frac{1}{\Delta\tau^2} + \frac{1}{\Delta\tau}\mathbf{R} - \frac{1}{2\Delta\tau}\mathbf{Q}\right) & -\left(\frac{2}{\Delta\tau^2} + \frac{1}{\Delta\tau}\mathbf{R} + \mathbf{A}\right) & \dots \\ \vdots & \vdots & \vdots & \ddots \end{bmatrix} \begin{bmatrix} P_\xi^0 \\ P_\xi^1 \\ P_\xi^2 \\ \vdots \end{bmatrix} = \begin{bmatrix} F_\xi^0 \\ F_\xi^1 \\ F_\xi^2 \\ \vdots \end{bmatrix} \tag{5.16}$$

which we can write in a compact form as

$$\mathbf{W}\mathbf{P}_\xi = \mathbf{F}_\xi. \tag{5.17}$$

Therefore, the adjoint equation has the equivalent matrix form

$$\mathbf{W}^\dagger\mathbf{F}_\xi = \mathbf{P}_\xi, \tag{5.18}$$

which expands to

$$\begin{bmatrix} -\left(\frac{2}{\Delta\tau^2}+\frac{1}{\Delta\tau}\mathbf{R}^\dagger+\mathbf{A}^\dagger\right) & \left(\frac{1}{\Delta\tau^2}+\frac{1}{\Delta\tau}\mathbf{R}^\dagger-\frac{1}{2\Delta\tau}\mathbf{Q}^\dagger\right) & 0 & \dots \\ \left(\frac{1}{\Delta\tau^2}+\frac{1}{2\Delta\tau}\mathbf{Q}^\dagger\right) & -\left(\frac{2}{\Delta\tau^2}+\frac{1}{\Delta\tau}\mathbf{R}^\dagger+\mathbf{A}^\dagger\right) & \left(\frac{1}{\Delta\tau^2}+\frac{1}{\Delta\tau}\mathbf{R}^\dagger-\frac{1}{2\Delta\tau}\mathbf{Q}^\dagger\right) & \dots \\ 0 & \left(\frac{1}{\Delta\tau^2}+\frac{1}{2\Delta\tau}\mathbf{Q}^\dagger\right) & -\left(\frac{2}{\Delta\tau^2}+\frac{1}{\Delta\tau}\mathbf{R}^\dagger+\mathbf{A}^\dagger\right) & \dots \\ \vdots & \vdots & \vdots & \ddots \end{bmatrix} \begin{bmatrix} F_\xi^0 \\ F_\xi^1 \\ F_\xi^2 \\ \vdots \end{bmatrix} = \begin{bmatrix} P_\xi^0 \\ P_\xi^1 \\ P_\xi^2 \\ \vdots \end{bmatrix} \tag{5.19}$$

where $\mathbf{A}^\dagger = \mathbf{M}^\dagger - \mathbf{H}^\dagger + \mathbf{T}^\dagger + \mathbf{N}^\dagger$ and $\mathbf{M}^\dagger = \mathbf{M}_1^\dagger - \mathbf{M}_2^\dagger$, and the differential adjoint operators are given in Table 5.3. equation 5.19 can be re-written in a similar format to equation 5.15 as

$$\left(\frac{1}{\Delta\tau^2}+\frac{1}{2\Delta\tau}\mathbf{Q}^\dagger\right)F_\xi^- - \left(\frac{2}{\Delta\tau^2}+\frac{1}{\Delta\tau}\mathbf{R}^\dagger+\mathbf{A}^\dagger\right)F_\xi^0 + \left(\frac{1}{\Delta\tau^2}+\frac{1}{\Delta\tau}\mathbf{R}^\dagger-\frac{1}{2\Delta\tau}\mathbf{Q}^\dagger\right)F_\xi^+ = P_\xi^0. \tag{5.20}$$

We can respectively write equations 5.15 and 5.20 in a time recursion representation as

$$\left(1+\frac{\Delta\tau}{2}\mathbf{Q}\right)P_\xi^+ = 2P_\xi^0 + \Delta\tau\mathbf{R}\left(P_\xi^0 - P_\xi^-\right) + \Delta\tau^2\left(\mathbf{A}P_\xi^0 + F_\xi^0\right) + \frac{\Delta\tau}{2}\mathbf{Q}P_\xi^- - P_\xi^- \tag{5.21}$$

and

$$\left(1+\frac{\Delta\tau}{2}\mathbf{Q}^\dagger\right)F_\xi^- = 2F_\xi^0 + \Delta\tau\mathbf{R}^\dagger\left(F_\xi^0 - F_\xi^+\right) + \Delta\tau^2\left(\mathbf{A}^\dagger F_\xi^0 + P_\xi^0\right) + \frac{\Delta\tau}{2}\mathbf{Q}^\dagger F_\xi^+ - F_\xi^+ \tag{5.22}$$

The forward and adjoint time recursion equations (equations 5.21 and 5.22) show that the receiver wavefield computed by a simple time reversal is not equivalent to the adjoint wavefield, although the time-stepping solutions are similar for the forward and adjoint operation formulated forward and backward in time, respectively. In ocean-bottom acquisition, one can compute the receiver wavefield using the Cartesian AWE adjoint for simplification because receivers are stationary, although using equation 5.22 is the appropriate approach. This simplification is not applicable when using our imaging procedure on streamer data because receivers are in continuous motion.

Table 5.3 Forward and adjoint operators within the AWE for a moving source.

forward operator	adjoint operator
$\mathbf{R} = 2v\alpha\frac{\partial}{\partial\xi^1}$	$\mathbf{R}^\dagger = 2v\alpha\frac{\partial}{\partial\xi^1}$ (self-adjoint)
$\mathbf{M}_1 = \gamma^2\tau^2v^2\alpha^2c^2\frac{\partial}{\partial\xi^1}\left(\frac{\partial}{\partial\xi^1}\right)$	$\mathbf{M}_1^\dagger = \frac{\partial}{\partial\xi^1}\left(\frac{\partial}{\partial\xi^1}\right)\gamma^2\tau^2v^2\alpha^2c^2$
$\mathbf{M}_2 = v^2\alpha^2\frac{\partial}{\partial\xi^1}\left(\frac{\partial}{\partial\xi^1}\right)$	$\mathbf{M}_2^\dagger = v^2\alpha^2\frac{\partial}{\partial\xi^1}\left(\frac{\partial}{\partial\xi^1}\right)$ (self-adjoint)
$\mathbf{H} = \gamma^2\tau v\alpha c^2\frac{\partial}{\partial\xi^1}$	$\mathbf{H}^\dagger = \frac{\partial}{\partial\xi^1}\gamma^2\tau v\alpha c^2$
$\mathbf{T} = 2\gamma\tau v\alpha c^2\frac{\partial}{\partial\xi^1}\left(\frac{\partial}{\partial\xi^3}\right)$	$\mathbf{T}^\dagger = \frac{\partial}{\partial\xi^1}\left(\frac{\partial}{\partial\xi^3}\right)2\gamma\tau v\alpha c^2$
$\mathbf{N} = c^2\nabla^2$	$\mathbf{N}^\dagger = \nabla^2c^2$
$\mathbf{Q} = c^2\eta$	$\mathbf{Q}^\dagger = c^2\eta$ (self-adjoint)

5.9.2 APPENDIX: Born modeling (single scattering)

To derive the Born modeling source term, we start by splitting the seismic wavefield into a background or incident wavefield ($P_\circ$) and a perturbation or scattered wavefield (δP), such that the total wavefield is $P = P_\circ + \delta P$ (omitting the subscript ξ for clarity). Also, we split the acoustic medium velocity into a background velocity ($c_\circ$) and perturbation velocity (δc), such that the total medium velocity is $c = c_\circ + \delta c$. Next, we define a generic functional $B(P, c)$ of P and c such that

$$B(P,c) := \left[\frac{1}{c^2}\left(\frac{\partial^2}{\partial\tau^2} - \tilde{\mathbf{R}}\frac{\partial}{\partial\tau} + \tilde{\mathbf{M}}_2\right) - \tilde{\mathbf{M}}_1 + \tilde{\mathbf{H}} - \tilde{\mathbf{T}} - \tilde{\mathbf{N}} + \tilde{\mathbf{Q}}\frac{\partial}{\partial\tau}\right]P - F, \tag{5.23}$$

where $B(P, c) = 0$ and the tilde over the differential operators imply $\tilde{\chi} \equiv \frac{1}{c^2}\chi$. Given a background velocity ($c_\circ$) and a source function (F), the background wavefield ($P_\circ$) is given by

$$B(P,c)|_{p_\circ,c_\circ} = 0 \tag{5.24}$$

or in expanded form is

$$\left[\frac{1}{c_\circ^2}\left(\frac{\partial^2}{\partial\tau^2} - \tilde{\mathbf{R}}\frac{\partial}{\partial\tau} + \tilde{\mathbf{M}}_2\right) - \tilde{\mathbf{M}}_1 + \tilde{\mathbf{H}} - \tilde{\mathbf{T}} - \tilde{\mathbf{N}} + \tilde{\mathbf{Q}}\frac{\partial}{\partial\tau}\right]P_\circ - F = 0, \tag{5.25}$$

which can be rewritten as

$$\frac{\partial^2 P_\circ}{\partial\tau^2} = \left[\mathbf{R}\frac{\partial}{\partial\tau} + \mathbf{A} - \mathbf{Q}\frac{\partial}{\partial\tau}\right]P_\circ + F. \tag{5.26}$$

Now, Given the background velocity ($c_\circ$); background wavefield ($p_\circ$); and perturbation velocity (δc), we compute wavefield perturbation (δp) by linearizing B relative to the background wavefield ($P_\circ$) and background velocity model ($c_\circ$) such that

$$dB|_{P_\circ,c_\circ} = \left.\frac{\partial B}{\partial P}\right|_{P_\circ,c_\circ} \delta P + \left.\frac{\partial B}{\partial c}\right|_{P_\circ,c_\circ} \delta c, \tag{5.27}$$

where

$$\left.\frac{\partial B}{\partial P}\right|_{P_\circ,c_\circ} \delta P = \left[\frac{1}{c_\circ^2}\left(\frac{\partial^2}{\partial \tau^2} - \tilde{\mathbf{R}}\frac{\partial}{\partial \tau} + \tilde{\mathbf{M}}_2\right) - \tilde{\mathbf{M}}_1 + \tilde{\mathbf{H}} - \tilde{\mathbf{T}} - \tilde{\mathbf{N}} + \tilde{\mathbf{Q}}\frac{\partial}{\partial \tau}\right]\delta P \tag{5.28}$$

and

$$\left.\frac{\partial B}{\partial c}\right|_{P_\circ,c_\circ} \delta c = \frac{-2\delta c}{c_\circ^3}\left(\frac{\partial^2}{\partial \tau^2} - \tilde{\mathbf{R}}\frac{\partial}{\partial \tau} + \tilde{\mathbf{M}}_2\right) P_\circ. \tag{5.29}$$

Using equations 5.27-5.29, the perturbation wavefield can be written as

$$\frac{\partial^2 \delta P}{\partial \tau^2} = \left[\mathbf{R}\frac{\partial}{\partial \tau} + \mathbf{A} - \mathbf{Q}\frac{\partial}{\partial \tau}\right]\delta P + \frac{2\delta c}{c_\circ}\left(\frac{\partial^2}{\partial \tau^2} - \tilde{\mathbf{R}}\frac{\partial}{\partial \tau} + \tilde{\mathbf{M}}_2\right) P_\circ. \tag{5.30}$$

The advantage of using Born modeling (equations 5.26 and 5.30) is that seismic data can be modeled under the assumption of single scattering and without including unwanted signal (e.g., direct arrivals, refractions, multiples), which is useful for validating imaging algorithms (e.g., RTM) especially given that most such algorithms assume single scattering (Sava and Hill, 2009).

CHAPTER 6
CONCLUSIONS

In this thesis, I propose various approaches to modeling, processing, and imaging relevant to marine seismic data. In Chapter 2, I develop a convolutional neural network (CNN) solution to remove source- and receiver-side ghost reflections for pressure data acquired using horizontal streamers. I review the theory of ghost reflections and proposed solutions in the literature and review the principles of CNNs highlighting features that make this approach feasible for deghosting. I generate pairs of ghost-free and ghost-contaminated data for training of the neural network using modeling with an absorbing air-water interface. To model ghost reflections, I use virtual sources and receivers above the air-water interface. I also experimentally build and train a neural network to map ghost-contaminated gathers to corresponding ghost-free gathers using supervised learning. To demonstrate the effectiveness of the solution, I test the developed CNN-based deghosting operator using synthetic and field data. In all numerical results, I train the NN with noise-free data; thus, showing the developed deghsoting approach is robust to random noise in field data.

In Chapter 3, I develop the theory and numerical approach for modeling moving and long-emitting sources, i.e., marine vibrators. To model marine vibrator data under quiescent sea-surface conditions, I use a coordinate transformation to map an irregular and time-varying physical domain that horizontally shears to track the source movement to a regular computational domain that is regularly spaced and fixed in time. The time-varying physical mesh grid is formulated in Cartesian coordinates, whereas the computational domain is defined in a generalized coordinate system. I use a second-order formulation of the tensorial acoustic wave equation to model moving source data. I demonstrate the robustness of the developed approach using synthetic examples with unrealistically high source velocities. Additionally, I formulate an analytical expression to predict frequency shifts (Doppler effect) due to source

motion in heterogeneous media and derive an analytical expression of the Green's function that predicts the seismic wavefield triggered by a moving source in 3D homogeneous media. I use the formulated analytical expression to validate the correctness and accuracy of the developed theory and modeling approach. Furthermore, I investigate the effects of source motion on recorded seismic data and ghost reflections, as well as the implications of velocity model heterogeneity on frequency shifts due to source motion.

In Chapter 4, I extend the work done in Chapter 3 to incorporate a time-varying free-surface boundary condition (i.e., time-varying sea-surface effects) into seismic modeling. The modeling approach I adopt is similar to that in Chapter 3. However, I use a first-order coupled-system tensorial formulation of the acoustic wave equation (that accounts for velocity model heterogeneity). A common element between Chapters 3 and 4 is the introduction of user-defined parameters that confine the physical mesh deformation to the homogeneous water layer, thus avoiding the need for a repeated and computationally expensive interpolation of the velocity model from Cartesian coordinates to a generalized coordinate system or of the seismic wavefield from a generalized coordinate system to Cartesian coordinates. I examine the accuracy and stability of the developed modeling approach using complex velocity models with realistic and unrealistic time-varying sea surfaces. Additionally, I investigate the effects source movement and a dynamic sea surface have on ocean-bottom data.

In Chapter 5, I exploit the developed methodology in Chapter 3 to image marine vibrator data, taking into consideration source motion effects. Within this chapter, I formulate the theoretical framework for imaging that includes: (1) forward modeling operator, (2) adjoint modeling operator, and (3) Born approximation modeling operator. I numerically demonstrate that the developed imaging approach can accurately account for source motion effects and produce RTM images that closely match RTM images from stationary acquisition and imaging, even with an unrealistically high source velocity that is typically not used in marine acquisition. The work developed in Chapters 3-5 is not limited to marine vibrator data in ocean-bottom acquisition, but is also applicable to streamer data acquisition using

conventional seismic air-gun sources and marine vibrators.

This thesis spans fields from differential geometry, numerical modeling, machine learning, seismic data processing, and acquisition design. The development of robust and reliable processing and imaging solutions aims to reduce seismic interpretation uncertainties and improve the quality of subsurface images in complex and heterogeneous media. Additionally, exploring machine learning methodologies facilitates the development of a wide range of seismic data processing and imaging techniques. These techniques are not limited to ghost removal but extend beyond that, including velocity picking and model building, among other applications. By developing modeling tools to simulate moving sources, we can utilize the Doppler effect to push the low-frequency limit for full-waveform inversion in a cost-effective way and improve seismic resolution. Employing machine learning methodologies and using numerical solutions could lead to new acquisition designs that overcome the limitations of standard processing and imaging technology. Finally, the developed approaches are not limited to the work presented in this thesis but are also applicable to other fields and problems (e.g., modeling radar data from a moving satellite).

REFERENCES

Ahrens, J., and S. Spors, 2011, Wave field synthesis of moving virtual sound sources with complex radiation properties: The Journal of the Acoustical Society of America, **130**, no. 5, 2807–2816, doi: 10.1121/1.3640850.

Alexandrov, D., B. Kashtan, A. Bakulin, and P. Leger, 2014, Dual-sensor summation with buried land sensors: 84th Annual International Meeting, SEG, Expanded Abstracts, 1929–1933, doi: 10.1190/segam2014-1082.1.

Almuteri, K., and P. Sava, 2021, A convolutional neural network approach for ghost removal: First International Meeting for Applied Geoscience & Energy, SEG, Expanded Abstracts, 2550–2554, doi: 10.1190/segam2021-3584059.1.

———, 2023, Seismic deghosting using convolutional neural networks: Geophysics, **88**, no. 3, V113–V125, doi: 10.1190/geo2021-0521.1.

Almuteri, K., P. Sava, and J. Shragge, 2022a, Reverse-time migration of mobile marine vibrator data: Second International Meeting for Applied Geoscience & Energy, 2694–2698, doi: 10.1190/image2022-3751755.1.

Almuteri, K., J. Shragge, and P. Sava, 2022b, Finite-difference modeling of marine vibrator sources: Second International Meeting for Applied Geoscience & Energy, SEG, Expanded Abstracts, 2561–2565, doi: 10.1190/image2022-3746278.1.

Amundsen, L., 1993, Wavenumber-based filtering of marine point-source data: Geophysics, **58**, no. 9, 1335–1348, doi: 10.1190/1.1443516.

Amundsen, L., F. Andersson, D.-J. van Manen, J. O. A. Robertsson, and K. Eggenberger, 2018, Multisource encoding and decoding using the signal apparition technique: Geophysics, **83**, no. 1, V49–V59, doi: 10.1190/geo2017-0206.1.

Amundsen, L., Pedersen, A. Osen, J. O. Robertsson, and M. Landrø, 2017, Broadband seismic over/under sources and their designature-deghosting: Geophysics, **82**, no. 5, P61–P73, doi: 10.1190/geo2016-0512.1.

Amundsen, L., B. G. Secrest, and B. Arntsen, 1995, Extraction of the normal component of the particle velocity from marine pressure data: Geophysics, **60**, no. 1, 212–222, doi: 10.1190/1.1443749.

Amundsen, L., and H. Zhou, 2013, Low-frequency seismic deghosting: Geophysics, **78**, no. 2, WA15–WA20, doi: 10.1190/geo2012-0276.1.

Amundsen, L., H. Zhou, A. Reitan, and A. Weglein, 2013, On seismic deghosting by spatial deconvolution: Geophysics, **78**, no. 6, WA55–WA70, doi: 10.1190/GEO2013-0198.1.

Appelö, D., and N. A. Petersson, 2009, A stable finite difference method for the elastic wave equation on complex geometries with free surfaces: Communications in Computational Physics, **5**, no. 1, 84–107.

Araya-Polo, M., J. Jennings, A. Adler, and T. Dahlke, 2018, Deep-learning tomography: The Leading Edge, **37**, no. 1, 58–66, doi: 10.1190/tle37010058.1.

Baysal, E., D. D. Kosloff, and J. W. Sherwood, 1983, Reverse time migration: Geophysics, **48**, no. 11, 1514–1524.

Bearnth, R. E., and N. A. Moore, 1989, Air gun-slant cable seismic results in the Gulf of Mexico: 59th Annual International Meeting, SEG, Expanded Abstracts, 649–652, doi: 10.1190/1.1889556.

Beasley, C. J., R. Coates, Y. Ji, and J. Perdomo, 2013a, Wave equation receiver deghosting: A provocative example: 83th Annual International Meeting, SEG, Expanded Abstracts, 4226–4230, doi: 10.1190/segam2013-0693.1.

Beasley, C. J., R. Coates, and C. Lapilli, 2013b, Wave equation receiver deghosting: 2013 5th IEEE international workshop on computational advances in multi-sensor adaptive processing (CAMSAP), 280–283, doi: 10.1109/CAMSAP.2013.6714062.

Bennett, J. A., 1968, The ray theory of Doppler frequency shifts: Australian Journal of Physics, **21**, no. 3, 259–272.

Birnie, C., M. Ravasi, and T. Alkhalifah, 2021, Self-supervised learning for random noise suppression in seismic data: First International Meeting for Applied Geoscience & Energy, SEG, Expanded Abstracts, 2869–2873, doi: 10.1190/segam2021-3583248.1.

Biswas, R., M. K. Sen, V. Das, and T. Mukerji, 2019, Prestack and poststack inversion using a physics-guided convolutional neural network: Interpretation-a Journal of Bible and Theology, **7**, no. 3, SE161–SE174, doi: 10.1190/INT-2018-0236.1.

Biswas, R., A. Vassiliou, R. Stromberg, and M. K. Sen, 2018, Stacking velocity estimation using recurrent neural network: 88th Annual International Meeting, SEG, Expanded Abstracts, 2241–2245, doi: 10.1190/segam2018-2997208.1.

Blacquière, G., and H. O. Sertlek, 2019, Modeling and assessing the effects of the sea surface, from being flat to being rough and dynamic: Geophysics, **84**, no. 2, T13–T27, doi: 10.1190/geo2018-0294.1.

Bunks, C., F. M. Saleck, S. Zaleski, and G. Chavent, 1995, Multiscale seismic waveform inversion: Geophysics, **60**, no. 5, 1457–1473, doi: 10.1190/1.1443880.

Cambois, G., D. Carlson, C. Jones, M. Lesnes, W. Söllner, and H. Tabti, 2009, Dual-sensor streamer data: calibration, acquisition QC and attenuation of seismic interferences and other noises: 79th Annual International Meeting, SEG, Expanded Abstracts, 142–146, doi: 10.1190/1.3255117.

Carcione, J. M., 1994, The wave equation in generalized coordinates: Geophysics, **59**, no. 12, 1911–1919, doi: 10.1190/1.1443578.

Carlson, D. H., A. Long, W. Söllner, H. Tabti, R. Tenghamn, and N. Lunde, 2007, Increased resolution and penetration from a towed dual-sensor streamer: First Break, **25**, no. 12, 71–77, doi: 10.3997/1365-2397.25.12.27722.

Carothers, N. L., 1998, A short course on approximation theory: Bowling Green State University.

Castillo, J. E., J. M. Hyman, M. Shashkov, and S. Steinberg, 2001, Fourth- and sixth-order conservative finite difference approximations of the divergence and gradient: Applied Numerical Mathematics, **37**, no. 1, 171–187, doi: 10.1016/S0168-9274(00)00033-7.

Castillo, J. E., and G. F. Miranda, 2013, Mimetic discretization methods: CRC Press.

Cecconello, E., E. G. Asgedom, O. C. Orji, M. W. Pedersen, and W. Söllner, 2018, Modeling scattering effects from time-varying sea surface based on acoustic reciprocity: Geophysics, **83**, no. 2, T49–T68, doi: 10.1190/geo2017-0410.1.

Claerbout, J. F., 1971, Toward a unified theory of reflector mapping: Geophysics, **36**, no. 3, 467–481.

———, 1976, Fundamentals of geophysical data processing: McGraw-Hill, New York.

Clayton, R., and B. Engquist, 1977, Absorbing boundary conditions for acoustic and elastic wave equations: Bulletin of the Seismological Society of America, **67**, no. 6, 1529–1540.

Corbino, J., and J. E. Castillo, 2020, High-order mimetic finite-difference operators satisfying the extended Gauss divergence theorem: Journal of Computational and Applied Mathematics, **364**, 112326, doi: 10.1016/j.cam.2019.06.042.

Cybenko, G., 1989, Approximation by superpositions of a sigmoidal function: Mathematics of Control, Signals, and Systems, **2**, no. 4, 303–314, doi: 10.1007/BF02551274.

Das, V., and T. Mukerji, 2020, Petrophysical properties prediction from pre-stack seismic data using convolutional neural networks: Geophysics, **85**, no. 5, N41–N55, doi: 10.1190/geo2019-0650.1.

Das, V., A. Pollack, U. Wollner, and T. Mukerji, 2019, Convolutional neural network for seismic impedance inversion: Geophysics, **84**, no. 6, R869–R880, doi: 10.1190/geo2018-0838.1.

Davies, K., 1965, Ionospheric radio propagation: US Department of Commerce, National Bureau of Standards, **80**.

Day, A., T. Klüver, W. Söllner, H. Tabti, and D. Carlson, 2013, Wavefield-separation methods for dual-sensor towed-streamer data: Geophysics, **78**, no. 2, WA55–WA70, doi: 10.1190/geo2012-0302.1.

de la Puente, J., M. Ferrer, M. Hanzich, J. E. Castillo, and J. M. Cela, 2014, Mimetic seismic wave modeling including topography on deformed staggered grids: Geophysics, **79**, no. 3, T125–T141, doi: 10.1190/geo2013-0371.1.

Dellinger, J., and E. Díaz, 2020, Efficient modelling of extended-duration moving seismic sources: EAGE 2020 Annual Conference & Exhibition Online, 1–5, doi: 10.3997/2214-4609.202010838.

Dellinger, J., A. Ross, D. Meaux, A. Brenders, G. Gesoff, J. Etgen, J. Naranjo, G. Openshaw, and M. Harper, 2016, Wolfspar®, an "FWI-friendly" ultra-low-frequency marine seismic source: 86th Annual International Meeting, SEG, Expanded Abstracts, 4891–4895, doi: 10.1190/segam2016-13762702.1.

Dondurur, D., 2018, Acquisition and processing of marine seismic data: Elsevier.

Doppler, C., 1842, Ueber das farbige licht der Doppelsterne und einiger anderer Gestirne des Himmels: Versuch einer das Bradley'sche Aberrations-Theorem als integrirenden Theil in sich schliessenden allgemeineren Theorie: K. Böhm Gesellschaft der Wissenschaften, 465–482.

Dragoset, W. H., 1988, Marine vibrators and the Doppler effect: Geophysics, **53**, no. 11, 1388–1398, doi: 10.1190/1.1442418.

Duquet, B., A. Guitton, S. Secker, A. Feltham, and J.-P. Mascomere, 2021, Impact of non-impulsive moving source correction for structural and 4D imaging: First international meeting for applied geoscience & energy, SEG, Expanded Abstracts, 31–35, doi: 10.1190/segam2021-3594448.1.

E, W., 2020, Machine learning and computational mathematics: Communications in Computational Physics, **28**, no. 5, 1639–1670, doi: 10.4208/cicp.OA-2020-0185.

Egan, M., K. G. El-Kasseh, and N. Moldoveanu, 2007, Full deghosting of OBC data with over/under source acquisition: 77th Annual International Meeting, SEG, Expanded Abstracts, 31–35, doi: 10.1190/1.2792376.

Egorov, A., S. Glubokovskikh, A. Bóna, R. Pevzner, B. Gurevich, and M. Tokarev, 2018, How rough sea affects marine seismic data and deghosting procedures: Geophysical Prospecting, **66**, no. 1, 3–12, doi: 10.1111/1365-2478.12535.

Fomel, S., P. Sava, I. Vlad, Y. Liu, and V. Bashkardin, 2013, Madagascar: Open-source software project for multidimensional data analysis and reproducible computational experiments: Journal of Open Research Software, **1**, no. 1, doi: 10.5334/jors.ag.

Fornberg, B., 1988, Generation of finite difference formulas on arbitrarily spaced grids: Mathematics of Computation, **51**, no. 184, 699—-706, doi: 10.1090/S0025-5718-1988-0935077-0.

Glasbey, C. A., and K. V. Mardia, 1998, A review of image-warping methods: Journal of Applied Statistics, **25**, no. 2, 155–171, doi: 10.1080/02664769823151.

Goodfellow, I., Y. Bengio, A. Courville, and Y. Bengio, 2016, Deep learning: MIT Press.

Griebel, M., 2005, Sparse grids and related approximation schemes for higher dimensional problems: SFB.

Grion, S., R. Telling, and S. Holland, 2016, Rough sea estimation for phase-shift deghosting: 86th Annual International Meeting, SEG, Expanded Abstracts, 5129–5133, doi: 10.1190/segam2016-13688475.1.

Grobbe, N., J. van der Neut, E. Slob, K. Wapenaar, C. A. Vidal, and G. Drijkoningen, 2016, Unified multi-depth-level field decomposition: Geophysical Prospecting, **64**, no. 2, 361–391, doi: 10.1111/1365-2478.12290.

Grohs, P., A. Jentzen, and D. Salimova, 2019, Deep neural network approximations for Monte Carlo algorithms: arXiv preprint arXiv:1908.10828.

Guitton, A., B. Duquet, S. Secker, J. P. Mascomere, and A. Feltham, 2021, A deconvolution-interpolation approach with sparse inversion to mitigate the Doppler effect in marine vibrators data: First International Meeting for Applied Geoscience & Energy, 2555–2559, doi: 10.1190/segam2021-3593897.1.

Guitton, A., A. Valenciano, D. Bevc, and J. Claerbout, 2007, Smoothing imaging condition for shot-profile migration: Geophysics, **72**, no. 3, S149–S154, doi: 10.1190/1.2712113.

Géron, A., 2019, Hands-on machine learning with scikit-learn, keras, and TensorFlow: Concepts, tools, and techniques to build intelligent systems: O'Reilly Media.

Haavik, K. E., and M. Landrø, 2015, Variable source depth acquisition for improved marine broadband seismic data: Geophysics, **80**, no. 3, A69–A73, doi: 10.1190/geo2014-0437.1.

Halliday, D. F., and I. Moore, 2018, A comparison of random and periodic marine simultaneous-source encoding: The Leading Edge, **37**, no. 6, 471a1–471a11, doi: 10.1190/tle37060471a1.1.

Hampson, G., and H. Jakubowicz, 1995, The effects of source and receiver motion on seismic data: Geophysical Prospecting, **43**, no. 2, 221–244, doi: 10.1111/j.1365-2478.1995.tb00133.x.

Hanka, R., and T. P. Harte, 1997, Curse of dimensionality: classifying large multi-dimensional images with neural networks, *in* Computer intensive methods in control and signal processing: Springer, 249–260.

He, J.-W., W.-K. Lu, and Z.-X. Li, 2013, An adaptive over/under data combination method: Applied Geophysics, **10**, no. 4, 469–476, doi: 10.1007/s11770-013-0397-x.

Hestholm, S., 1999, Three-dimensional finite difference viscoelastic wave modelling including surface topography: Geophysical Journal International, **139**, no. 3, 852–878, doi: 10.1046/j.1365-246x.1999.00994.x.

Hestholm, S., and B. Ruud, 2002, 3D free-boundary conditions for coordinate-transform finite-difference seismic modelling: Geophysical Prospecting, **50**, no. 5, 463–474, doi: 10.1046/j.1365-2478.2002.00327.x.

Hinton, G., L. Deng, D. Yu, G. E. Dahl, A. Mohamed, N. Jaitly, A. Senior, V. Vanhoucke, P. Nguyen, T. N. Sainath, and others, 2012, Deep neural networks for acoustic modeling in speech recognition: The shared views of four research groups: IEEE Signal Processing Magazine, **29**, no. 6, 82–97, doi: 10.1109/MSP.2012.2205597.

Hornik, K., 1991, Approximation capabilities of multilayer feedforward networks: Neural Networks, **4**, no. 2, 251–257, doi: 10.1016/0893-6080(91)90009-T.

Hornik, K., M. Stinchcombe, H. White, and others, 1989, Multilayer feedforward networks are universal approximators: Neural Networks, **2**, no. 5, 359–366, doi: 10.1016/0893-6080(89)90020-8.

Hu, W., Y. Jin, X. Wu, and J. Chen, 2020, Physics-guided self-supervised learning for low frequency data prediction in FWI: 90th Annual International Meeting, SEG, Expanded Abstracts, 875–879, doi: 10.1190/segam2020-3423396.1.

Huang, S., and Y. Huang, 1990, Bounds on number of hidden neurons of multilayer perceptrons in classification and recognition: IEEE international symposium on circuits and systems, 2500–2503, doi: 10.1109/72.80290.

Ikelle, L. T., and L. Amundsen, 2018, Introduction to petroleum seismology: Society of Exploration Geophysicists. doi: 10.1190/1.9781560803447.

Jackson, J. D., 1999, Classical electrodynamics: John Wiley & Sons.

JafarGandomi, A., and S. Grion, 2021, Modelling of marine vibrator data: 82nd EAGE Annual Conference & Exhibition, 1–5, doi: 10.3997/2214-4609.202113202.

Jeffreys, H., and B. Jeffreys, 1950, Methods of mathematical physics: Cambridge University Press.

Jovanovich, D. B., R. D. Sumner, and S. L. Akins-Easterlin, 1983, Ghosting and marine signature deconvolution: A prerequisite for detailed seismic interpretation: Geophysics, **48**, no. 11, 1468–1485, doi: 10.1190/1.1441431.

Kapoor, J., C. Stork, and M. Egan, 2005, Benefits of low frequencies for subsalt imaging: 75th Annual International Meeting, SEG, Expanded Abstracts, 1993–1996, doi: 10.1190/1.2148099.

King, S., and G. Poole, 2015, Hydrophone-only receiver deghosting using a variable sea surface datum: 85th Annual International Meeting, SEG, Expanded Abstracts, 4610–4614, doi: 10.1190/segam2015-5891123.1.

Knapp, R. W., 1990, Vertical resolution of thick beds, thin beds, and thin-bed cyclothems: Geophysics, **55**, no. 9, 1183–1190, doi: 10.1190/1.1442934.

Kolano, R. A., 1978, Doppler shift in layered media.

Komatitsch, D., F. Coutel, and P. Mora, 1996, Tensorial formulation of the wave equation for modelling curved interfaces: Geophysical Journal International, **127**, no. 1, 156–168, doi: 10.1111/j.1365-246X.1996.tb01541.x.

Komatitsch, D., and J. P. Vilotte, 1998, The spectral element method: An efficient tool to simulate the seismic response of 2D and 3D geological structures: Bulletin of the Seismological Society of America, **88**, no. 2, 368–392, doi: 10.1785/BSSA0880020368.

Konuk, T., and J. Shragge, 2020, Modeling full-wavefield time-varying sea-surface effects on seismic data: A mimetic finite-difference approach: Geophysics, **85**, no. 2, T45–T55, doi: 10.1190/geo2019-0181.1.

Kosloff, R., and D. Kosloff, 1986, Absorbing boundaries for wave propagation problems: Journal of Computational Physics, **63**, no. 2, 363–376, doi: 10.1016/0021-9991(86)90199-3.

Kragh, E., E. Muyzert, T. Curtis, M. Svendsen, and D. Kapadia, 2010, Efficient broadband marine acquisition and processing for improved resolution and deep imaging: The Leading Edge, **29**, no. 4, 464–469, doi: 10.1190/1.3378309.

Krizhevsky, A., I. Sutskever, and G. E. Hinton, 2017, ImageNet classification with deep convolutional neural networks: Communications of the ACM, **60**, no. 6, 84–90, doi: 10.1145/3065386.

Kurzmann, A., A. Przebindowska, D. Köhn, and T. Bohlen, 2013, Acoustic full waveform tomography in the presence of attenuation: a sensitivity analysis: Geophysical Journal International, **195**, no. 2, 985–1000, doi: 10.1093/gji/ggt305.

Käser, M., and M. Dumbser, 2006, An arbitrary high-order discontinuous Galerkin method for elastic waves on unstructured meshes—I. The two-dimensional isotropic case with external source terms: Geophysical Journal International, **166**, no. 2, 855–877, doi: 10.1111/j.1365-246X.2006.03051.x.

Landrø, M., 2008, The effect of noise generated by previous shots on seismic reflection data: Geophysics, **73**, no. 3, Q9–Q17, doi: 10.1190/1.2894453.

Lapedes, A., and R. Farber, 1987, How neural nets work: Conference on neural information processing systems, 442–456.

Laws, R., D. Halliday, J.-F. Hopperstad, D. Gerez, M. Supawala, A. Özbek, T. Murray, and E. Kragh, 2019, Marine vibrators: the new phase of seismic exploration: Geophysical Prospecting, **67**, no. 6, 1443–1471, doi: 10.1111/1365-2478.12708.

Laws, R., and E. Kragh, 2002, Rough seas and time-lapse seismic: Geophysical Prospecting, **50**, no. 2, 195–208, doi: 10.1046/j.1365-2478.2002.00311.x.

LeCun, Y., Y. Bengio, and G. Hinton, 2015, Deep learning: Nature, **521**, no. 7553, 436–444, doi: 10.1038/nature14539.

LeCun, Y., L. Bottou, Y. Bengio, and P. Haffner, 1998, Gradient-based learning applied to document recognition: Proceedings of the IEEE, **86**, no. 11, 2278–2324, doi: 10.1109/5.726791.

Lipnikov, K., G. Manzini, and M. Shashkov, 2014, Mimetic finite difference method: Journal of Computational Physics, **257**, 1163–1227, doi: 10.1016/j.jcp.2013.07.031.

Lisitsa, V., and D. Vishnevskiy, 2010, Lebedev scheme for the numerical simulation of wave propagation in 3D anisotropic elasticity: Geophysical Prospecting, **58**, no. 4, 619–635, doi: 10.1111/j.1365-2478.2009.00862.x.

Liu, S., C. Birnie, and T. Alkhalifah, 2022a, Coherent noise suppression via a self-supervised deep learning scheme: 83rd EAGE Annual Conference & Exhibition, European Association of Geoscientists & Engineers, 1–5, doi: 10.3997/2214-4609.202210382.

Liu, S., C. Birnie, T. Alkhalifah, and A. Bakulin, 2022b, Aiding self-supervised coherent noise suppression by the introduction of signal segmentation using blind-spot networks: Second International Meeting for Applied Geoscience & Energy, SEG, Expanded Abstracts, 2857–2861, doi: 10.1190/image2022-3742756.1.

Liu, X., 2023, Modeling seismic waves in ocean with the presence of irregular seabed and rough sea surface: Journal of Geophysics and Engineering, **20**, no. 1, 49–66, doi: 10.1093/jge/gxac093.

Ma, Y., X. Ji, T. Fei, and Y. Luo, 2018, Automatic velocity picking with convolutional neural networks: 88th Annual International Meeting, SEG, Expanded Abstracts, 2066–2070, doi: 10.1190/segam2018-2987088.1.

Marfurt, K. J., 1984, Accuracy of finite-difference and finite-element modeling of the scalar and elastic wave equations: Geophysics, **49**, no. 5, 533–549, doi: 10.1190/1.1441689.

Martin, G. S., K. J. Marfurt, and S. Larsen, 2002, Marmousi-2: An updated model for the investigation of AVO in structurally complex areas: 72th Annual International Meeting, SEG, Expanded Abstracts, 1979–1982, doi: 10.1190/1.1817083.

Mayhan, J. D., and A. B. Weglein, 2013, First application of Green's theorem-derived source and receiver deghosting on deep-water Gulf of Mexico synthetic (SEAM) and field data: Geophysics, **78**, no. 2, WA77–WA89, doi: 10.1190/geo2012-0295.1.

McMechan, G. A., 1983, Migration by extrapolation of time-dependent boundary values: Geophysical Prospecting, **31**, no. 3, 413–420, doi: 10.1111/j.1365-2478.1983.tb01060.x.

Moldoveanu, N., 2000, Vertical source array in marine seismic exploration: 70th Annual International Meeting, SEG, Expanded Abstracts, 53–56, doi: 10.1190/1.1816117.

Moldoveanu, N., L. Combee, M. Egan, G. Hampson, L. Sydora, and W. Abriel, 2007, Over/under towed-streamer acquisition: A method to extend seismic bandwidth to both higher and lower frequencies: The Leading Edge, **26**, no. 1, 41–58, doi: 10.1190/1.2431831.

Morse, P. M., and K. U. Ingard, 1986, Theoretical acoustics: Princeton University Press.

Mueller, M. B., D. F. Halliday, D.-J. van Manen, and J. O. Robertsson, 2015, The benefit of encoded source sequences for simultaneous source separation: Geophysics, **80**, no. 5, V133–V143.

O'Brien, M., 1994, 1994 amoco statics test.

Orji, O. C., W. Söllner, and L.-J. Gelius, 2012, Effects of time-varying sea surface in marine seismic data: Geophysics, **77**, no. 3, P33–P43, doi: 10.1190/geo2011-0361.1.

Ozdemir, A. K., B. A. Kjellesvig, A. Ozbek, and J. E. Martin, 2012, Digital noise attenuation of particle motion data in a multicomponent 4C towed streamer: 74th EAGE Conference and Exhibition incorporating EUROPEC 2012, European Association of Geoscientists & Engineers, cp–293, doi: 10.3997/2214-4609.20148301.

Pawelec, I., M. Wakin, and P. Sava, 2022, Multichannel compressive sensing for seismic data reconstruction using joint sparsity, *in* Second International Meeting for Applied Geoscience & Energy: Society of Exploration Geophysicists and American Association of Petroleum Geologists, SEG Technical Program Expanded Abstracts, 2636–2640.

Pierson, W. J., and L. Moskowitz, 1964, A proposed spectral form for fully developed wind seas based on the similarity theory of S. A. Kitaigorodskii: Journal of Geophysical Research, **69**, no. 24, 5181–5190, doi: 10.1029/JZ069i024p05181.

Poole, T. L., A. Curtis, J. O. A. Robertsson, and D.-J. van Manen, 2010, Deconvolution imaging conditions and cross-talk suppression: Geophysics, **75**, no. 6, W1–W12, doi: 10.1190/1.3493638.

Posthumus, B. J., 1993, Deghosting of twin streamer configuration: Geophysical Prospecting, **41**, no. 3, 267–286, doi: 10.1111/j.1365-2478.1993.tb00570.x.

Provenzano, G., T. J. Henstock, J. M. Bull, and G. Bayrakci, 2020, Attenuation of receiver ghosts in variable-depth streamer high-resolution seismic reflection data: Marine Geophysical Research, **41**, no. 2, 1–15, doi: 10.1007/s11001-020-09407-9.

Pérez, J. S., E. Meinhardt-Llopis, and G. Facciolo, 2013, TV-L1 optical flow estimation: Image Processing On Line, **3**, 137–150, doi: 10.5201/ipol.2013.26.

Reilly, J. M., 2016, Marine broadband technology: History and remaining challenges from an end-user perspective: The Leading Edge, **35**, no. 4, 316–321, doi: 10.1190/tle35040316.1.

Rentsch, S., S. Bodyakin, L. P. Espezua, A. Özbek, W. G. Brouwer, and P. Watterson, 2013, Multidomain noise attenuation for multimeasurement towed streamer data: 75th EAGE Conference & Exhibition incorporating SPE EUROPEC 2013, European Association of Geoscientists & Engineers, cp–348, doi: 10.3997/2214-4609.20130887.

Robertsson, J. O., I. Moore, M. Vassallo, K. Özdemir, D.-J. van Manen, and A. Özbek, 2008, On the use of multicomponent streamer recordings for reconstruction of pressure wavefields in the crossline direction: Geophysics, **73**, no. 5, A45–A49, doi: 10.1190/1.2953338.

Robertsson, J. O. A., L. Amundsen, and Å. S. Pedersen, 2016, Signal apparition for simultaneous source wavefield separation: Geophysical Journal International, **206**, no. 2, 1301–1305.

Robertsson, J. O. A., R. Laws, C. Chapman, J. P. Vilotte, and E. Delavaud, 2006, Modelling of scattering of seismic waves from a corrugated rough sea surface: a comparison of three methods: Geophysical Journal International, **167**, no. 1, 70–76, doi: 10.1111/j.1365-246X.2006.03115.x.

Russell, S., and P. Norvig, 2016, Artificial intelligence: a modern approach: Pearson Education Limited.

Sabbione, J. I., and D. Velis, 2010, Automatic first-breaks picking: New strategies and algorithms: Geophysics, **75**, no. 4, V67–V76, doi: 10.1190/1.3463703.

Sartori, M. A., and P. J. Antsaklis, 1991, A simple method to derive bounds on the size and to train multilayer neural networks: IEEE Transactions on Neural Networks, **2**, no. 4, 467–471, doi: 10.1109/72.88168.

Sava, P., and S. J. Hill, 2009, Overview and classification of wavefield seismic imaging methods: The Leading Edge, **28**, no. 2, 170–183, doi: 10.1190/1.3086052.

Schleicher, J., J. C. Costa, and A. Novais, 2008, A comparison of imaging conditions for wave-equation shot-profile migration: Geophysics, **73**, no. 6, S219–S227, doi: 10.1190/1.2976776.

Schultz, P. S., A. W. Pieprzak, G. R. Johnson, and L. Walker, 1989, Simple theory for correction of marine vibroseis phase dispersion: 59th Annual International Meeting, SEG, Expanded Abstracts, 660–662, doi: 10.1190/1.1889560.

Shragge, J., 2014, Solving the 3D acoustic wave equation on generalized structured meshes: A finite-difference time-domain approach: Geophysics, **79**, no. 6, T363–T378, doi: 10.1190/geo2014-0172.1.

Shragge, J., and B. Tapley, 2017, Solving the tensorial 3D acoustic wave equation: A mimetic finite-difference time-domain approach: Geophysics, **82**, no. 4, T183–T196, doi: 10.1190/geo2016-0691.1.

Smith, J. G., and M. R. Jenkerson, 1998, Acquiring and processing marine vibrator data in the transition zone: 68th Annual International Meeting, SEG, Expanded Abstracts, 136–139, doi: 10.1190/1.1820159.

Sochacki, J., R. Kubichek, J. George, W. R. Fletcher, and S. Smithson, 1987, Absorbing boundary conditions and surface waves: Geophysics, **52**, no. 1, 60–71, doi: 10.1190/1.1442241.

Soubaras, R., 2010, Deghosting by joint deconvolution of a migration and a mirror migration: 80th Annual International Meeting, SEG, Expanded Abstracts, 3406–3410, doi: 10.1190/1.3513556.

Soubaras, R., and R. Dowle, 2010, Variable-depth streamer–a broadband marine solution: First Break, **28**, no. 12, 89–96, doi: 10.3997/1365-2397.28.12.44692.

Stein, E. M., and R. Shakarchi, 2011, Fourier analysis: An introduction: Princeton University Press.

Sun, H., and L. Demanet, 2020, Extrapolated full-waveform inversion with deep learning: Geophysics, **85**, no. 3, R275–R288, doi: 10.1190/geo2019-0195.1.

Sun, J., S. Slang, T. Elboth, T. Larsen Greiner, S. McDonald, and L.-J. Gelius, 2020, A convolutional neural network approach to deblending seismic data: Geophysics, **85**, no. 4, WA13–WA26, doi: 10.1190/geo2019-0173.1.

Sutskever, I., J. Martens, G. Dahl, and G. Hinton, 2013, On the importance of initialization and momentum in deep learning: International Conference on Machine Learning, 1139–1147.

Sutskever, I., O. Vinyals, and Q. V. Le, 2014, Sequence to sequence learning with neural networks: Advances in Neural Information Processing Systems, 3104–3112.

Sønneland, L., L. E. Berg, P. Eidsvig, A. Haugen, B. Fotland, and J. Vestby, 1986, 2-d deghosting using vertical receiver arrays: 56th Annual International Meeting, SEG, Expanded Abstracts, 516–519, doi: 10.1190/1.1893019.

Tamura, S., and M. Tateishi, 1997, Capabilities of a four-layered feedforward neural network: four layers versus three: IEEE Transactions on Neural Networks, **8**, no. 2, 251–255, doi: 10.1109/72.557662.

ten Kroode, F., S. Bergler, C. Corsten, J. W. de Maag, F. Strijbos, and H. Tijhof, 2013, Broadband seismic data - The importance of low frequencies: Geophysics, **78**, no. 2, WA3–WA14, doi: 10.1190/geo2012-0294.1.

Tenghamn, R., S. Vaage, and C. Borresen, 2007, A dual-sensor towed marine streamer: Its viable implementation and initial results: 77th Annual International Meeting, SEG, Expanded Abstracts, 989–993, doi: 10.1190/1.2792571.

Teyssandier, B., and J. J. Sallas, 2019, The shape of things to come—Development and testing of a new marine vibrator source: The Leading Edge, **38**, no. 9, 680–690.

Van der Baan, M., and C. Jutten, 2000, Neural networks in geophysical applications: Geophysics, **65**, no. 4, 1032–1047, doi: 10.1190/1.1444797.

Van Renterghem, T., and D. Botteldooren, 2007, Prediction-step staggered-in-time FDTD: an efficient numerical scheme to solve the linearised equations of fluid dynamics in outdoor sound propagation: Applied Acoustics, **68**, no. 2, 201–216.

Vassallo, M., A. Özbek, K. Özdemir, and K. Eggenberger, 2010, Crossline wavefield reconstruction from multicomponent streamer data: Part 1—Multichannel interpolation by matching pursuit (MIMAP) using pressure and its crossline gradient: Geophysics, **75**, no. 6, WB53–WB67, doi: 10.1190/1.3496958.

Virieux, J., 1986, P-SV wave propagation in heterogeneous media: Velocity-stress finite-difference method: Geophysics, **51**, no. 4, 889–901, doi: 10.1190/1.1442147.

Virieux, J., and S. Operto, 2009, An overview of full-waveform inversion in exploration geophysics: Geophysics, **74**, no. 6, WCC127–WCC152, doi: 10.1190/1.3238367.

Vrolijk, J.-W., and G. Blacquière, 2021, Source deghosting of coarsely sampled common-receiver data using a convolutional neural network: Geophysics, **86**, no. 3, V185–V196, doi: 10.1190/geo2020-0186.1.

Wang, M., S. Xu, and H. Zhou, 2020, Self-supervised learning for low frequency extension of seismic data: 90th Annual International Meeting, SEG, Expanded Abstracts, 1501–1505, doi: 10.1190/segam2020-3427086.1.

Wang, Y., A. C. Ramirez, and A. Osen, 2017, A low-frequency deghosting method: Analysis and numerical tests: Geophysics, **82**, no. 5, V285–V296, doi: 10.1190/geo2016-0116.1.

Wason, H., and F. J. Herrmann, 2013, Time-jittered ocean bottom seismic acquisition: 83rd Annual International Meeting, SEG, Expanded Abstracts, 1–4.

Wedel, A., T. Pock, C. Zach, H. Bischof, and D. Cremers, 2009, An improved algorithm for TV-L1 optical flow: Statistical and Geometrical Approaches to Visual Motion Analysis, 23–45, doi: 10.1007/978-3-642-03061-1_2.

Weekes, K., 1958, On the interpretation of the Doppler effect from senders in an artificial satellite: Journal of Atmospheric and Terrestrial Physics, **12**, no. 4, 335–338.

Weglein, A. B., H. Liang, J. Wu, J. D. Mayhan, L. Tang, and L. Amundsen, 2013, A new green's theorem dehgosting method that simultaneously: (1) avoids a finite difference approximation for the normal derivative of the pressure and, (2) avoids the need for replacing the normal derivative of pressure with the vertical component of particle velocity, thereby avoiding issues that can arise within each of those two assumptions/approaches: theory and analytic and numeric examples: Journal of Seismic Exploration, **22**, no. 5, 413–426.

Whitcombe, D., and L. Hodgson, 2007, Stabilizing the low frequencies: The Leading Edge, **26**, no. 1, 66–72, doi: 10.1190/1.2431833.

Whitmore, N. D., 1983, Iterative depth migration by backward time propagation: 53rd Annual International Meeting, SEG, Expanded Abstracts, 382–385, doi: 10.1190/1.1893867.

Wolfram Research, Inc., 2021, Mathematica, Version 12.3: Champaign, IL.

Wu, Y., and G. A. McMechan, 2018, Feature-capturing full waveform inversion using a convolutional neural network: 88th Annual International Meeting, SEG, Expanded Abstracts, 2061–2065, doi: 10.1190/segam2018-2963265.1.

Yang, F., and J. Ma, 2019, Deep-learning inversion: A next-generation seismic velocity model building method: Geophysics, **84**, no. 4, R583–R599, doi: 10.1190/geo2018-0249.1.

Zach, C., T. Pock, and H. Bischof, 2007, A duality based approach for realtime TV-L1 optical flow: Pattern Recognition, 214–223, doi: 10.1007/978-3-540-74936-3_22.

Zhang, J., and A. B. Weglein, 2005, Extinction theorem deghosting method using towed streamer pressure data: Analysis of the receiver array effect on deghosting and subsequent free surface multiple removal: 75th Annual International Meeting, SEG, Expanded Abstracts, 2095–2098, doi: 10.1190/1.2148125.

Zhang, Z., Z. Wu, Z. Wei, J. Mei, R. Huang, and P. Wang, 2023, Enhancing salt model resolution and subsalt imaging with elastic FWI: The Leading Edge, **42**, no. 3, 207–215, doi: 10.1190/tle42030207.1.

Zhou, W., R. Brossier, S. Operto, J. Virieux, and P. Yang, 2018, Velocity model building by waveform inversion of early arrivals and reflections: A 2D case study with gas-cloud effects: Geophysics, **83**, no. 2, R141–R157, doi: 10.1190/geo2017-0282.1.

Özbek, A., M. Vassallo, K. Özdemir, D.-J. van Manen, and K. Eggenberger, 2010, Crossline wavefield reconstruction from multicomponent streamer data: Part 2—Joint interpolation and 3D up/down separation by generalized matching pursuit: Geophysics, **75**, no. 6, WB69–WB85, doi: 10.1190/1.3497316.

Özdemir, K., A. Özbek, D.-J. van Manen, and M. Vassallo, 2010, On data-independent multicomponent interpolators and the use of priors for optimal reconstruction and 3D up/down separation of pressure wavefields: Geophysics, **75**, no. 6, WB39–WB51, doi: 10.1190/1.3494621.

APPENDIX A
ABSORBING BOUNDARY CONDITIONS

In this Appendix, I formulate the absorbing boundary conditions I use in Chapters 3 and 4.

A.1 Clayton-Enquist boundary condition

In Chapter 3, I use Clayton-Enquist boundary condition (BC) to simulate marine vibrator data for a quiescent sea surface. The BC is applied to all sides of the modeling domain, i.e., I do not implement a free surface BC. Clayton-Enquist BC assumes the incident wavefield is a plane wave, which is not necessarily true even in simple models. However, our numerical examples show that such assumption is adequate to suppress most artificial reflections from the boundary region. To implement such absorbing BCs, I assume the source is stationary in the governing boundary condition PDEs (i.e., I use the boundary condition PDEs as derived in Clayton and Engquist (1977) without any modification that would account for the source motion). Such an assumption is reasonable for low-velocity moving sources because the mesh deformation at the top boundary of the modeling domain is negligible, thus the plane wave assumption in Clayton-Enquist BC is still applicable. However, for fast moving sources, the Clayton-Enquist BC is not applicable. In fact, our numerical tests show that the numerical solution become unstable for all types of implemented absorbing BCs (Clayton-Enquist, Perfectly matched layer (PML), and sponge layer) for fast moving sources. The Clayton-Enquist BC, however, is more stable and can handle source velocities higher than PML and sponge layer BC.

The detailed derivation of the Clayton-Enquist BC can be found in Clayton and Engquist (1977). Here, I simply state the boundary condition PDEs. For the surface defined at

$\xi^3 = \xi^3_{\min}$ (top boundary), the governing PDE is

$$\frac{\partial^2 P_\xi}{\partial\tau\partial\xi^3} - \frac{1}{c_\xi}\frac{\partial^2 P_\xi}{\partial\tau^2} + \frac{c_\xi}{2}\left(\frac{\partial^2 P_\xi}{\partial\xi^1\partial\xi^1} + \frac{\partial^2 P_\xi}{\partial\xi^2\partial\xi^2}\right) = 0, \tag{A.1}$$

where P_ξ is the pressure wave field and c_ξ is the acoustic wavefield in the generalized coordinate system. Given a judicious choice of coordinate transformation, we have $c_\xi = c$, where c is the Cartesian medium velocity. For the surface defined at $\xi^3 = \xi^3_{\max}$ (bottom boundary), the governing PDE is

$$\frac{\partial^2 P_\xi}{\partial\tau\partial\xi^3} + \frac{1}{c_\xi}\frac{\partial^2 P_\xi}{\partial\tau^2} - \frac{c_\xi}{2}\left(\frac{\partial^2 P_\xi}{\partial\xi^1\partial\xi^1} + \frac{\partial^2 P_\xi}{\partial\xi^2\partial\xi^2}\right) = 0. \tag{A.2}$$

For surface defined at $\xi^2 = \xi^2_{\min}$, the governing PDE is given by

$$\frac{\partial^2 P_\xi}{\partial\tau\partial\xi^2} - \frac{1}{c_\xi}\frac{\partial^2 P_\xi}{\partial\tau^2} + \frac{c_\xi}{2}\left(\frac{\partial^2 P_\xi}{\partial\xi^1\partial\xi^1} + \frac{\partial^2 P_\xi}{\partial\xi^3\partial\xi^3}\right) = 0. \tag{A.3}$$

For surface defined at $\xi^2 = \xi^2_{\max}$, the governing PDE is

$$\frac{\partial^2 P_\xi}{\partial\tau\partial\xi^2} + \frac{1}{c_\xi}\frac{\partial^2 P_\xi}{\partial\tau^2} - \frac{c_\xi}{2}\left(\frac{\partial^2 P_\xi}{\partial\xi^1\partial\xi^1} + \frac{\partial^2 P_\xi}{\partial\xi^3\partial\xi^3}\right) = 0. \tag{A.4}$$

For surface defined at $\xi^1 = \xi^1_{\min}$ (left boundary), the governing PDE

$$\frac{\partial^2 P_\xi}{\partial\tau\partial\xi^1} - \frac{1}{c_\xi}\frac{\partial^2 P_\xi}{\partial\tau^2} + \frac{c_\xi}{2}\left(\frac{\partial^2 P_\xi}{\partial\xi^2\partial\xi^2} + \frac{\partial^2 P_\xi}{\partial\xi^3\partial\xi^3}\right) = 0, \tag{A.5}$$

and for surface defined at $\xi^1 = \xi^1_{\max}$ (right boundary), the governing PDE is

$$\frac{\partial^2 P_\xi}{\partial\tau\partial\xi^1} + \frac{1}{c_\xi}\frac{\partial^2 P_\xi}{\partial\tau^2} - \frac{c_\xi}{2}\left(\frac{\partial^2 P_\xi}{\partial\xi^2\partial\xi^2} + \frac{\partial^2 P_\xi}{\partial\xi^3\partial\xi^3}\right) = 0. \tag{A.6}$$

A.2 Perfectly matched layer boundary condition

In Chapter 4, I use PML boundary condition to simulate marine vibrator data in the presence of a time-varying sea surface. The BC is applied to all sides of the modeling domain, except for the top boundary, where I use a free-surface BC to model the effects of a time-varying sea surface. The PML boundary condition is implemented by expanding the modeling domain to add a layer that attenuates the seismic wavefield in the PML boundary region. The linearized continuity equation (4.11) with added PML attenuating term is given

by

$$-g^{0\nu}\frac{\partial P_\xi}{\partial \xi^\nu} + d(\xi^j)P_\xi = \frac{\rho_\xi c_\xi}{\sqrt{|g|}}\frac{\partial}{\partial \xi^i}\left(\sqrt{|g|}u^i\right) + F_\xi, \tag{A.7}$$

with $d(\xi^j)$ given by

$$d(\xi^j) = \frac{-3c_\xi}{2L}\ln(R)\left(\frac{\xi^j}{L}\right)^2, \tag{A.8}$$

where ξ^j is the jth axis in the boundary region (distance from the internal boundary region of the modeling domain), c_ξ is the generalized medium velocity, L is the thickness of the PML boundary region, and R is a constant that is typically chosen between 10^{-3} and 10^{-6}. Similarly, the linearized Euler equation (4.12) with added PML attenuating term is

$$\frac{\rho_\xi c_\xi}{\sqrt{|g|}}\frac{\partial}{\partial \xi^0}\left(\sqrt{|g|}u^i_\xi\right) + d(\xi^j)u^i_\xi = g^{i\nu}\frac{\partial P_\xi}{\partial \xi^\nu}, \tag{A.9}$$

For the top boundary, I implement the free-surface boundary condition given by

$$P_\xi = 0 \tag{A.10}$$

for the pressure wavefield, and

$$\begin{cases} \dfrac{\partial u^1_\xi}{\partial \xi^3} = & -\dfrac{\partial u^3_\xi}{\partial \xi^1} \\ \dfrac{\partial u^2_\xi}{\partial \xi^3} = & -\dfrac{\partial u^3_\xi}{\partial \xi^2} \\ \dfrac{\partial u^3_\xi}{\partial \xi^3} = & -\left(\dfrac{\partial u^1_\xi}{\partial \xi^1} + \dfrac{\partial u^2_\xi}{\partial \xi^2}\right) \end{cases} \tag{A.11}$$

for the particle velocity wavefield.

APPENDIX B
COPYRIGHT PERMISSION

This appendix details the permission to reproduce papers published in *Geophysics* in the dissertation. On their website (https://library.seg.org/page/policies/open-access) they state ***Authors may reuse all or part of their papers published with SEG in a thesis or dissertation that authors write and are required to submit to satisfy criteria of degree-granting institutions***, which is annotated with a red box in Figure B.1.

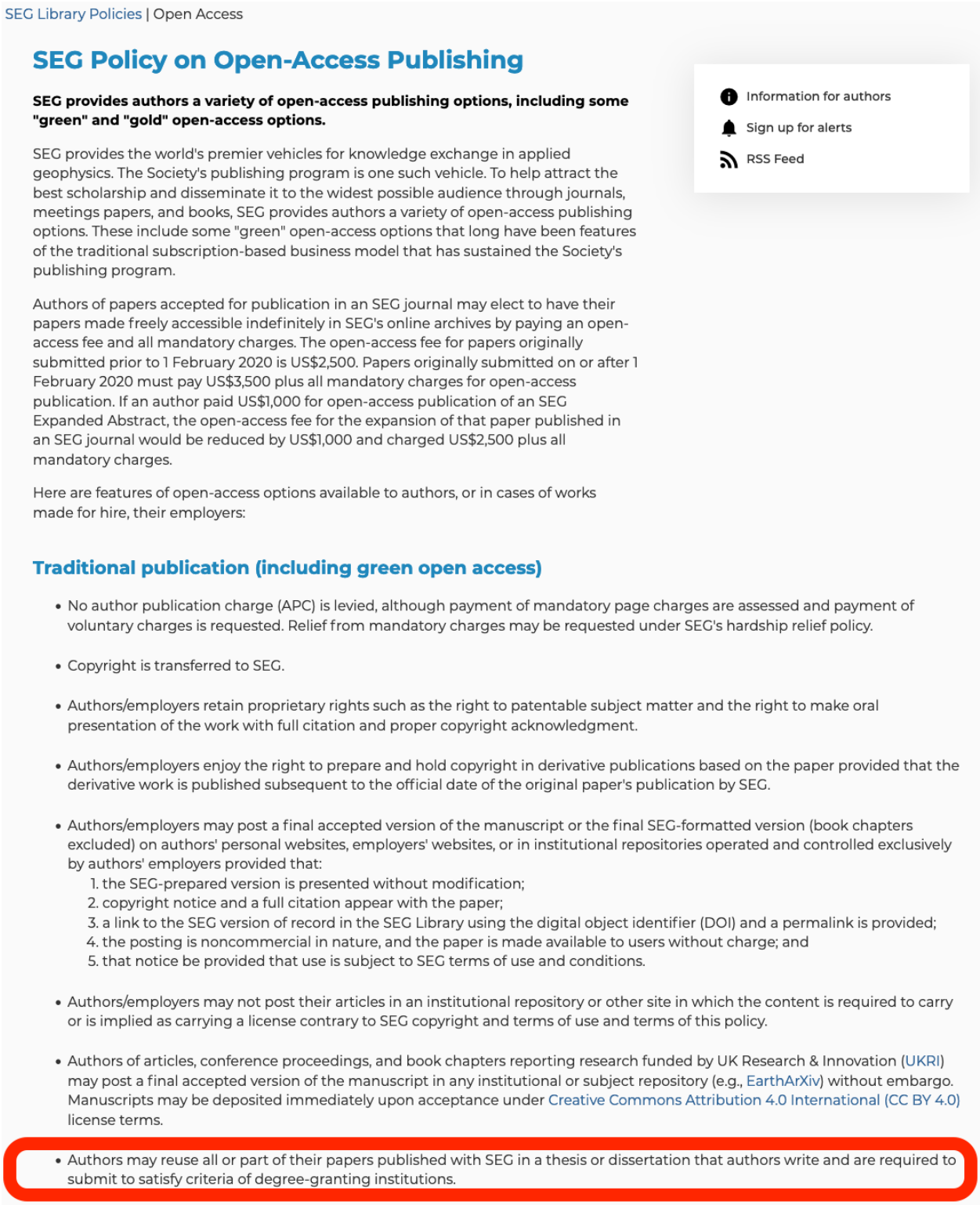

SEG Library Policies | Open Access

SEG Policy on Open-Access Publishing

Information for authors
Sign up for alerts
RSS Feed

SEG provides authors a variety of open-access publishing options, including some "green" and "gold" open-access options.

SEG provides the world's premier vehicles for knowledge exchange in applied geophysics. The Society's publishing program is one such vehicle. To help attract the best scholarship and disseminate it to the widest possible audience through journals, meetings papers, and books, SEG provides authors a variety of open-access publishing options. These include some "green" open-access options that long have been features of the traditional subscription-based business model that has sustained the Society's publishing program.

Authors of papers accepted for publication in an SEG journal may elect to have their papers made freely accessible indefinitely in SEG's online archives by paying an open-access fee and all mandatory charges. The open-access fee for papers originally submitted prior to 1 February 2020 is US$2,500. Papers originally submitted on or after 1 February 2020 must pay US$3,500 plus all mandatory charges for open-access publication. If an author paid US$1,000 for open-access publication of an SEG Expanded Abstract, the open-access fee for the expansion of that paper published in an SEG journal would be reduced by US$1,000 and charged US$2,500 plus all mandatory charges.

Here are features of open-access options available to authors, or in cases of works made for hire, their employers:

Traditional publication (including green open access)

- No author publication charge (APC) is levied, although payment of mandatory page charges are assessed and payment of voluntary charges is requested. Relief from mandatory charges may be requested under SEG's hardship relief policy.
- Copyright is transferred to SEG.
- Authors/employers retain proprietary rights such as the right to patentable subject matter and the right to make oral presentation of the work with full citation and proper copyright acknowledgment.
- Authors/employers enjoy the right to prepare and hold copyright in derivative publications based on the paper provided that the derivative work is published subsequent to the official date of the original paper's publication by SEG.
- Authors/employers may post a final accepted version of the manuscript or the final SEG-formatted version (book chapters excluded) on authors' personal websites, employers' websites, or in institutional repositories operated and controlled exclusively by authors' employers provided that:
  1. the SEG-prepared version is presented without modification;
  2. copyright notice and a full citation appear with the paper;
  3. a link to the SEG version of record in the SEG Library using the digital object identifier (DOI) and a permalink is provided;
  4. the posting is noncommercial in nature, and the paper is made available to users without charge; and
  5. that notice be provided that use is subject to SEG terms of use and conditions.
- Authors/employers may not post their articles in an institutional repository or other site in which the content is required to carry or is implied as carrying a license contrary to SEG copyright and terms of use and terms of this policy.
- Authors of articles, conference proceedings, and book chapters reporting research funded by UK Research & Innovation (UKRI) may post a final accepted version of the manuscript in any institutional or subject repository (e.g., EarthArXiv) without embargo. Manuscripts may be deposited immediately upon acceptance under Creative Commons Attribution 4.0 International (CC BY 4.0) license terms.
- Authors may reuse all or part of their papers published with SEG in a thesis or dissertation that authors write and are required to submit to satisfy criteria of degree-granting institutions.

Figure B.1 Permission from *Geophysics*.